Wideband, Highly Directional Antennas with Fixed and Steerable Patterns

by

Dong-Chan Son

B.S., Ajou University, 2017

M.S., Ajou University, 2019

A thesis submitted to the

Faculty of the Graduate School of the

University of Colorado in partial fulfillment

of the requirements for the degree of

Doctor of Philosophy

Department of Electrical, Computer, and Energy Engineering

2024

Committee Members:

Dejan S. Filipović, Chair

Zoya B. Popović

Cody Scarborough

Mohamed A. Elmansouri

Aman Samaiyar

Son, Dong-Chan (Ph.D., Electrical Engineering)

Wideband, Highly Directional Antennas with Fixed and Steerable Patterns

Thesis directed by Prof. Dejan S. Filipović

This dissertation introduces various wideband, highly directional antennas and examines their design and performance. Initially, it discusses a dual-polarized quad-ridge horn (QRH) antenna with a 3:1 bandwidth. This antenna incorporates a spline-based aspheric dielectric lens with a unique protrusion at its base to ensure sufficient gain across ±4° field of view (FOV). The antenna features exponential-shaped horns and ridges to enhance impedance bandwidth and radiation pattern quality. It also includes a dual-polarization orthomode transducer (OMT) with a turnstile junction (TJ) and custom-designed single- and double-ridge waveguides. A coaxial transition has been developed to adapt the horn for non-waveguide-based transmitters. The design achieves a minimum gain of 21 dBi within the FOV and over 24 dBi in broadside gain, with low sidelobe levels (SLLs) below -15 dB and a cross-polarization discrimination exceeding 30 dB.

The second part of the thesis proposes a wideband, dual-polarized QRH antenna, enabled by additive manufacturing (AM), that operates from 36 to 90 GHz. This modular setup integrates a QRH antenna, a waveguide OMT, a dielectric lens, and an absorber-lined cavity to control radiation patterns. Adding a plano-convex AM dielectric lens augments aperture efficiency to over 70% across the bandwidth. The configuration also features a cavity module with a current sheet absorber, significantly improving the SLL and beam efficiency (BE) and allowing for flush mounting. Achievements include a broadside gain exceeding 26 dBi and radiation and beam efficiencies above 75% and 88%, respectively, with SLLs below -25 dB.

Further, the dissertation presents a 3-D printed wideband, multibeam array with an inhomogeneous lens operating from 36 to 90 GHz. This design consists of five double-ridge horn (DRH) antennas, an absorber-lined ring, a structural spacer, and a shielding cover. Integrating an annular ring-shaped structure with a current sheet absorber notably improves gain and SLL, while the shielding cover reduces electromagnetic interference/compatibility (EMI/EMC) risks. Employing digital light processing (DLP) 3-D printing technology enables prototype fabrication while maintaining tight tolerances. Performance metrics include gains of over 12 dBi for five feeds and a radiation efficiency above 62% at the high frequency end, with SLLs below -12 dB and minimal scan loss (< 0.5 dB).

Finally, the thesis showcases a compact unit-cell design for a circularly polarized microstrip patch array. The unit-cell consists of four sequentially rotated microstrip patch elements with chamfered corners and a cross-slot mounted on a single substrate. This configuration results in a compact size and broadens the axial ratio (AR) and impedance bandwidths. The closely placed elements induce strong mutual coupling. The design methodology and its feasibility are substantiated with a 2x2 finite array prototype featuring integrated series power dividers. Experimental results demonstrate symmetric radiation patterns with a VSWR under 2:1 and a 1dB AR bandwidth over a 56% range, validating the design's application potential in various RF scenarios.

Dedication

To my family

Acknowledgements

Firstly, I sincerely thank my advisor, Prof. Dejan Filipović, for his unwavering support and guidance throughout my Ph.D. journey. His enthusiasm, motivation, and tireless energy have shaped my development as a researcher. I am also profoundly thankful to Dr. Mohamed Elmansouri for being a remarkable role model and friend during my time in the program. Additionally, I appreciate my thesis committee members, including Prof. Zoya Popović, Prof. Cody Scarborough, and Dr. Aman Samaiyar—for their valuable time and contributions to my research. I extend heartfelt thanks to all my friends, and alumni who have accompanied me on this academic journey: David Garrido Lopez, Ehab Etellisi, Prathap Valale Prasannakumar, Haq Nawaz, Amrita Ball, Ljubodrag Boskovic, Liliana C. Filipovic, Carlos Mulero Hernandez, Conrad Andrews, Jake Cazden, Gaeron Friedrichs, Songyi Yen, Theodore Prince, Collin Wallish, Jori Platt, Benjamin Cross, Isaiah Pisani, Aadesh Neel, Joseph Abroquah, Gabriel Altman—your support has been indispensable. My family deserves special mention; I am forever grateful to my wife, parents, parents-in-law, sisters, and brothers-in-law for prioritizing my well-being over theirs. Additionally, I am thankful to the funding agencies, the Office of Naval Research, and Lockheed Martin for supporting my research. Your assistance has been crucial to my academic and professional growth. Lastly, thank you to Prof. Yong Bae Park who gave me the chance and set me on the path to become an RF engineer.

Contents

Chapter

Tables

Table

Figures

Figure

Chapter 1

Introduction

1.1 Background

1.1.1 Quad-Ridge Horn Antenna

Dual-ridged waveguides have been widely used for their wideband characteristic, with analyses predominantly employing transverse-resonance techniques and equivalent circuit formulations to determine cutoff frequencies [1, 2]. Expanding on previous work, reference [3] conducted parametric studies focusing on cutoff frequencies, attenuation, and related parameters. Reference [4] extended these analyses to encompass the complete eigenvalue spectrum of dual-ridged structures. It was demonstrated that dual-ridged waveguides could achieve substantially wider bandwidths than traditional hollow waveguides because the ridges reduce the cutoff frequency of the dominant mode. In this context, "bandwidth" refers to the inverse ratio of the cutoff frequency of the dominant mode to that of the next higher-order mode, representing the single-mode bandwidth [1]. The principal drawback of dual-ridged waveguides and associated horns is their limitation to single linear

polarization. This limitation led to the adoption of quad-ridged structures, which were initially presumed to support comparably wide bandwidths and were necessary for dual linear polarization applications. These quad-ridged waveguides have been studied through finite-element methods and magnetic field integral equations to analyze cutoff frequencies and mode fields for the initial modes, considering variables [5-7]. These studies indicate that although quad-ridged structures also exhibit a reduction in the dominant mode cutoff frequency by nearly a factor of four, their single-mode bandwidth does not match that of dual-ridged designs due to mode splitting, particularly of the TE_{21} and TE_{20} modes in circular and square waveguides, respectively [2]. This splitting causes a significant decrease in the cutoff frequency of one of the split modes due to the ridge loading, affecting the overall bandwidth. Despite these bandwidth limitations, quad-ridged structures remain prevalent in numerous microwave applications that require octave to multi-octave bandwidths [8-12].

1.1.2 Lens Antenna

Lens antennas are a specialized type of directional antenna that utilize dielectric lenses to focus and direct radio waves, thereby improving the performance of the antenna system. This concept was initially explored and developed in the early 20th century, with significant advancements during World War II for radar applications [13]. The principle behind lens antennas is similar to optical lenses such as plano-convex, bi-convex, equi-convex, and meniscus [13, 14], which manipulate light waves; in lens antennas, dielectric materials are used to focus and shape radio frequency (RF) waves. The history of lens antennas began in the 1940s when they were first used in radar technology to enhance signal directionality and range [13].

The early designs were primarily Luneburg lenses, spherical lenses with a radially varying dielectric constant, allowing for the focusing of electromagnetic waves to a point on the lens's surface regardless of the direction of wave incidence, making it highly effective for radar applications. Over the decades, various materials and configurations, such as the Rotman and Fresnel zone lenses, have been developed to address specific technical challenges and application needs [15, 16]. Lens antennas offer several advantages, including high directivity and gain, focusing the energy more efficiently than many other antenna types, which results in better range and signal quality. They can also be designed to have broad bandwidth capabilities, making them suitable for broadband applications. They can be engineered to have low sidelobes, reducing the reception or transmission of interfering signals. Their ability to precisely focus electromagnetic waves also allows for improved spatial filtering, enhancing signal clarity and reducing noise. However, lens antennas also have disadvantages such as their size and weight, especially at lower frequencies where large lenses are required to effectively manipulate the longer wavelengths, making them impractical for portable or space-constrained applications. Additionally, the cost of materials and manufacturing of dielectric lenses can be high, especially for large or specially tailored designs. The performance of lens antennas can significantly degrade if the lens material absorbs too much energy or if imperfections in the lens shape lead to wave scattering.

1.1.3 Antenna Systems for Wideband Direction Finding

This study argues that the difficulties of developing wideband antennas for direction finding and spectrum sensing are manageable and can be effectively addressed. Design of the multi-beam array for amplitude-only direction finding

(AODF) and spectrum sensing is possible by maintaining stringent pattern control across a broad, absolute instantaneous bandwidth. This approach allows for high accuracy and enhanced gain at millimeter-wave frequencies. Furthermore, wide relative bandwidth for AODF and spectrum sensing can be realized through mode and pattern management, incorporating dual polarization for improved performance and efficiency. Additionally, the advent of 3-D printing technologies is crucial in enhancing the feasibility of developing sophisticated, high-performance components for wideband antennas. These technologies enable the fabrication of multi-beam arrays and related devices that not only meet the criteria for wideband and low-loss performance but also allow for significant internal complexity and miniaturization. The integration of 3D printing in the antenna design process reassures the future of antenna design, as it enhances the feasibility of developing sophisticated, high-performance components tailored to the specific needs of wideband communication systems. This innovation in manufacturing could pave the way for more advanced, efficient, and compact antenna systems, facilitating improvements in wideband direction finding and spectrum sensing technologies.

1.1.4 Phased Array

Since their first experimental demonstration in 1905 [17], phased array technologies have developed remarkably, evolving into highly dynamic, responsive, and capable systems. These systems find widespread applications across diverse sectors, including radar, electronic warfare, and communications. Traditionally confined to military and high-budget scientific endeavors due to their steep costs, recent reductions in production expenses have been propelled by the increased availability of cost-effective front-end electronics and enhancements in

manufacturing processes. This shift has enabled the widespread adoption of phased arrays in commercial and civilian sectors, finding uses in satellite internet services, cellular towers, automotive radars, and Wi-Fi routers.

The structure of phased arrays, which allows for the electronic steering of beams without moving parts, contributes significantly to their versatility and reliability in various applications. This electronic beam steering is achieved through the precise timing and phasing of signals across multiple antenna elements, enabling rapid directional changes of the beam. Such capabilities are critical in applications requiring quick response times and high accuracy, such as tracking fast-moving objects in military radar systems or managing multiple data streams in communications satellites. As communication technologies continue to advance, the role of phased arrays is expected to become increasingly significant. This growth is driven by developments in the Internet of Things and the progressive upgrades of cellular networks, including the implementation of 5G Advanced and the forthcoming introduction of 6G technologies. These advancements are set to offer enhanced connectivity and more sophisticated network functionalities, with phased array technologies playing a pivotal role in shaping the future of communication infrastructures. With ongoing advancements, phased arrays are anticipated to become even more integrated and prevalent in telecommunication systems, cementing their status as a fundamental component of modern communications.

1.1.5 Sequential Rotation Technique

The sequential rotation technique in antenna arrays is a sophisticated method used to generate circular polarization (CP) and improve polarization purity across the antenna bandwidth [19]. This technique involves arranging multiple

antenna elements in a specific geometric configuration, often in a circular or square lattice, and systematically rotating each successive element by a predefined angle, typically in increments of 90 degrees, corresponding to phase shifts of {0, ±90°, 180°, ±270°}. This rotation alters the phase of the radiation emitted by each element, resulting in a composite beam that exhibits circular polarization. The technique exploits the phase differences introduced by the rotation, where each component of the array is fed with the same signal amplitude but with a sequential phase shift, leading to circularly polarized radiation, where the electric field vector rotates in a circle perpendicular to the propagation direction. Circular polarization is advantageous for satellite and mobile communications, where antenna orientation might vary and is less susceptible to multipath interference and reflections. Benefits of this technique include enhanced polarization control, allowing for tailored antenna arrays without additional components, and improved signal integrity, which is crucial in environments where the receiver orientation varies. However, challenges such as the complexity of design and implementation, which requires precise control over phase and amplitude and limited aperture efficiency. Despite those drawbacks, the sequential rotation technique remains a viable solution for enhancing communication system performance through high-quality circular polarization, with ongoing research and technological advancements continually expanding its potential and easing implementation hurdles.

1.2 Hypothesis and Objectives

The hypothesis of this dissertation is that high quality, low-cost, multifunctional antennas and arrays are enabled by modern design and manufacturing techniques. The thesis introduces a variety of wideband, strongly directional antennas customized for jamming, communication, and spectrum sensing

across various frequency ranges, including mmWave utilization. These designs include primarily additively manufactured horn antennas and an array equipped with a dielectric lens for augmentation of the gain or compact unit-cell configurations.

Specifically, the dissertation examines a variety of wideband antennas, showcasing several methodologies with well-established designs that achieve bandwidth across multiple octaves. The ridge horn antennas, detailed in Chapters 2, 3, and 4, function by transitioning broad waveguide modes into the free space where they propagate as spherical modes [19]. Additionally, wideband microstrip patch array is explored in Chapter 5. This array comprises multiple antenna elements fed in a precise phase alignment to ensure that the radio waves from different elements merge effectively. This superposition helps enhance the power radiated in preferred directions while minimizing it in less desired ones, thus supporting wideband functionality [19]. Moreover, a robust coupling techniques is proposed to achieve wider bandwidth. Through capacitive coupling among neighboring elements, both the aperture and impedance bandwidths of the array are expanded [20-24]. Thus, the thesis focuses on developing three key antenna types: quad-/dual-ridge horn antennas and strongly coupled microstrip patch arrays.

1.3 Methodology and Tools

Full-wave simulation is used throughout this work to study and design antennas and arrays. Commercial tools include Ansys HFSS [25], Altair Feko [26], and CST Studio Suite [27]. These provide three different computational electromagnetic methods (finite element method, method of moments, and finite integration technique, respectively), each with its advantages and disadvantages, in addition to validating results between them. Custom numerical processing and data

plotting is done by using MATLAB [28]. Keysight ADS [29] is used for circuit simulations. When ready for fabrication, the devices go through a design for manufacture (DFM) phase with practical considerations.

Prototyping is performed through a comprehensive combination of subtractive (e.g., computer numerical control milling) and additive methods, ensuring the most accurate representation of the final product. The latter include fused deposition modeling (FDM), stereolithography (SLA), digital light processing (DLP), and 3D printing with copper electroplating. Scattering parameter measurements are performed using vector network analyzers (VNAs). Models used are the Keysight E8363B PNA Network Analyzer. Radiation patterns are measured using the NSI 700S-30 combined spherical near-field and far-field anechoic chamber at the University of Colorado Boulder. The experimental validation is necessary to confirm the theories, simulations, and synthesized expectations presented herein, providing reassurance about the reliability of the results.

1.4 Thesis Organization

This thesis is organized into chapters as follows:

- Chapter 2 discusses the design and performance of a dual-polarized QRH operating over 3:1 bandwidth. In the proposed configuration, the QRH is loaded with a spline-based aspheric dielectric lens having a protrusion on the bottom designed to achieve the required gain over the ±4º FOV. Exponential-shaped horn and ridges are employed to improve both, the impedance bandwidth, and the quality of radiation patterns. An OMT with a TJ and custom single and double-ridge waveguides are developed for dual-polarization. A coaxial transition is also engineered to expand the

horn's use with non-waveguide-based transmitters. More than 24 dBi broadside and 21 dBi minimum gain within the FOV are achieved. Moreover, low sidelobe levels below -15 dB, cross-polarization discrimination greater than 30 dB, and symmetric patterns are demonstrated.

- Chapter 3 presents additive manufacturing enabled wideband, dual-polarized antenna operating from 36 to 90 GHz. This highly modular configuration comprises a QRH antenna with a monolithically integrated waveguide orthomode transducer, a dielectric lens, and an absorber-lined cavity for pattern control. Exponential tapering of the horn, cavity, and ridges enhances the impedance bandwidth and radiation patterns. A 3D-printed plano-convex dielectric lens was added to increase aperture efficiency by over 70% across the band. Moreover, including a cavity module with a current sheet absorber has significantly enhanced the SLL and BE while enabling flush mounting implementation. Various additive manufacturing techniques such as FDM, DLP and SLA are deployed to allow for a prototype with measured VSWR < 2.5:1 from 36 to 44 GHz and < 2:1 for the rest of the band in both channels. Broadside gain exceeding 26 dBi, radiation, and BEs above 75% and 88%, respectively, are obtained. The SLLs < -25 dB and symmetric patterns are also demonstrated. Good agreement between simulation and measurements validates the robustness of the proposed modular antenna system.

- Chapter 4 discusses a 3-D printed wideband, multibeam array with an inhomogeneous lens operating from 36 to 90 GHz.. This configuration comprises five double-ridge horn antennas with a monolithically

integrated absorber-lined ring, an inhomogeneous lens with a structural spacer, and a shielding cover for pattern control. Including a ring structure with a current sheet absorber has been shown to significantly enhance the gain and SLL, while the shielding cover helps mitigate the potential issues of electromagnetic interference and compatibility. DLP 3-D printing technique is deployed to enable a prototype with a measured VSWR < 2.1:1 across the entire frequency band. Gains of five channels exceeding 12 dBi and radiation efficiency above 62% at the end of the frequency band are achieved. The SLLs < -12 dB, a crossover level < 3.5 dB, and symmetric patterns in the E- and H-planes are also demonstrated. The good agreement between theory and measurements validates the robustness of the proposed array system. The feasibility of correlation-based AODF systems is also discussed.

- Chapter 5 proposes a compact unit-cell configuration for a circularly polarized microstrip patch array. This unit-cell comprises four sequentially rotated microstrip patch elements with chamfered corners and a cross-slot on a single substrate. Incorporated features lead to a more compact size ($0.22\lambda_{26GHz} \times 0.22\lambda_{26GHz}$), wider axial ratio (AR), and impedance bandwidths. Designed elements are placed close to each other with an inter-element spacing of $0.22\lambda_{26GHz}$, thus leading to strong mutual coupling. An 8×8 finite array example achieves >56% bandwidth with radiation and aperture efficiencies of >95%, and >97%, respectively. Moreover, the array can scan within an elevation cone of ±60° while maintaining < 3.8 dB scan loss and AR < 3.5 dB from 20 to 32 GHz. The design methodology and its feasibility are validated with a proof-of-concept prototype consisting of a simplified 2×2 finite array with

integrated series power dividers. Measured results showcase symmetric radiation patterns over >56% wide VSWR < 2:1 and 1dB AR bandwidth. Good agreement between simulation and experiments validates the proposed unit-cell, its design concept, and its candidacy for many RF applications.

- Chapter 6 summarizes the work, lists contributions to this thesis, and outlines possible extensions to the research contained herein.

Chapter 2

High EIRP Dielectric Lens-Corrected Quad-Ridge Horn Antenna

2.1. Introduction

Horn antennas have been deployed in traditional and innovative terrestrial- and space-based RF systems for applications such as microwave communications, metrology, remote sensing, ground penetrating radars, and electronic warfare. These systems can achieve high directivity, gain, and power handling capability across their operating bandwidth [1, 30]. To further enhance bandwidth, horns typically use ridges within smooth walls to simultaneously lower cutoff frequency while increasing the turn on frequency of the higher-order modes. A quad-ridge embodiment is used in the context of dual-polarized operation, making them even more desirable candidates for the previously mentioned applications. One of the significant challenges to achieving high gain with single-mode horns is the long axial length required to compensate for the aperture's quadratic phase errors [31]. To overcome

this, methods such as corrugations, metamaterials, or reflectors [32-35] are often considered. It is seen that a corrugated horn with a short axial length and 15-20° flare angle has radiation shoulders that broaden the pattern and increase the spillover [32, 33]. Reflectors are more difficult to integrate on a platform [34, 35], whereas metamaterials reduce power handling and typically restrict bandwidth to an octave [36]. A well-known method to correct phase errors on horn aperture is to use dielectric fill or lens. Various shapes and materials can be combined to correct the phase error of relatively short horns and thus improve their directivity [36]-[46]. Interesting results are obtained with metamaterial structures having artificially engineered permittivity profiles [36-39]. Whereas these antennas demonstrate some size and weight reductions, their realizability at very high frequencies [37, 38], dispersion, and anisotropy [39] may present a challenge for widespread use. Gradient refractive index (GRIN) [40-42] lenses are broadband and particularly interesting for aperture phase correction. They can achieve high gain at the expense of one or more between heavy/bulky structures, complicated realization, and/or high cost. For mechanical, cost, and technology maturation considerations, a constant dielectric lens [43-46] remains a viable solution when high gain over a wide bandwidth is required. Furthermore, lower-weight dielectrics, such as high-density polyethylene (HDPE), can be utilized in cases where weight and environmental exposure are critical.

In this chapter, the design of a lens-corrected dual-polarized quad-ridged horn antenna (Fig. 2.1) operating over 3:1 bandwidth (6.5-20 GHz) is discussed. Based on our initial work in [46], to achieve high/constant minimum gain in the required narrow 8° field of view, the lens profile is modified into a spline curve with a protrusion at the bottom. As a result, high directivity, gain in FOV >21 dBi, and cross-polarization discrimination (XPD), as well as low side lobe levels, are obtained. For dual-polarized operation, a turnstile junction orthomode transducer with custom designed single and double-ridge waveguide lines is designed and integrated with the

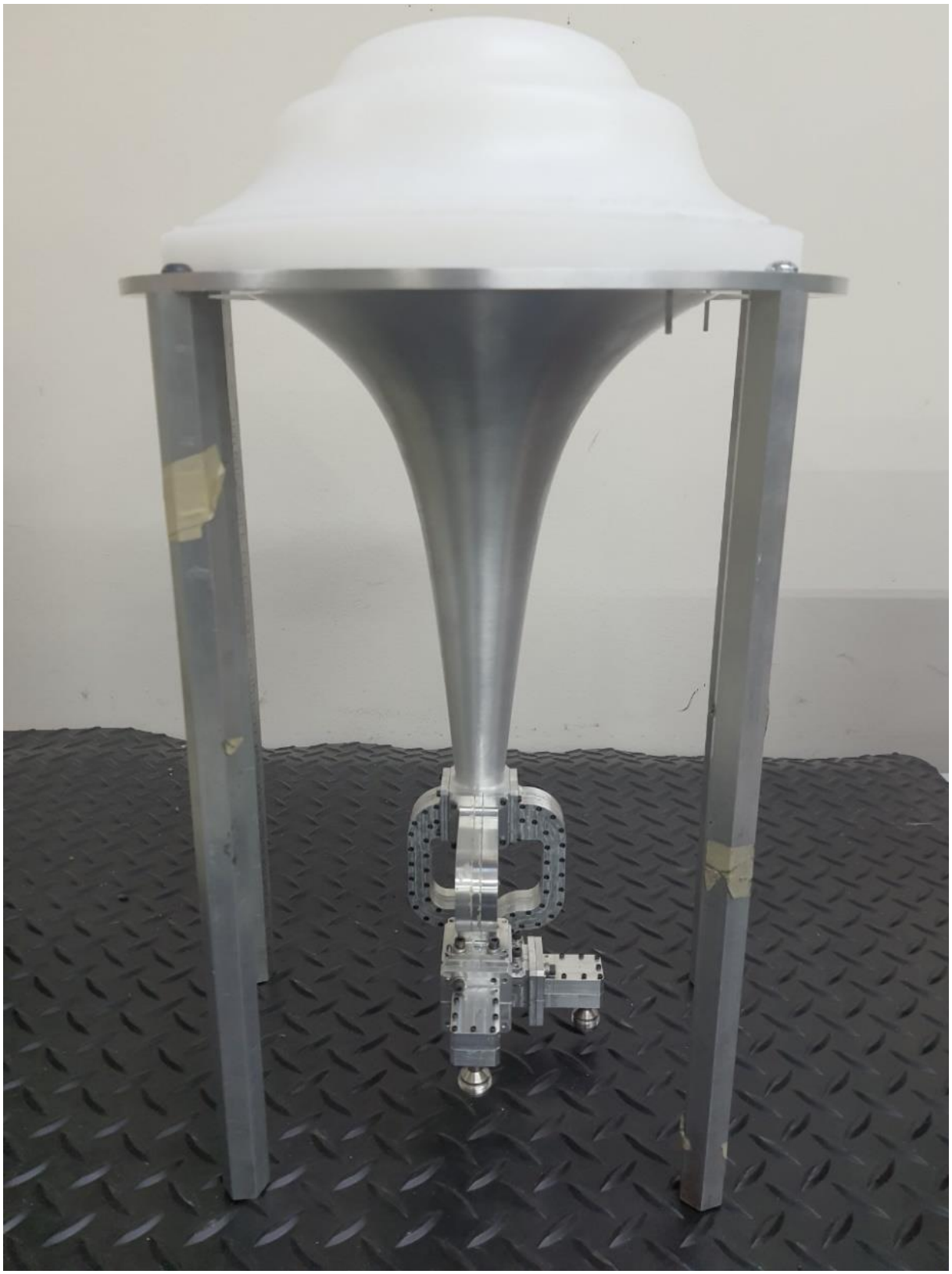

Fig. 2.1: Photograph of the fabricated lens-corrected dual-polarized QRH antenna

lens loaded QRH. Whereas double-ridge waveguide allows integration with the traveling wave tubes, custom coaxial adapters have also been developed to connect with contemporary solid-state amplifiers. The impact of mechanical tolerances and theoretical peak power are studied, and relevant conclusions are provided. Good agreement between the measurements and simulations validates the robustness of the delivered configuration.

This chapter is organized as follows. Sections 2.2 and 2.3 discuss the quad-ridge horn and spline-based aspheric dielectric lens, respectively. Antenna and lens fabrication/measurement are described in section 2.4. Finally, Section 2.5 concludes the chapter.

2.2. Quad-Ridge Horn Antenna

Fig. 2.2 shows the configuration of the QRH antenna having an exponential profile tuned to obtain the highest minimum gain in FOV over the operating frequency band. ai and ao are the radii at the feed point and horn aperture, respectively. L is the horn taper length. The aperture diameter and horn length predominately control the low-frequency performance and impedance matching, respectively. Wri is the ridge width, and sr is the gap between the ridges at the feed. The designed values for horn parameters are given in Table 2.1. The basic design of the conical horn antenna profiles consists of tuning several key parameters to achieve the requirements [47]. Since the horn/ridge profiles have a significant impact on the gain response, we studied sinusoid, tangential, elliptical, x^p, and exponential profiles (see Fig. 2.3). As the outcome of this study, the exponentially tapered profile, defined in (2.1) is selected due to the reduced aperture phased errors and wider return loss

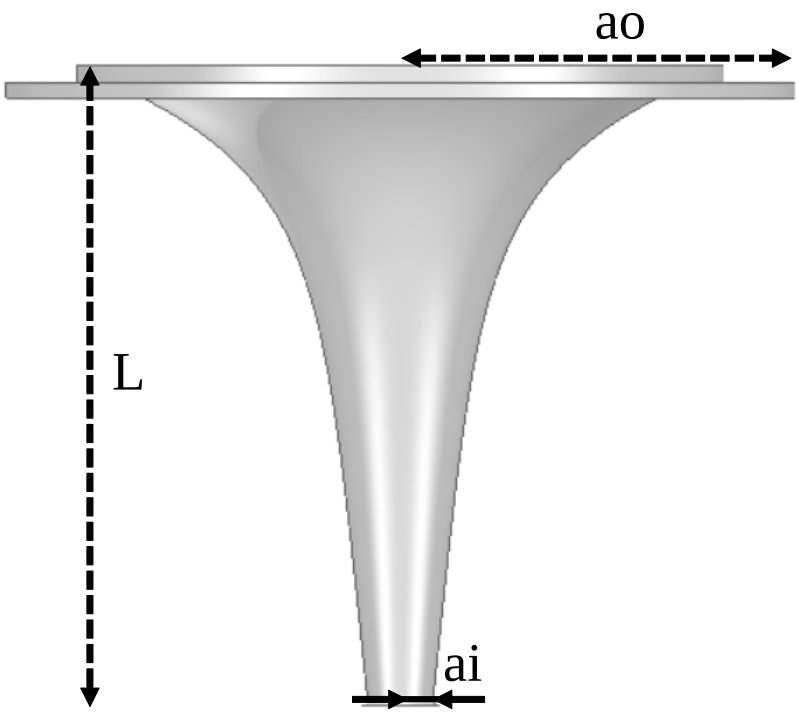

(a)

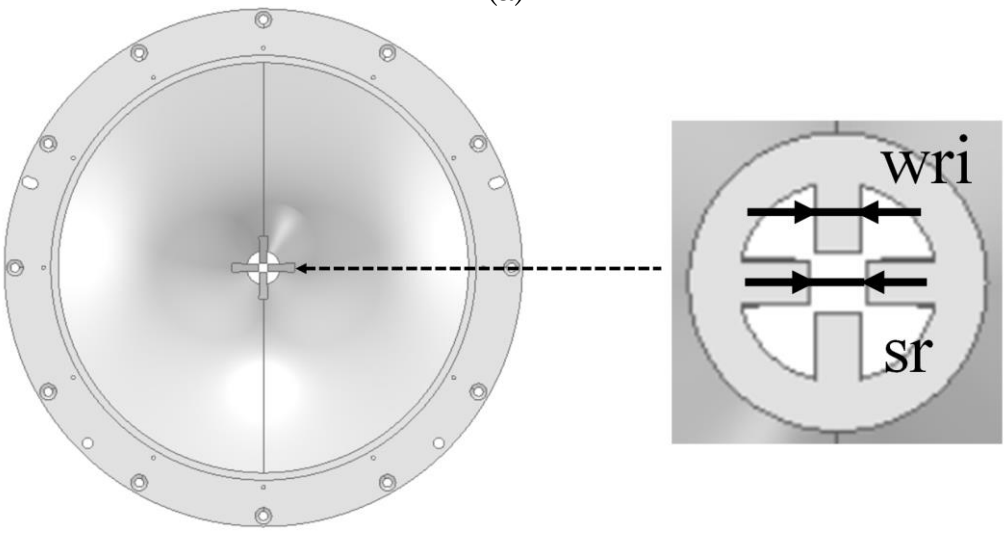

(b) (c)

Fig. 2.2: QRH antenna: (a) Configuration (b) Aperture, and (c) Feed.

Table 2.1 Design Parameters of QRH Antenna

Parameter	ai	ao	L	Wri	sr
Value (mm)	12.9	124.7	252	4.4	6.06

bandwidth. Moreover, the exponential taper has a higher degree of freedom in design than other profiles [47]:

$$a(z) = A(C_1 e^{Rz} + C_2) + (1-A)[\, a_i + (a_o - a_i)(z/L)] \tag{2.1}$$

where $C_1 = (a_o - a_i)/(e^{RL} - 1)$, $C_2 = (a_i\, e^{RL} - a_o)/(e^{RL} - 1)$, parameter A (= 0.86) should be between 0 and 1 for the added linear taper. R (= 28.31) is the exponential opening rate. Note that the former significantly affects the impedance bandwidth such that when the radius is increased, the return loss bandwidth of the horn is broadened while that of the turnstile junction is decreased. The horn aperture diameter and axial length significantly affect both directivity and bandwidth. The ridge and wall profiles are determined by tuning their constitutive parameters to achieve the highest minimum gain in the 8º FOV. The exponentially tapered profile is chosen due to the reduced aperture phased errors, wider return loss bandwidth, lower cross-polarization, and higher design degree of freedom compared to other common options discussed in [47].

2.3. Spline-Based Aspheric Dielectric Lens

In a conventional horn, the tapering of the throat inherently leads to lower directivity. By lens-loading the horn aperture, one can achieve improved directivity or, if desired, a specific beam shape. This is accomplished by correcting and collimating the wavefronts, effectively transforming them from spherical to planar. Specifically, the phase correction is achieved with a dielectric lens having a refractive index ($=\sqrt{\varepsilon_r}$) greater than unity, where εr represents the relative permittivity of the lens material. The conventional design approach for such lenses assumes the

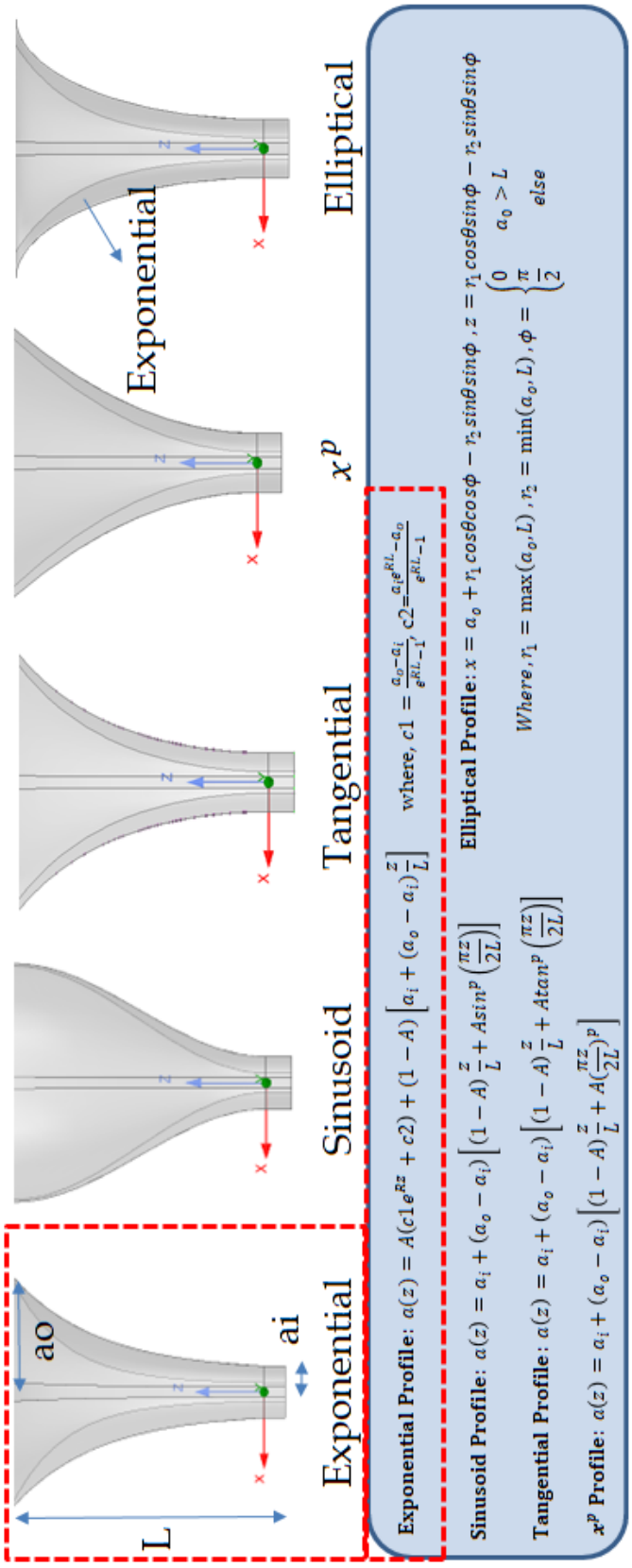

Fig. 2.3. Configurations and equations of ridge-horn profiles.

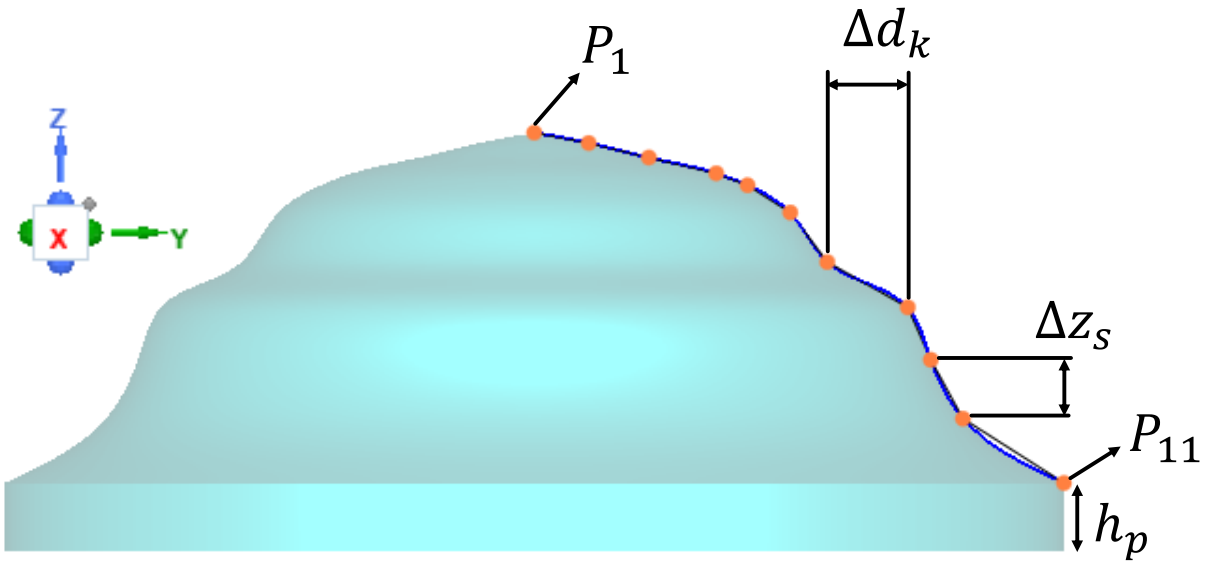

Fig. 2.4: Lens configuration with denoted critical parameter needed to fully reconstruct the three-dimensional lens shape.

applicability of geometric optics, conceptualizing the power emerging from the horn apex as a ray. The foremost principle in geometric optics postulates that power is transmitted along ray paths, and the cumulative power traversing any enclosed surface constitutes a tube of rays. This implies constancy in the total power across any cross-sectional area of a ray tube. The second principle, Fermat's principle, indicates that energy traversing between two points follows the route that minimizes the optical path length [48].

When it comes to lens design, the practical application of an aspheric shape based on cubic spline curves is a crucial consideration. This shape, controlled by several connected nodes, is particularly useful in the context of the lens's axis-symmetry. Only half of the full 2-D profile, as seen in Fig. 2.4, is used for optimization, demonstrating the efficiency and practicality of this design approach. This shape comprises 11 spline nodes (P_1-P_{11}) defined by Δd_k and Δz_s (k and s = 1,…,10), whereas the optimal number of nodes is based on the parametric study. Specifically, the values of P_1 and P_{11} along the y-direction are fixed due to the horn aperture size, and the lens shape is determined by the remaining y- and z-direction values. A protrusion (h_p

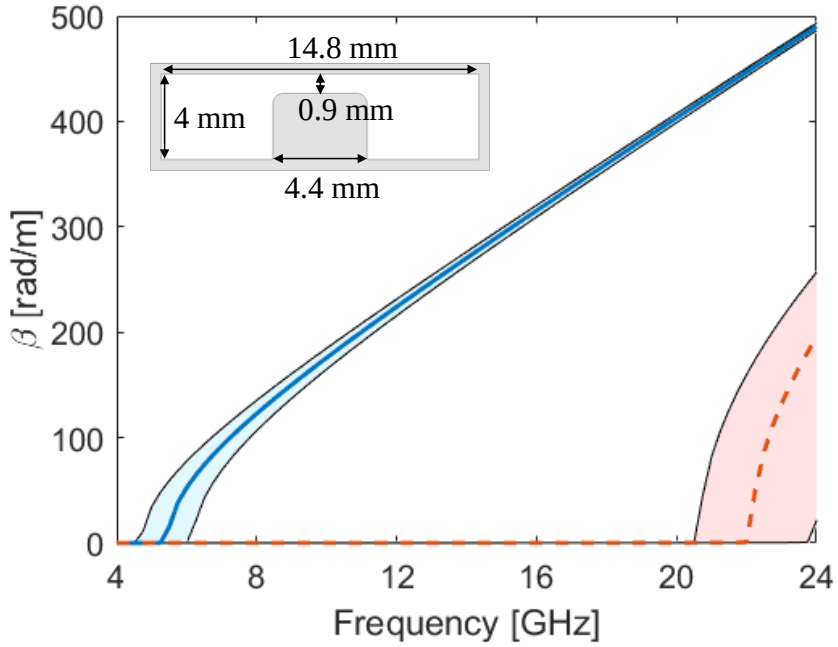

Fig. 2.5: Propagation constants of custom single-ridge waveguide with sensitivity analysis.

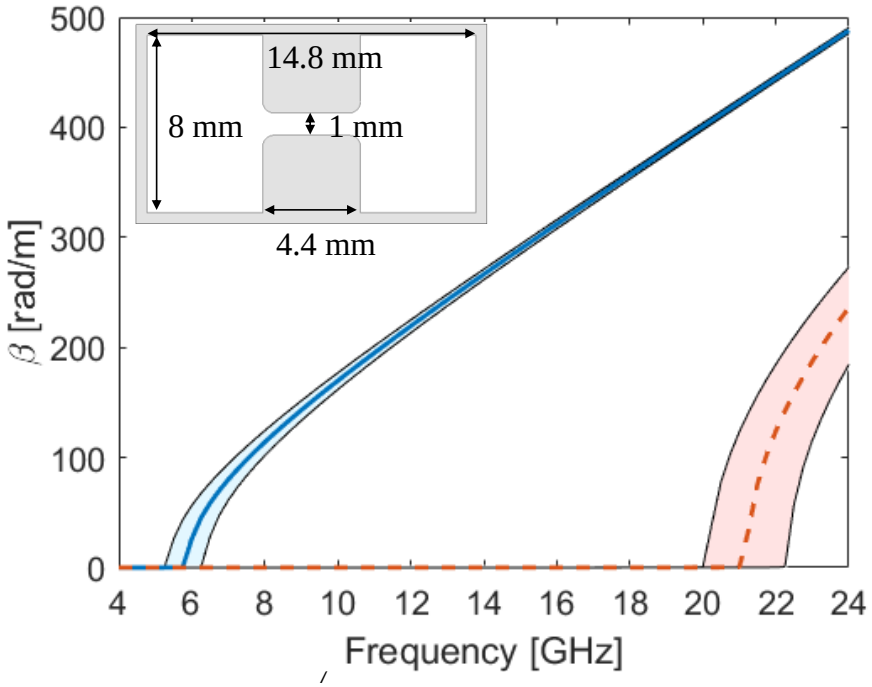

Fig. 2.6: Propagation constants of custom double-ridge waveguide with sensitivity analysis.

= 15.9 mm) on the bottom of the lens is chosen to improve the minimum gain in the FOV further. Due to its low loss, weight, cost, and manufacturability, the HDPE material (ε_r = 2.26 and $tan\delta$ = 0.0005 @ 12.4 GHz, ρ = 0.91 g/cm^3) is used for the lens. The HDPE lens was fabricated in-house using computer numerical control (CNC) 3-axis machining. Since the geometrical algorithm method from [49] cannot accurately calculate the impacts on impedance matching, internal reflections, diffraction, interference, and polarization, the full-wave optimization of the horn and lens is carried out in CST-MWS with the covariance matrix adaptation evolutionary strategy global, and trust region framework local optimizers. The optimization goal was the highest minimum gain in the 8° FOV over the operating frequencies while keeping the SLL lower than -15 dB. The co-design/optimization of the horn and lens is carried out considering the design for manufacturing of both the horn and lens, as well as the desired high-power operation. The OMT consists of a quad-ridge circular waveguide that feeds the horn, a cone-loaded turnstile junction, two bifurcations, both transitioning from single-ridge waveguide to double-ridge waveguide and two custom double-ridge waveguide ports. This design achieves wide fractional bandwidth, reduced insertion loss, high-power handling, and polarization division/combination control while preserving similar electric lengths in both polarization paths [50]. Figs. 2.5 and 2.6 show propagation constants for two dominant modes (to delineate the single-mode bandwidth) and the cross-section of the designed SRWG and DRWG. Shaded regions are the results of sensitivity analysis based on fabrication tolerances. As seen, even with the considered tolerances, the single mode bandwidth is safely within the desired bandwidth of the antenna. The single-ridge waveguide is the same width but one-half height as the double-ridge waveguide. Its ridge-width and -height are 4.4 and 3.1 mm, respectively. To evaluate the peak-power handling capability of the waveguides densely meshed HFSS and CST models are analyzed (see Fig. 2.7). In the inset formula of Fig. 2.7(b), Ec = 3 MV/m is the air dielectric strength. E_{max}/1W

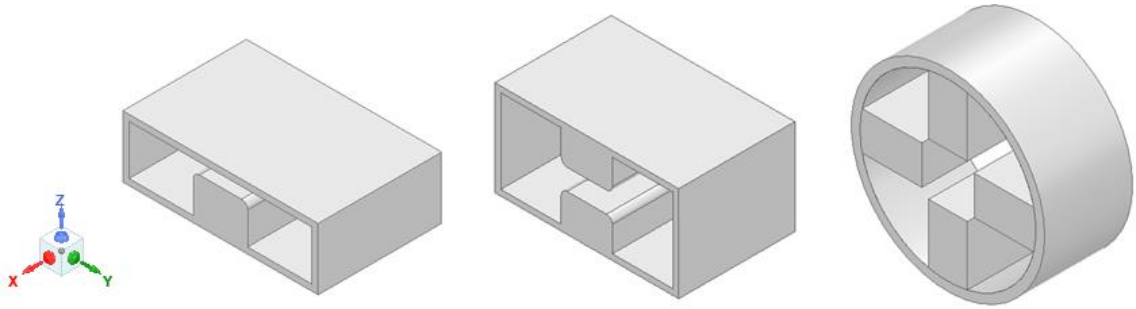

(a)

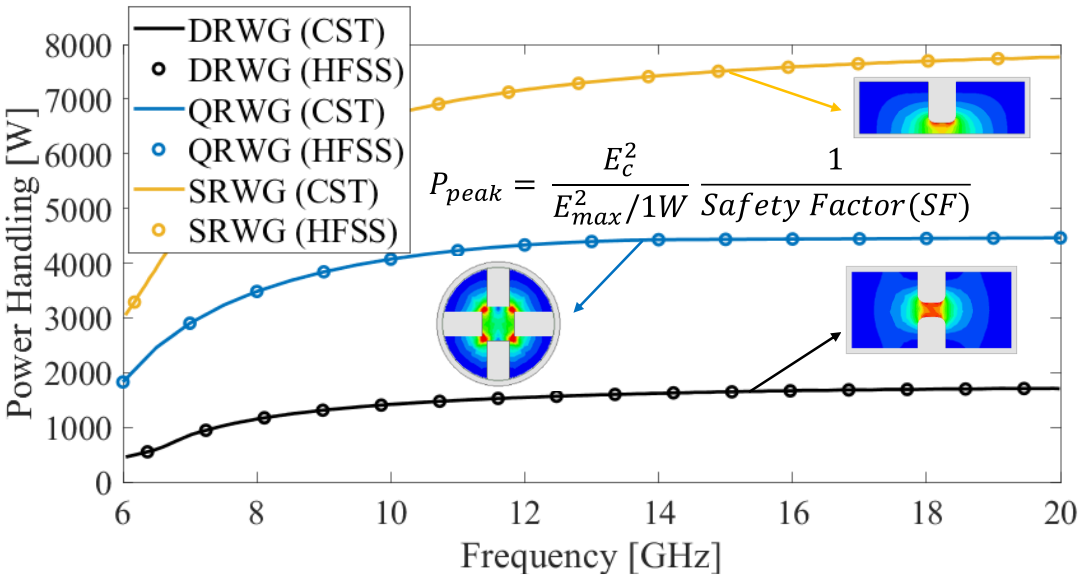

(b)

Fig. 2.7: (a) Waveguide configurations to calculate power handling capability, (b) Peak-power handling capability of waveguides

is the max electric field intensity for 1W input power. The safety factor is 4. In Fig. 2.8, turnstile-junction in OMT has a metallic cone-shaped tuning stub located at the center of the waveguide and machined such to maintain symmetry (needed for wideband operation) [51]. A custom adapter with an orthogonal E-plane transition and N-type connector completes each branch (polarization) of the antenna. Note that N-type connectors can sustain up to 400 W of continuous power through 18GHz [52]. This adapter is built from 3 pieces and resembles a conventional WRD-650 to coax

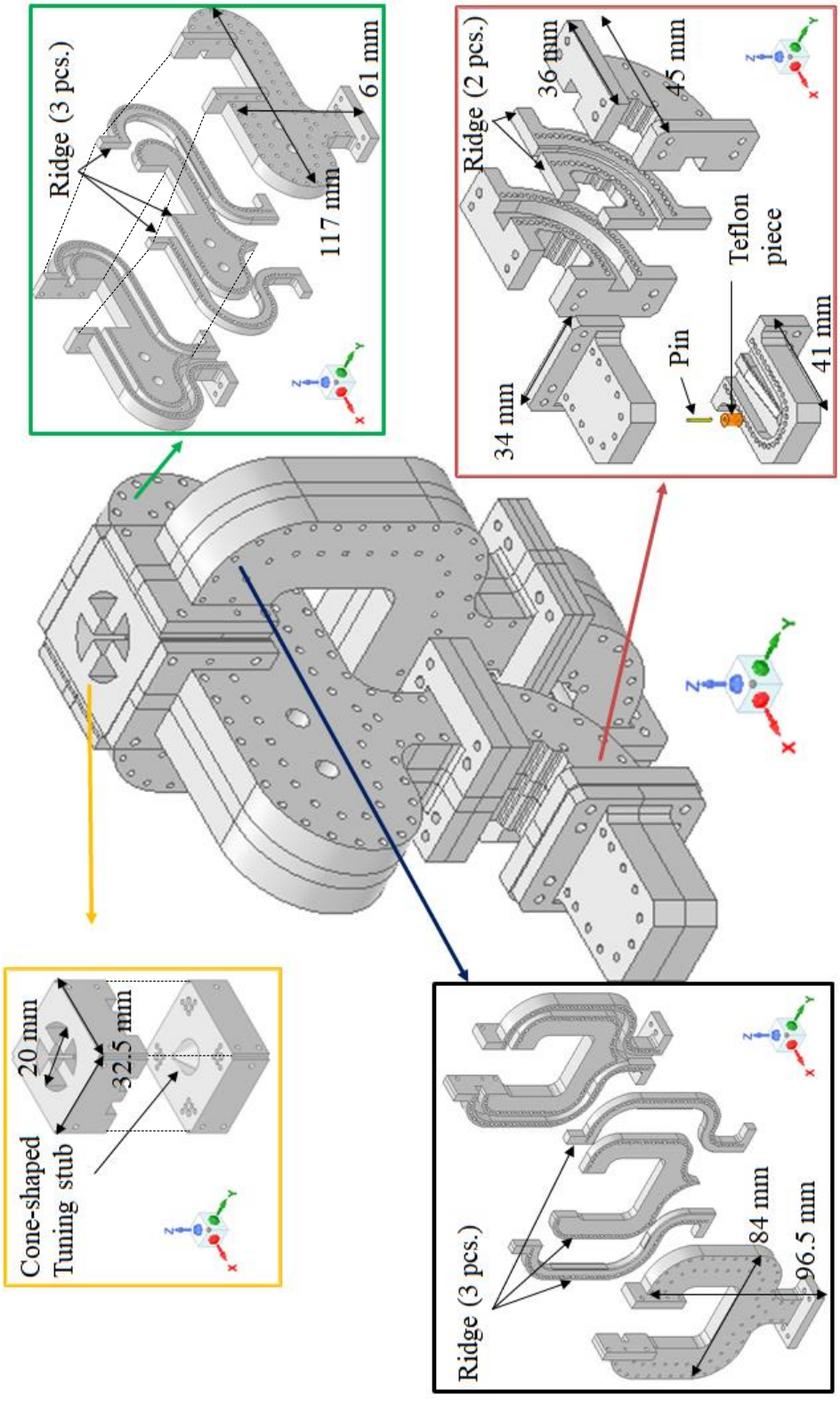

Fig. 2.8: OMT and custom adapter configurations.

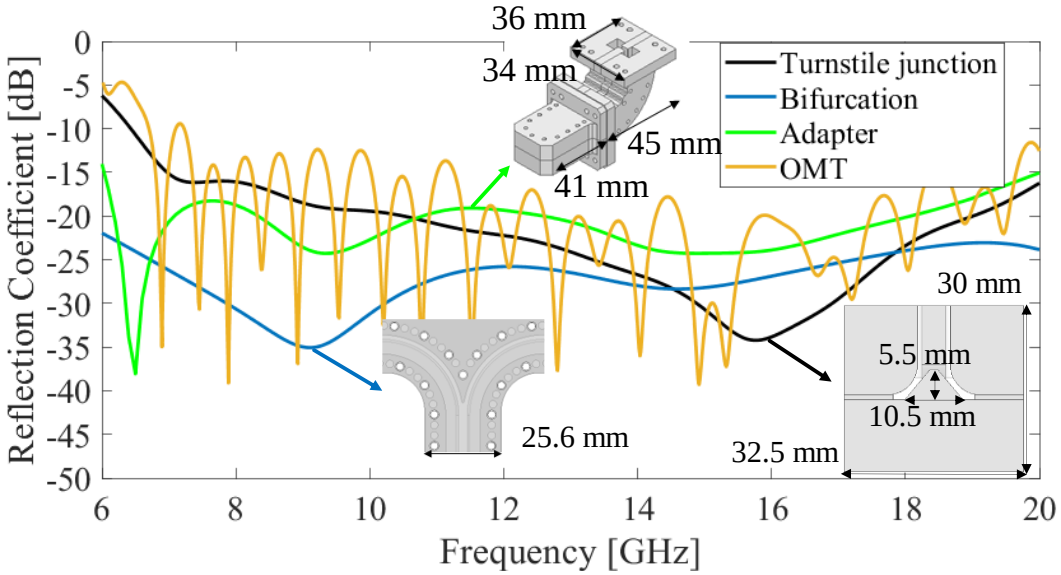

Fig. 2.9: Reflection coefficients of turnstile junction, bifurcation, and custom adapter.

adapter [53]. However, its design is customized for a given application to enable a perpendicular connection between the waveguide and connector in the reduced volumetric footprint. Fig. 2.9 shows the simulated reflection coefficients of the turnstile junction, bifurcation, adapter, and OMT. The OMT reflection coefficients are below -10 dB from 6.7 to 20 GHz. The OMT and adapters are built using split-block machining [54]. The RF leakage and harmful performance spikes are significantly suppressed by placing metallic pin walls at the split block seams [55]. The proposed configuration is shown in Fig. 2.10. The horn is built as a single aluminum piece by combined high-precision electrical discharge machining and CNC processes. The total assembly weighs 4.6 kg (QRH, OMT, and lens are at 1.9 kg, 1.1 kg, and 1.6 kg, respectively). A fluid dynamic module for thermal analysis in Ansys Mechanical Workbench was used to estimate the power handling capability of the proposed lens. Considering an HFSS computed power loss of up to 3% at the high-frequency end, the lens temperature reaches ~ 76°C under a 300 W excitation. Given the continuous usage temperature range for HDPE from -46° to 82° C [56], this confirms the suitability of this lens for operation even with input powers up to 350W

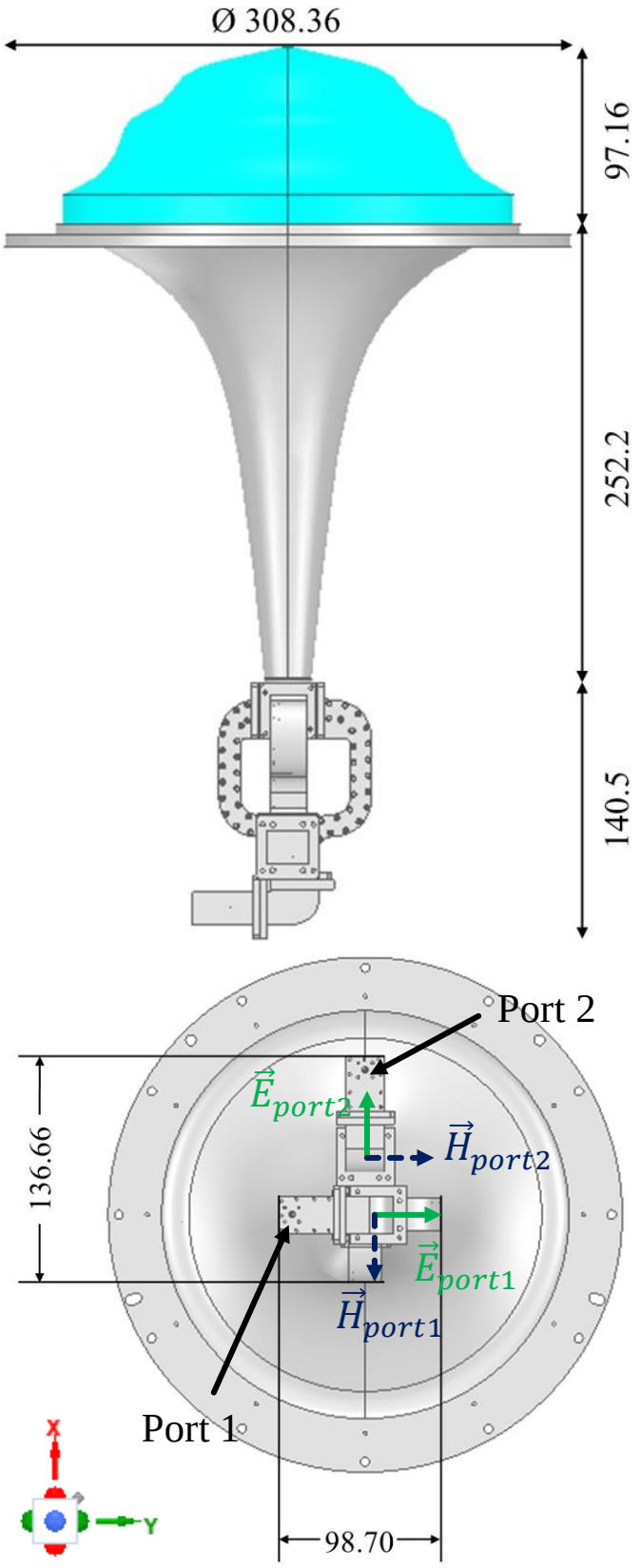

Fig. 2.10: Proposed configuration with custom adapters.

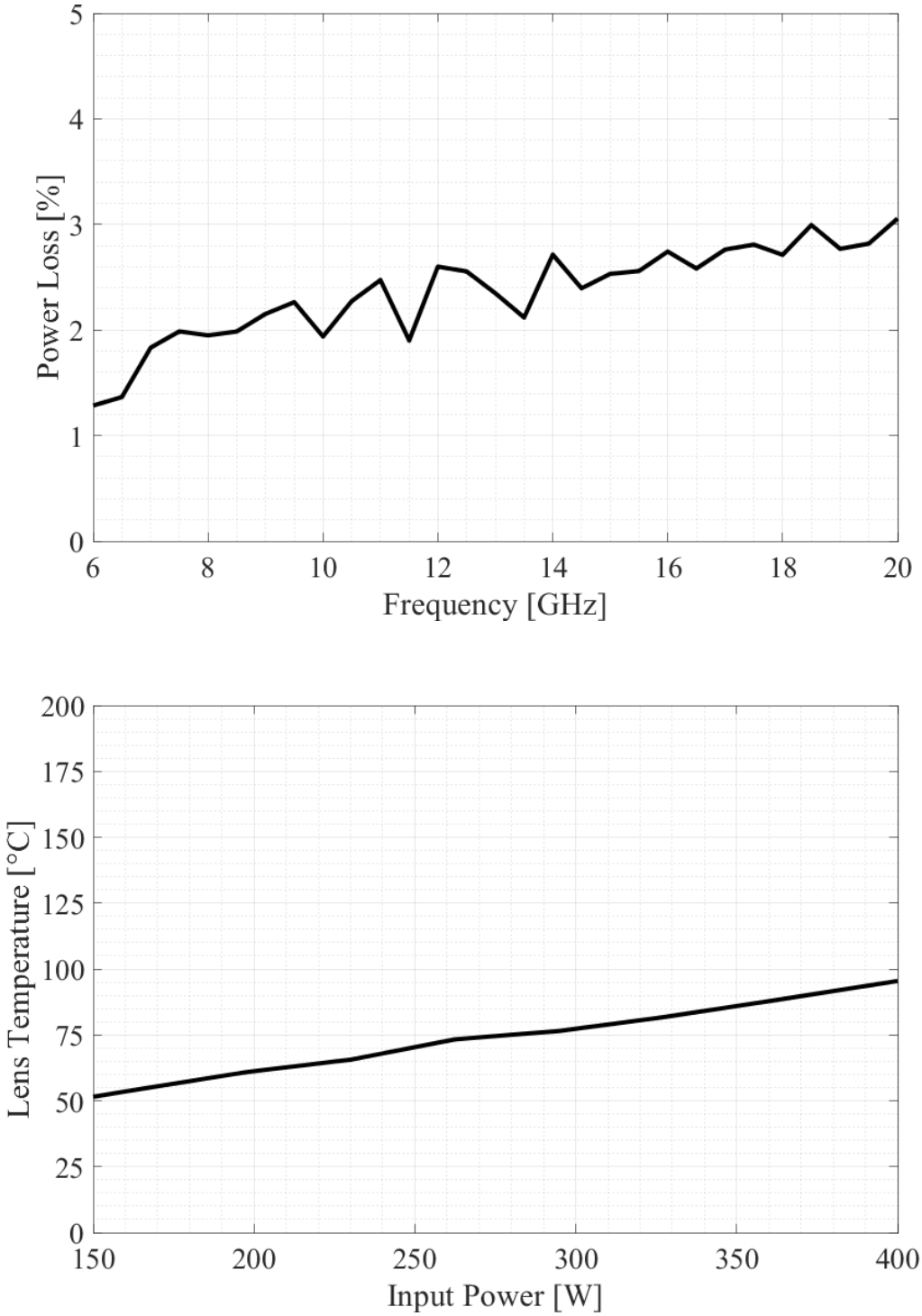

Fig. 2.11: (a) Power loss of a dielectric lens, (b) Simulated lens temperature attributed to input power.

in Fig. 2.11. Notably, a coated matching layer with the lens is not considered. The lens-corrected quad ridge horn antenna with an ideal feed (waveguide port in HFSS)

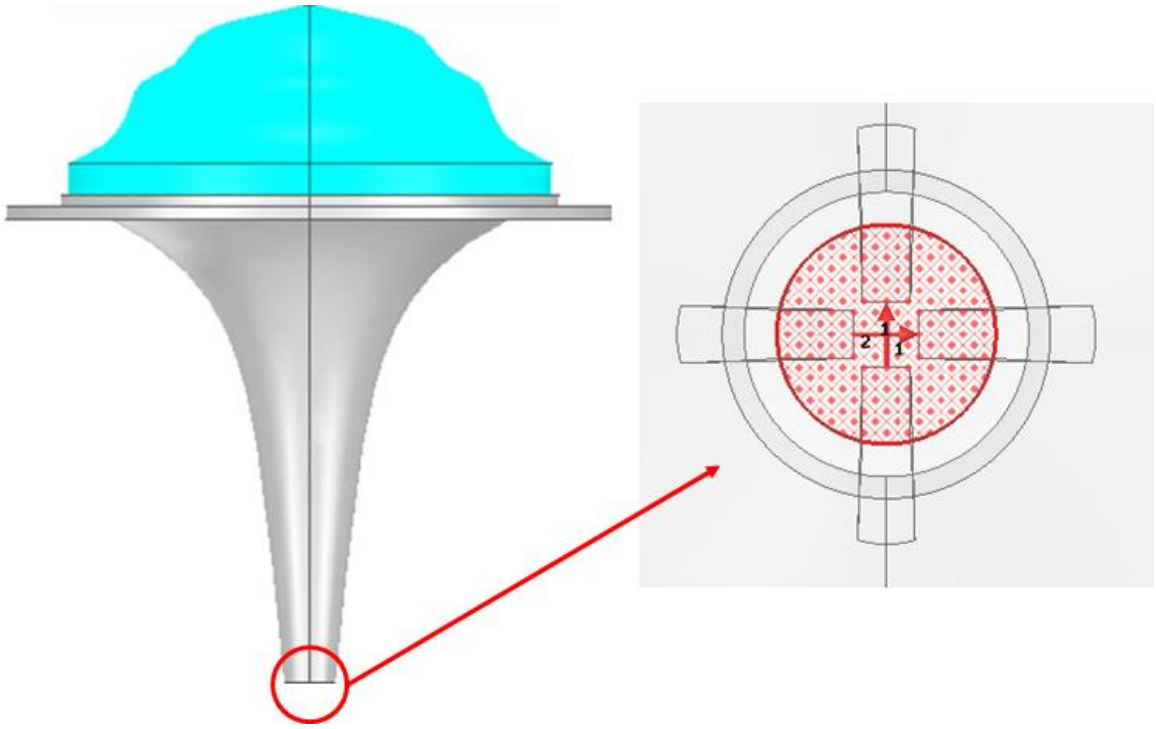

(a)

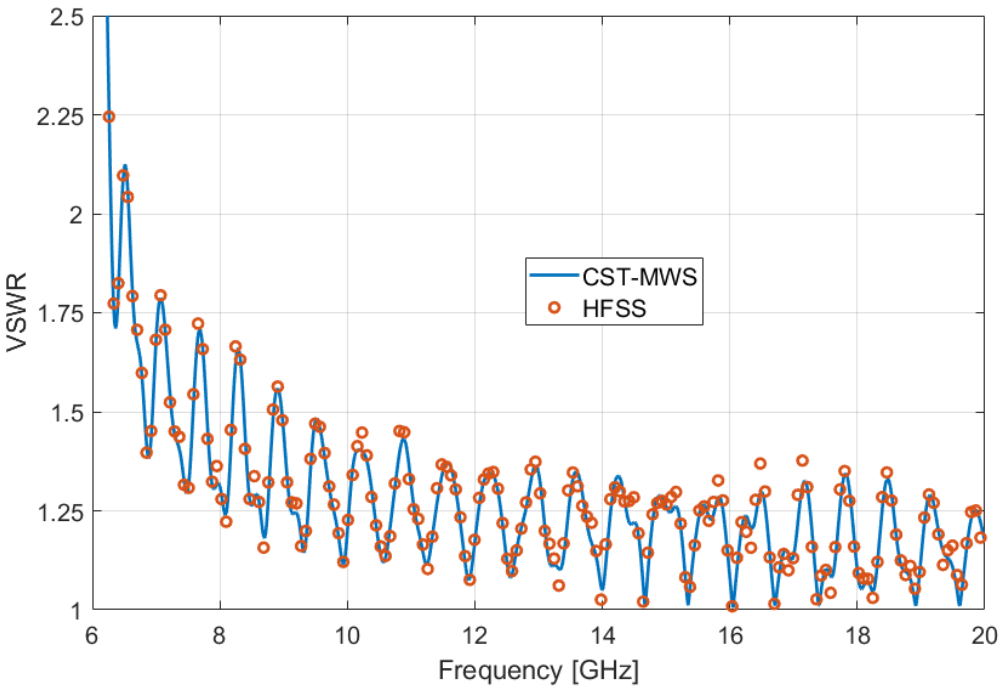

(b)

Fig. 2.12: (a) Lens-corrected quad-ridge horn antenna with the ideal feed (Waveguide Port) in HFSS, (b) Simulated VSWR in both CST-MWS and HFSS.

.

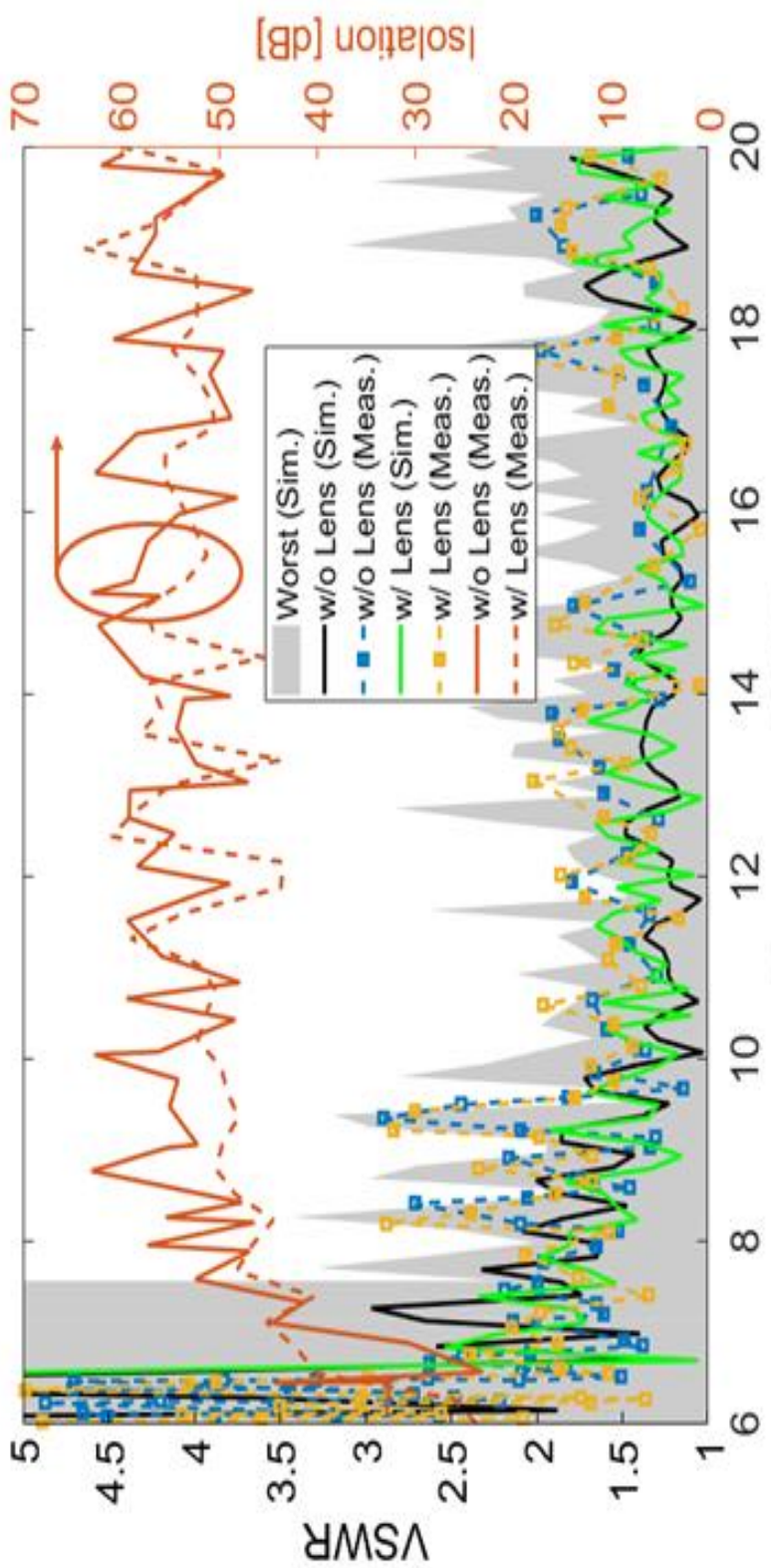

Fig. 2.13: Measured and simulated VSWRs (with sensitivity analysis) and measured isolation of the fabricated dual-polarized horn for the cases with and without the lens.

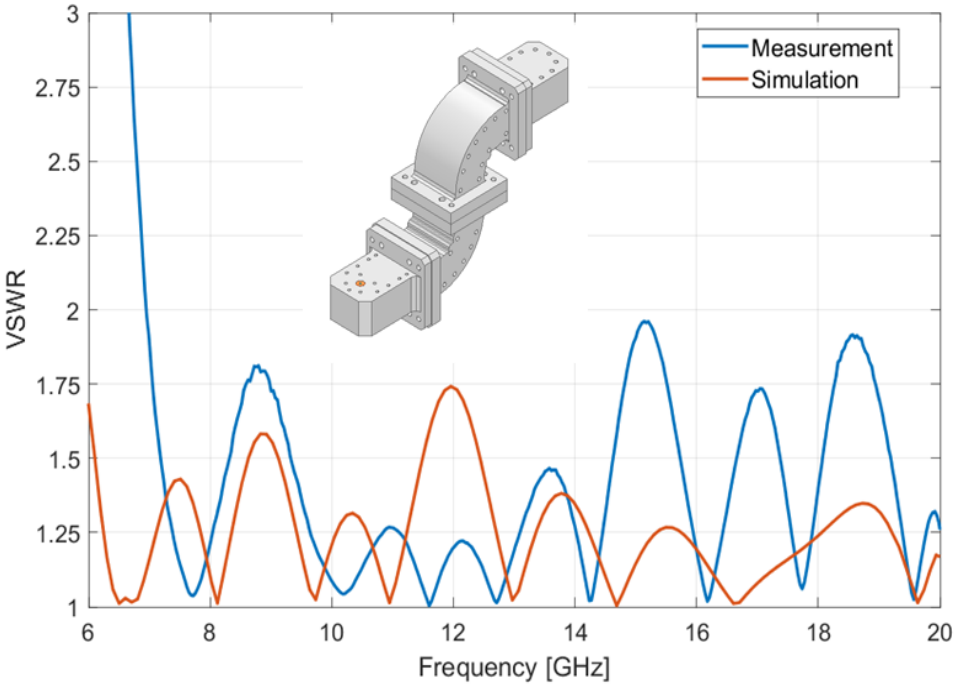

Fig. 2.14: Back-to-back results of custom adapters.

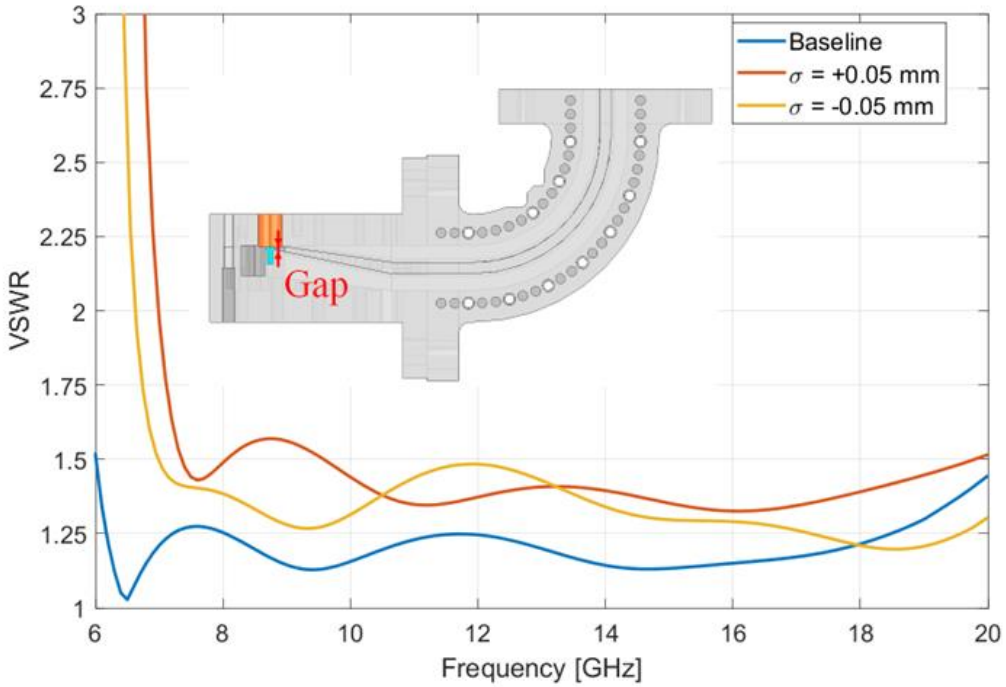

Fig. 2.15: Adapter sensitivity analysis.

has good VSWR (<2:1) over the entire band as depicted in Fig. 2.12. However, the issues with impedance match arise mainly from manufacturing tolerances of the

OMT and custom adapter. In Fig. 2.13, the simulation result for the worst-case scenario (highlighted in gray) is provided with measurement derived from a sensitivity analysis considering tolerances based on the DIN ISO 2768 standard [58] potentially arising in the fabrication process. As seen, VSWR < 3 is measured over 6.5-10 GHz, and VSWR < 2 for the remainder of the bandwidth. Note that the higher mismatches are often tolerated in antenna systems aimed for wideband high-power operation [59, 60]. In our analysis, we observed that the designed custom adapter is more sensitive to fabrication tolerances and is the chief reason for impedance match issues at the low frequency end. We can conclude that the coated matching layer could mitigate the effect of possible reflection on the low frequency end while complicating the lens realization and introducing additional signal losses due to absorption and/or scattering. Furthermore, as depicted in Fig. 2.14, the measured back-to-back results of the custom adapter distinctly indicate a high VSWR in the low frequency band, which cutoff frequency was shifted. This finding leads to the inference that the matching result of the antenna may have been impacted due to the observed impedance mismatching of the adapter in low frequency end, potentially affecting the antenna's performance. Furthermore, the simulation results in Fig. 2.15 reveal that altering the gap between the Teflon piece and the ridge has a considerable influence on the impedance bandwidth (cutoff frequency).

Even a small deviation in the spacing, such as ±0.05 mm from the designed baseline dimension (0.5 mm), can shift the cutoff frequency of the adapter at a low frequency band, leading to the observed mismatching problem. Thus, we can conclude that this is attributed to the manufacturing tolerances in the design of the custom adapters. It is reassuring to know that the custom adapters with N-type connectors were designed as a temporary measure to verify the horn antenna and OMT's design, as mentioned previously in the paper. The intention to use traveling wave tubes (TWTs) in practice is a sound approach to solving the mismatching issue in the low-

frequency band. TWTs have excellent capabilities to handle wider impedance bandwidth and high-power levels, making them a suitable choice for addressing the practical requirements of the antenna system. Considering the limitations of the custom adapters used for testing purposes and planning to utilize TWTs in actual applications, our research demonstrates a comprehensive approach to address mismatching challenges. It ensures that the high-gain antenna system will be well-suited for real-world high-power applications.

2.4. Far-Field Measurements

The far-field measurement is conducted in the anechoic chamber at the University of Colorado Boulder (see Fig. 2.16 for a photo of the antenna inside the range). The unmeasured port is terminated with a 50 Ω load to eliminate unwanted reflections that could interfere with the measurements. Fig. 2.17. shows the measured and simulated far-field behavior of the QRH with (w/) and without (w/o) the lens. Results between ports show good agreement. As seen in Fig. 2.17(a), the lens-loaded horn has a directivity > 24 dBi, corresponding to aperture efficiency variation from 62 to 88% (the lowest value is at the high end of the band). Since the axial length of the horn optimized with the lens is relatively short, the aperture efficiency of the horn itself becomes very low, i.e., from 8 to 20%. Fig. 2.17(b) shows the minimum gain in the required 8° FOV over all azimuth planes. As seen, values greater than 21 dBi over 6.5-20 GHz are achieved, with shaded areas and dashed lines representing the range and average values of minimum gain, respectively. By loading the QRH with the designed lens, minimum gain in the FOV is improved significantly at the low frequency end (6.5-12 GHz), and highly stable gain is achieved over the entire band. The radiation efficiency extracted from measurements and

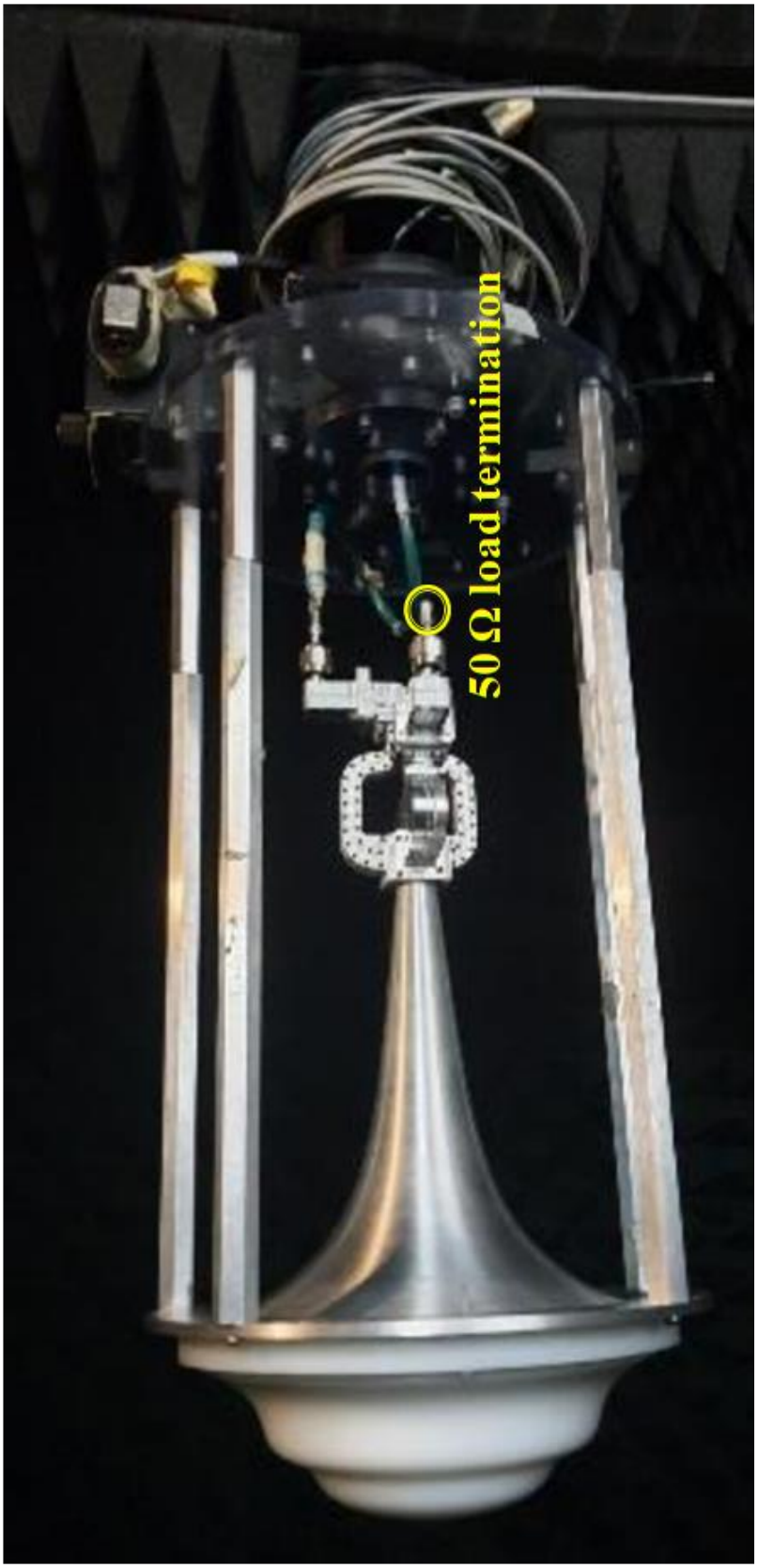

Fig. 2.16: Far-field measurements performed at the University of Colorado Boulder.

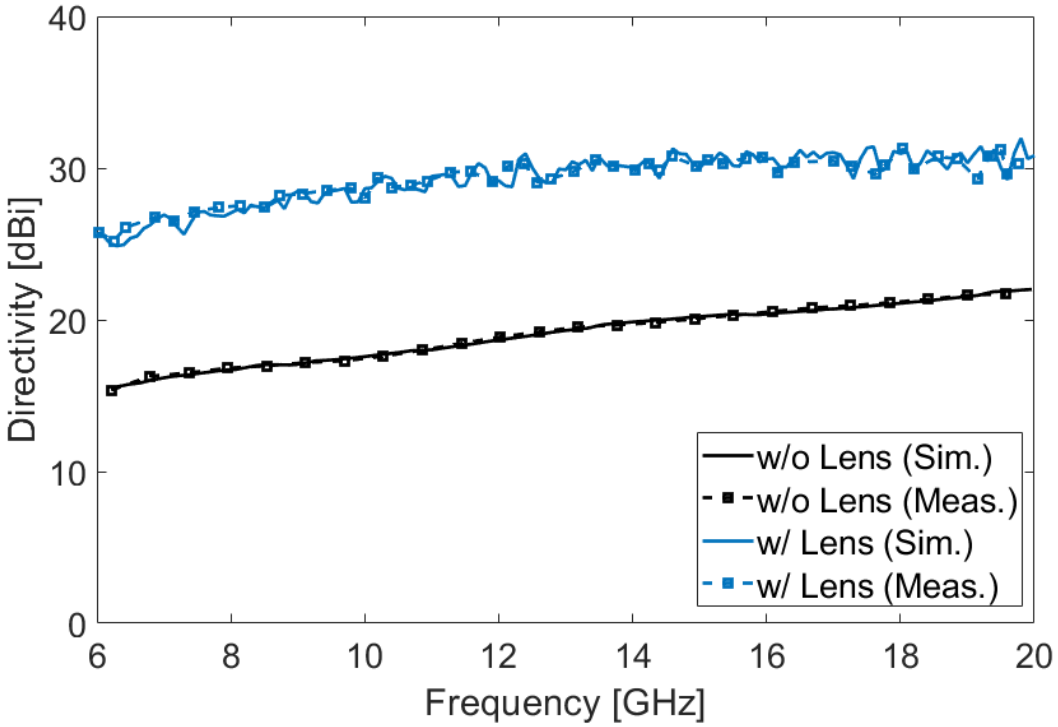

(a)

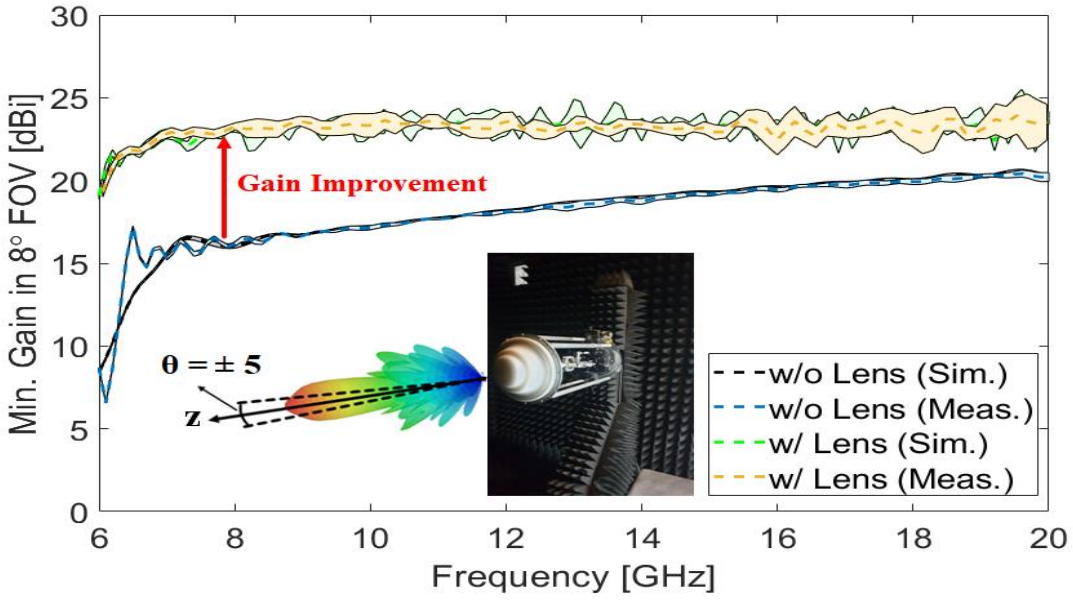

(b)

Fig. 2.17: Simulated and measured far-field performance of the designed QRH with and without the lens, specifically (a) Directivity, (b) Minimum gain in FOV.

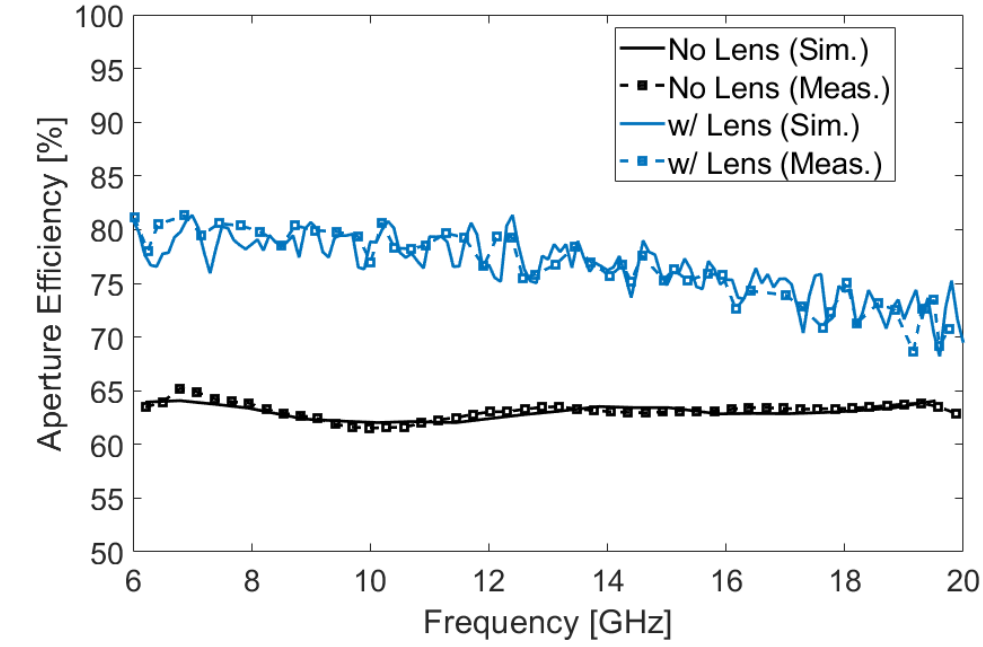

(a)

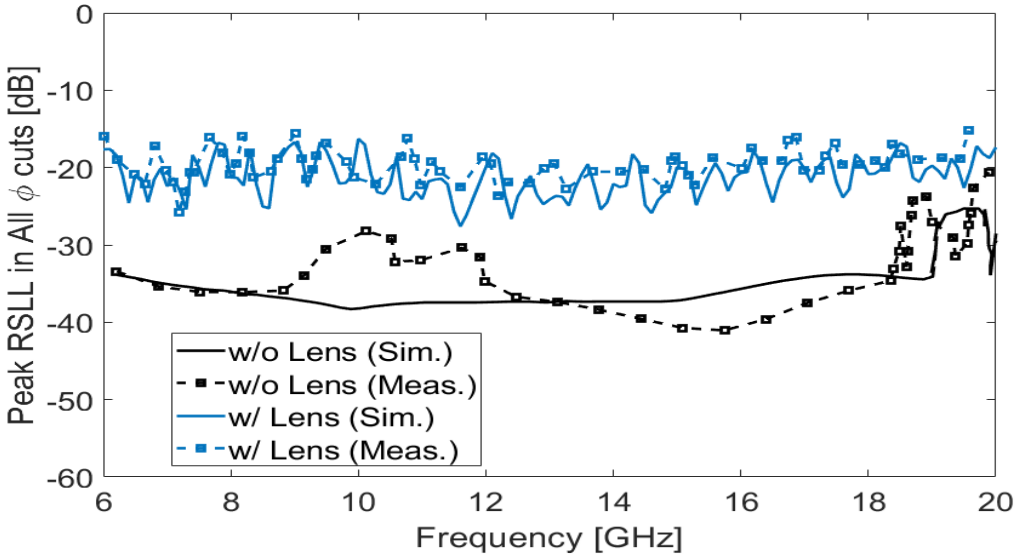

(b)

Fig. 2.18: Simulated and measured far-field performance of the designed QRH with and without the lens, specifically and (a) Aperture efficiency. (b) Peak RSLL in all ϕ cuts.

simulations is over 90%. As seen in Fig. 2.18(a), aperture efficiency with a lens is significantly increased from 7 to 15 %. Additionally, in Fig. 2.18(b), as expected, the

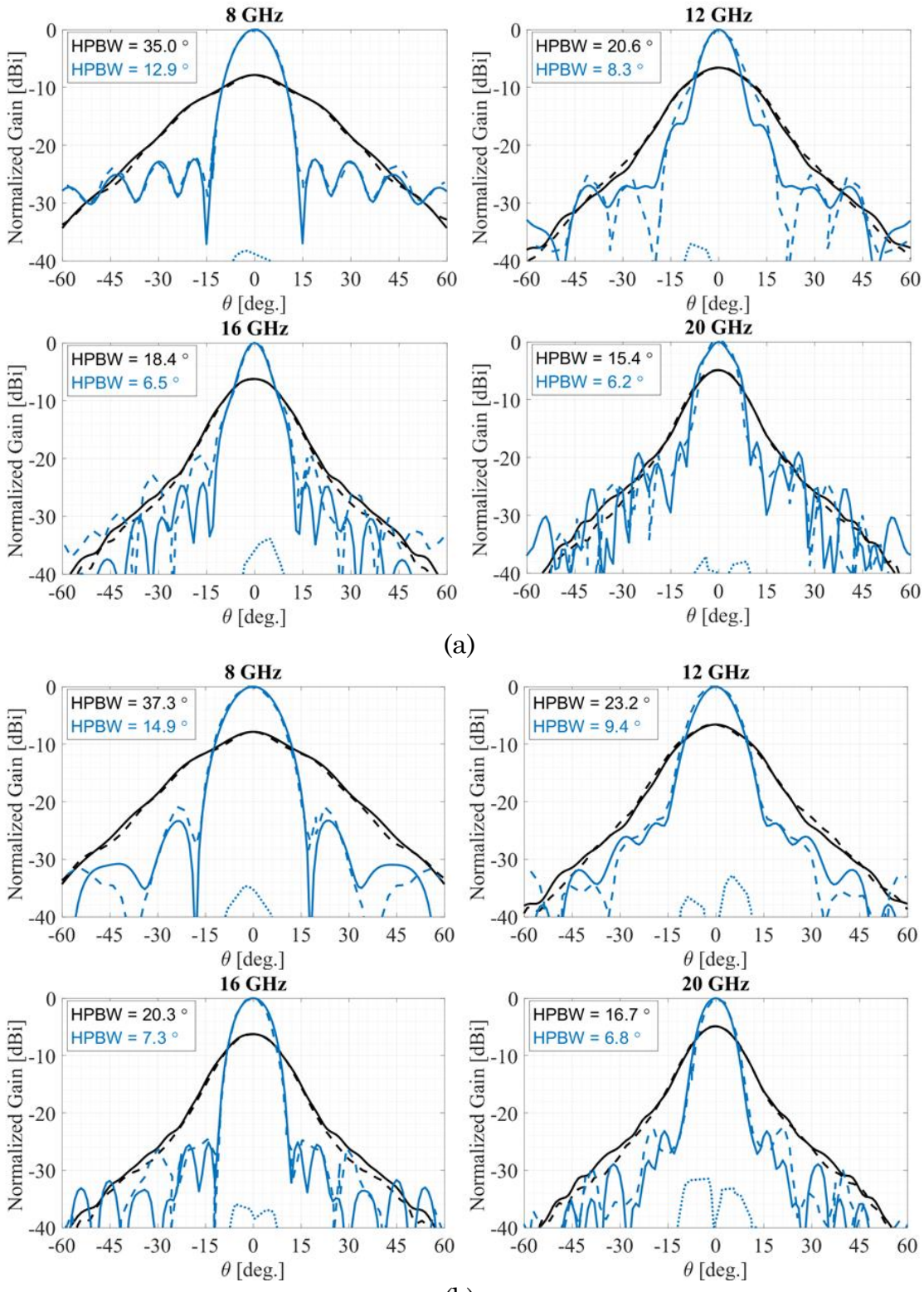

Fig. 2.19: Simulated (solid) and measured (dashed [co-polarization] and dotted [cross-polarization]) (a) E- and (b) H-plane radiation patterns of the fabricated antenna with (light-color) and without (dark-color) the lens.

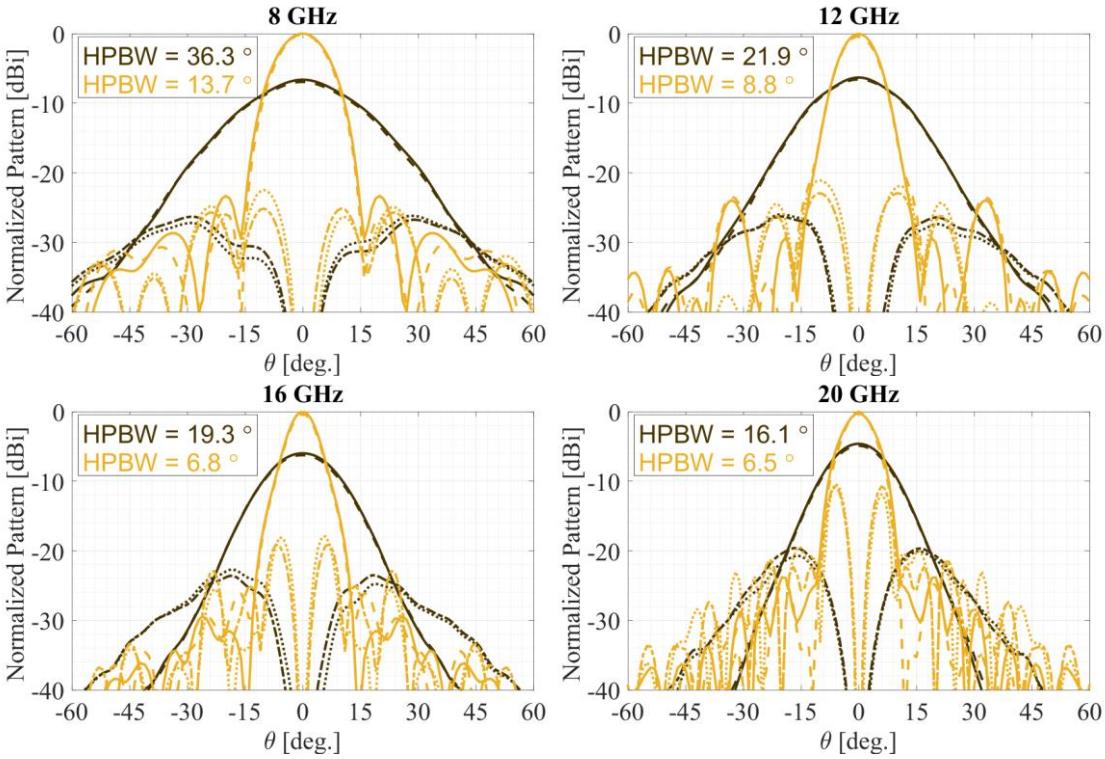

Fig. 2.20: Simulated (solid) and measured (dashed [co-polarization] and dotted [cross-polarization]) D-plane radiation patterns of the fabricated antenna with (light-color) and without (dark-color) the lens.

peak SLLs in all ϕ cuts noticeably deteriorate with the lens; however, their value remains < -15 dB over the operating bandwidth.

The electric far-field components of the fabricated antenna are measured over a full sphere in our anechoic chamber. Then, the directivity is calculated using (2.2) [21] through subsequent post-processing in MATLAB.

$$D(\theta,\phi) = \frac{U(\theta,\phi)}{U_0}, \text{ where } U(\theta,\phi) \approx \frac{1}{2\eta}\left(|E_\theta(\theta,\phi)|^2 + \left|E_\phi(\theta,\phi)\right|^2\right)$$
$$U_0 = \frac{1}{4\pi}\int_{\theta=0}^{\pi}\int_{\phi=0}^{2\pi} U(\theta,\phi)sin\theta\, d\theta d\phi \qquad (2.2)$$

Finally, utilizing directivity results, the aperture efficiency of the antenna is calculated using (2.3).

Table 2.2: Comparison with the existing horns

Ref.	Loading Technique	Frequency (Bandwidth)	Gain	Aperture Efficiency
[36]	Metasurface	Extended C-band (2:1)	> 17.3 dBi	> 46 %
[37]	Metasurface	X- to Ku-bands (1.26:1)	> 19 dBi	> 18 %
[38]	Metasurface (Metallic)	X-band (1.27:1)	> 12 dBi	> 27 %
[39]	Metasurface	X-band (1.11:1)	> 14.5 dBi	> 60 %
[40]	GRIN	X-band (1.51:1)	> 17 dBi	> 49 %
[41]	GRIN	X- to Ku-bands (2.4:1)	> 13 dBi	> 63 %
[42]	GRIN	X-band (1.5:1)	> 21.2 dBi	> 57 %
[43]	Dielectric (Homogeneous)	C- to Ku-bands (3:1)	> 15 dBi	> 35 %
[44]	Dielectric (Homogeneous)	W-band (1.21:1)	> 24 dBi	> 44 %
[45]	Dielectric (Homogeneous)	Ka-band (1.22:1)	> 16 dBi	> 61 %
This work	Dielectric (Homogeneous)	C- to Ku-bands (3.1:1)	> 24 dBi	> 62 %

$$e_{ap} = \frac{\lambda^2}{4\pi}\frac{D_0}{A_p} \tag{2.3}$$

Where λ is wavelength and A_p is the physical area ($= \pi r^2$) of the aperture with radius r.

The measured E-, H- and D-plane radiation patterns, shown in Fig. 2.19 and 20 are symmetric for both configurations. As expected, the lens loading leads to more directive patterns with deteriorated XPD and SLL than a stand-alone QRH. Within the FOV, the measured XPD surpasses 30 dB in both the E- and H-planes while exceeding 12 dB in the D-plane. Slight variations observed between the measured cross-polarization and simulation results can be ascribed to asymmetry during fabrication. Excellent agreement between measurements and full-wave simulations

is a clear indicator of the robustness of the developed prototype and the configuration. The comparison between the proposed configuration and several high gain antennas published in the literature is given in Table 2.2. As seen, the herein proposed aspheric dielectric lens-loaded QRH stands out in terms of combined gain and aperture efficiency over a wide bandwidth.

2.5. Conclusion

A lens-corrected QRH antenna operating from 6.5 to 20 GHz is introduced. The proposed horn has exponentially tapered ridges and is top-loaded with a spline-based aspheric lens. These features enable directional patterns with improved gain profiles over a wide bandwidth and required FOV. A phase-matched OMT with cone-loaded turnstile junction and custom single- and double-ridge waveguides are developed to achieve dual polarized operation and theoretical high-power handling. The fabricated antenna has VSWR < 3, minimum gain in the desired FOV of > 21.5 dBi, and high-quality radiation patterns with low SLL and high XPD over the entire bandwidth. A comparison with other designs shows that the combination of wide bandwidth, high directivity, effective isotropic radiated power, and robust design makes this antenna a good choice for various uses across commercial and defense sectors.

Chapter 3

Modular Lens-Corrected Dual-Polarized Horn with Cavity

3.1. Introduction

Advancements in wireless communication technologies have perpetuated the need for diverse, highly directional antenna systems, including those that offer wide bandwidth, dual-polarization, and modular configuration to adapt to ever-changing and expanding needs. Applications span from satellite/terrestrial communications to electronic warfare, where sensing, efficiency, pollution, signal integrity, and range are of utmost importance. Among the broad family of antenna topologies, the horn has long been a mainstay in high-frequency applications due to its simplicity, good understanding, wide achievable bandwidth, and consistent radiation patterns [1]. Furthermore, the QRH, an advanced iteration of a classical horn, significantly augments its fundamental characteristics by enabling dual-polarization, further bandwidth enhancement, and higher XPD. Despite these intrinsic benefits, wideband QRHs share similar limitations with traditional horns regarding lower aperture efficiency, which leads to reduced directivity and gain.

Moreover, a substantial axial length is necessary to counteract the quadratic phase errors inherent to their geometry [61], which makes their fabrication expensive. To address some of these challenges, integrating a corrective lens offers a viable approach compatible with the existing mechanical framework, cost-effectiveness, and established technological maturity [62]-[65]. A dielectric lens, in particular, can correct a planar phase front, thus reducing quadratic phase errors and increasing directivity. Nevertheless, incorporating a lens into the design introduces some challenges, particularly in controlling SLLs and mismatch arising from the discontinuities between the air and dielectric at the horn aperture. Various techniques have been explored to mitigate this issue, including the use of corrugations, curved edges, and trifurcation and the recent integration of periodic structures or graphene [66]-[74]. Corrugations effectively tailor sidelobes and improve the patterns overall [66]-[68].

Similarly, curved edges can reduce the impact of scattering from the edges of the horn aperture [69, 70]. A trifurcated horn is used to create a stepped amplitude pattern in the E-plane [71], whereas the periodic structures such as mushroom [72] or pyramidal [73] have been applied on the inner walls to create a high-impedance electromagnetic band gap that is proven effective in suppressing surface waves. All these configurations contribute to reducing energy in undesired lobes by controlling aperture field distribution and, therefore, the radiation pattern. Finally, graphene was proposed in [74] to address the abovementioned challenges. However, achieving the desired aperture distribution over the wide bandwidth often necessitates trade-offs, including bulky structure, complex fabrication, reduced bandwidth, and/or increased overall costs. This paper demonstrates a low-cost, high-performance, lens-loaded, dual-polarized horn, shown in Fig. 3.1, as a viable, highly modular option for wide bandwidth needs at millimeter-wave (mmWave) frequencies.

Conventional QRHs are typically prototyped using metal-based CNC machining due to its precision, well understood split-block assembly, and maturity. At mmWaves, manufacturing precision is often critically important, and the proposed design, a low-cost, high-performance, lens-loaded, dual-polarized horn, maintains this precision. This precision, combined with the advantages of AM techniques, commonly referred to as 3-D printing, offers a high level of confidence in the performance of the design, particularly during the research and development stage.

In this chapter, we demonstrate design for AM fabrication and performance

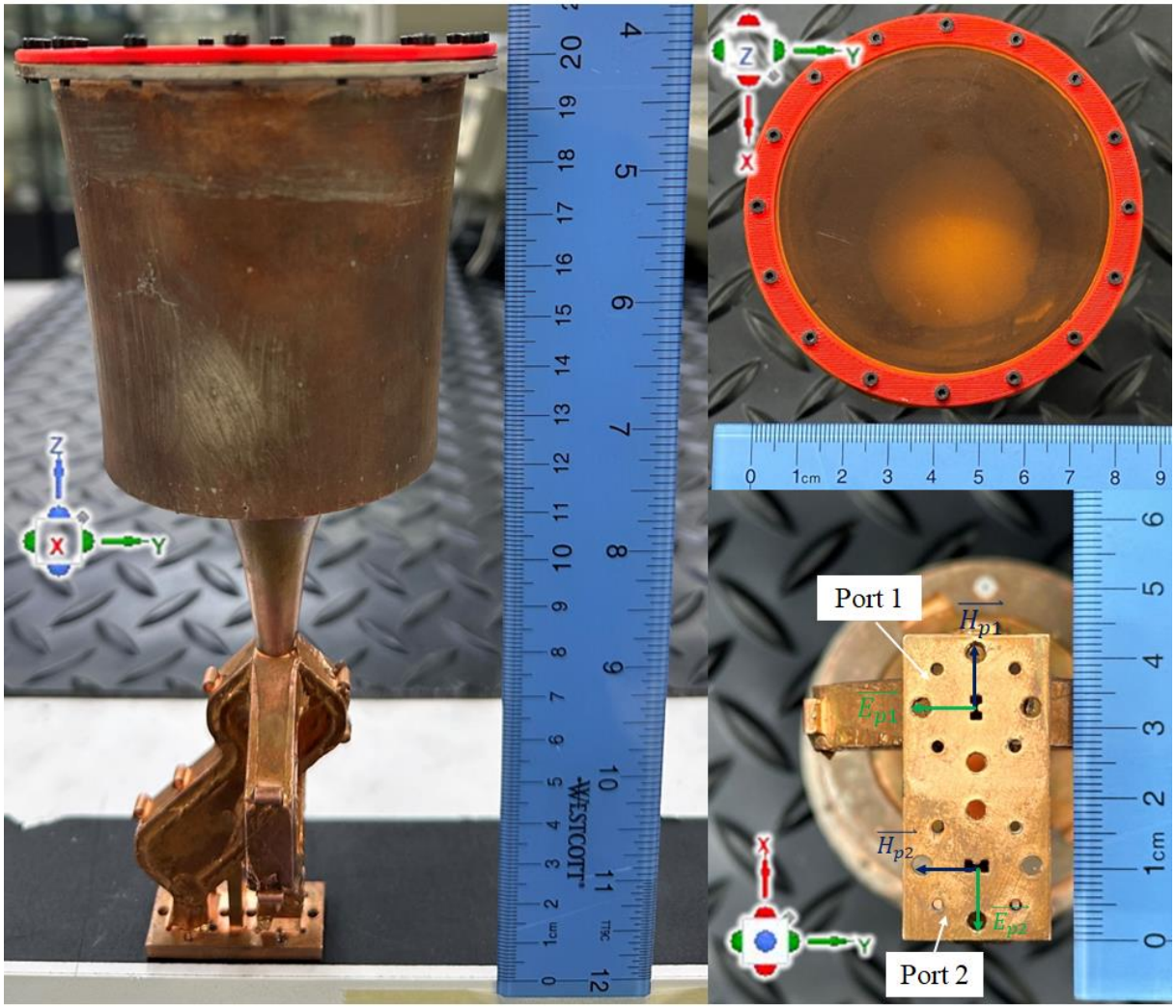

Fig. 3.1: (a) Proposed configuration of the lens-corrected QRH with cavity. (b) Fabricated cavity with absorber and Kapton cover.

over 36-90 GHz bandwidth of a monolithic, wideband, OMT backed, dual-polarized QRH integrated with a phase-correcting dielectric lens. The initial steps of the horn-only design in [76] are expanded upon with not only greater detail in the design and fabrication but also measurements and new features added to further develop the range of applications while enabling improved performance. Specifically, to lower the SLLs and enable flush-mounting while preserving other performance features, an exponentially shaped cavity with a current sheet absorber is added to the system, as shown in Fig. 3.1. This arrangement effectively functions as a spatial filter engineered to mitigate wave propagation in undesired directions. This minimizes reflection and diffraction effects while preserving wideband and dual-polarized characteristics as well as main-beam performance. The OMT is backed by custom double-ridge waveguide orthogonal channels designed to cover the entire 36-90 GHz range with safe margins on both sides of the band. The measured performance agrees well with simulations, therefore demonstrating the maturity of the proposed designs and the ability of the AM technology to create highly functional prototypes in this and other parts of the RF spectrum.

The rest of the chapter is organized as follows: Section 3.2 discusses the lens-correction design, detailing the lens process and realization using two different AM techniques. Section 3.3 is dedicated to the design of a 3-D printable OMT monolithically integrated with the horn. Section 3.4 describes fabrication and measurement results, whereas Section 3.5 discusses the modular cavity design, fabrication, and measurement results along with the comparisons with the state-of-art 3-D printed antennas.

3.2. 3-D Printed Lens-Corrected Quad-Ridge Horn

The foundations of a 36-90 GHz QRH horn were introduced in [76], where a computational design of a (lens-less) dual-polarized antenna was first proposed. This model had a simulated VSWR < 2.2, directivity > 18 dBi, and symmetric radiation patterns with peak SLL in all ϕ planes < -32 dB. To achieve dual-polarization, a phase-matched OMT was integrated with the QRH and a photograph of the monolithic fabrication was provided. However, no measured results or further enhancements were discussed. The main focus of this section is to introduce and discuss the design and performance of an AM dielectric lens, a key element in improving the directivity (aperture efficiency).

In a conventional horn, the tapering of the throat inherently leads to lower directivity. By lens-loading the horn aperture, one can achieve improved directivity or, if desired, a specific beam shape. This is accomplished by correcting and collimating the wavefronts, effectively transforming them from spherical to planar. Specifically, the phase correction is achieved with a dielectric lens having a refractive index ($=\sqrt{\varepsilon_r}$) greater than unity, where εr represents the relative permittivity of the lens material. The conventional design approach for such lenses assumes the applicability of geometric optics, conceptualizing the power emerging from the horn apex as a ray. The foremost principle in geometric optics postulates that power is transmitted along ray paths, and the cumulative power traversing any enclosed surface constitutes a tube of rays. This implies constancy in the total power across any cross-sectional area of a ray tube. The second principle, Fermat's principle, indicates that energy traversing between two points follows the route that minimizes the optical path length [48]. Based on these foundational principles, the subsequent subsections discuss the designs and results for homogeneous and perforated lenses with a plano-convex profile.

3.2.1. Design and Realization of Plano-Convex Lenses

The designed lens aims to achieve a constant phase front at the horn aperture. To achieve this goal, various convergent lens configurations, such as plano-convex, bi-convex, equi-convex, and meniscus, are considered in the literature. All these lenses are depicted in Fig. 3.2 [77]. As seen, the biconvex and equi-convex lenses (characterized by their two convex surfaces) and meniscus lenses (with their crescent moon-like appearance due to one convex and one concave side) have more complex geometrical characteristics compared to the plano-convex lenses that exhibit just one curved surface. Employing a design that reduces the number of curvatures and incorporates a flat surface not only supports the explanation of "simplicity and seamless integration" but also helps in mitigating challenges such as increased manufacturing and design complexity, more significant spherical aberrations, a restricted range of applications, alignment difficulties, and even prolonged setup times [78]. Among these, the plano-convex lens stands out for design simplicity and

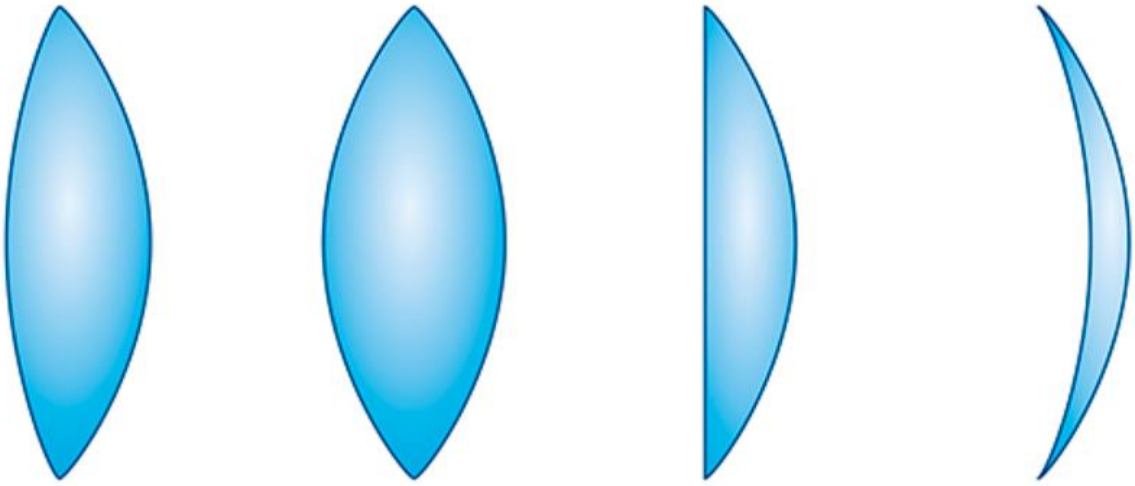

Fig. 3.2: Lens profiles [77]: (a) Biconvex (b) Equi-convex (c) Plano-convex (d) Meniscus lenses.

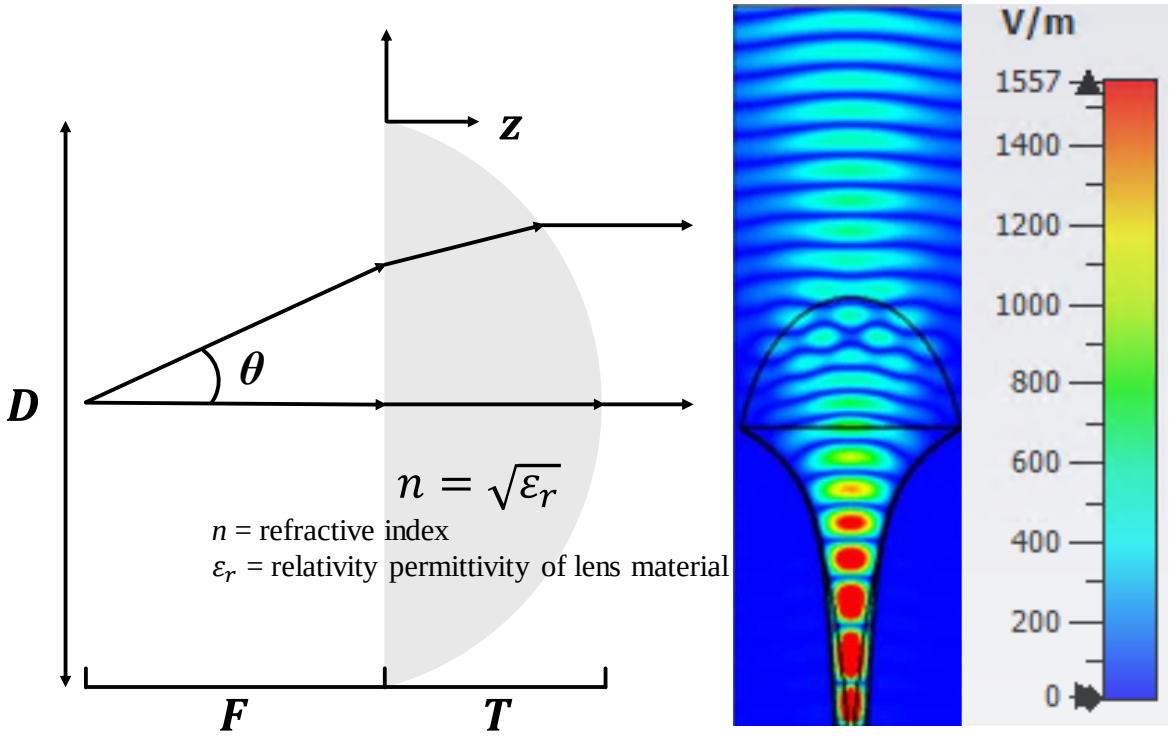

(a) (b)

Fig. 3.3: (a) Depiction of a shaded plano-convex lens with its critical parameters including focal distance (F), thickness (T), and diameter (D) alongside ray paths for the two rays with angular separation of θ; and (b) achieved phase-front correction when this lens is integrated with a QRH antenna. (1-W power excitation).

seamless integration [48]. The surface of the plano-convex lens is described in (3.1), (3.2), and (3.3) [78]:

$$r = \frac{F+(n-1)T+(n^2-1)Fsec\theta-FS\,tan\theta}{\left(\frac{n^2}{sin\theta}-S\right)} \tag{3.1}$$

$$z = (r - Ftan\theta)S \tag{3.2}$$

$$\frac{T}{D} = \left[\sqrt{\left\{1+\frac{1}{(2F/D)^2}\right\}}-1\right]\frac{F/D}{n-1} \tag{3.3}$$

where r is the transverse radius of the lens while F, T and D denote focal length, thickness, and diameter of the lens, respectively. θ represents semi-flare angle, whereas S can be computed as $\sqrt{\left\{\left(\frac{n}{sin\theta}\right)^2 - 1\right\}}$. z is the longitudinal co-ordinate. As delineated by the equations (3.1)-(3.3), there is a discernible relationship between the F/D ratio and the semi-flare angle. An increase in the semi-flare angle necessitates a longer axial length to transform the spherical phase front into the planar. The axial length of the lens is exclusively determined by the dielectric constant of the lens material. At mmWave wavelengths, a smaller F/D ratio offers manufacturing benefits by simplifying lens fabrication. As senn in Fig. 3.3, this lens, with its singular curvature, offers a more straightforward fabrication process compared to lenses with two curved surfaces. The planarity of one of its surfaces not only aids in the manufacturing process but also ensures versatile mounting options. This, in turn, guarantees precise alignment, making the audience feel secure about the accuracy of the system.

Referring to the QRH in [76], the lens is meticulously optimized to achieve maximum aperture efficiency across the operating frequencies. This is achieved by fine-tuning the F/D ratio, thickness, and material permittivity. The particle swarm optimizer (PSO) in CST-MWS, a fitting choice for structures with multiple variables, is employed for this purpose [27]. The result is an optimal lens design for operation over 36-90 GHz, featuring a permittivity of 2.15, a height of 20 mm, and an F/D ratio of 0.64. With an aperture size of 45.1 mm, this design ensures over 70% aperture efficiency throughout the frequency band, instilling confidence in its performance.

Two approaches, which rely on modern AM, are explored to realize this lens. The first method yields a homogeneous lens of 3-D printable bulk material specifically chosen for its permittivity that closely aligns with the optimal value. As seen in Fig. 3.4(a), a 19.5 mm ($2.35\lambda_{36GHz}$) tall homogeneous lens made of polypropylene (PP) (ε_r =

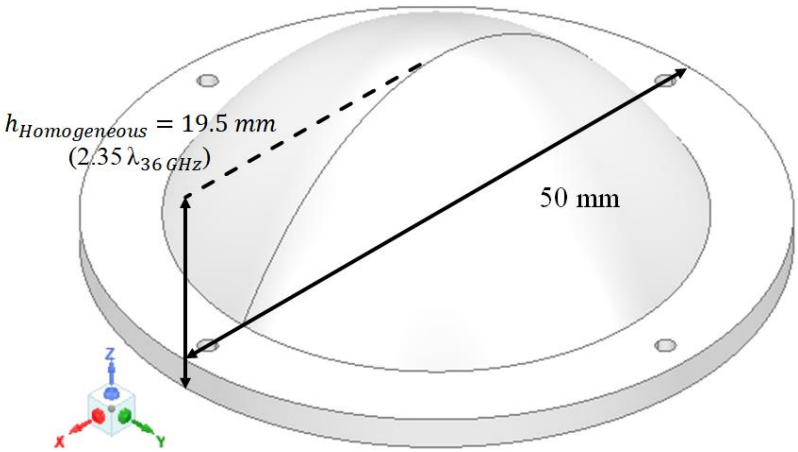

(a)

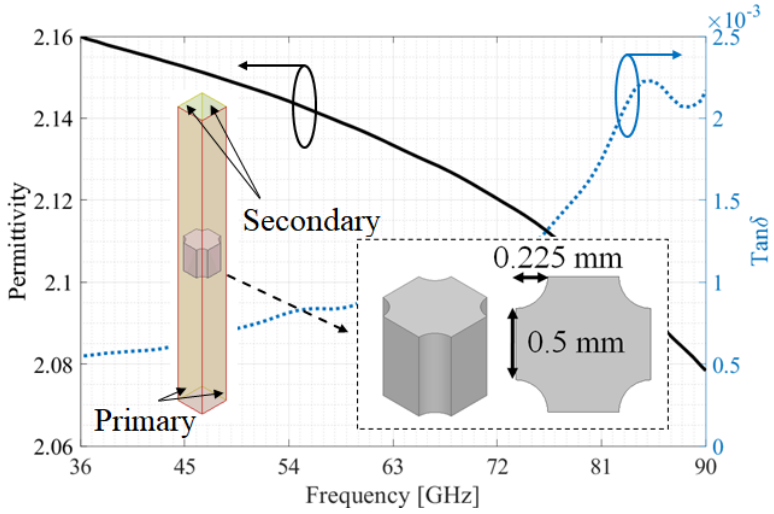

(b)

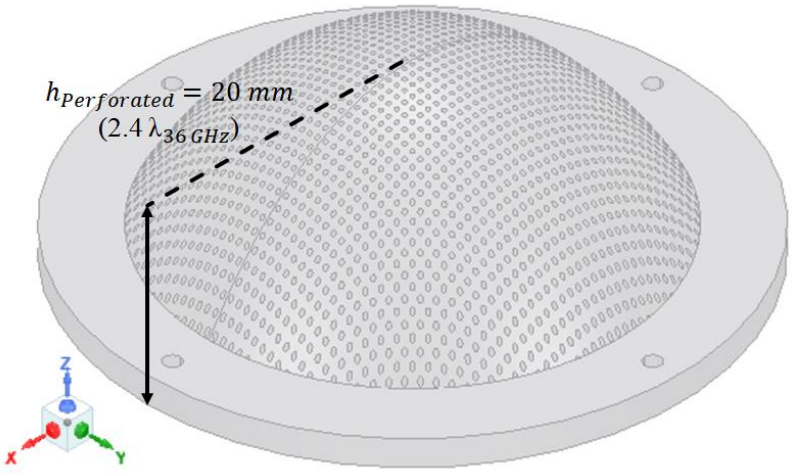

(c)

Fig. 3.4: (a) Homogeneous lens configuration. (b) Permittivity and loss tangent characterized for the unit-cell of the perforated lens with the associated periodic boundary conditions delineated in the inset. (c) Perforated lens configuration.

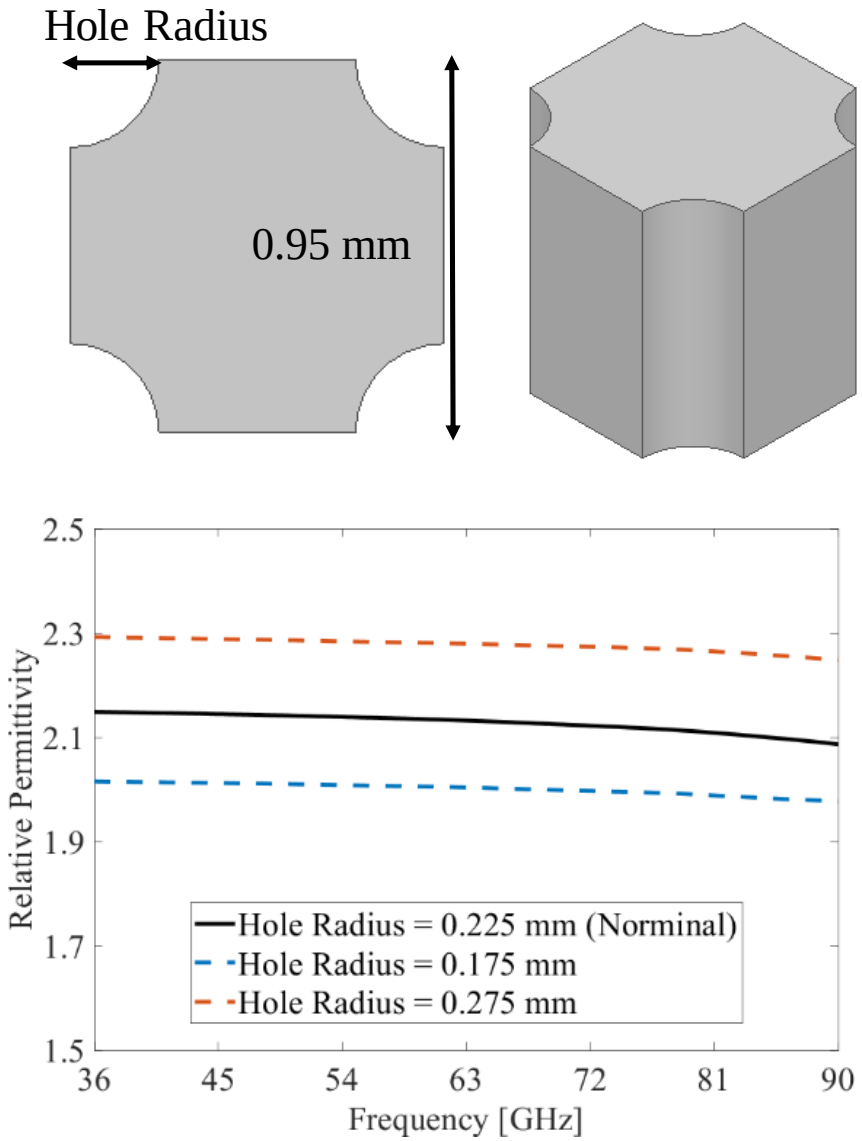

Fig. 3.5: Variation of relative permittivity with the diameter of cylindrical perforations.

2.2, $tan\delta$ = 0.0005) [79], is designed. The second approach fully exploits AM to realize a lens with perforations such that the effective permittivity is ideally the same as the optimal value. This is accomplished by placing the cylindrically perforated air holes [44, 80] into a higher permittivity material. Shown in the inset of Fig. 3.4(b) are the unit-cell features for this perforated lens, featuring a square lattice pattern and prototyping resin with measured ε_r = 2.5 and $tan\delta$ = 0.005 at the Ka-band [81]. The

hole diameter and spacing between the holes are 0.45 mm and 0.5 mm, respectively. As seen within the operating bandwidth, the effective permittivity of this material varies between 2.08 and 2.16, while the loss tangent is maintained consistently below 0.0025. To reduce the impact of the dispersion seen in Fig. 3.4(c), the height of the optimized perforated lens is changed to 20 mm. Contrary to functioning as quarter-wavelength transformers or matching layers, our perforated lens utilizes cylindrical perforations to attain a specific effective permittivity (approximately 2.15), as delineated by the effective medium theory (EMT) [82], leveraging 3-D printing resin that inherently possesses high permittivity (~2.5). EMT is a conceptual framework that predicts a composite material's macroscopic properties, such as permittivity, permeability, and refractive index, based on the properties and proportions of its constituent materials. Fig. 3.5 illustrates the simulation results for varying permittivity, achieved by adjusting the air-to-material ratio through changes in the hole radius, while the unit-cell size remains constant at 0.95 mm. Based on the previously discussed for achieving maximum aperture efficiency, we explored two

Table 3.1: Comparison of mechanical properties with each lens type

Homogeneous Lens (FDM)	Perforated Lens (DLP)
✓ **Strength and Durability** Stronger and more durable than the perforated lens, as the process involves the extrusion of thermoplastic filaments, which bond layer by layer.	✓ **Surface Finish and Precision** Achieve a high-quality surface finish and intricate details because the process involves curing photopolymer resins with light, which allows for finer control over the shape and surface.
× **Surface Finish** Relatively rough surface finish due to the layer-by-layer deposition × **Precision** Struggle with fabricating the high precision due to the nature of the extrusion process and the size of the nozzle	× **Brittleness** Photopolymer resin tend to be more brittle compared to thermoplastics

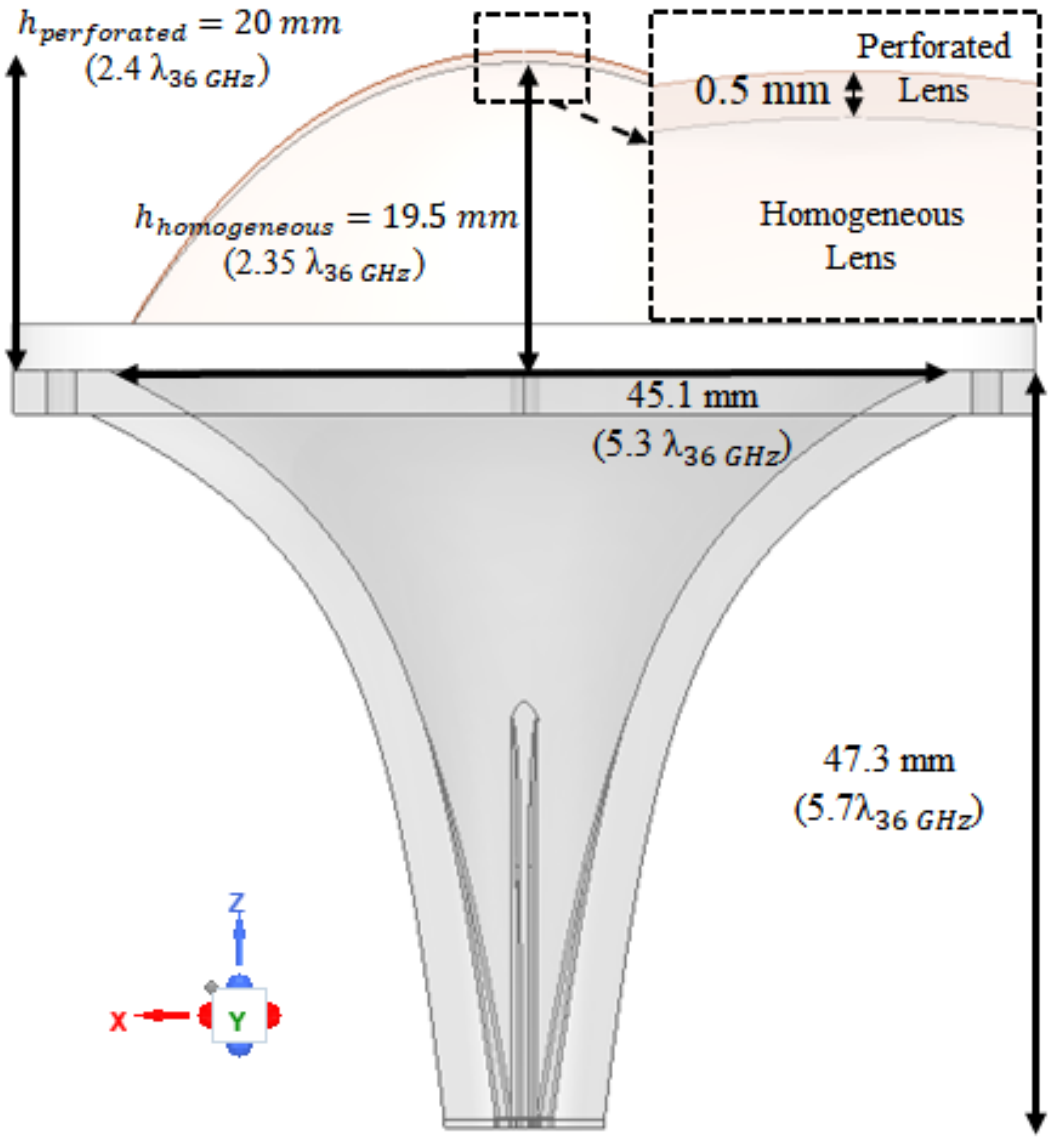

Fig. 3.6: Lens-corrected QRH with perforated and homogeneous lenses.

approaches for fabricating the optimized lens. Upon utilizing the perforated lens, we anticipated results comparable to those of a homogeneous lens rather than an enhancement in performance.

The conclusion is that different 3D printing technologies (in this case, FDM and DLP) can be utilized to achieve optimal results. Thus, antenna engineers have flexible options based on which 3D printer and resin are available to them.

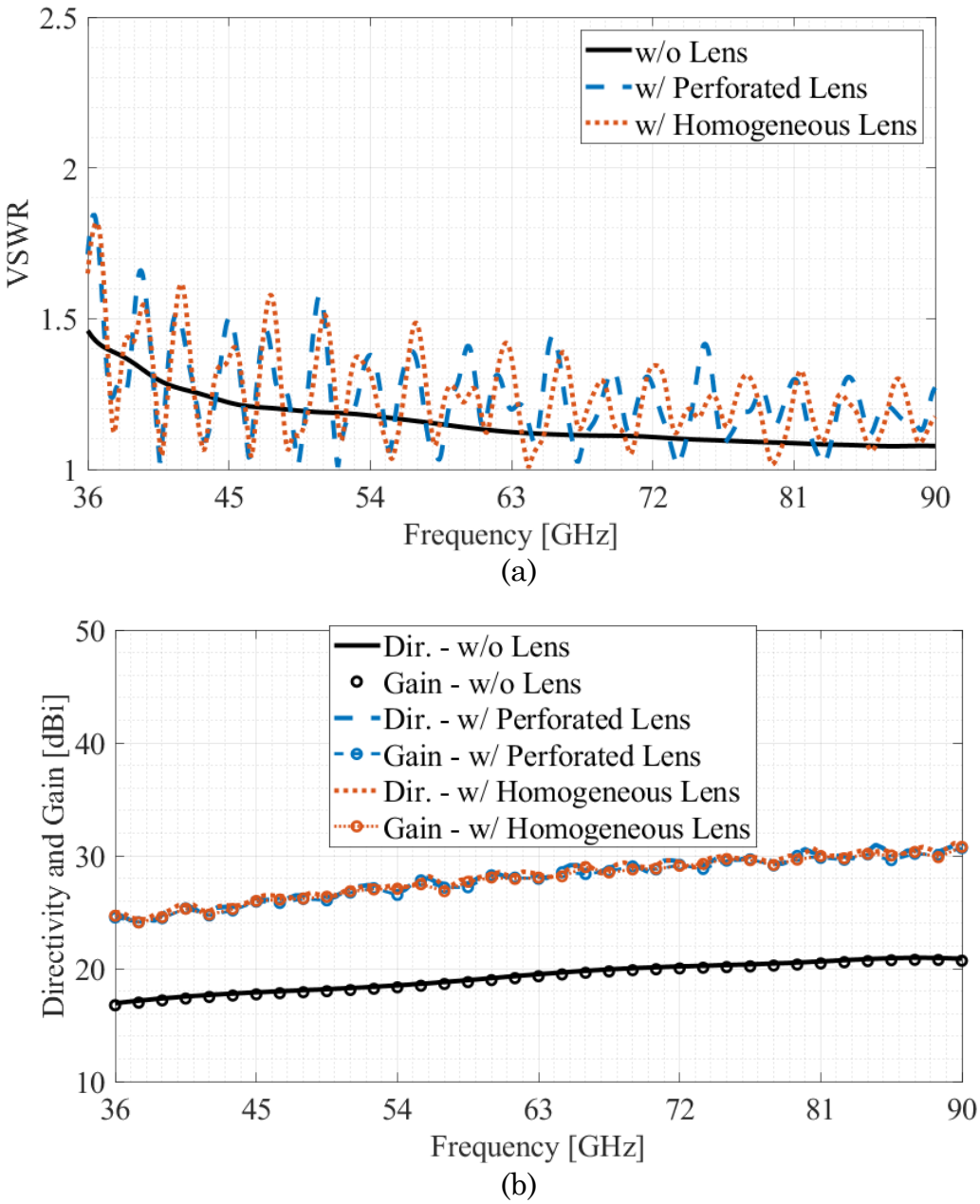

Fig. 3.7: Performance of QRH without (w/o) lens and with (w/) perforated and homogeneous lenses. (a) VSWR. (b) Directivity and gain.

Additionally, Table 3.1 provides each lens type's mechanical advantages and disadvantages. Fig. 3.6 illustrates the geometry differences between the homogeneous and perforated lenses.

3.2.2. Performance Comparison

The performance of the lens-corrected QRH antenna is shown in Fig. 3.6. As expected, the dielectric lens leads to additional reflections and diffraction, resulting

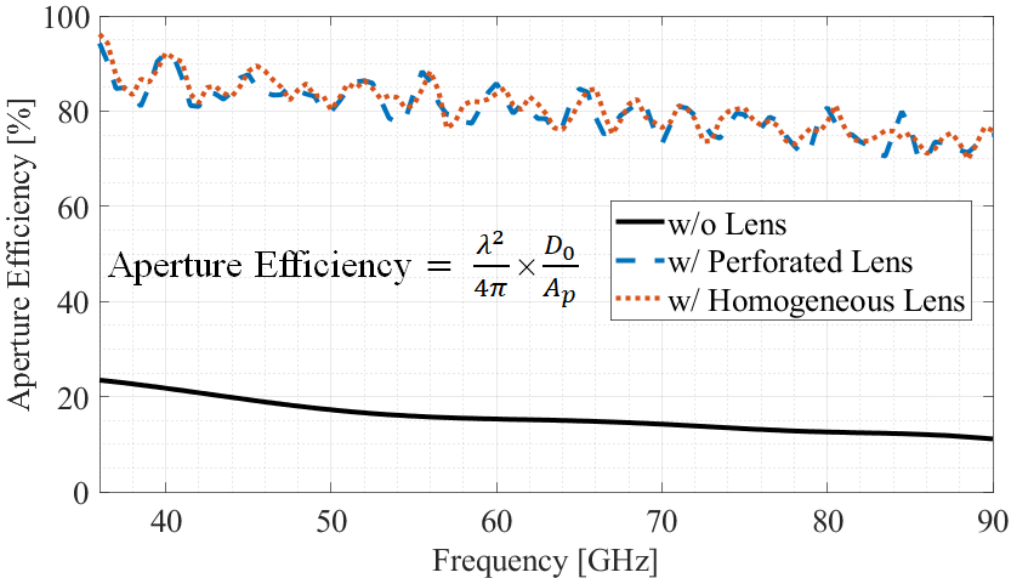

(c)

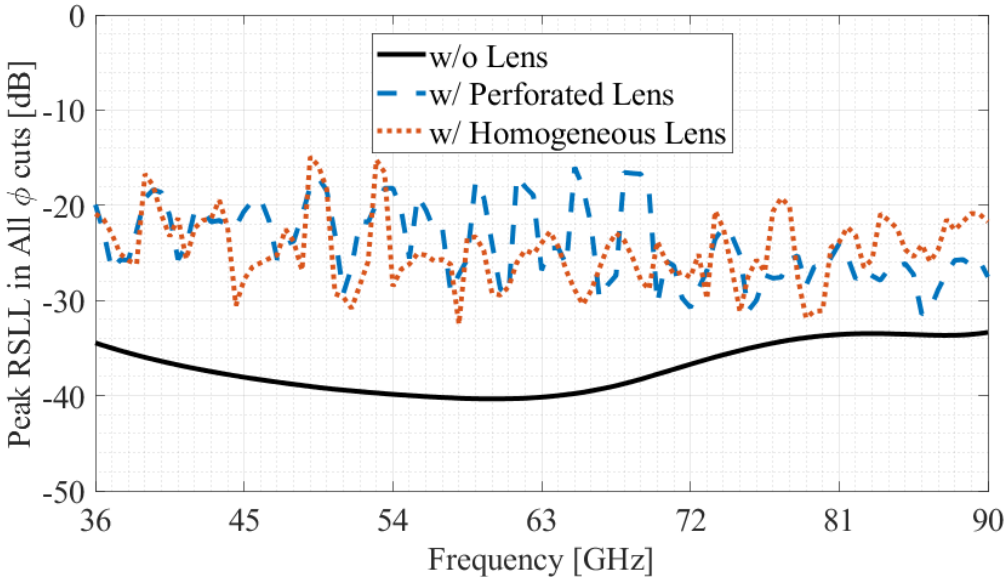

(d)

Fig. 3.7: Performance of QRH without (w/o) lens and with (w/) perforated and homogeneous lenses. (c) Aperture efficiency. (d) Peak relative SLL in all ϕ cuts.

in the standing waves within the QRH throat. This causes fluctuations in the VSWR seen in Fig. 3.7(a), with their periodicity closely related to the horn's axial length. Nevertheless, the VSWR remains below 2:1 across the operating frequency band. Regarding directivity and IEEE gain, as shown in Fig. 3.7(b), the loading lens yields a significant increase of approximately 8 dB compared with the lens-less QRH. The computed radiation efficiency exceeds 97%. As seen in Fig. 3.7(c), the aperture efficiency varies from 70 to 96%, with the lowest value at the high end of the band. Also seen is that the substantially lower aperture efficiency is observed without the lens, i.e., from 8 to 20%. Note that this

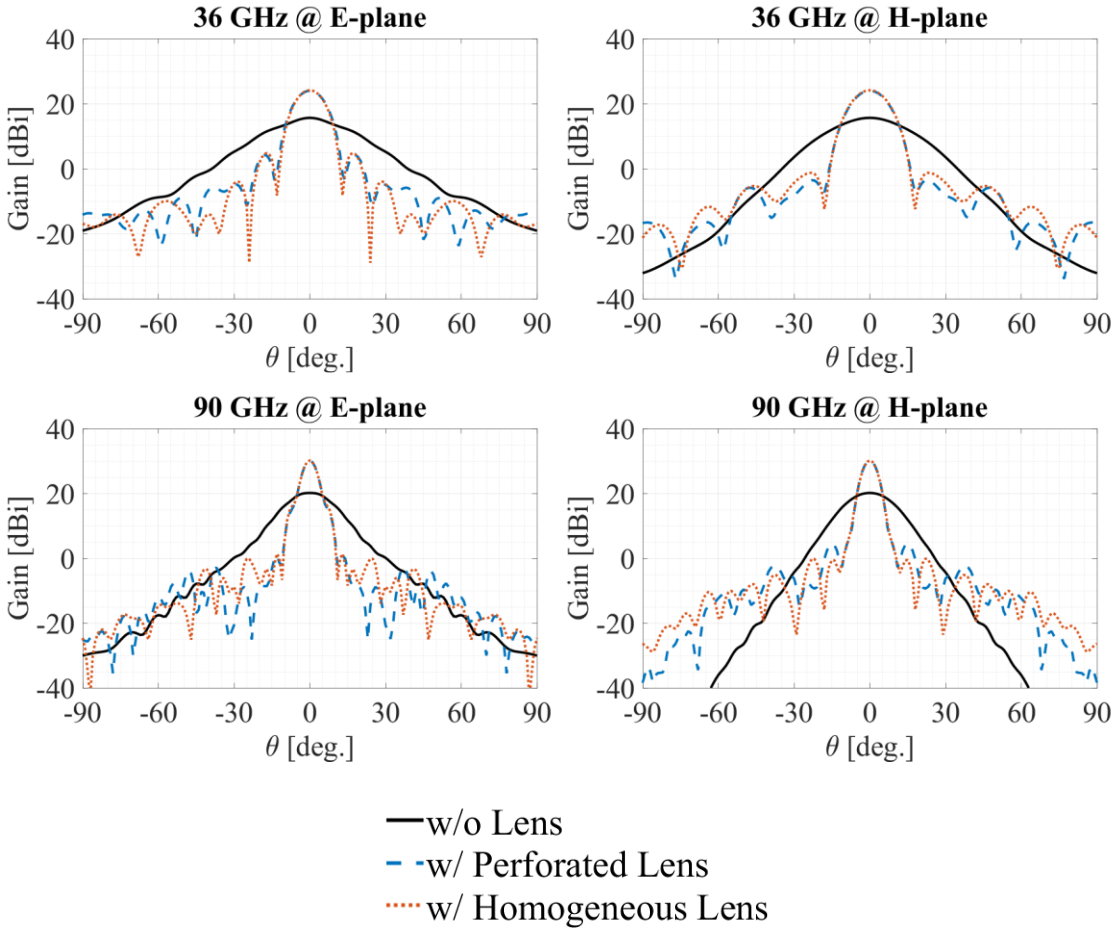

Fig. 3.8: Radiation patterns of QRH without lens and with perforated and homogeneous lenses at 36 (upper) and 90 (lower) GHz in E- (left) and H- (right) planes.

range can be improved with the more extended horn. However, this is not attempted here as it would require a much larger 3D printing volume, making monolithic integration with OMT impossible with our current resources. Fig. 3.7(d) shows the worst-case relative SLL across all ϕ planes sampled in 5º increments. As expected, the SLLs noticeably deteriorate with the lens; however, their value remains < -15 dB over the operating bandwidth. The radiation patterns shown in Fig. 3.8 show increased directivity with more pronounced lobing, as expected from the discussion above. The comparative analysis between the homogeneous and perforated lenses reveals a decent agreement, underscoring the validity of both design and realization approaches for this purpose.

3.3. 3-D Printable Orthomode Transducer

A discussion leading to the design of the 3-D printable OMT is given in this section. To achieve dual-polarization with a QRH, the typical methods include coaxial probes with a balun [83, 84], microstrip/stripline [85, 86], and OMT [87, 88]. Though geometrically complex, OMTs are often favored among these approaches due to their compact form factor, power handling, high isolation, and achievable wide bandwidth. Moreover, with the recent advances in AM, these complex structures can now be monolithically integrated with the QRH, further reducing the cost and removing the need to deal with the leakage and other issues associated with split block assembly. The OMT topology in this work is comprised of a quad-ridge circular waveguide (QRWG) facing QRH, a turnstile-junction, two bifurcations transitioning from custom single-ridge waveguide (SRWG) to custom double-ridge waveguide (DRWG), and two DRWG outputs. Conceptually, this OMT is similar to those fabricated in primarily subtractive technologies [50, 57, 87, 89, 90]; however, its design is guided by modern AM abilities.

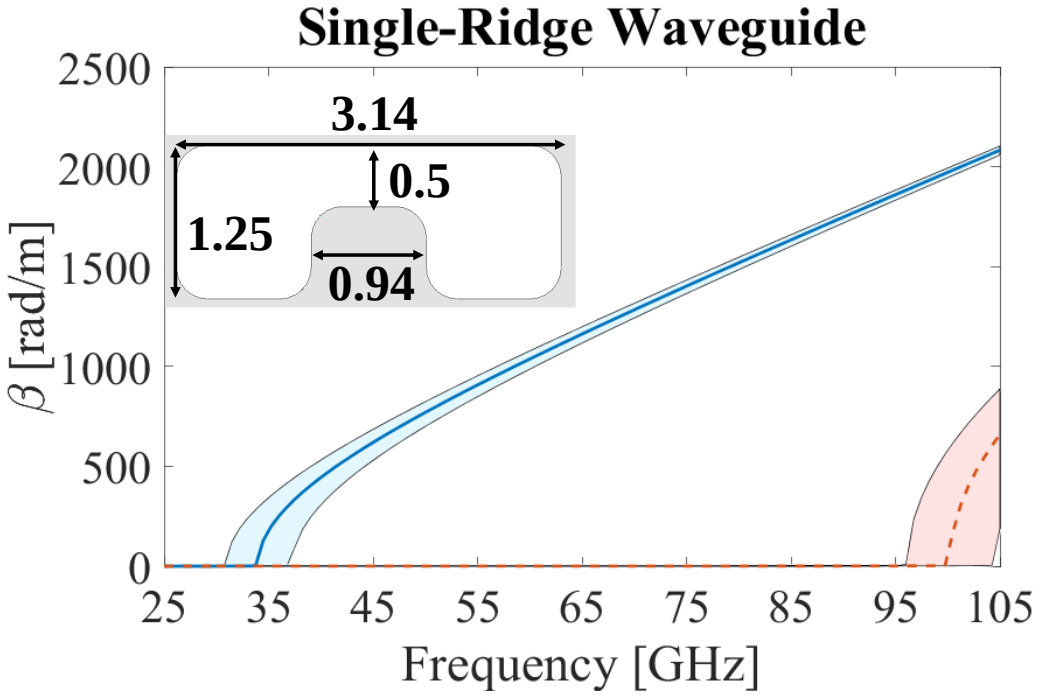

Fig. 3.9: Propagation constants of custom single-ridge waveguide with sensitivity analysis (Dimensions are in millimeters).

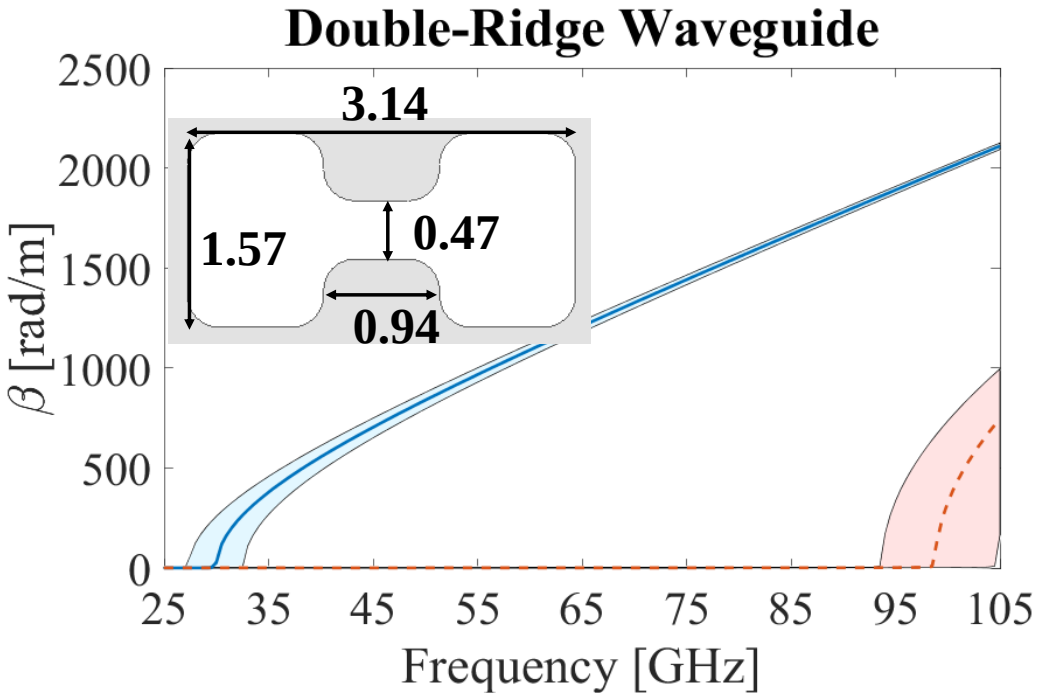

Fig. 3.10: Propagation constants of custom double-ridge waveguide with sensitivity analysis (Dimensions are in millimeters).

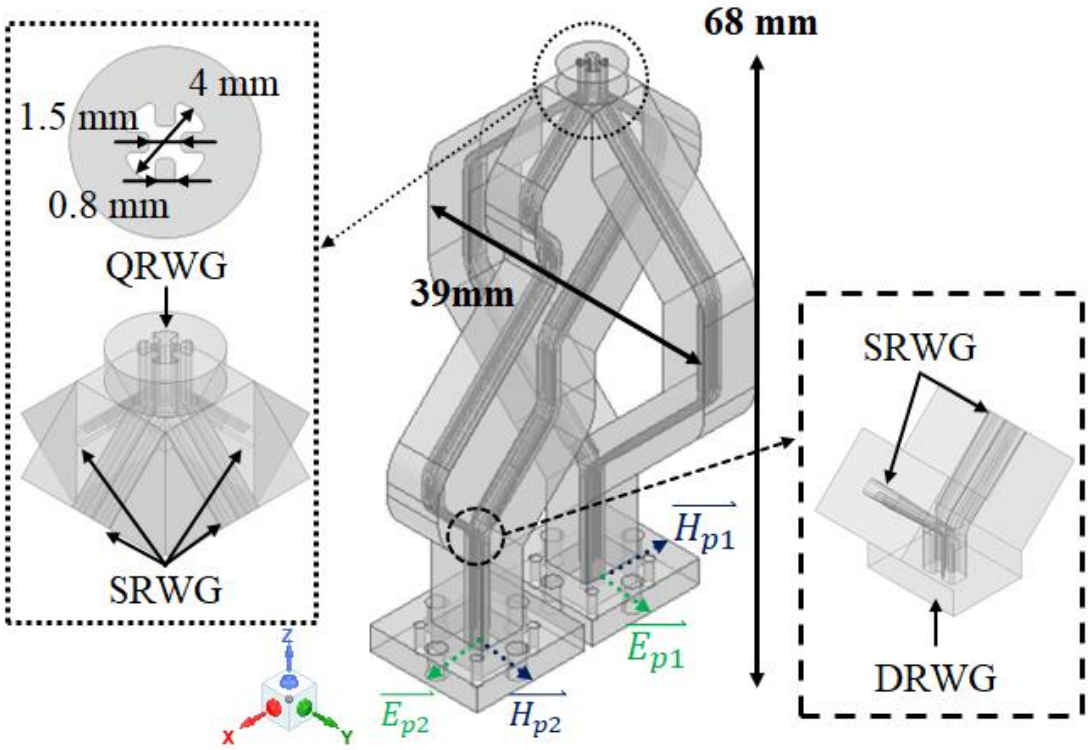

(a)

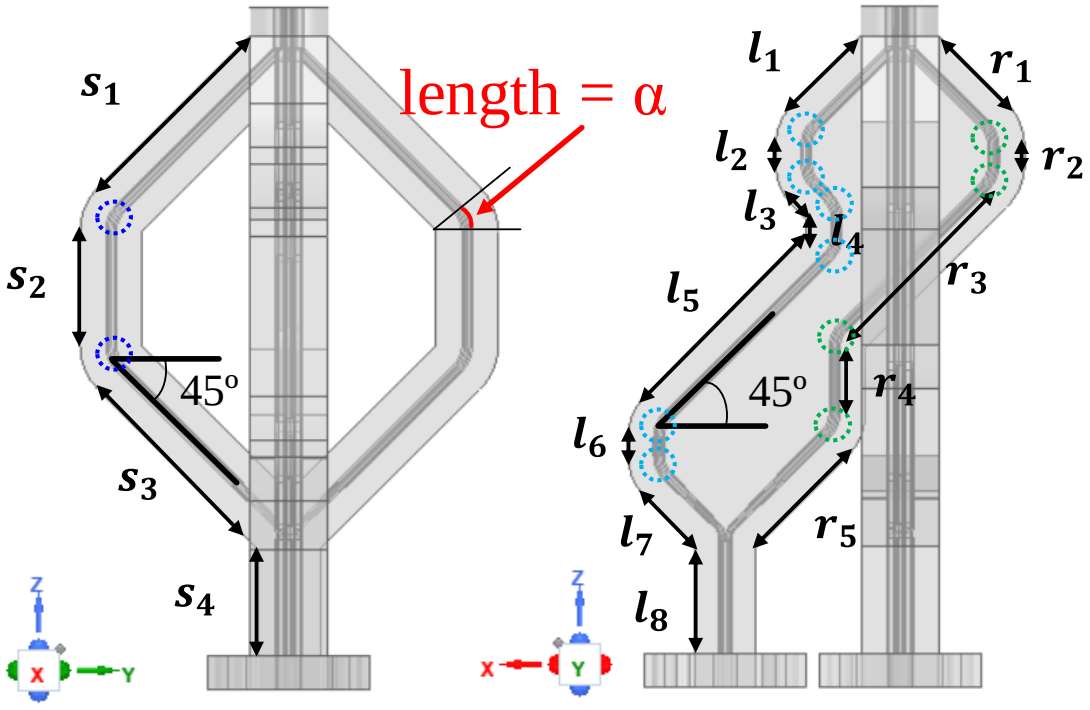

(b)

Fig. 3.11: (a) OMT with turnstile-junction and bifurcation in the insets. (b) Side views of OMT.

Table 3.2: OMT Parameters and corresponding dimensions

Parameter	Dimension (mm)	Parameter	Dimension (mm)
s_1	28.2	l_1	11.1
s_2	13.5	l_2	2
s_3	28.2	l_3	2
s_4	12.6	l_4	2
r_1	11.1	l_5	26.3
r_2	2	l_6	2
r_3	23.4	l_7	8.1
r_4	7.6	l_8	12.6
r_5	15.1		

Shown in Figs. 3.9 and 3.10 are the results of the sensitivity analysis for propagation constant of the OMT's SRWG and DRWG. Their baseline dimensions, shown in the insets, are chosen to ensure 36-90 GHz coverage with some margins on both sides. All custom lines (SRWG, DRWG, and QRWG) have fillets with a 0.2mm radius to account for the 3-D printing fabrication. The sensitivity analysis shows that even with tolerances varying by ±5%, the single-mode propagation bandwidth is safely maintained across the operating band, underscoring the design robustness. The turnstile-junction has a metallic cone-shaped tuning stub located in the center designed based on the parametric studies, with dimensions including a bottom radius of 1.43 mm, a top radius of 0.25 mm, and a height of 1.3 mm. This tuning stub is crucial for preserving the symmetry needed to ensure wideband operation with high channel-to-channel isolation. Since the split position of the bifurcation significantly affects the impedance match, its value is determined using PSO in CST-MWS. A notable design feature of the waveguide in OMT channels is a 45º inclination angle, intentionally selected to facilitate the layer-by-layer AM process. This allows printing

without sacrificing support, enhancing printing quality and simplifying post-processing. It is shown in Figs. 3.11(a)-(b) are the parametrized model of the designed OMT, with Table 3.2 providing corresponding dimensions. If we assume the length of the bent waveguide indicated by the dotted circle marker in Fig. 3.11(b) to be α, the feed parameters must satisfy (3.4) to align the electrical lengths of the two ports:

$$s_1 + s_2 + s_3 + s_4 + 2\alpha = l_1 + l_2 + l_3 + l_4 + l_5 + l_6 + l_7 + l_8 + 6\alpha = r_1 + r_2 + r_3 + r_4 + r_5 + l_8 + 4\alpha \quad (3.4)$$

Each parameter has been calculated to ensure consistency with the 45° inclination angle required for effective 3D printing while minimizing its overall volume based on TJ and bifurcation designs. While adhering to equation (3.4), designing an OMT with increased volume by extending the dimensions of its parameters does not substantially impact its matching performance. This configuration allows for precise control over the polarization division and combination processes while ensuring that both channel pathways have equivalent electrical lengths. This balance is essential for maintaining consistent performance across both polarization channels [57]. As seen in Fig. 3.12, the OMT topology in this work is comprised of a quad-ridge circular waveguide facing QRH, a TJ, two bifurcations (Y-junctions) transitioning from custom single-ridge waveguide to custom double-ridge waveguide, and two double-ridge waveguide outputs. A turnstile-junction in the proposed OMT consists of a quad-ridge circular waveguide aligned with the QRH, which splits into four single-ridge waveguides arranged in a cross pattern. Fig. 3.13 illustrates the concept of the turnstile as a polarization discriminator, where each linear polarization is directed to its corresponding pair of output ports aligned with the input's H-plane orientation. Specifically, port 1 is capable of receiving two independent linear polarizations, denoted as A and B. Due to the symmetry of the

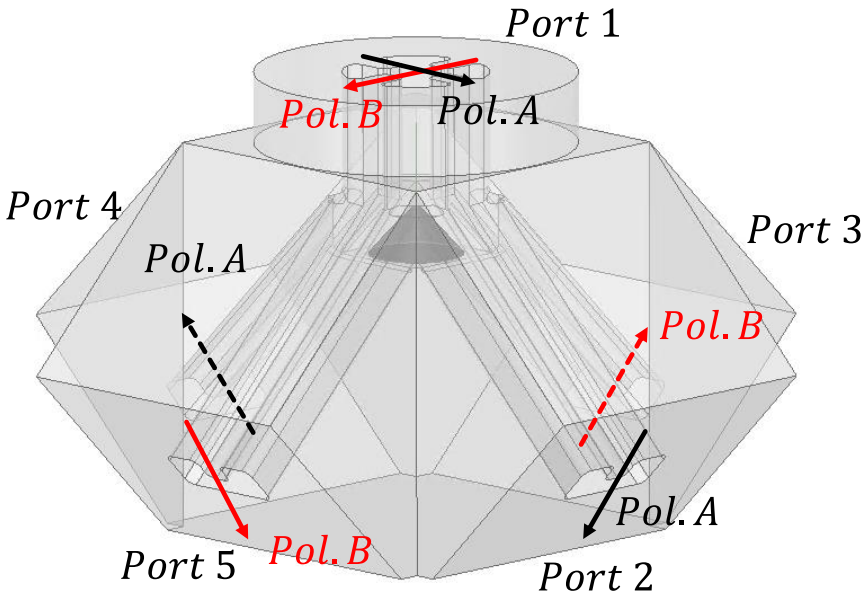

Fig. 3.12: Description of operation for the turnstile-junction.

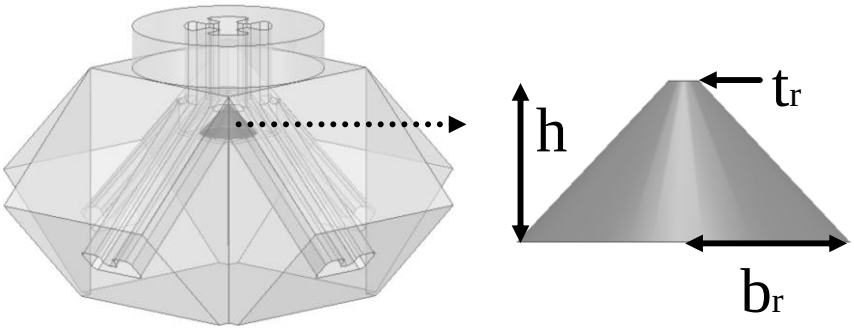

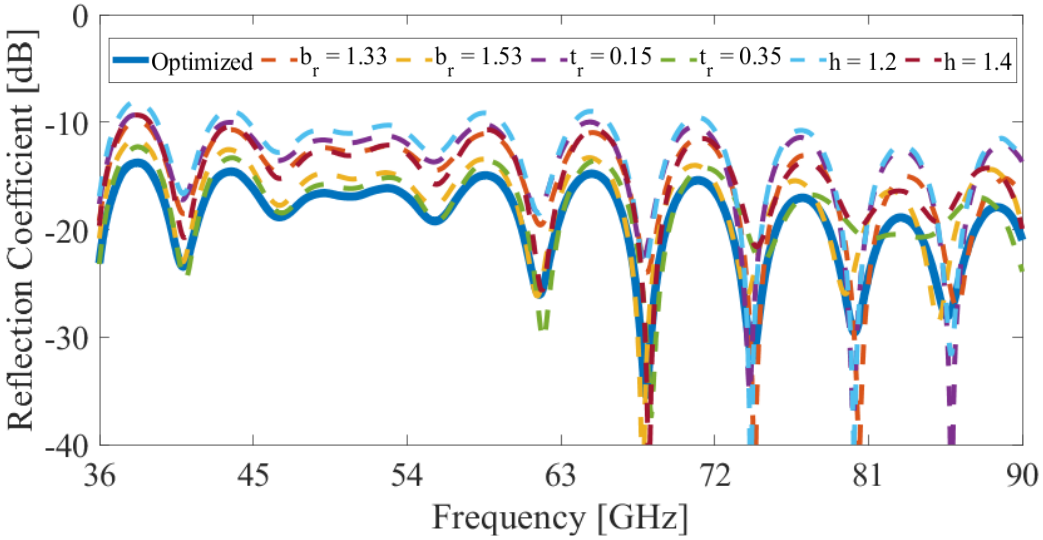

Fig. 3.13: Parametric study of cone-shape tuning stub in turnstile-junction.

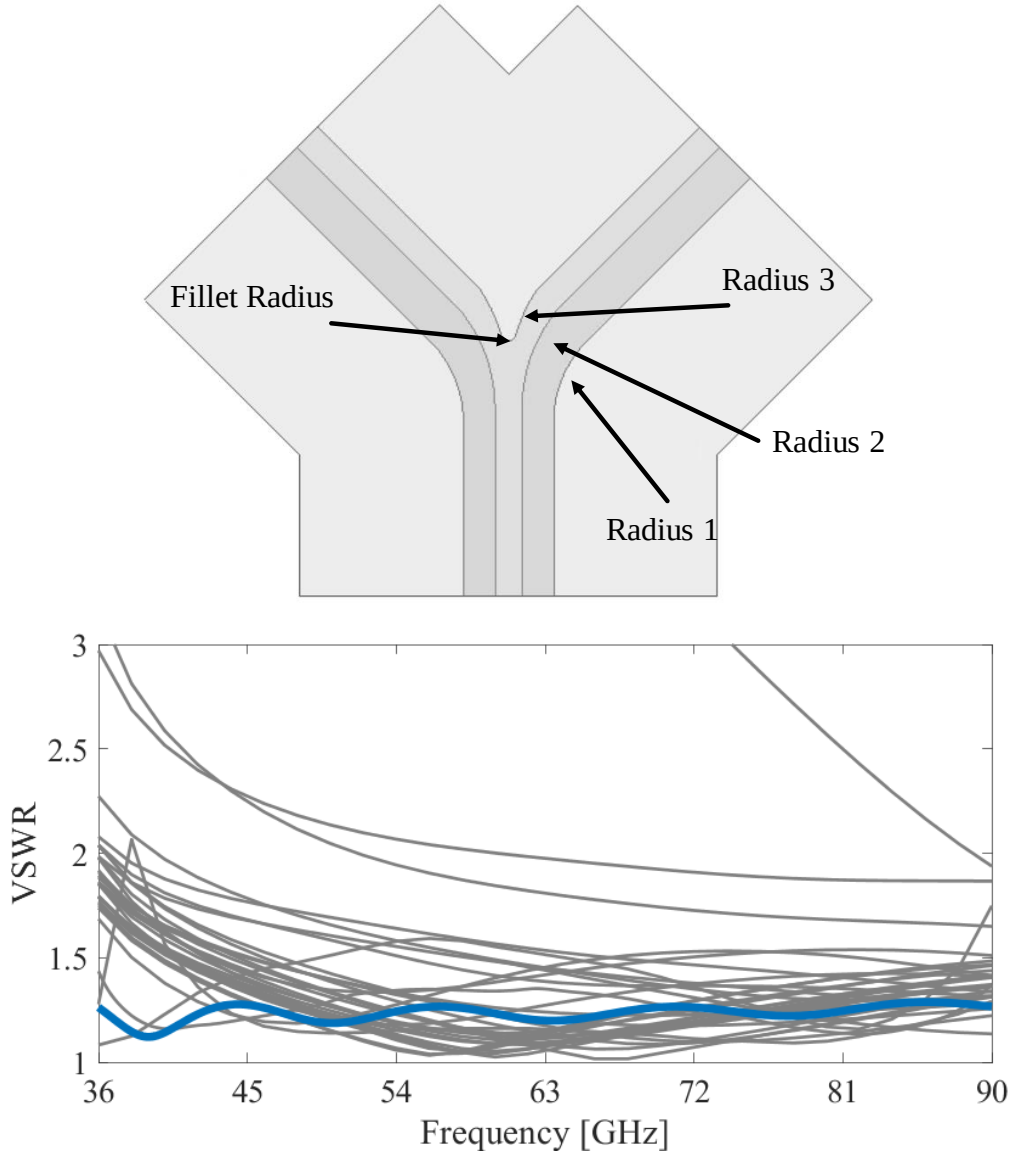

Fig. 3.14: Parametric study of bifurcation in OMT.

junction, the signal is evenly split between the aligned output ports, albeit with opposite phases.

Consequently, minimal signal leakage into the opposing ports ends the turnstile with its characteristic high cross-polarization separation. The turnstile-junction features a cone-shaped tuning stub centrally positioned and designed following parametric studies. The dimensions of this stub include a bottom radius (b_r) of 1.43 mm, a top radius (t_r) of 0.25 mm, and a height (h) of 1.3 mm. This tuning stub

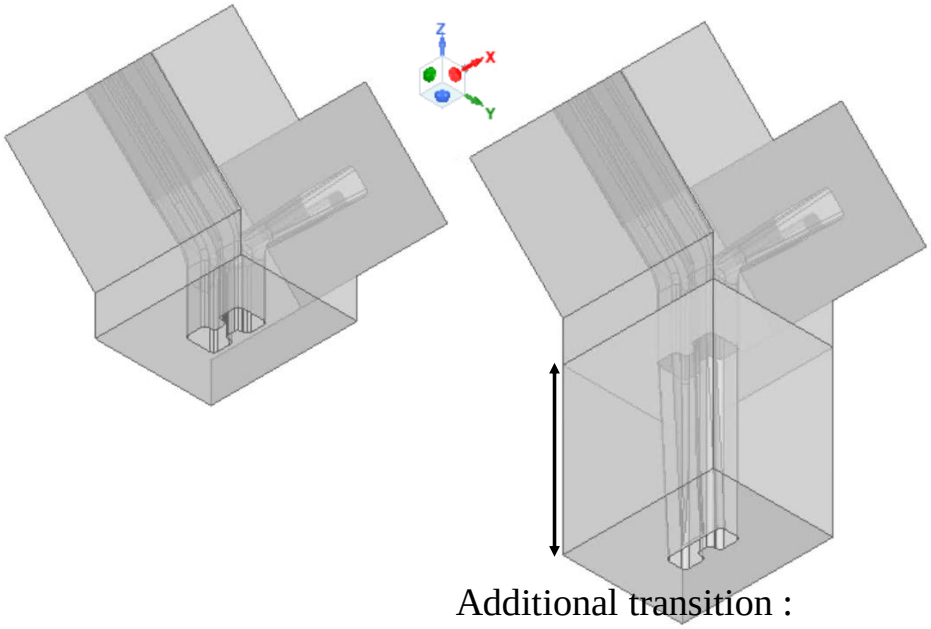

Fig. 3.15: Bifurcation comparison

plays a pivotal role in maintaining symmetry that ensures wideband operation. Fig.3.14 presents the simulation results of the parametric analysis, illustrating the impact of the tuning stub's dimensions. Furthermore, the studies into bifurcation demonstrate that the impedance matching at the common port depends on the various radii (radii 1-3 and the fillet radius) of the bends, as illustrated in Fig. 3.14. Consequently, selections were made for the fillet radius at 1.5mm, radius 1 at 2.25 mm, radius 2 at 2 mm, and radius 3 at 1.46 mm, leading to a VSWR of less than 1.28 across the operational bandwidth. For the final OMT structure, waveguides extending from the turnstile-junction have been meticulously calculated to align the electrical lengths of the two ports [57], ensuring consistency with a 45º inclination angle and minimizing its overall volume. This chapter uses single, double, and quad-ridge waveguides for the OMT to enhance its performance and reduce the overall

volume. As discussed in the paper, the quad-ridge waveguide cross section is selected at the input of the QRH horn to achieve a wideband dual-polarization operation. The proposed OMT consists of three primary elements: the turnstile junction, E-plane bends, and bifurcations. The turnstile-junction, a six-port device, merges two polarizations from four single-ridge waveguides into the QRH antenna. The bifurcation, functioning as a three-port power divider, is designed by dividing a double-ridge waveguide into two single-ridge waveguides of equal cross-sectional areas. Employing a single-ridge for the turnstile-junction and a combined

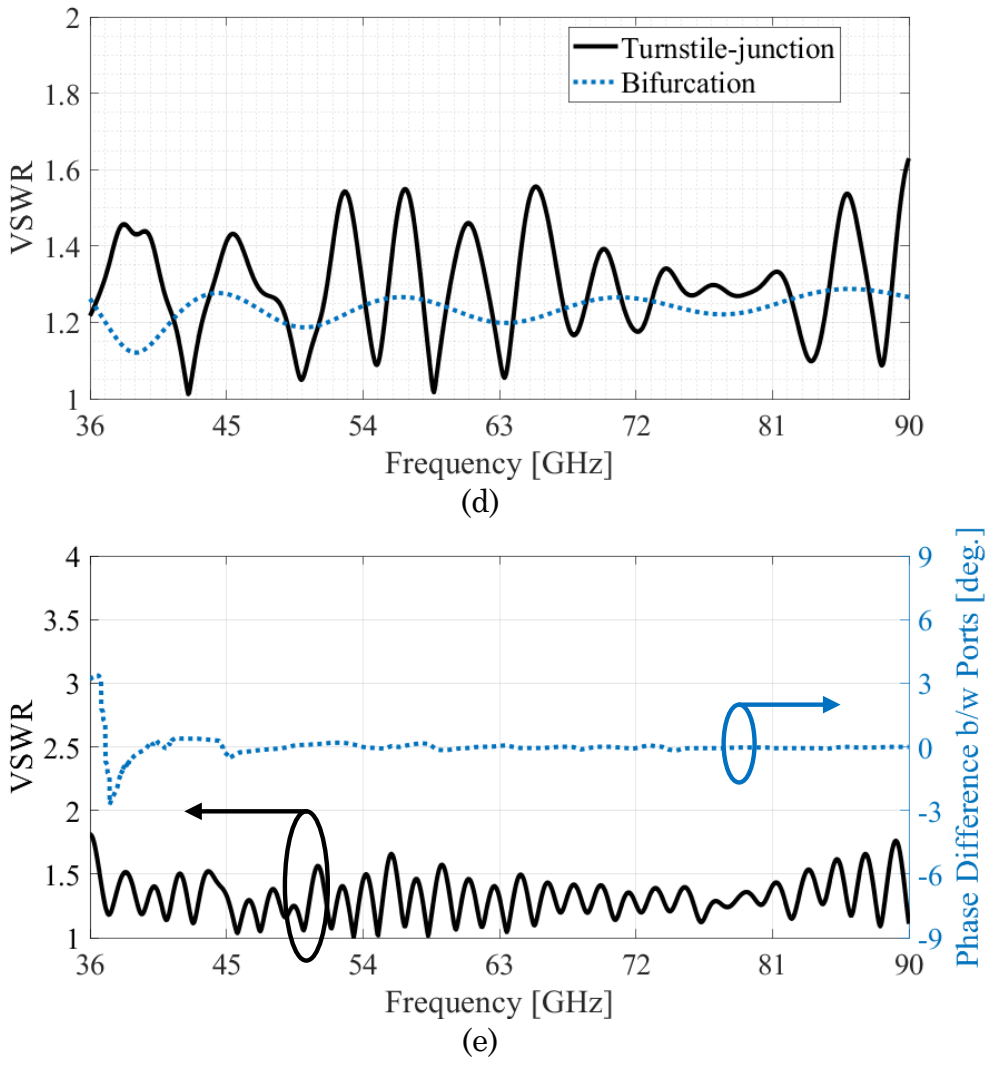

Fig. 3.16: (a) VSWRs of turnstile-junction and bifurcation. (b) VSWR at the DRWG port of the OMT and phase difference between two DRWG ports.

double/single ridge waveguide configuration for bifurcation facilitates the design of an OMT with a shorter overall length (see Fig. 3.15) compared to traditional methods referenced in [89, 91, 92], which is crucial for achieving high-quality 3D-printing. Simulations of the proposed bifurcation, turnstile-junction, and OMT are shown in Figs. 3.16(a)-(b), show good impedance match with VSWR < 1.3:1, 1.6:1, and 1.8:1, respectively. Moreover, the phase difference between the two polarization channels of the OMT is confined within ±3° across the entire bandwidth.

3.4. Fabrication and Measurement

The QRH and OMT discussed in Sections 3.2 and 3.3, respectively, are integrated and fabricated as a single piece with a Formlabs Form3 SLA 3-D printer [93] using Rigid 4000 resin. To help with the copper plating uniformity, the elliptical holes [94] and long cuts along one of the H-plane walls in OMT are added to the model. The hole size is chosen to minimize their impact on RF performance, i.e., ellipse major/minor axis lengths are 1.6/0.75 mm, and spacing between center to center of ellipse is 1.55 mm. The waveguide walls are covered with copper tape attached to identical 3-D printed pieces, as shown in the inset of Fig. 3.17(a). The tape is applied across the entire OMT to reduce leakage from the holes. Destructive tests after plating have shown tolerances and surface roughness of < 0.03 mm and < 20μm, respectively.

The homogeneous lens, made from PP using FDM with a Raise 3D Pro2 printer [95], is a key component in the antenna system. The perforated lens, built in the DLP with a Phrozen Sonic Mini 8K 3D printer [96] with prototyping resin, serves a specific function in the system. Both lenses are shown in Fig. 3.17(b). The VSWR comparison of all simulated and fabricated antennas with and without lenses is

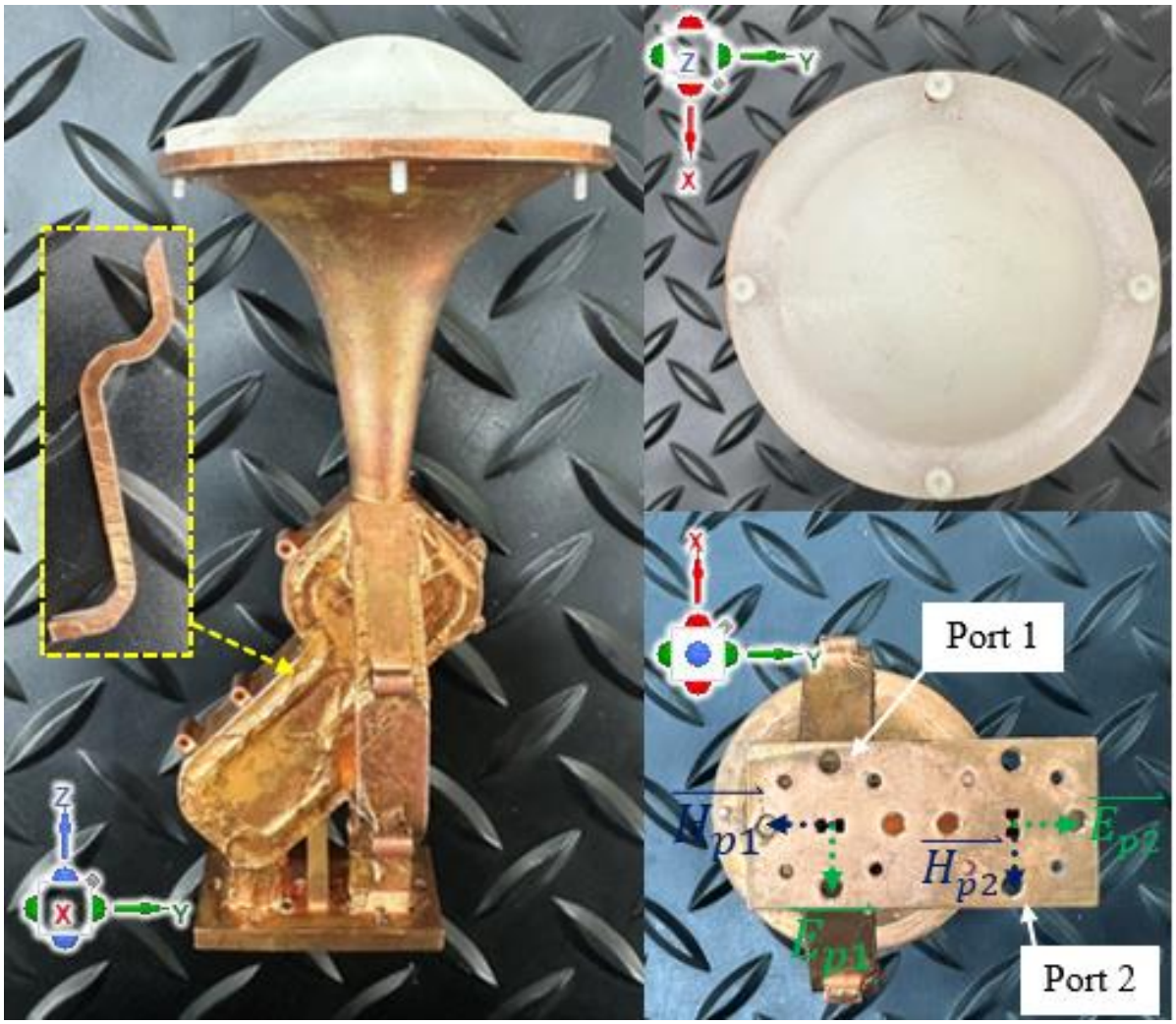

(a)

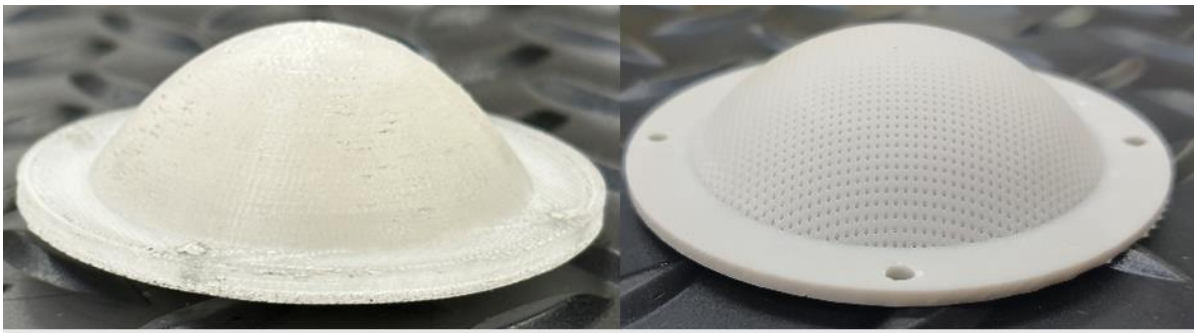

(b)

Fig. 3.17: (a) 3-D printed lens-corrected QRH with OMT. (b) Fabricated lenses (homogeneous: left, perforated: right).

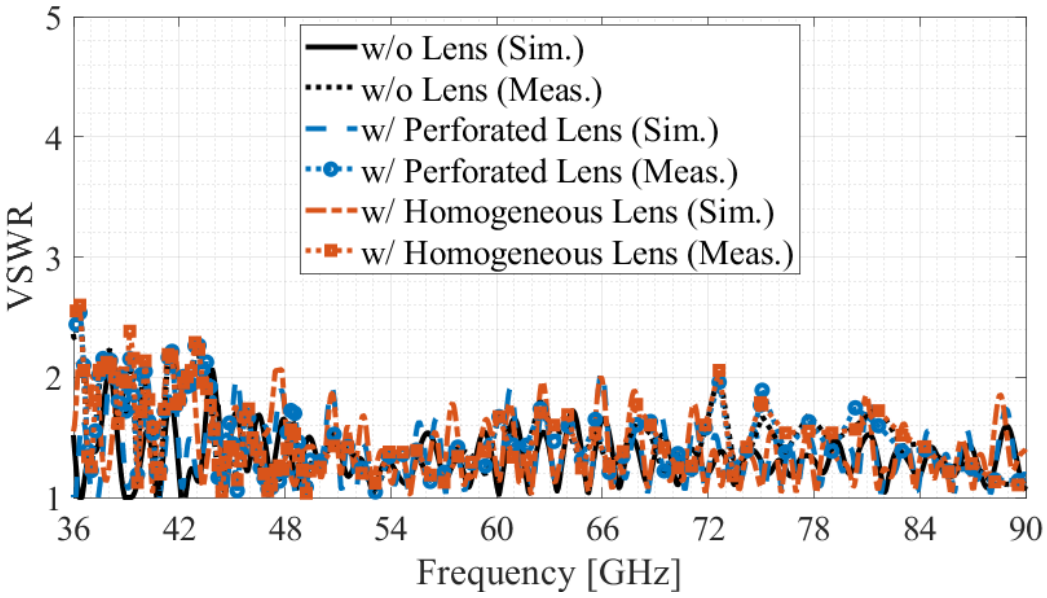

Fig. 3.18: VSWRs of fabricated QRH with and without lens loading.

plotted in Fig. 3.18. As seen, the level below 2.5:1 is achieved at the lower-end of the band, specifically, within the 36-44 GHz range and <2:1 across the remaining frequencies. The VSWR results exceeding 2:1 at lower frequencies in Fig. 3 .18 are attributed to some issues with the 3-D-printed custom adapter (Fig. 3.19) utilized in our measurement setup. This adapter is needed to enable the tests with a 2.4mm connector and is not part of the final system. This is evidenced by the discrepancy between the experimental back-to-back measurements of the custom adapter and its simulated performance at these frequencies, as illustrated in Fig. 3.20. It is important to note that this adapter is only required to facilitate the measurements of our antenna system, and it is not an integral component of the antenna system itself. As seen in Fig. 3.18, simulation results indicate that our antenna system achieves a VSWR of less than 2.1:1 across the entire frequency band. We believe these simulation results are trustworthy and clearly show a good impedance match over the claimed bandwidth of operation. The far-field is measured in the anechoic chamber at the University of Colorado Boulder (see the inset of Fig. 3.21(a)). Results from the two channels show good agreement; therefore, only the port 1 data are

Fig. 3.19. 3-D printed adapter configuration.

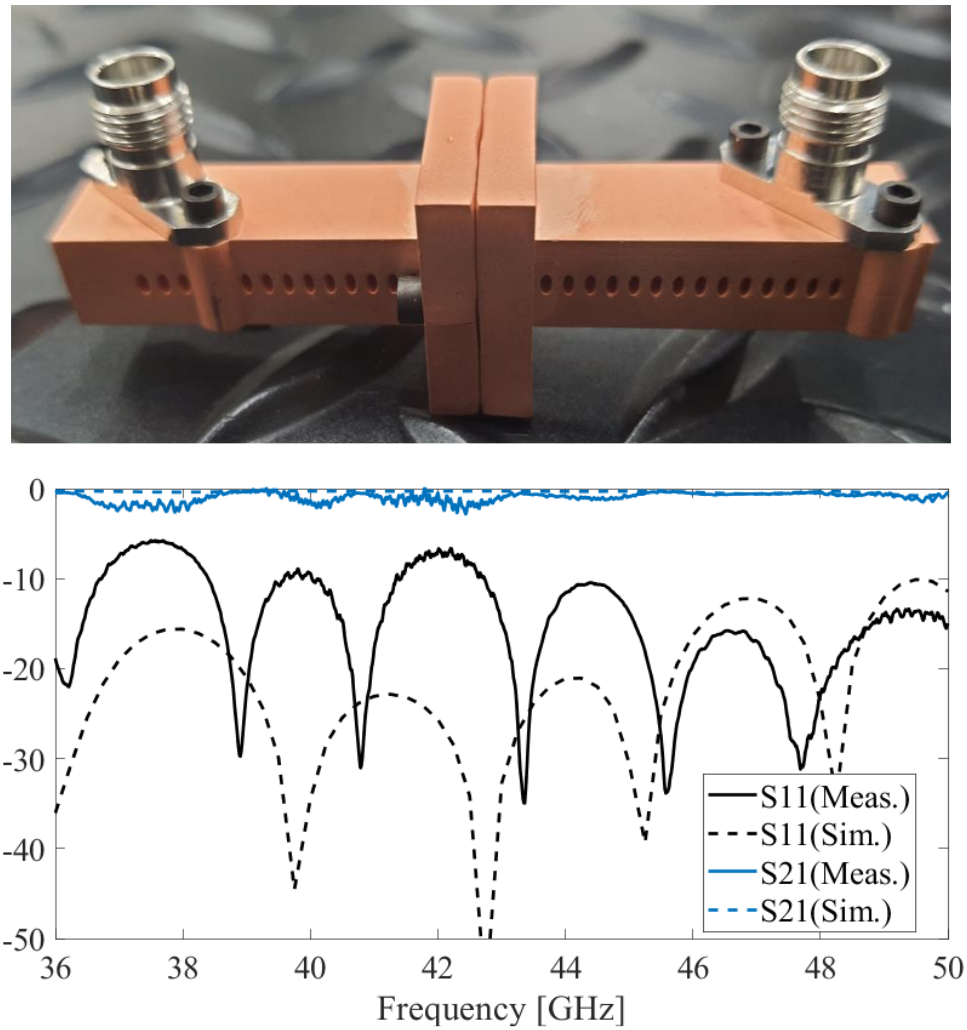

Fig. 3.20: Configuration and performance of the back-to-back 3-D printed adapters that transition from the 2.4mm connectors.

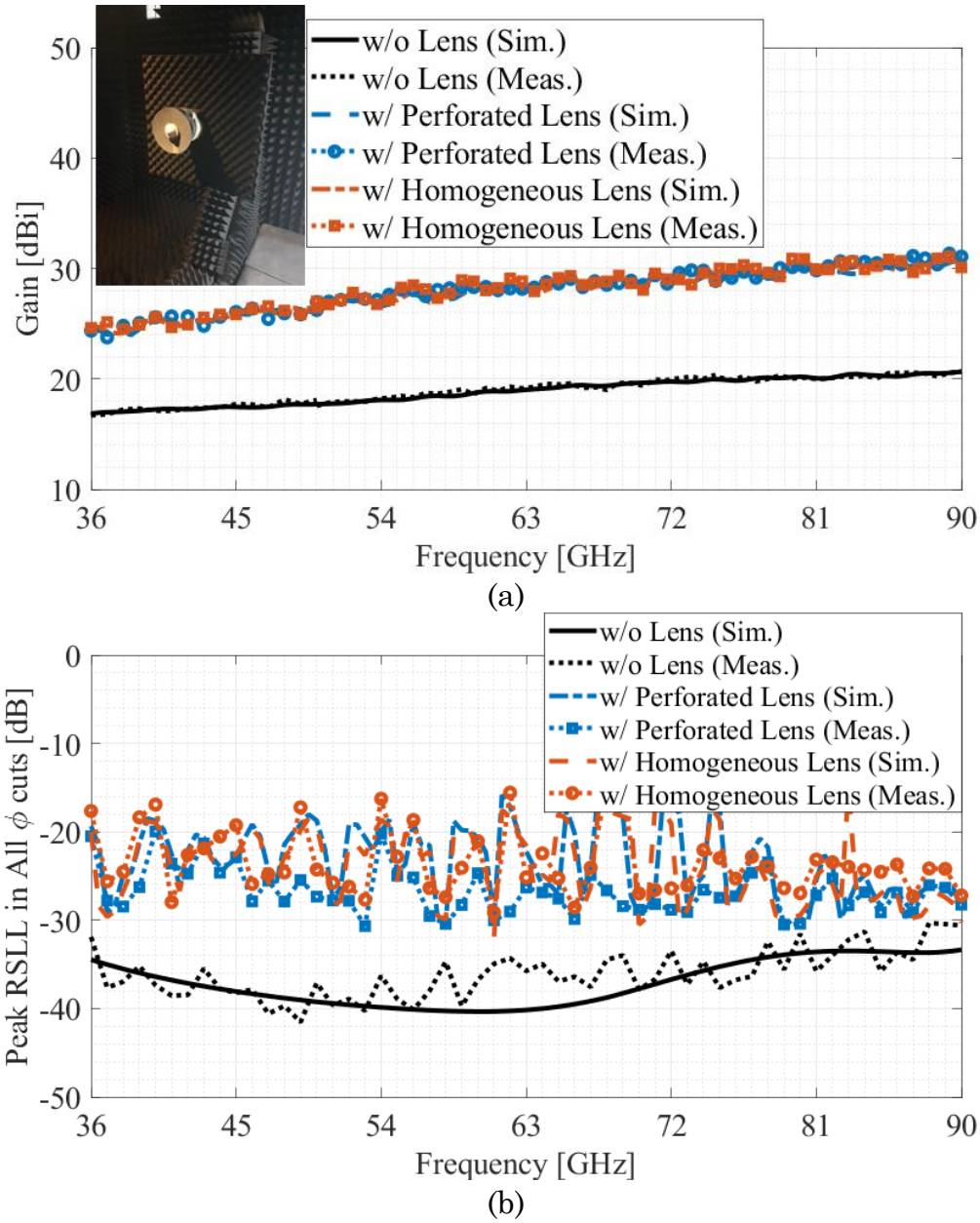

Fig. 3.21: Far-field performance of the fabricated QRH with and without lens loading. (a) Gain. (b) Worst-case SLL across all ϕ cuts.

plotted. As seen in Figs. 3.21(a)-(b), the lens-corrected QRH achieves a significant gain improvement at the expense of slightly worsened SLLs compared to a baseline, lens-less case. The measured gain is > 24.5 dBi with relative worst-case SLL for all ϕ cuts < -15 dB. The radiation patterns in Fig. 3.22 are symmetric in both E-and H-planes, with maintained high cross-polarization rejection (>40 dB) and increased

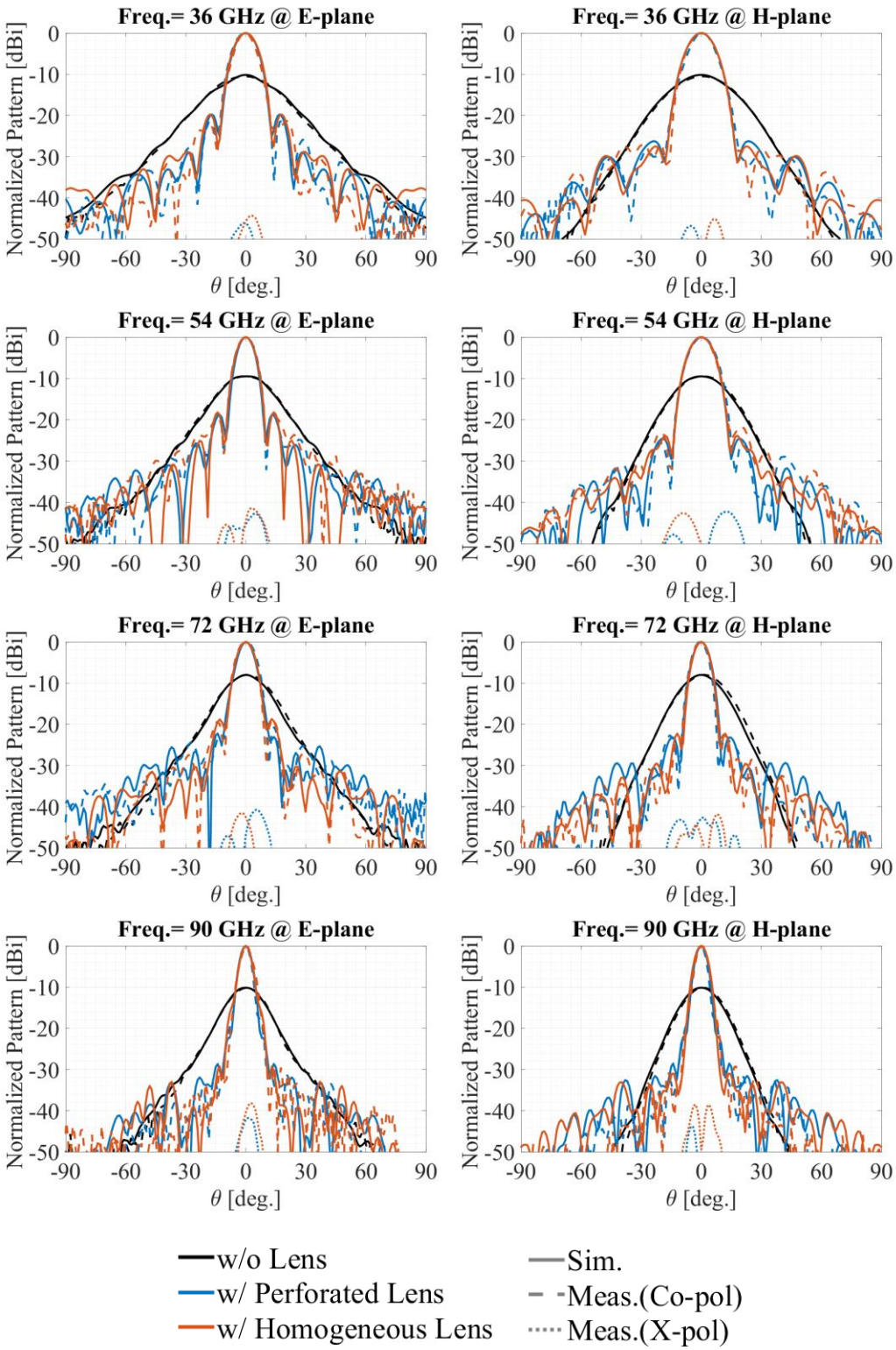

Fig. 3.22: Simulated (solid line) and measured (dashed and dotted lines) radiation patterns of QRH without(black) and with perforated (blue) and homogeneous (red) lenses at 36, 54, 72 and 90 GHz in E-(left) and H-(right) planes.

directionality compared to the lens-less case. This indicates that the fabrication imperfections with FDM and DLP are not detrimental to the lens performance. Excellent agreement between the measurements and full-wave simulations demonstrates the proposed designs' robustness and the maturity of the 3-D printing needed to achieve such well-performing prototypes.

3.5. Cavity Module for SLL Reduction

As discussed in previous Sections 3.2 and 3.4, the integration of the lens significantly enhances gain while deteriorating SLLs. This trade-off is important for applications such as spectrum sensing, polarimetry, direction finding, and resilient communications, just to mention a few. To address the increased SLLs with lens loading, an approach that utilizes a cavity and current sheet absorber is proposed and demonstrated over the entire operational bandwidth. This method, which allows for flush-mounting of the entire system, is not just a solution to a problem, but a potential game-changer in the field of antenna design. The cavity, also designed for AM, is strategically positioned around the QRH/lens with absorbers laid on the interior walls, as illustrated in Fig. 3.23.

The objective is for the absorber to tailor the aperture distribution such that the desired amplitude taper across the new cavity opening is maintained. If done correctly, this can lead to improved SLLs with minimum compromise in directivity, thus effectively functioning as a spatial SLL filter. The absorber sheet primarily influences the performance impact and bandwidth with this module. Herein, the Coolzorb 600 current sheet absorber ($\varepsilon_r = 19,\ \mu_r = 1,\ tan\delta_E = 0.04 - 0.09,\ tan\delta_M = 0.13 - 0.28$) is used due to its listed performance from 1 to 90 GHz [97] and favorable mechanical features that allow for easy integration with curved cavity walls. To offer

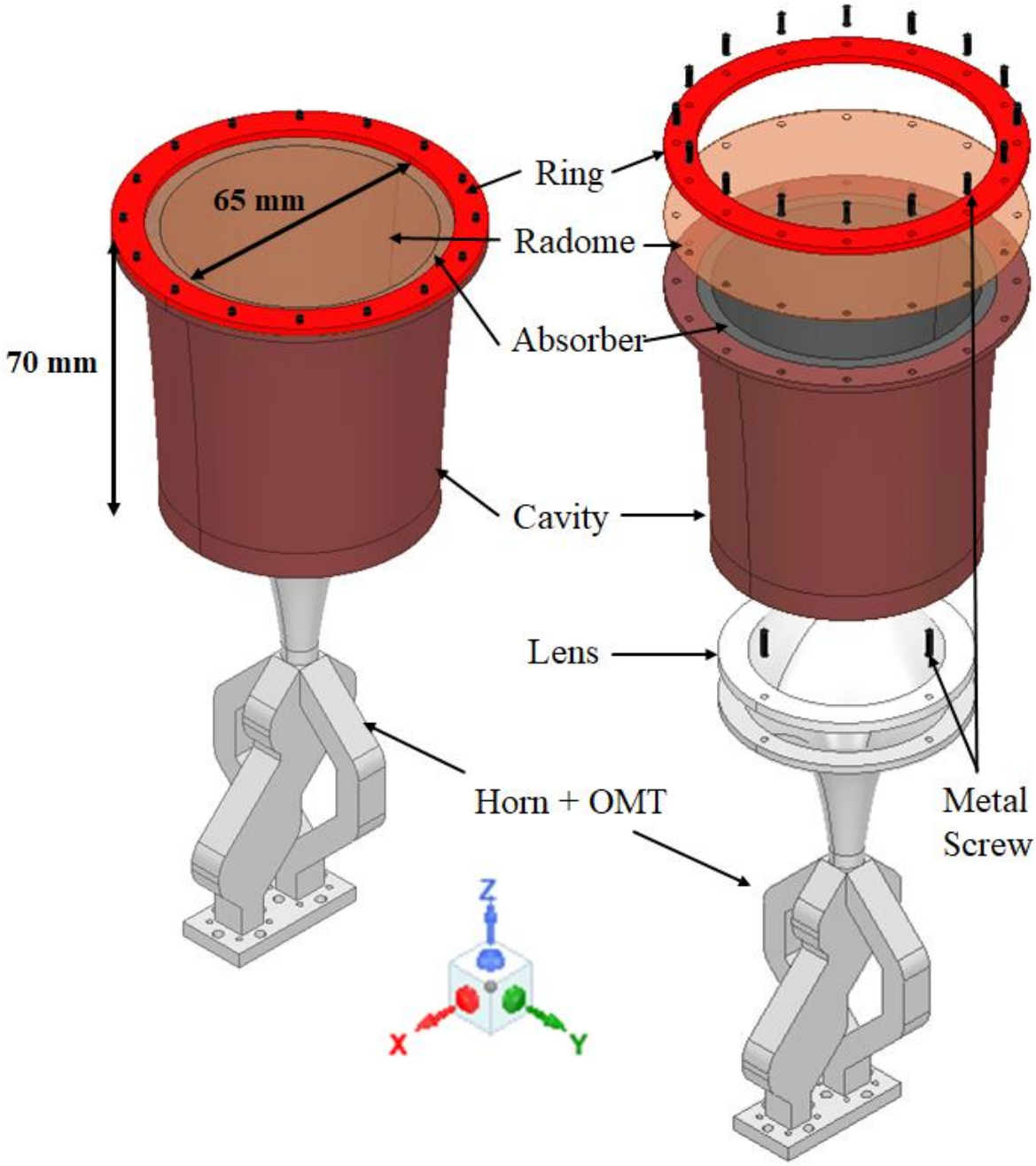

Fig. 3.23: Proposed configuration of the lens-corrected QRH with cavity

the designer greater tuning options, the cavity walls have an exponentially tapered profile. Their mathematical formulation is given in (3.5) [47]:

$$a(z) = A(C_1 e^{Rz} + C_2) + (1-A)[R_i + (R_o - R_i)(z/L)] \quad (3.5)$$

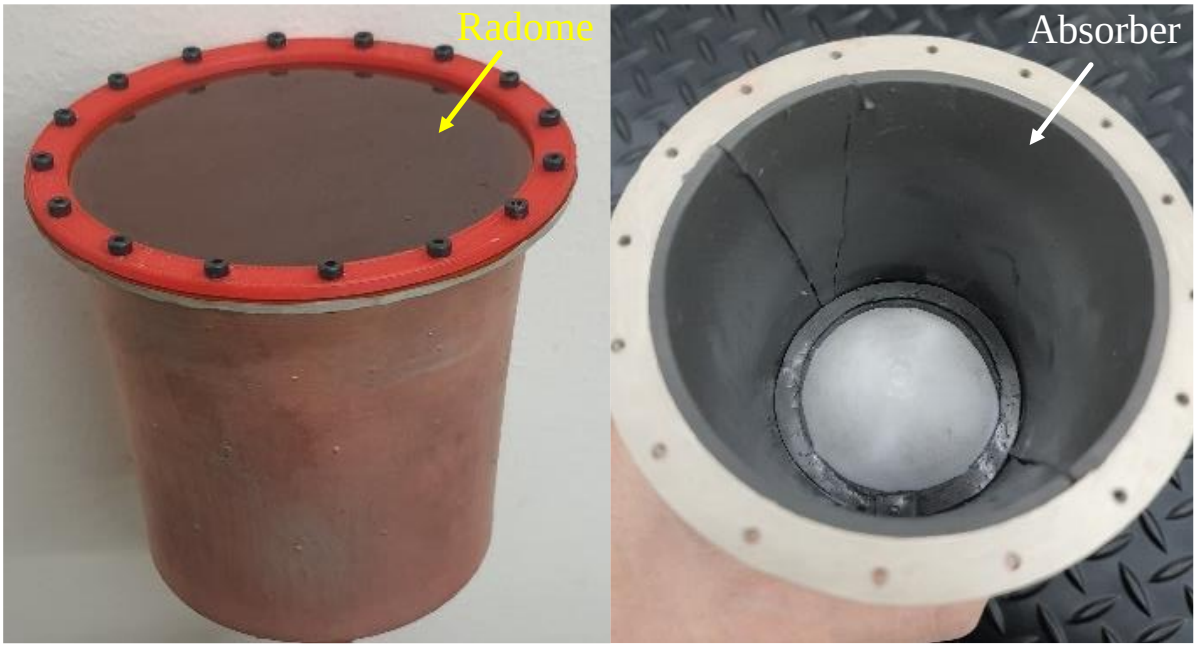

(a)

(b)

Fig. 3.24: (a) Fabricated cavity with absorber and Kapton cover. (b) Weight of the proposed antenna system.

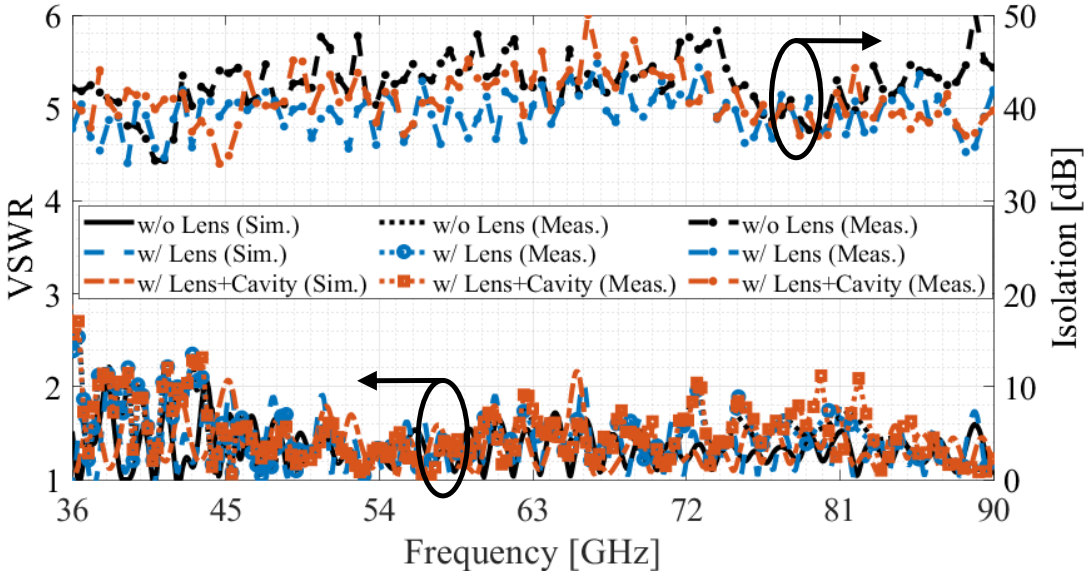

(a)

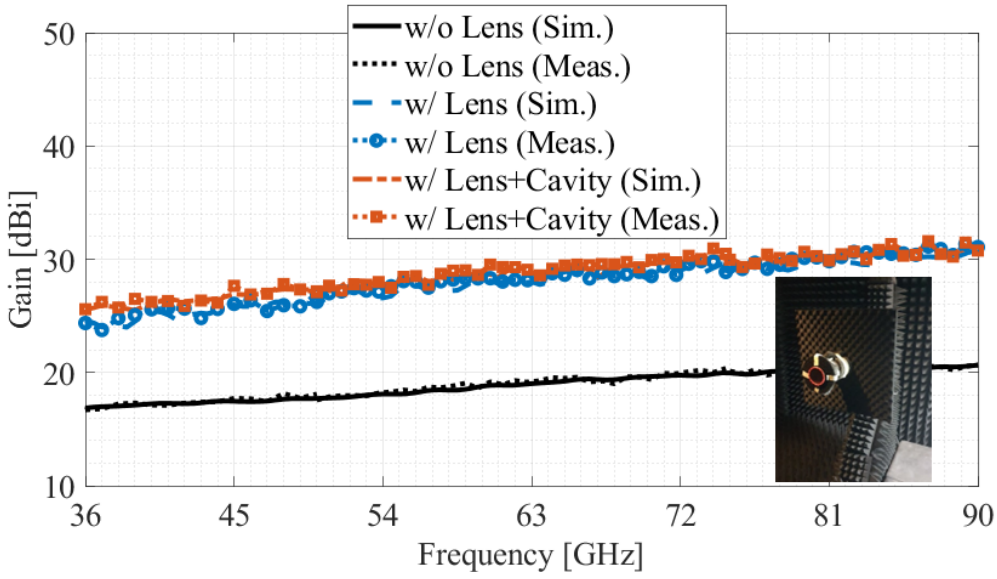

(b)

Fig. 3.25: Performance of QRH without(w/o) and with(w/) perforated and homogeneous lenses. (a) VSWR. (b) Gain.

where $C_1 = (R_o - R_i)/(e^{RL}-1)$, $C_2 = (R_i\, e^{RL} - R_o)/(e^{RL}-1)$, R_i and R_o are the radii at the bottom and the top of the cavity, respectively. L is the cavity axial length, $A = 0.79$, and $R = 21.9$ is the exponential opening rate. As before, the PSO is used to find the cavity parameters that yield the lowest SLLs. The cavity is fabricated in SLA and

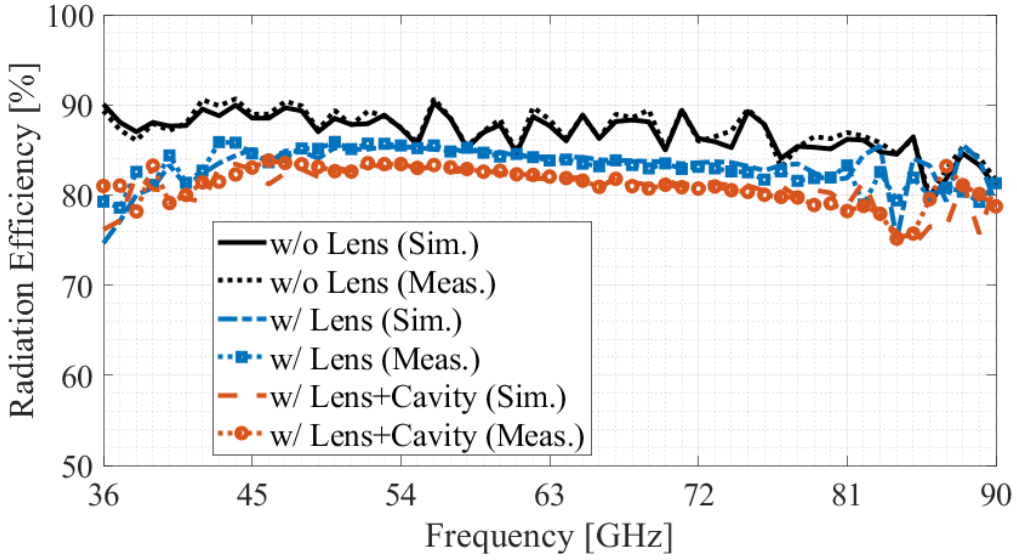

(a)

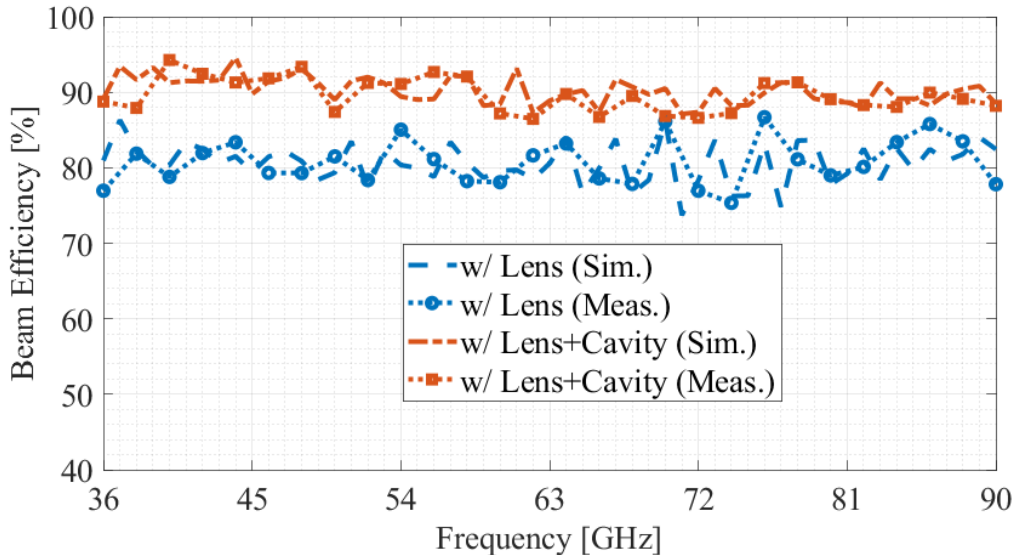

(b)

Fig. 3.26: Performance of QRH without(w/o) and with(w/) perforated and homogeneous lenses. (a) Radiation efficiency. (b) Beam efficiency.

plated with in-house electrolytic copper plating process. A thin layer of 50µm-thick Kapton (ε_r = 4.1, $tan\delta$ = 0.003) is used to provide the environmental protection (see Fig. 3.24(a)). The weight of the new antenna assembly including 3-D printed adapters (12.2oz = 0.346kg) is provided in Fig. 3.24(b). The measurements in Figs. 3.25 (a)- (b) show that the cavity has a negligible impact on VSWR (2.5:1) and isolation (> 34 dB).

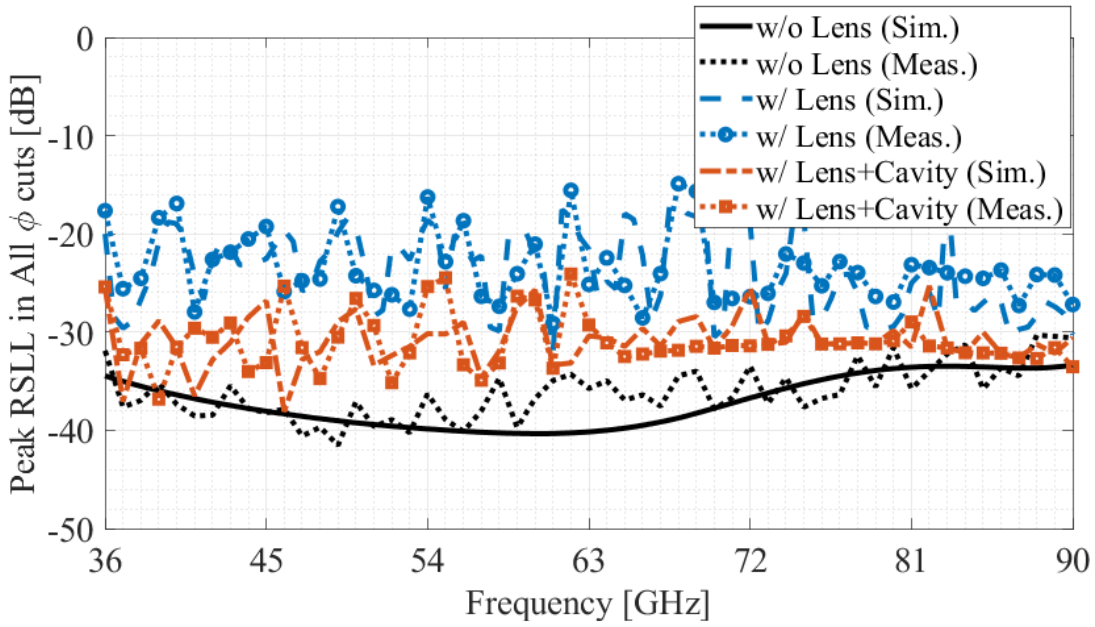

(e)

Fig. 3.27: Peak RSLL in all ϕ cuts performance of QRH without(w/o) and with(w/) perforated and homogeneous lenses.

A gain increase to >26 dBi in the lower frequency band is also obtained. Considering that the new aperture is slightly larger than the lens loaded QRH, this increase is expected. Due to the absorber, the cavity slightly reduces the radiation efficiency above 46 GHz (Fig. 3.26(a)); however, the BE increases by approximately 10% (Fig. 3.26(b)). Most importantly, as shown in Fig. 3.27, the proposed design reduces the worst-case SLLs by about 10 dB to values below -25 dB across the band. This impact on SLLs over a wider field of view is even more exhibited in the measured E-, H—and D-plane radiation patterns in Figs. 3.28 and 3.29. Adding the cavity module with a laid-in absorber yield much-reduced radiation in SLLs over the entire band and field of view with minimum impact on other important parameters, including XPD.

The E-field contour maps at 36 and 90 GHz clearly show how the absorber effectively suppresses the side lobes without impacting the main beam, as seen in Figs. 3.30 and 3.31. This design balance is further demonstrated by the addition of the cavity module, which yields reduced radiation in SLLs over the entire band and

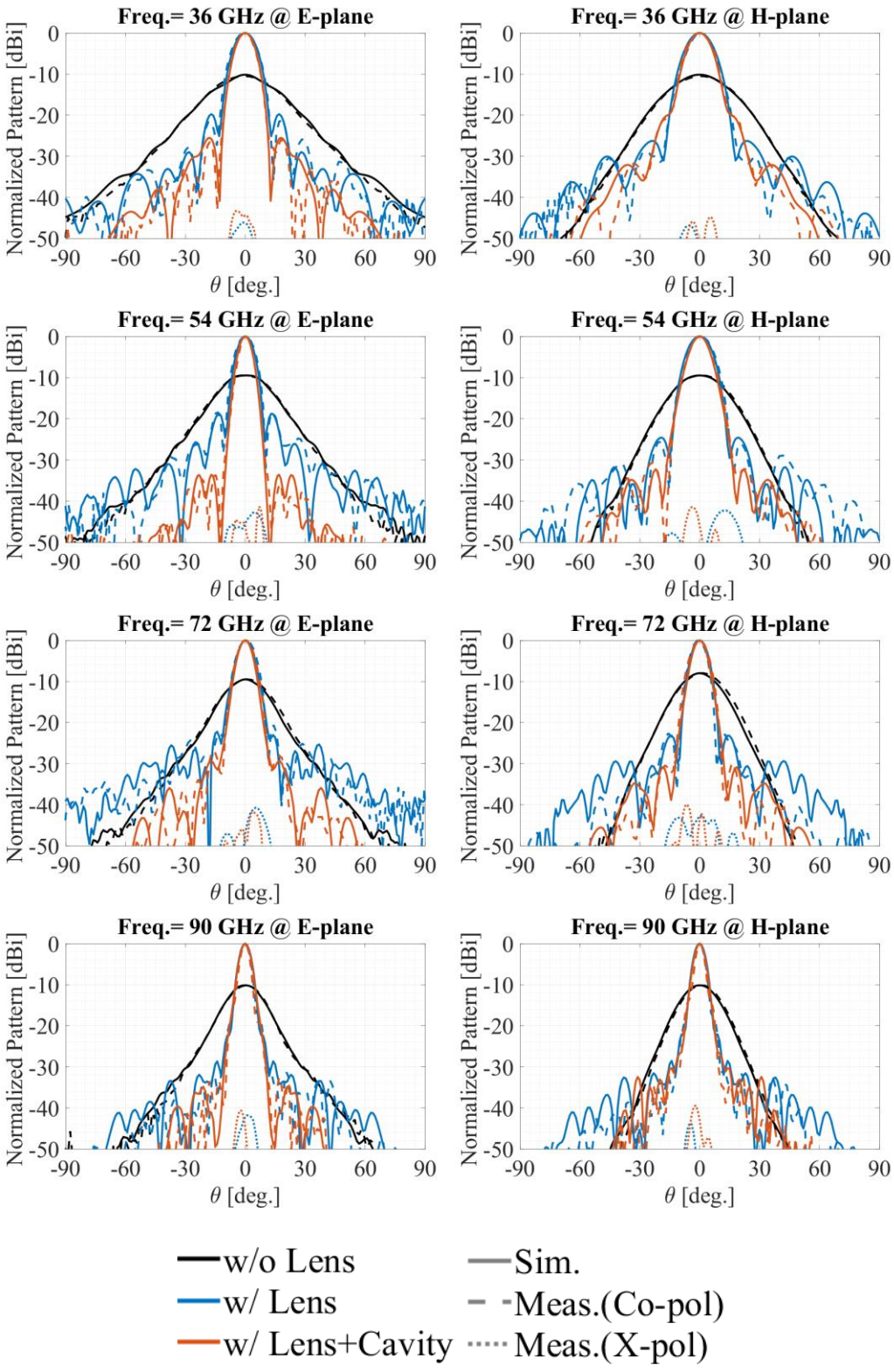

Fig. 3.28: Simulated (solid line) and measured (dashed and dotted lines) radiation patterns of QRH (black), with homogeneous lens (blue), and with cavity (red) at 36, 54, 72 and 90 GHz in E-(left) and H-(right) planes.

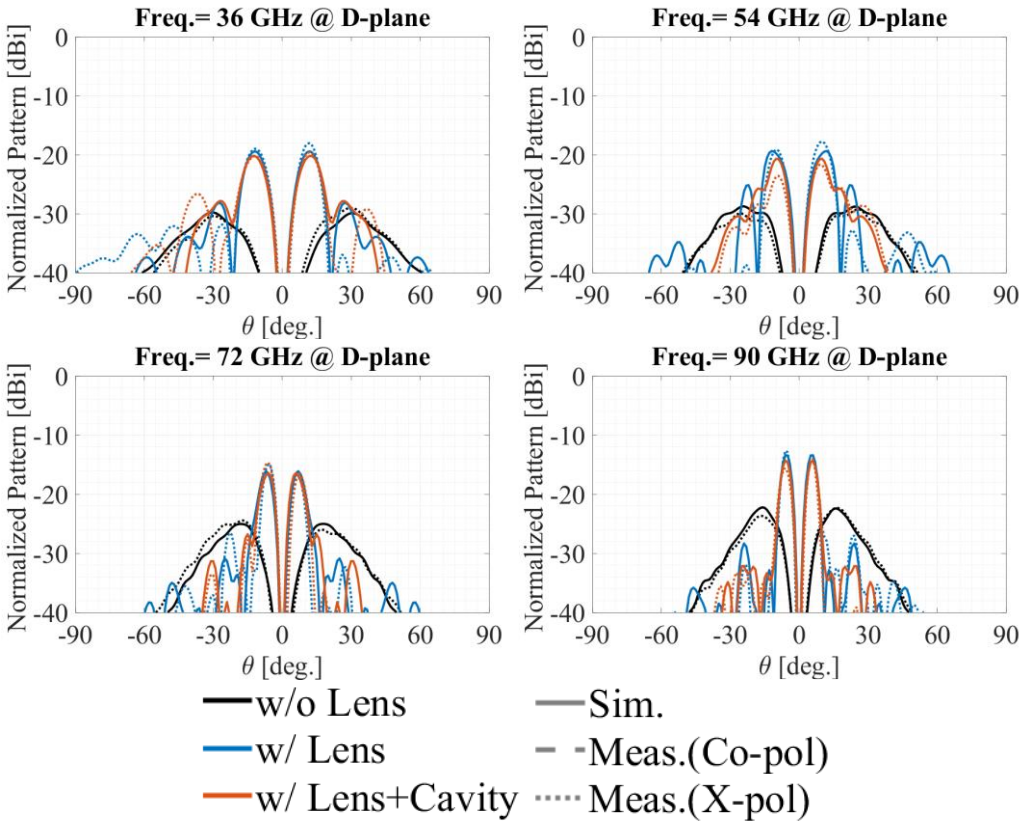

Fig. 3.29: Simulated (solid line) and measured (dashed and dotted lines) radiation patterns of QRH (black), with homogeneous lens (blue), and with cavity (red) at 36, 54, 72 and 90 GHz in D-plane.

field of view, with minimal impact on other important parameters, including XPD, instilling confidence in the overall design. This cavity-based approach is not just versatile, but also liberating in its independence from frequency constraints, as long as the absorber is operational within the desired frequencies. To highlight the performance and uniquness of this work, a comparison with other AM horns [73], [98]-[106], is presented in Table 3.3. Note that the only dual-polarized versions are [102], [105], and this work. As seen, a viable wideband mmWave option with good performance across all important parameters is demonstrated herein.

The SLL represents the peak value of sidelobes (i.e., a radiation lobe (local maxima) in any direction other than that of the major lobe [27]), and further

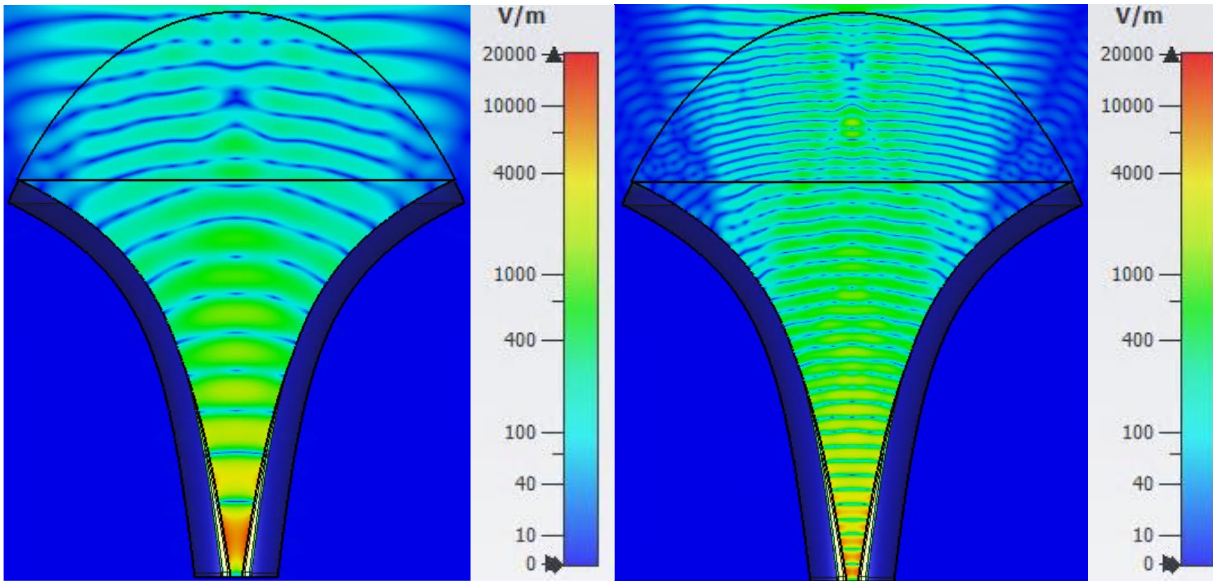

(a) (b)

Fig. 3.30: E-field contour maps of the lens-corrected QRH without cavity and absorber in yz-plane plane at (a) 36 GHz, (b) 90 GHz.

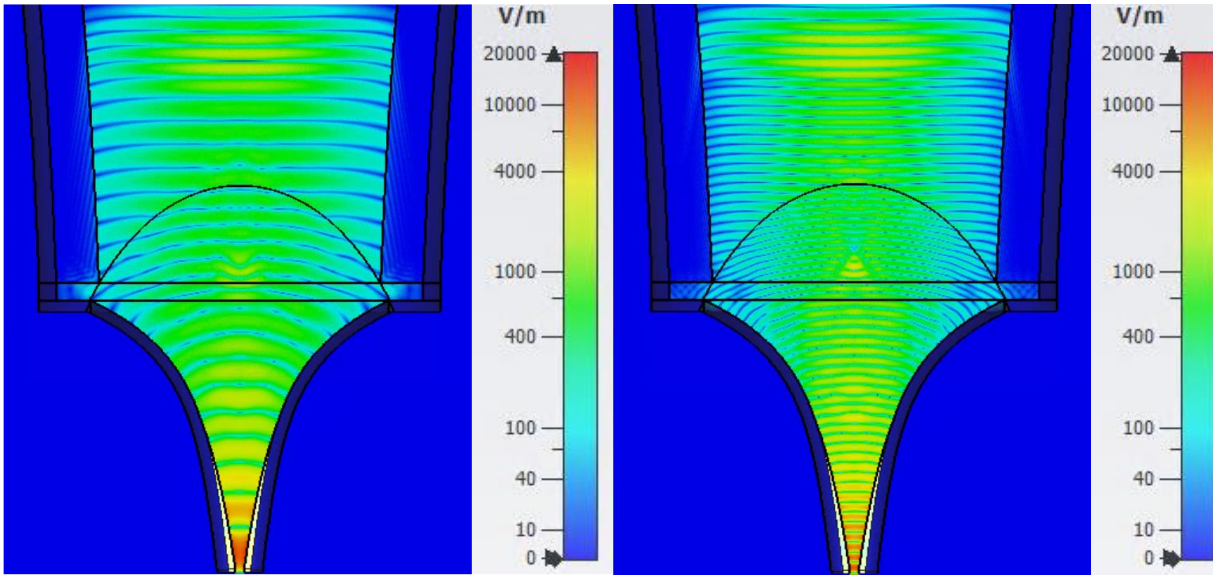

(c) (d)

Fig. 3.31: E-field contour maps of the lens-corrected QRH with cavity and absorber in yz-plane plane at (c) 36 GHz, (d) 90 GHz.

examination of the E-field phase results reveals that the phase near what is identified as a sidelobe should transition from positive to negative [87]. As illustrated in Fig. 3.32, the amplitude of the radiation patterns and the E-field phase result for the

Table 3.3: Comparison with other 3-D printed horns

Ref.	Fab. Technique	Topology	Frequency (GHz)	Gain (dBi)	SLL (dB)	XPD @ boresight (dB)
[73]	DMLS	EBG	8.2-12.4 (1.5:1)	>9	<-25	-
[98]	DLP	Slot	70-90 (1.29:1)	>20	<-11	>32
[99]	DMLS	Corrugation	26-40 (1.54:1)	>12	<-22	>29
[100]	DMLS	Double-Ridge	2-18 (9:1)	>5	<-20	>17
[101]	DMLS	Metal Lens	28.4-34.5 (1.21:1)	>25	< -16	>33
[102]	DMLS and FDM	Conventional Pyramidal Horn	8.2-12.4 (1.5:1)	>14	< -10	>45
[103]	FDM	GRIN Lens	8.2-12.4 (1.5:1)	>18	< -15	>35
[104]	FDM	Dielectric Loading	9-15 (1.67:1)	>16	< -19	>21
[105]	FDM	Quad-Ridge	3.5-11.4 (3.26:1)	>7	< -22	>9
[106]	SLS	Double-Ridge, and GRIN Lens	7.5-18 (2.4:1)	>12	< -12	>23
This work	**SLA, FDM, and DLP**	**Quad-Ridge, Dielectric Lens, and Cavity**	**36-90 (2.5:1)**	**>26**	**< -25**	**>40**

proposed antenna with a lens and cavity manifest that the sidelobe emerges around θ = 35 degrees. The minor shoulder lobe (A radiation lobe that has merged with the major lobe, thus causing the major lobe to have a distortion that is shoulder-like in appearance when displayed graphically) [86] observed with lens+cavity configuration H-plane pattern is not considered as a side lobe at 36 GHz. The simulation configurations and results in Figs. 3.33, 3.34, and 3.35 illustrate the impact of

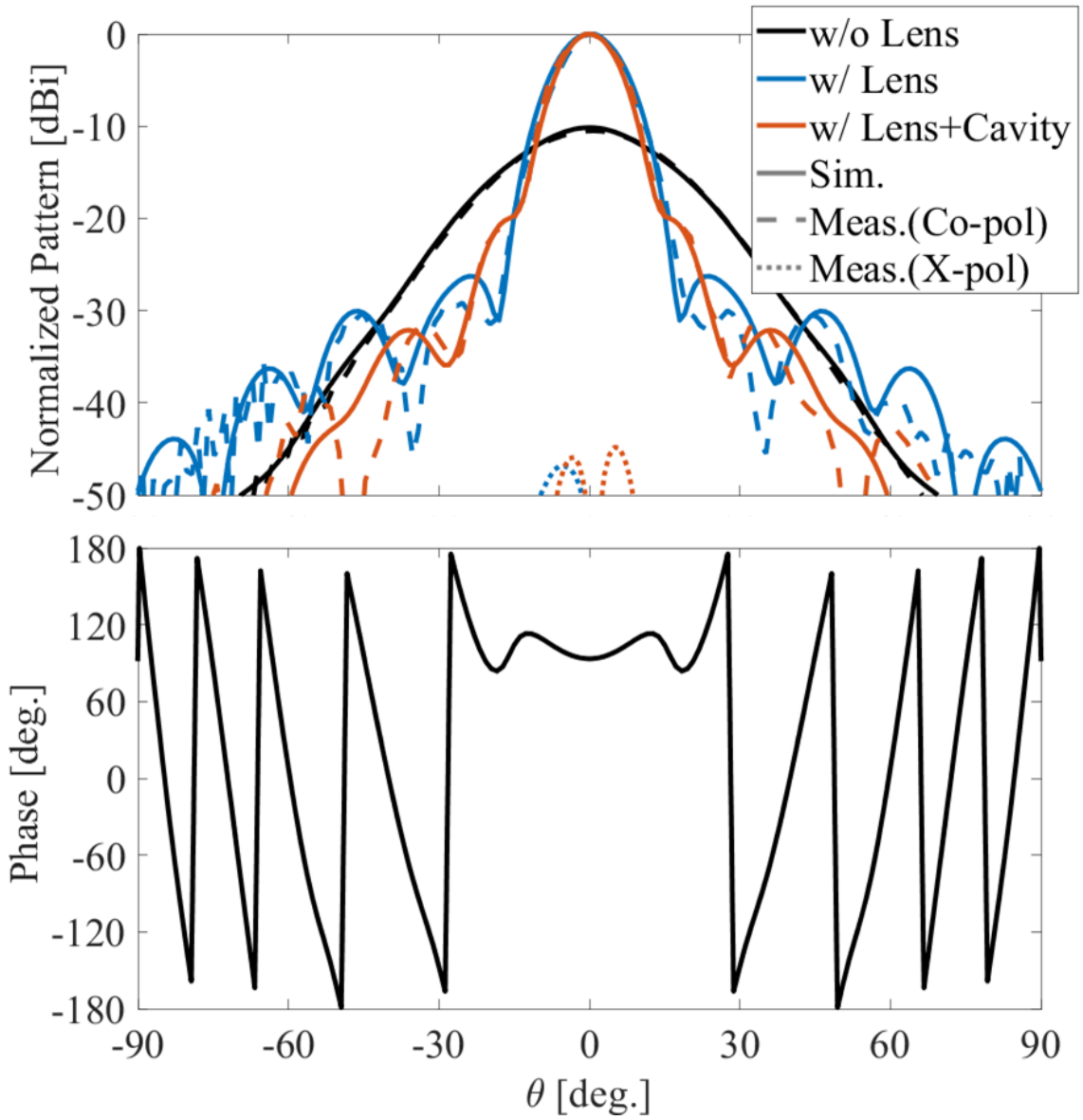

Fig. 3.32: Normalized pattern and E-field phase result of lens-corrected horn antenna with cavity in H-plane at 36 GHz.

elongating the lens-loaded horn axial length. Notably, increasing the horn axial length by an extra 50 mm, equivalent to the cavity-mounted structure, does not significantly enhance the SLL and directivity (i.e., aperture efficiency), as shown in red markers in Fig. 3.34 and 3.35. Given that the lens has been integrated, the flare angle is sufficiently small, thereby limiting the potential for enhancing the SLL by extending the horn length. Thus, despite leading to an increase in overall volume, our

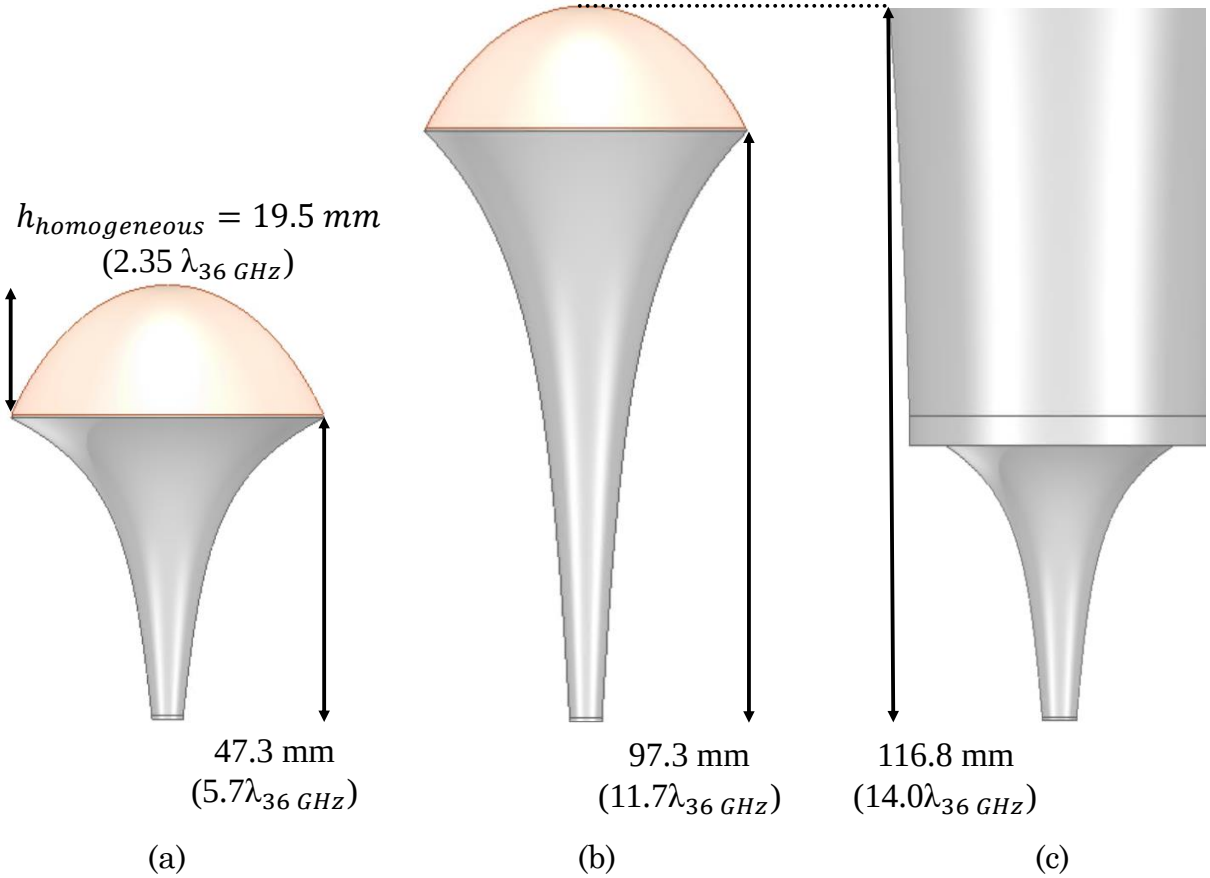

Fig. 3.33: QRH antenna configurations: (a) w/ Lens (axial length = 47.3 mm) (b) w/ Lens (axial length = 97.3 mm) (c) w/ Lens + Cavity lined absorber.

work offers a straightforward and effective approach to improve both SLL and BE. Furthermore, the methodology introduced herein encompasses aspects of both modularity and reconfigurability. Specifically, it introduces a compact horn antenna configuration that allows for adjustments to varying operational needs. Incorporating a cavity into the design facilitates an improvement in the SLL. Should the enhancement of SLL not be a priority or flush-mounting, the cavity can be readily disassembled from the configuration.

The distinctions between Chapter 2 and Chapter 3 are foundational, extending from the operating frequency range to the design objectives, manufacturing techniques, the lens/OMT designs tailored for 3-D printing, as well as

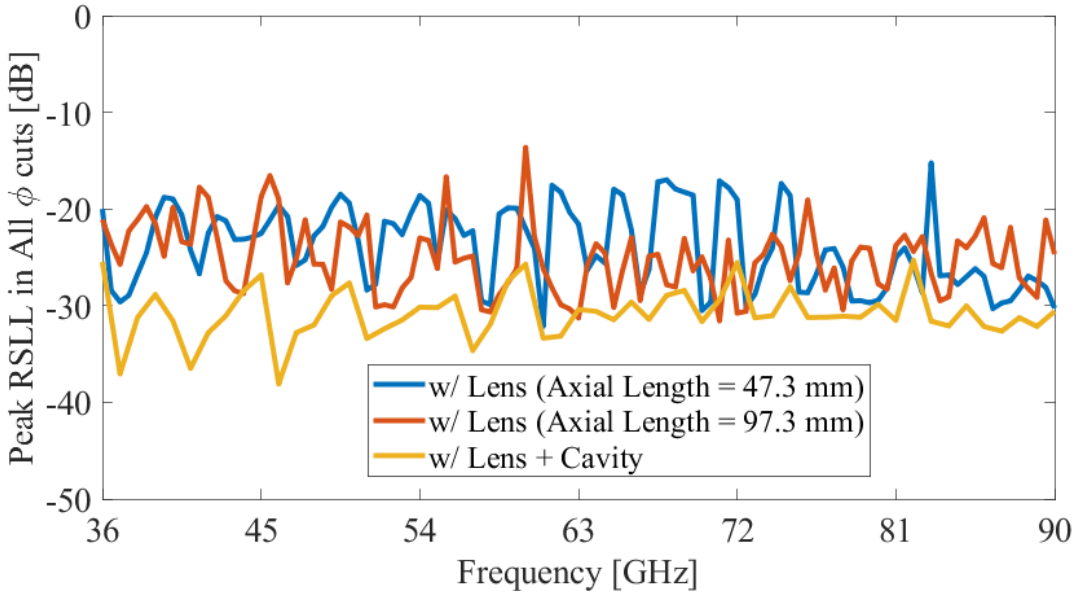

Fig. 3.34: Simulated RSLL with increased axial length of the lens-corrected quad-ridge horn antenna.

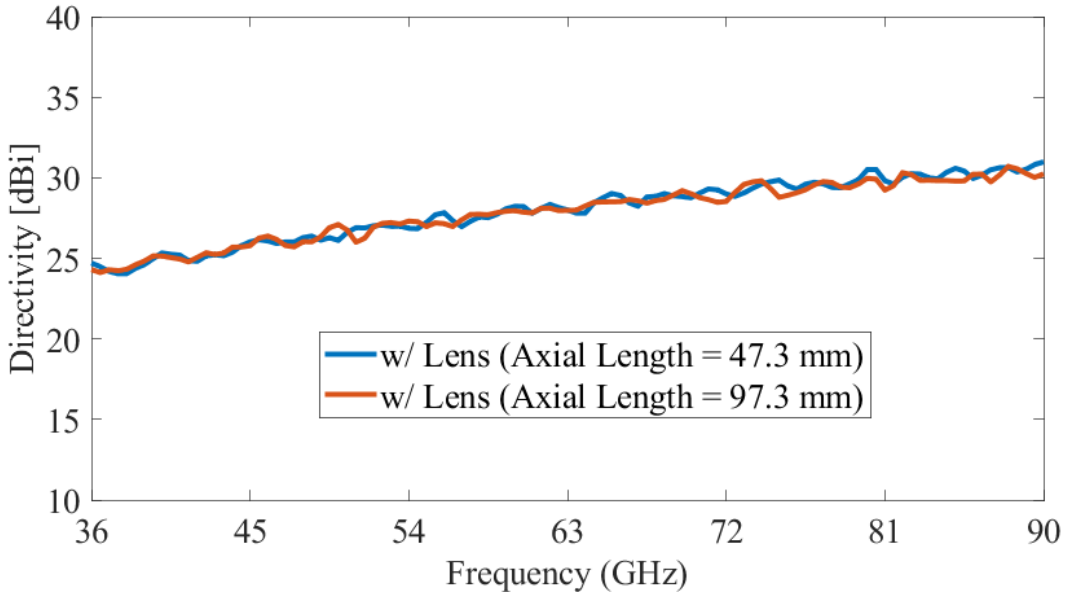

Fig. 3.35. Simulated directivity with increased axial length of the lens-corrected quad-ridge horn antenna.

performance enhancements achieved. In what follows, we detail these distinctions to emphasize the novelty and technical contribution of this chapter:

1. Operating frequency range

Chapter 3 explores the design and performance of a dual-polarization horn antenna within the frequency range of 36-90 GHz, a substantial shift from the 6-20 GHz range discussed in Chapter 2. This introduces new challenges and opportunities for antenna design, particularly relevant for millimeter-wave communications and sensing systems applications.

2. Objectives

While Chapter 2 concentrated on attaining a high minimum gain within a very narrow field of view, even if it sacrifices the antenna's directivity/aperture efficiency at a higher frequency band, this manuscript outlines two specific goals: enhancing aperture efficiency through loading the horn with a 3D-printed dielectric lens and achieving a substantial enhancement in SLL/BE by incorporating an absorber-lined cavity.

3. Manufacturing techniques

A significant innovation highlighted in our study is the adoption of several 3D-printing techniques for antenna manufacturing, diverging from the EDM and CNC manufacturing methods utilized in the prior research. This shift not only proves the practicality of 3D printing for constructing high-frequency antennas but also enables fast prototyping and lowers the cost thereof. Note that the horn in Chapter 2 was EDM-ed, which is impossible to fabricate in the 36-90GHz band.

4. Lens design

In pursuit of its objectives, Chapter 2 compromised on directivity/aperture efficiency in higher frequency ranges by designing a lens of intricate configuration (curved outline). The jammer using that antenna needed to cover specific EIRP field-of-view. Conversely, in Chapter 3, aiming for optimal aperture efficiency, we have developed,

fabricated, and measured both a homogeneous and perforated lens that exhibit comparable efficiency, employing two distinct 3-D printing methods (FDM and DLP).

5. OMT design

To maintain the feasibility of 3D-printing, the OMT was meticulously designed with a 45-degree inclination angle. This strategic design choice effectively eliminates overhanging areas. It reduces the necessity for supporting structures, thereby optimizing the printing process compared to traditional non-monolithic (split-block) CNC machining in Chapter 2.

6. Performance enhancements for sidelobe control

Our manuscript further distinguishes itself by implementing cavity and absorber structures, leading to significant SLL reduction and BE improvement. These improvements are important for some applications that require high accuracy and minimal interference.

7. Modularity and reconfigurability

Chapter 3 presents a dual-polarized horn antenna design with monolithically integrated OMT adaptable to different operational requirements. The integration of the lens and the cavity into the design contributes to enhancements in directivity and SLLs, respectively. If improving the SLL is not essential, whereas improving directivity is, then the cavity can easily be removed from the design.

8. Comparison with state-of-the-art papers of 3D printed horns

All the novelties are supported with favorable agreement between the measurements and simulations and high-quality performance that is on par and better than other possible solutions in commercial and/or academic domains.

Table 3.4 clearly summarizes our explanations as follows:

Table 3.4: Comparison with the structure of Chapter 2

	Chapter 2	Chapter 3
Frequency (GHz)	6.5-20	36-90
Objective	High min. gain over 8º FOV	1. High aperture efficiency w/ lens 2. SLL improvement w/ cavity
Manufacturing Technique	EDM, CNC machining	3-D printing (SLA, FDM, DLP)
Lens Design	Spline-based aspheric dielectric lens (Homogeneous)	Plano-convex lens (Homogeneous and Perforated)
OMT Design	Non-printable	Printable (45º inclination angle)
Performance Enhancement	-	SLL and BE
Modularity, Reconfigurability	-	✓

3.6. Conclusion

An additively manufactured, dual-polarized, cavity-integrated, lens-corrected QRH, operating from 36 to 90 GHz, is demonstrated. A phase-matched OMT with custom single- and double-ridge waveguides is integrated with an antenna to achieve wide bandwidth and dual-polarization. To increase gain and reduce the SLLs, 3D-printed homogeneous or perforated lenses and absorber lined cavity are added in a highly modular fashion. Gain improvements of 8-10 dBi, radiation and beam efficiencies of >75% and 88%, respectively, and SLL < -25 dB are measured. The VSWR at both channels < 2:1 over 85% of bandwidth (44-90 GHz) with port-to-port

isolation > 34 dB are obtained. This chapter shows the ability of AM to produce high-quality modular and versatile antennas for wideband uses across the mmWave spectrum.

Chapter 4

Inhomogeneous Spherical Lens Multi-Beam Array

4.1 Introduction

Beam steering technology is extensively employed across various domains such as communications, radar, remote sensing, just to name a few [107, 108]. The significance of beam steering lies in its ability to adaptively point the beam towards desired users or objects while reducing interference from undesired directions, thereby maximizing the efficiency and reach of the antenna system [108]. Over the decades, advancements in electronic and material technologies have transformed beam steering from mechanically adjusted antennas to sophisticated electronically steered phased arrays. Mechanically scanned antennas, while capable of directing beams to any chosen direction without degrading performance, are limited by cumbersome mechanical structures and slow scanning speeds. In contrast, phased array antennas, used in conjunction with digital signal processing algorithms, offer electrical scanning capabilities that mitigate these limitations. This method provides finer control over beam shaping and direction, enabling the simultaneous creation of multiple beams from a single physical array, though it comes with high costs and

complexity due to the extensive use of phase shifters and transceivers [109]. Alternatively, considerable interest and numerous studies have focused on multi-beam or switched-beam antennas [110, 111]. Although they usually provide less flexibility than digital beamforming solutions, they have several advantages, such as simplicity, lower power consumption/fabrication cost, and ease of integration. Additionally, in pursuit of achieving high directional characteristics, various forms of lens-based multi-beam arrays have been developed, including flat [112-114], ellipsoidal [115, 116], spherical [117, 118], and hemispherical configurations [119-121]. Notably, inhomogeneous spherical lenses (i.e., gradient-index lens) are frequently chosen for multi-beam arrays due to their distinct advantages that significantly improve system performance across multiple applications. The inherent spherical geometry of these lenses helps in precise focal point adjustment, which enables more accurate control over beam direction, covering a broad field of view. However, the necessity for a gradient-index at millimeter-wave (mmWave) frequencies introduces specific constraints in the traditional manufacturing process such as material limitation, quality control and scalability issues. Recently, AM techniques, also known as 3-D printing, have shown considerable promise in overcoming some inherent limitations associated with traditional manufacturing methods. These techniques provide significant benefits, including design flexibility and rapid and cost-effective prototyping, while achieving suitable precision for mmWave applications [122].

In this chapter, we demonstrate the design for AM fabrication and performance over 36-90 GHz bandwidth of a monolithic, wideband multi-beam array consisting of five double-ridge horns (DRHs) with a stable phase center and absorber-lined ring to achieve gain improvement and lower SLL and a phase-correcting 3-D printed lens with structural spacer. The initial step involves designing a phase-center stabilized DRH with a custom double-ridge waveguide [76] that covers the operating frequency.

Fig. 4.1: Photographs of the fabricated multi-beam array with an inhomogeneous lens and a shielding cover.

New features have been added to expand the range of applications and enhance performance. Specifically, an inhomogeneous lens (2 shells) with a structural spacer, a cylindrical-shaped ring with a current sheet absorber, additional beams with a ±12º tilt angle in both E- and H-planes, and a shielding cover designed to proactively mitigate potential issues related to electromagnetic interference (EMI) and compatibility (EMC), as shown in Fig. 4.1. This cylindrical-shaped ring effectively functions as a spatial filter, engineered to mitigate wave propagation in undesired directions. It minimizes reflection and diffraction effects while preserving wideband characteristics and improving main-beam directional performance. The measured performance agrees well with simulations, demonstrating the maturity of the proposed designs and the ability of AM technology to create highly functional prototypes in this and other parts of the RF spectrum.

The rest of the chapter is organized as follows: Section 4.2 discusses the design of a DRH, an inhomogeneous lens, and a multi-beam array. Section 4.3 is dedicated to the realization of 3-D printable prototypes. Section 4.4 describes fabrication and measurement results along with comparisons with state-of-the-art 3-D printed multi-beam arrays. Finally, Section 4.5 discusses the feasibility of amplitude-only direction finding (AODF) systems.

4.2 Multi-Beam Array Design

A 36-90 GHz double-ridge waveguide was firstpresented in [76], illustrating the cross-section of a non-standard waveguide along with its simulated propagation constants in CST-MWS, as shown in Fig. 4.2. The design of double-ridge waveguide aims to ensure good performance within the target frequency range of

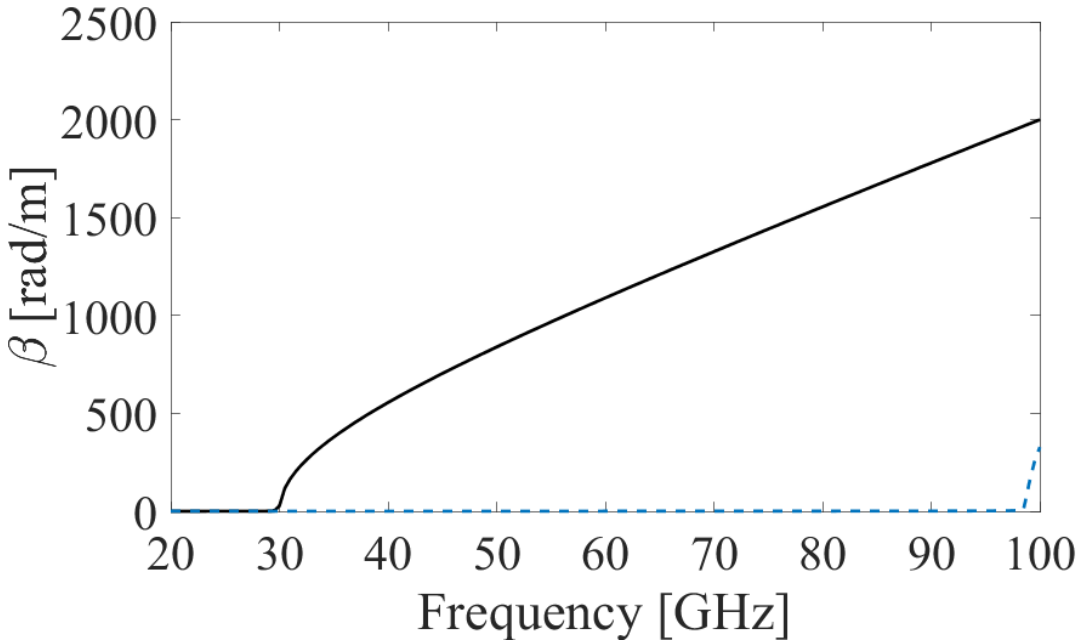

Fig. 4.2: Propagation constants of custom double-ridge waveguide.

36-90 GHz. Precisely, to determine the outer dimensions of the double-ridge waveguide, the cutoff wavelength for the higher-order mode TE_{01} is nearly equal to twice the waveguide height [123]. Fig. 4.3 corresponds to an outer height (b) = 1.57 mm if the TE_{01} mode is to be prevented from excitation below 99 GHz, which is ~ 10% above the desired upper-frequency end (i.e., 90 GHz). To achieve low attenuation, the outer width is set to twice the height (i.e., waveguide width (a) is 3.14 mm) [124]. Parametric studies concerning the ridge-width and -gap between ridges are undertaken to determine this transmission line's optimal dimensions (w = 0.94 and g = 0.47 mm respectively) while maintaining 3-D printing manufacturability. The sensitivity analysis accounts for ± 5% tolerances of all critical dimensions, ensuring that the single-mode propagation bandwidth is consistently maintained across the operating band, underscoring the design's robustness.

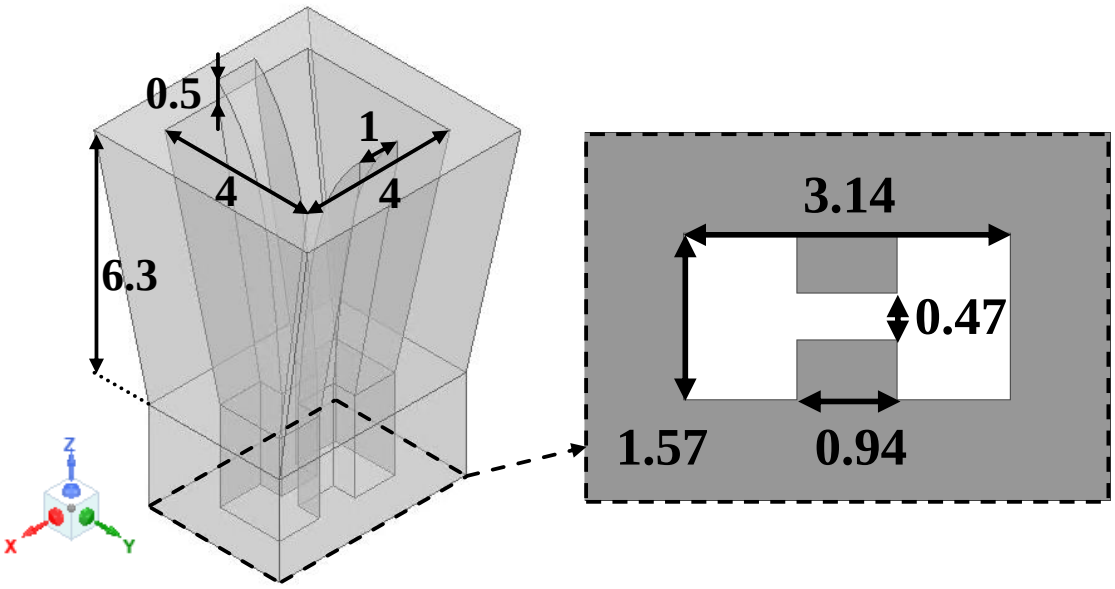

Fig. 4.3: Proposed DRH configuration (Dimensions are in millimeters).

4.2.1 Phase-Center Stabilized Double- Ridge Horn

Based on the proposed double-ridge waveguide cross-section, the objective is for the designed horn to achieve the stability of the phase-center (PC) position. To achieve this goal, the ridges have an exponential profile given in (4.1) [47]:

$$a(z) = A(C_1 e^{Rz} + C_2) + (1-A)[R_i + (R_o - R_i)(z/L)] \quad (4.1)$$

where $C_1 = (R_o - R_i)/(e^{RL} - 1)$, $C_2 = (R_i\, e^{RL} - R_o)/(e^{RL} - 1)$, R_i and R_o are the radii at the bottom and the top of the cavity, respectively. L is the cavity axial length, $A = 0.58$, and $R = 565.7$ (unitless) represents the exponential opening rate. The particle swarm optimizer (PSO) in CST-MWS [27] is employed to find the parameters that yield a stable phase center. In Fig. 4.3, the proposed DRH configuration is shown, while Fig. 4.4(a) illustrates VSWR below 2:1 across the operating frequency band and directivity > 7 dBi.

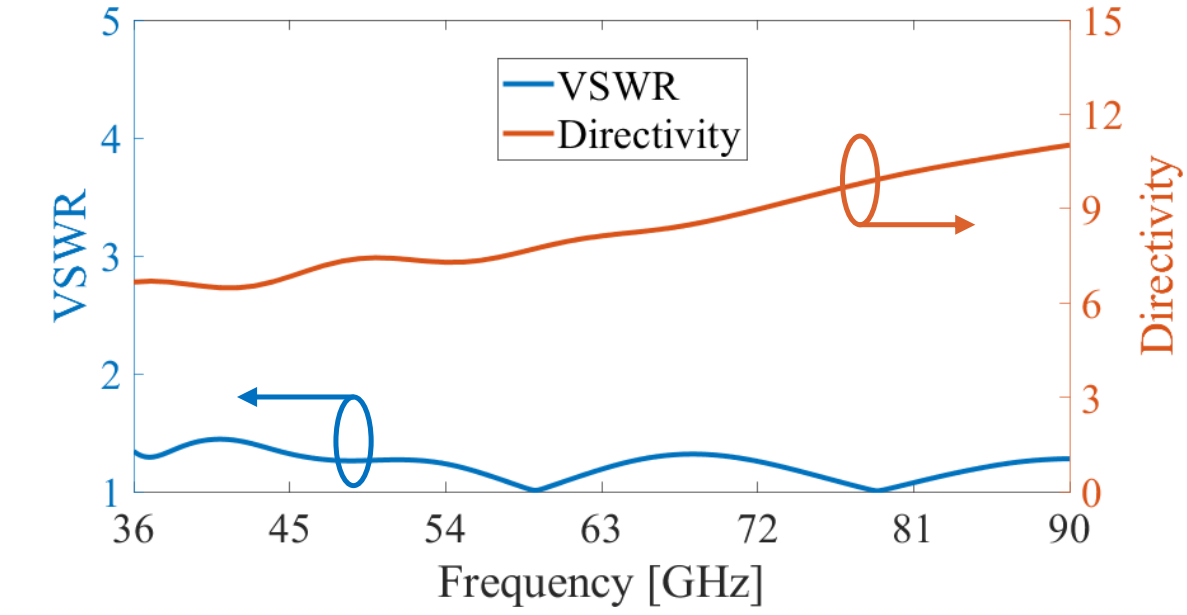

(a)

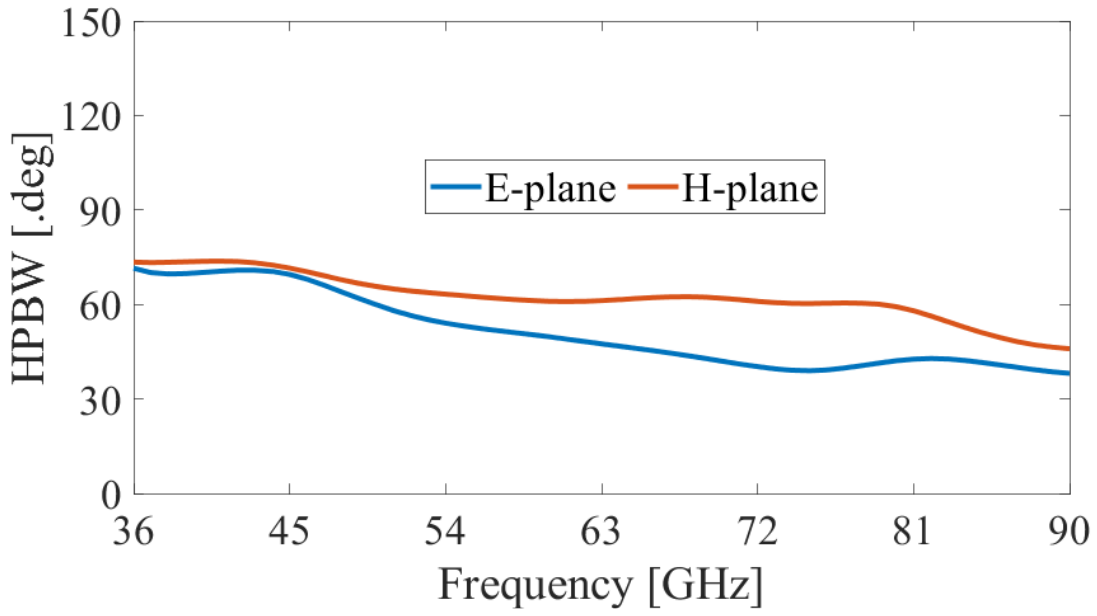

(b)

Fig. 4.4: Performance of the DRH: (a) VSWR and directivity, (b) HPBW.

Due to the compact aperture, the horn has the relatively wide half-power beamwidth at the lower frequency end (see Fig. 4.4(b)). The phase-center is established at 40º in FOV as determined from the radiated far-field within a 3 dB beamwidth on each cut-

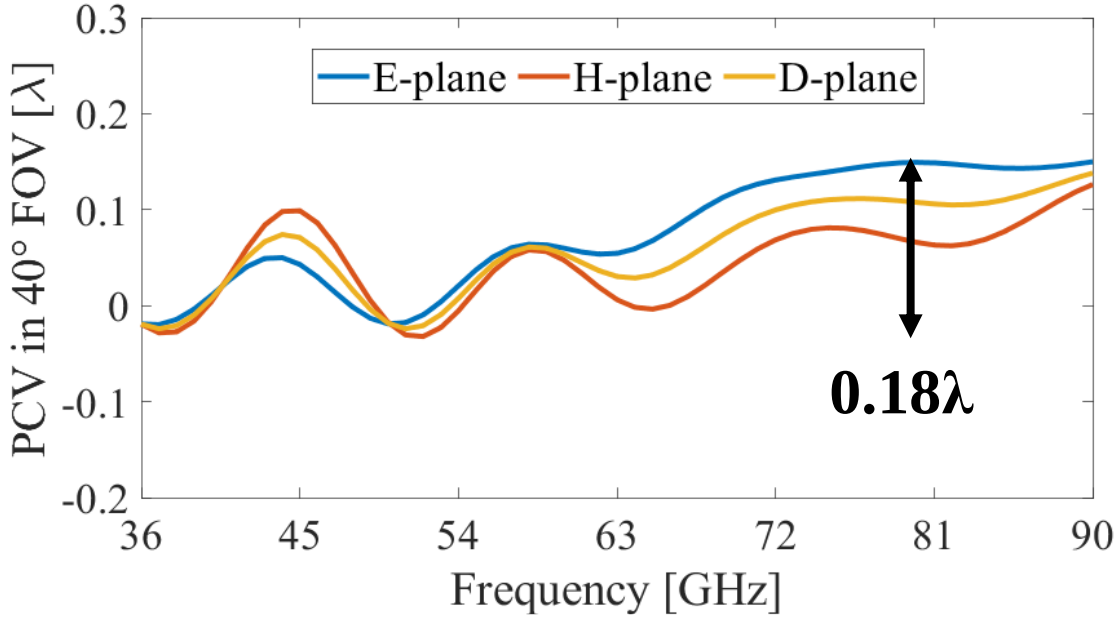

Fig. 4.5: Performance of the DRH a PCV in 40º FOV.

plane [125]. Consequently, the simulated phase center variation (PCV) remains below 0.18λ in the E-plane and 0.15λ in the H-plane in the worst cases as shown in Fig. 4.5.

4.2.2 Inhomogeneous Lens

The tapering of the throat inherently leads to lower directivity [19]. To overcome this, a horn with a lens can be used to achieve improved directivity or, if desired, a specific beam shape. This enhancement is achieved by correcting and collimating the wavefronts, effectively transforming them from spherical to planar forms. The conventional design approach for such lenses assumes the applicability of geometric optics, conceptualizing the power emerging from the horn apex as a ray. The foremost principle in geometric optics postulates that power is transmitted along ray paths, and the cumulative power traversing any enclosed surface constitutes a tube of rays. This implies constancy in the total power across any cross-sectional area of a ray tube. The second principle, Fermat's principle, indicates that energy

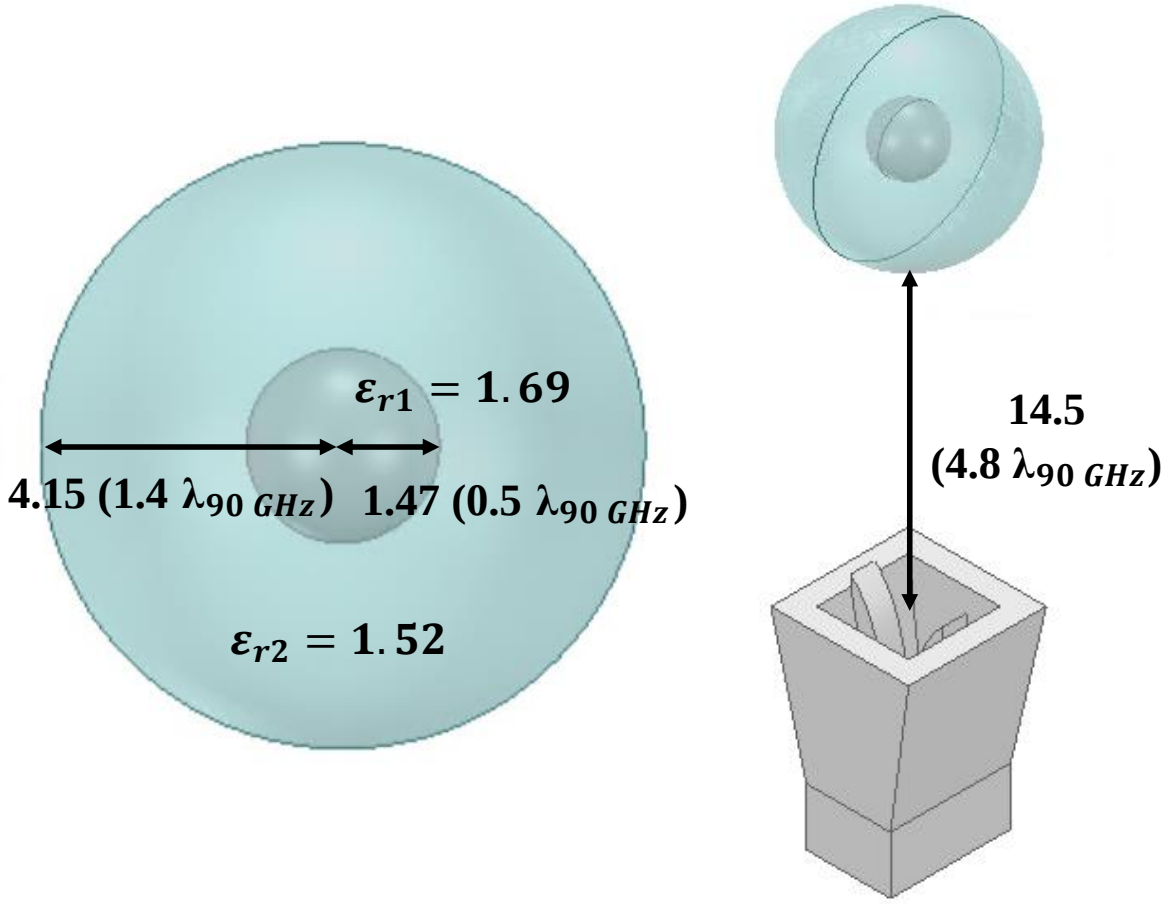

Fig. 4.6: Lens-corrected DRH antenna and cross-section of the lens (2 shells).

traversing between two points follows the route that minimizes the optical path length [48]. Furthermore, the radially varying refractive index from the center to the surface or along the lens's axis enables the lens to manipulate electromagnetic waves in more complex ways to achieve better performance than a traditional lens with uniform material properties.

In this chapter, as seen in Fig. 4.6, an inhomogeneous lens design consisting of two shells was developed to simplify the manufacturing process. Increasing the

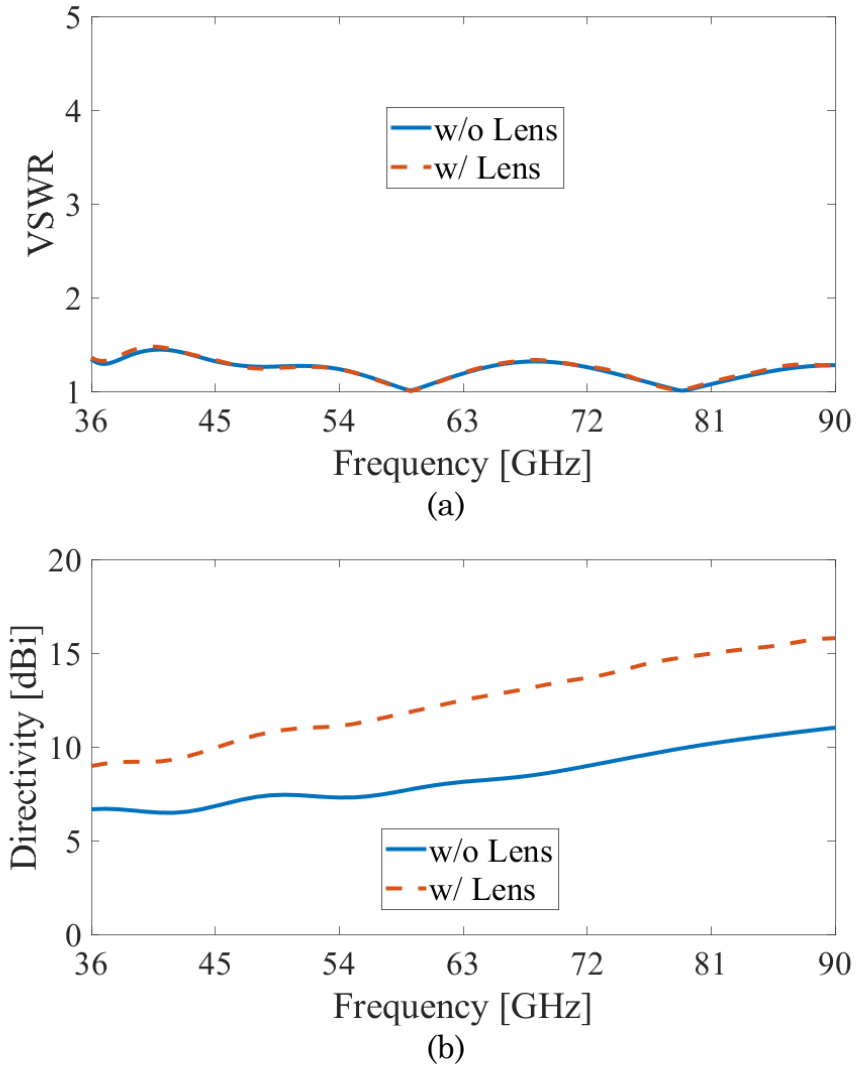

Fig. 4.7: Performance of the lens-corrected DRH: (a) VSWRs, (b) Directivity

number of shells does not yield a significant enhancement in directivity [126]. Furthermore, this is chosen to facilitate a more extended focal position in multi-beam array applications, reducing the crossover level and adjusting the tilt angle of the horn antennas [126]. To achieve high directivity, the inner and outer shells' permittivity values and lens radius are optimized using the PSO in CST-MWS. Fig. 4.6 shows the optimized lens, featuring inner(ε_{r1}) and outer(ε_{r2}) permittivity values of 1.69 and 1.52, respectively. The radii of each shell are determined at 1.47 mm (~0.5 λ_{90GHz}) and 4.15 mm (~1.4 λ_{90GHz}).

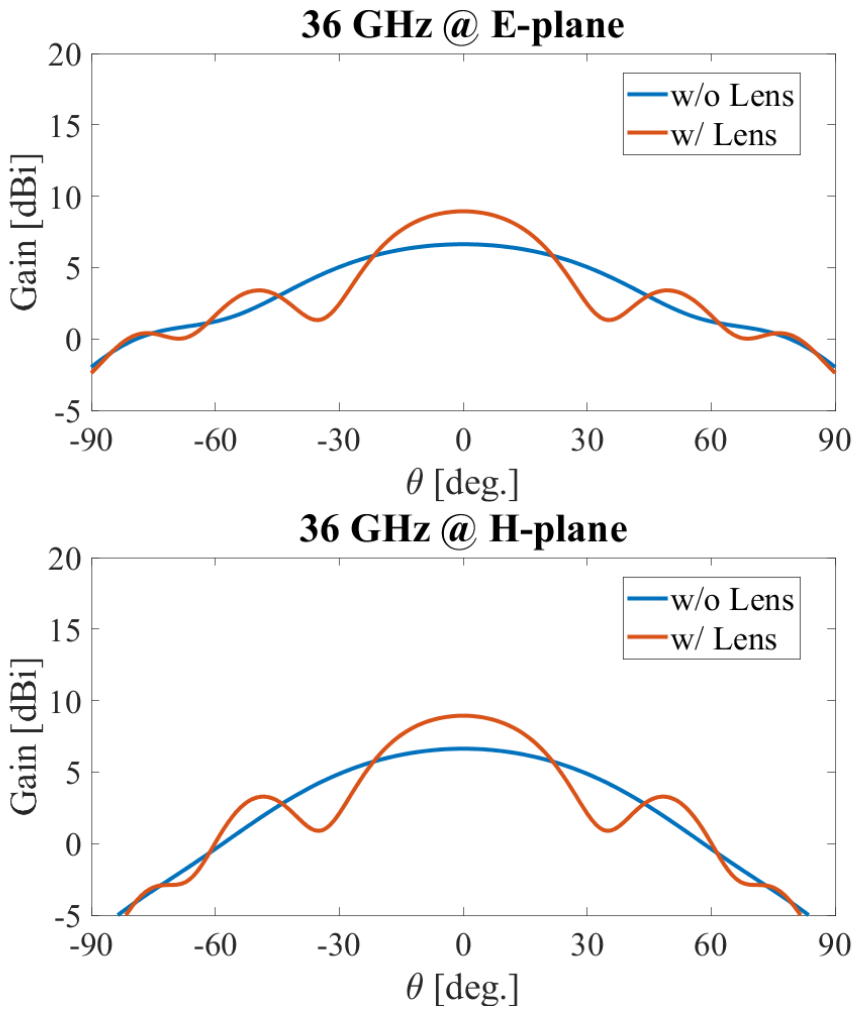

Fig. 4.8: Radiation patterns of DRH without (w/o) or with (w/) lens at 36 GHz in E- and H- planes.

As a result, there is an enhancement in gain through the lens in the radiation patterns shown in Figs. 4.8 and 4.9. However, Fig. 4.10 shows a deterioration of the SLL to <-3.9 and -4.5 dB in the E- and H-planes, respectively.

4.2.3 Multi-Beam Array

In Fig. 4.11, the proposed multi-beam array was engineered by integrating four additional beams with ±12ºtilting in both the E- and H- planes, an

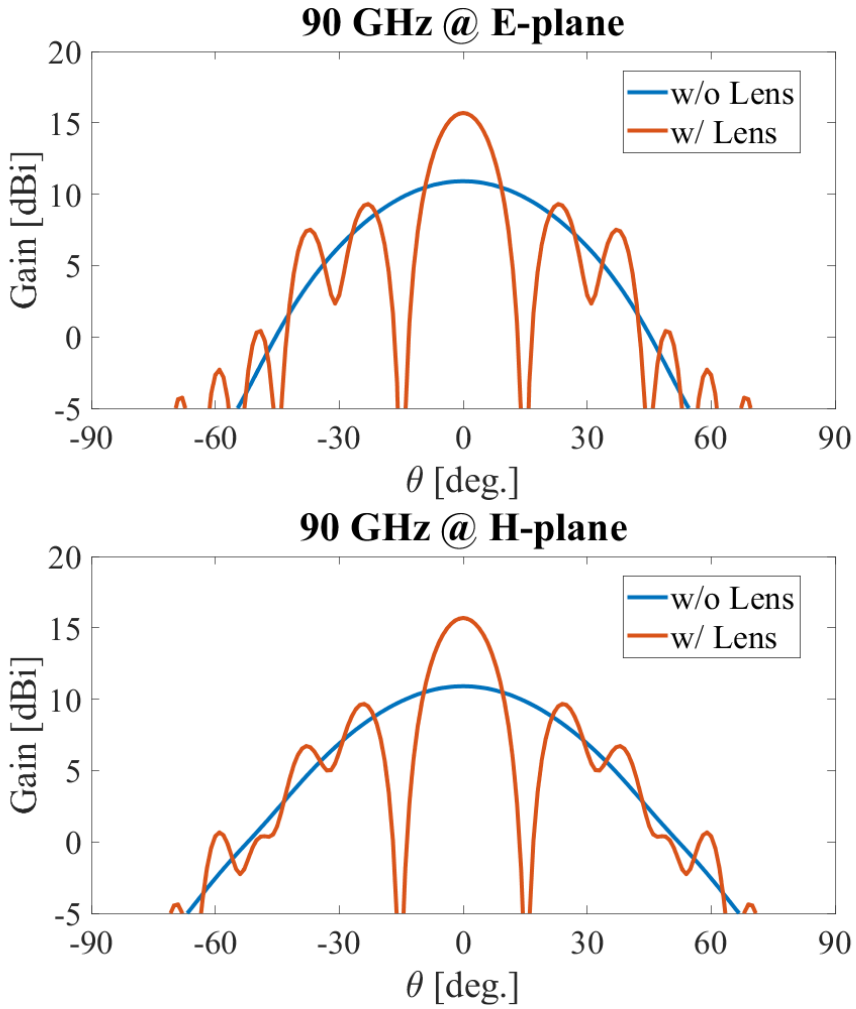

Fig. 4.9: Normalized pattern and E-field phase result of lens-corrected horn antenna with cavity in H-plane at 36 GHz.

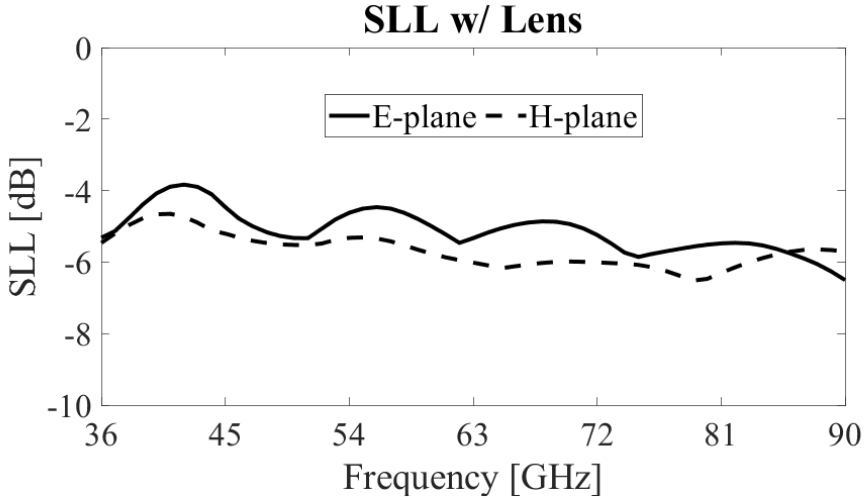

Fig. 4.10: SLL of DRH with inhomogeneous lens in E-(solid) and H-(dashed) planes.

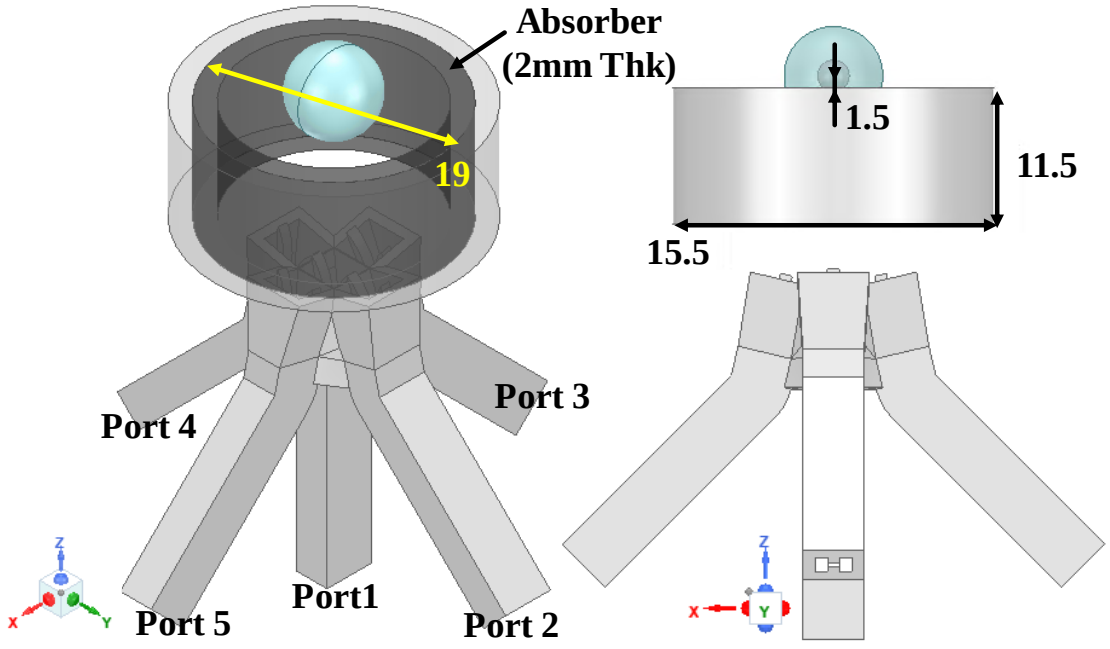

Fig. 4.11: Lens-corrected multi-beam array with absorber-lined ring structure. (Dimensions are in millimeters)

inhomogeneous lens, and an absorber-lined ring. As discussed in previous sections, the integration of the lens enhances gain while significantly deteriorating SLLs. This trade-off is important for the direction-finding system. As with a similar strategy in [127], the proposed approach that utilizes a ring and a current sheet absorber is demonstrated to address the increased SLLs with a lens over the entire operational bandwidth. With the absorber thickness set at 2 mm, the ring's radius, position, and height (see Fig. 4.11) are optimized to achieve the lowest peak SLL across the five beams. As presented in Figs. 4.12(a)-(b), the VSWRs are maintained below 2:1 at all ports of the array

The proposed configuration also results in a significant increase in directivity by approximately 7-10 dB compared to the PC stabilized DRH antenna, with peak SLL values in the E- and H- planes at -12 dB and -13 dB, respectively (see Fig. 4.13).

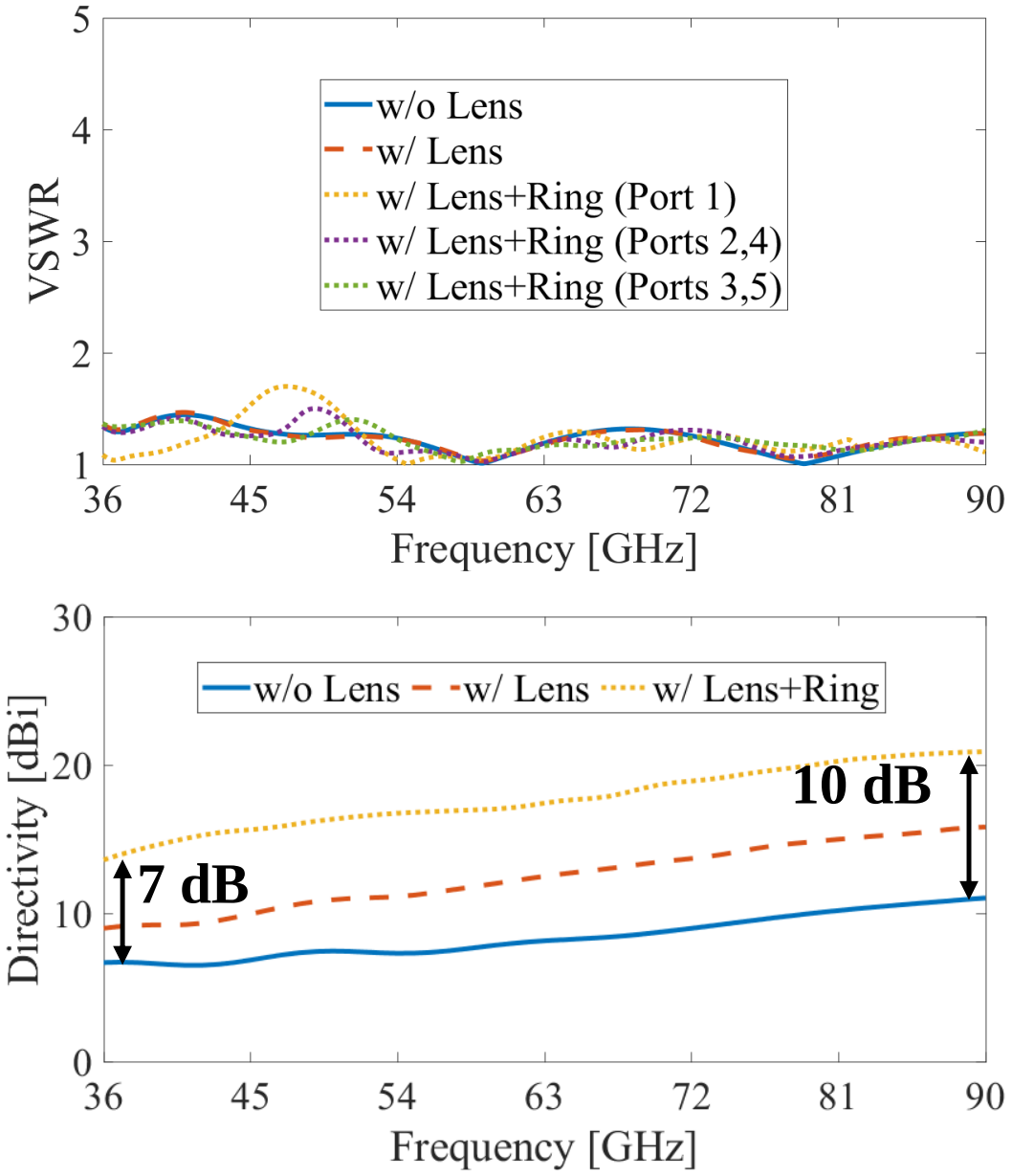

Fig. 4.12: Performance of multi-beam array compared to DRHs with/without lens. (a) VSWR. (b) Directivity.

Fig. 4.14 presents the boresight radiation patterns in the E and H planes for configurations using the horn alone, horn plus lens, and horn plus lens plus ring, highlighting the enhanced directional characteristics and reduced SLL. The objective is for the absorber to tailor the aperture distribution such that the desired amplitude

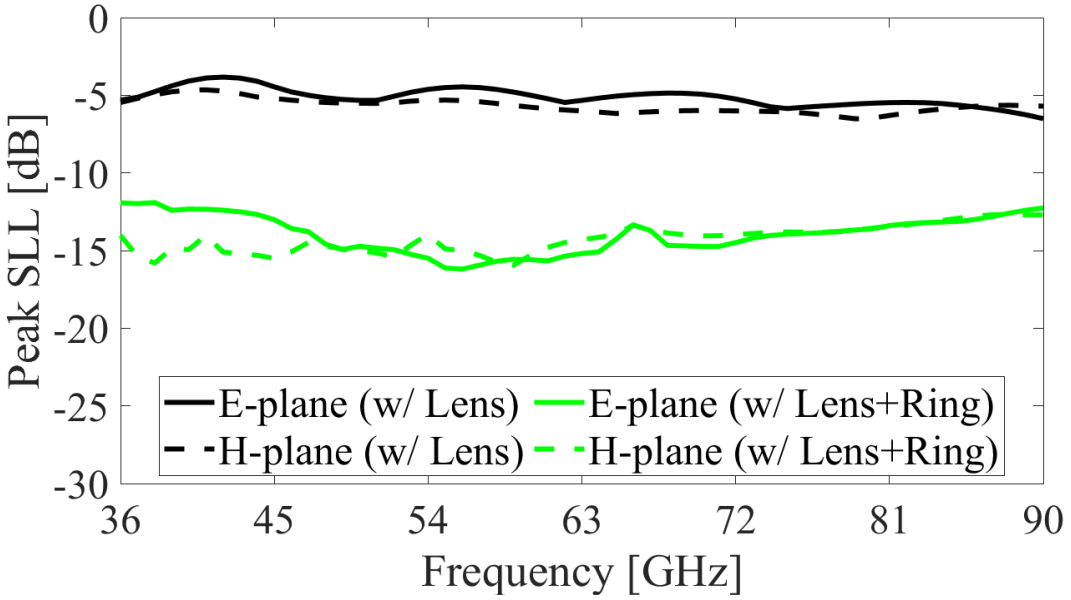

Fig. 4.13: Peak SLL performance of multi-beam array compared to lens-corrected DRH.

taper across the new ring opening is maintained. If done correctly, this can lead to improved directivity and SLLs, thus effectively functioning as a spatial SLL filter. Additionally, as shown in Fig. 4.15, the highest crossover level was observed to be around 3.5 dB at the highest frequency, indicating a narrow beamwidth.

4.3 Prototype Design

A 3-D printable DRH antenna with/without a lens and multi-beam array is prototyped to validate the proposed design. To realize a 2-shells lens with low permittivities (ε_r =1.69 and 1.52) using prototyping resin with measured ε_r = 2.5 and $tan\delta$ = 0.005 at the Ka-band [128], a unit-cell structure comprising three intersecting rods [129] is designed as shown in Fig. 4.16 (a). When the unit-cell size is fixed at 0.7 mm, permittivity values are achieved as follows: to obtain a permittivity of 1.69, w_1 and w_2 are set at 0.33 mm and 0.185 mm, respectively, and to achieve a permittivity of 1.52, w_1 is fixed at 0.2 mm and w_2 at

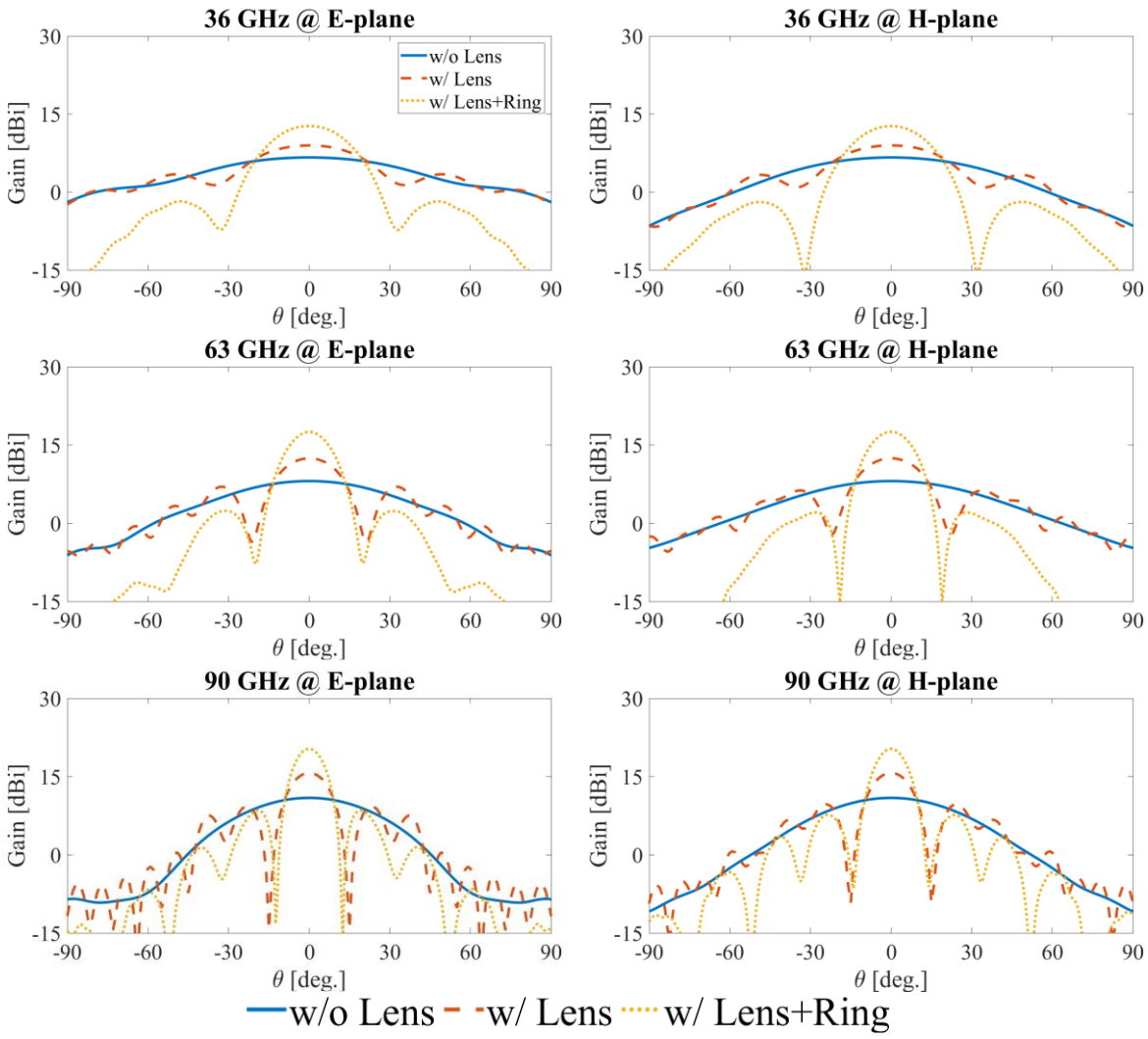

Fig. 4.14: Radiation patterns of DRH w/o lens, w/ lens and multi-beam array at boresight.

0.21 mm. As seen, within the operating bandwidth, the effective permittivities of those unit-cells vary between 1.63 and 1.69 or 1.47 and 1.52. Based on this lens design, Fig. 4.16(b) illustrates the assembly of a lens-corrected DRH antenna, where the lens is integrally designed with the lower radome. A top radome intended to encase the lens is also shown. As senn, dividing the radome into two sections facilitates resin drainage during 3-D printing. The performance of the antenna is not significantly affected by a thin radome featuring a thickness of 0.25 mm.

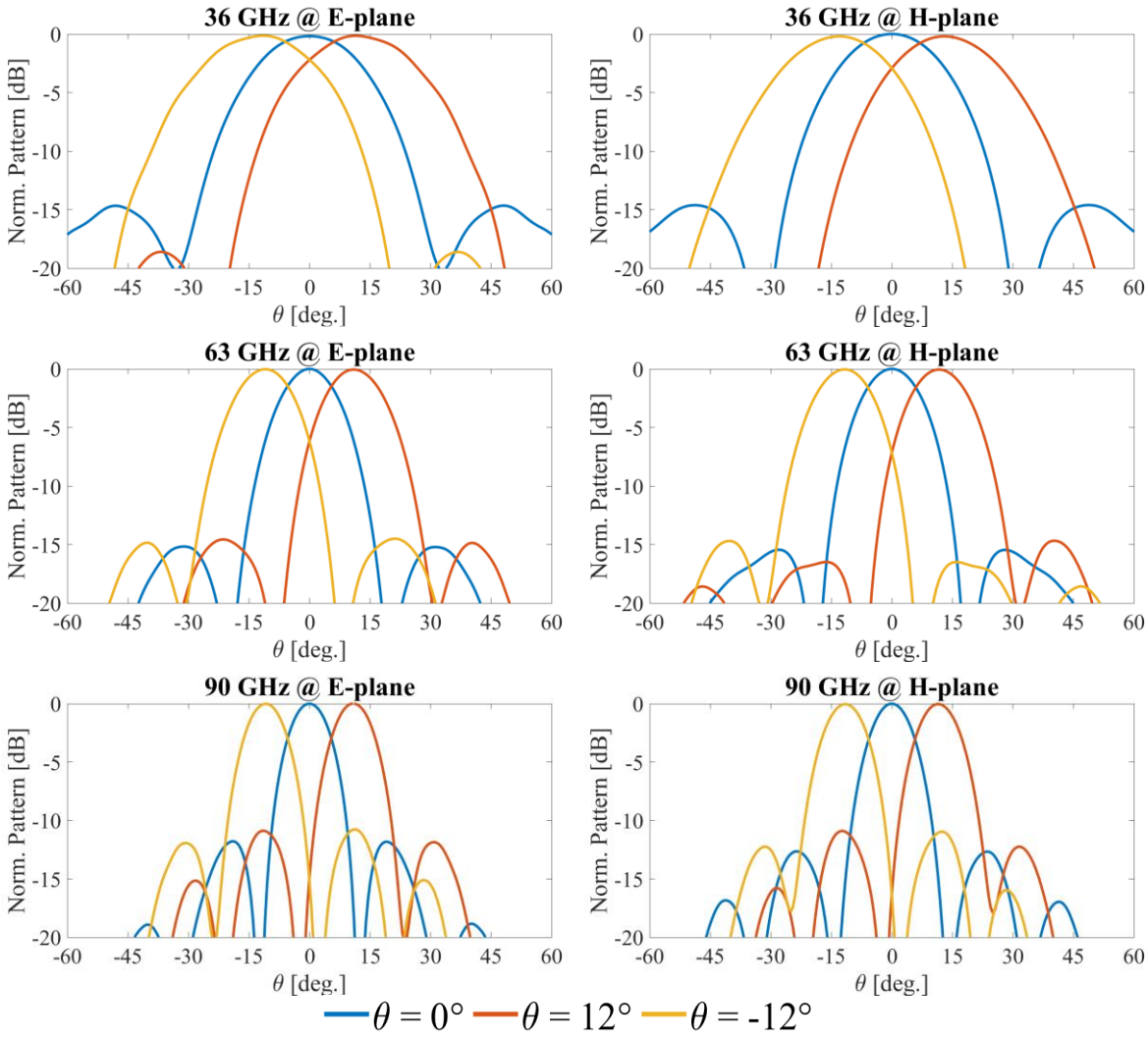

Fig. 4.15: Scanned radiation patterns of multi-beam array in E- and H-planes.

Furthermore, a 2 mm thick absorber is affixed to the flange of the horn antenna to effectively absorb any reflections from the radome interior. For the mounting of the lens onto the ring in the multi-beam array, a structural spacer characterized by a permittivity between 1.04 and 1.15 and a loss tangent of less than 0.003 within the operating frequency is designed with a cubic structure, as shown in Fig. 4.17(a). This design facilitates a monolithic integration with the inhomogeneous lens in Fig. 4.17(b).

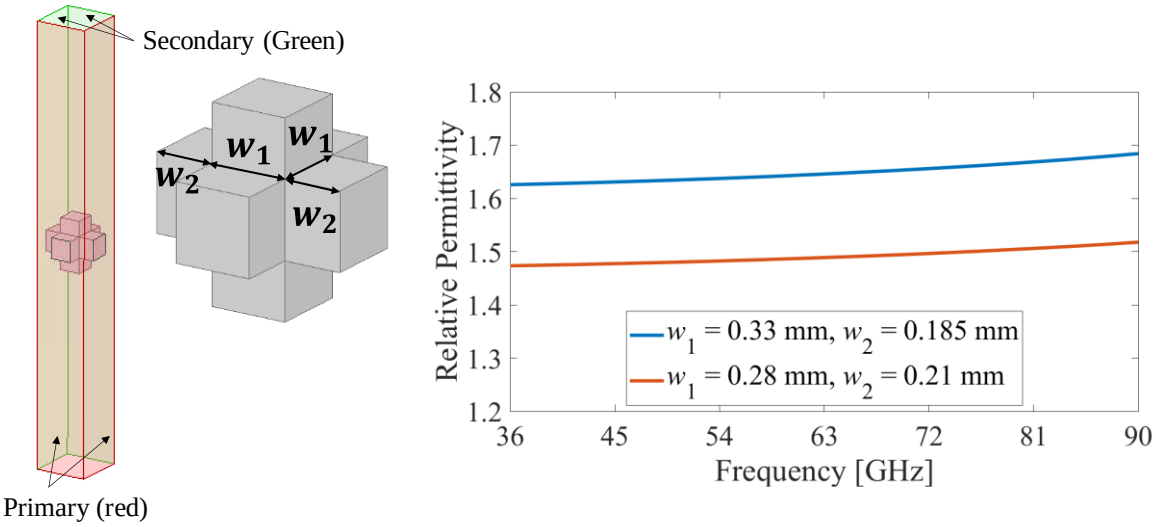

(a)

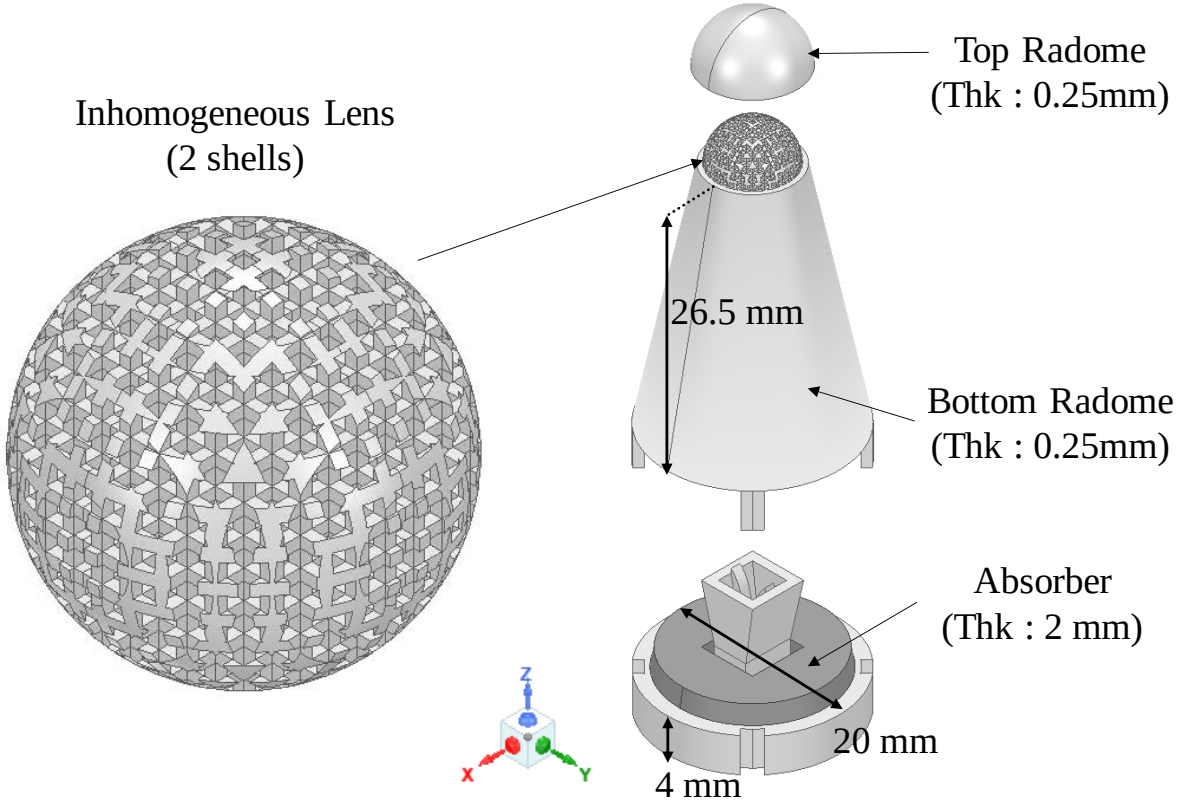

(b)

Fig. 4.16: (a) Permittivity characterized for the unit-cell of the inhomogeneous lens with the associated periodic boundary conditions. (b) Lens-corrected DRH antenna prototype.

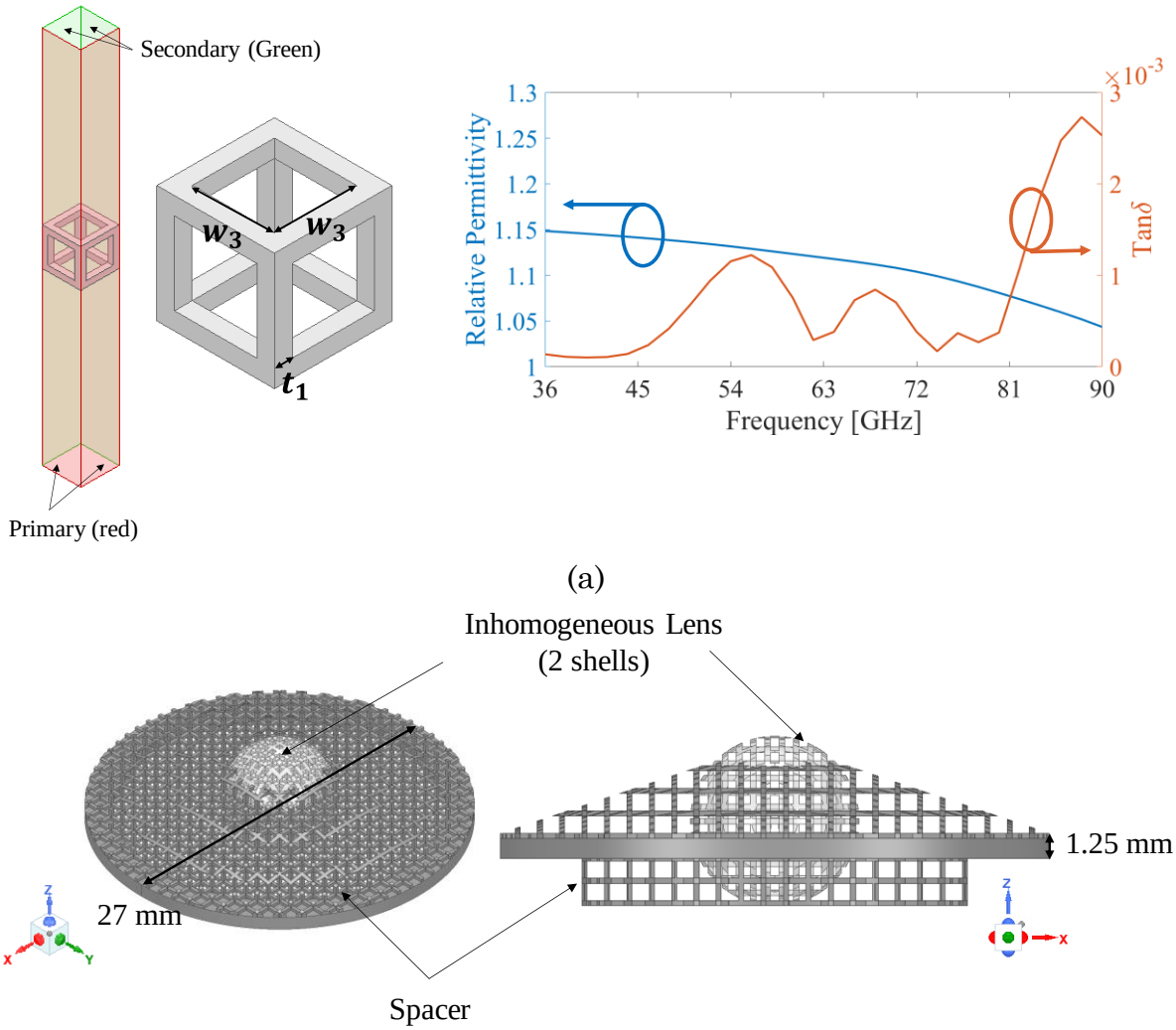

Fig. 4.17: (a) Permittivity and loss tangent characterized for the unit-cell of the structural spacer with the associated periodic boundary conditions. (b) Inhomogeneous lens with structural spacer for multi-beam array..

The unit-cell of the structural spacer has a thickness (t_1) of 0.15 mm and a spacing (w_3) of 0.7 mm. The proposed multi-beam array configuration is depicted in Fig. 4.18. Elliptical holes [130] have been incorporated into the array model to ensure uniform copper plating. These holes are dimensioned to minimize any adverse effects on RF performance, with the major and minor axes of the ellipses measuring 1.60 mm and 0.75 mm, respectively, and a center-to-center spacing of 1.55 mm. The array is

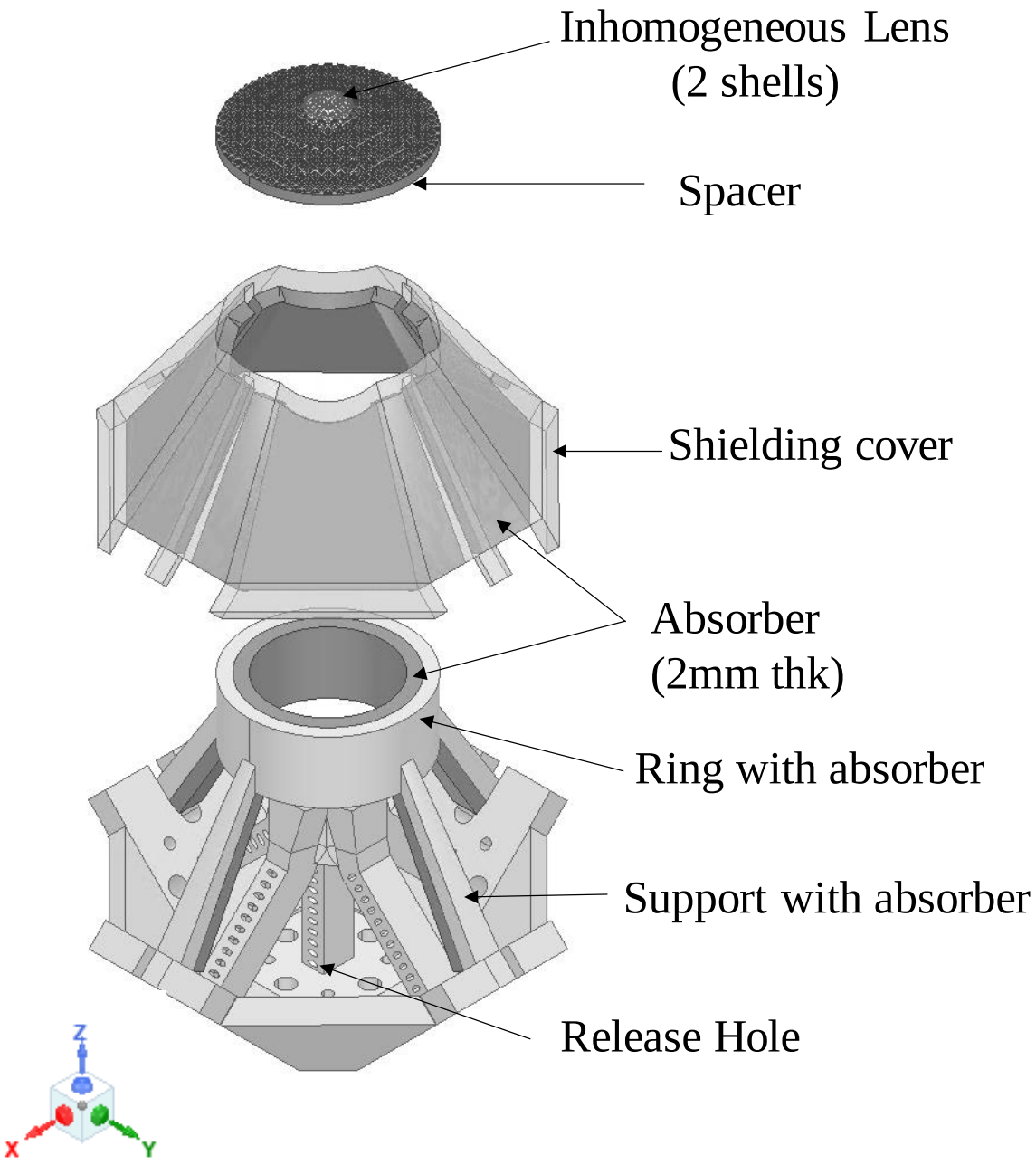

Fig. 4.18: Proposed multi-beam array configuration.

designed as a monolithic structure featuring an integrated ring structure and supporting frame. A shielding cover lined with an absorber is incorporated to address potential electromagnetic interference (EMI) and electromagnetic compatibility (EMC) issues.

4.4 Fabrication and Measurement

The DRH, lens and array discussed in previous Sections III are fabricated using a DLP with Phrozen Sonic Mini 8K 3D printer [96] with prototyping resin.

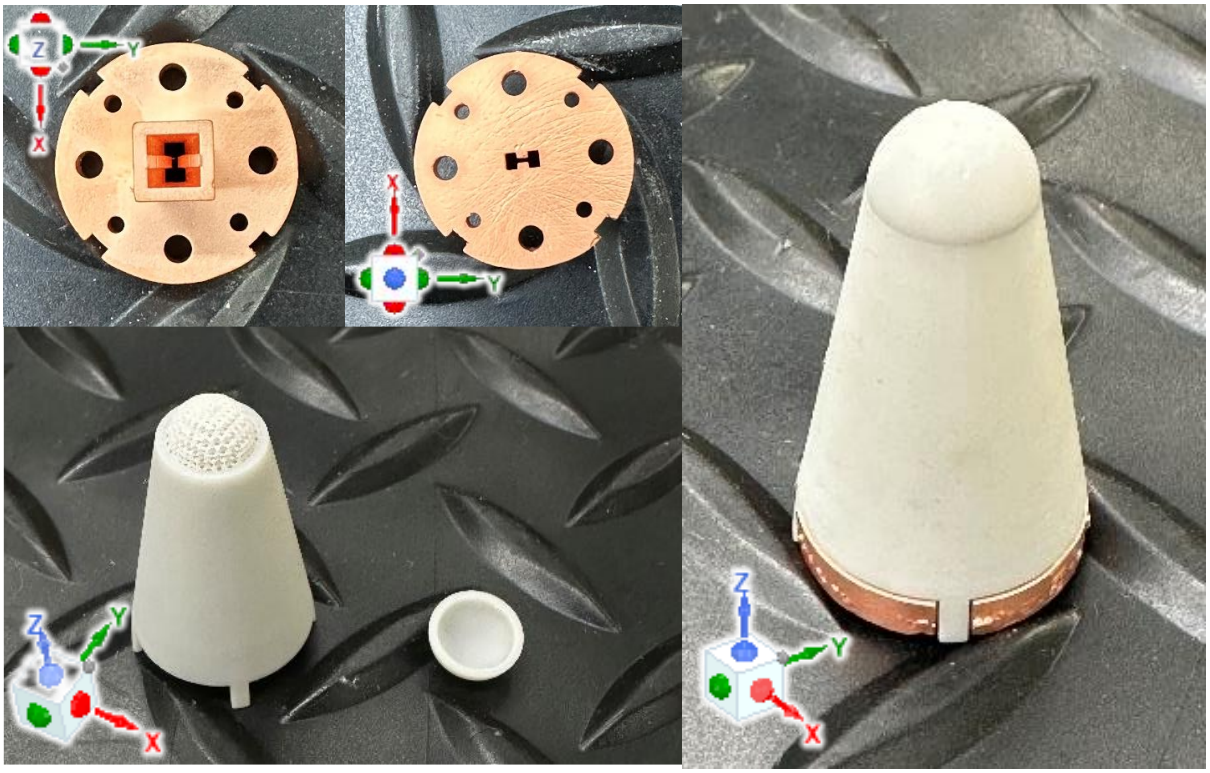

(a)

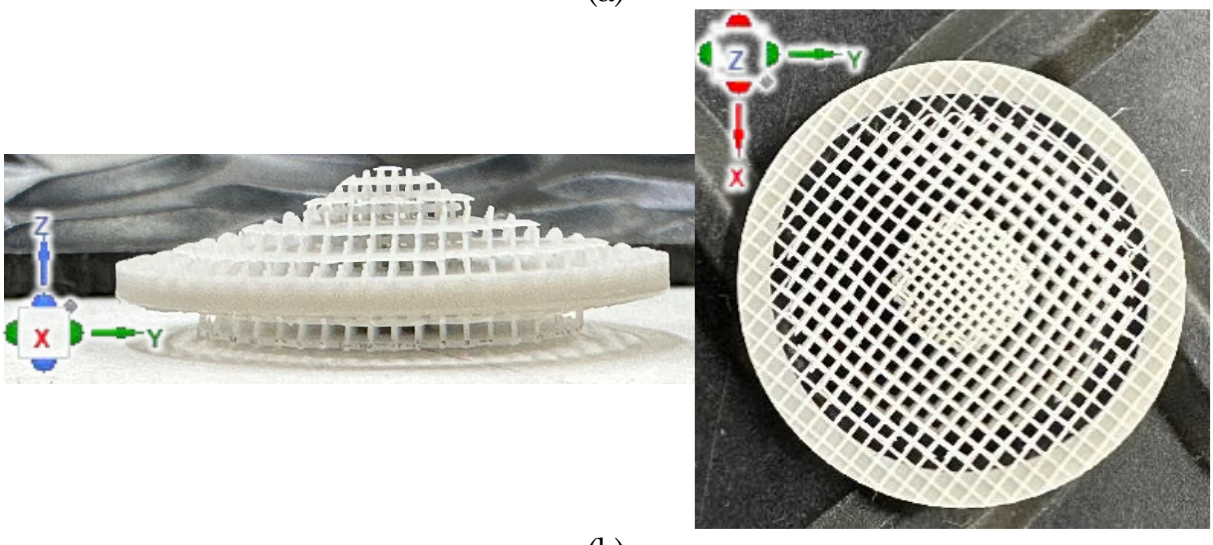

(b)

Fig. 4.19: Fabricated antenna configurations (a) DRH and inhomogeneous lens with radome. (b) Lens with structural spacer for multi-beam array.

The absorber sheet significantly influences the performance and bandwidth of this array. Due to its specified bandwidth range of 1 to 90 GHz [97] and its advantageous mechanical properties that facilitate integration with curved cavity walls, the 2 mm-thick Coolzorb 600 ($\varepsilon_r = 19$, $\mu_r = 1$, $tan\delta_E = 0.04–0.09$, $tan\delta_M = 0.13–0.28$) current sheet absorber is utilized. Tape is applied across the entire waveguide

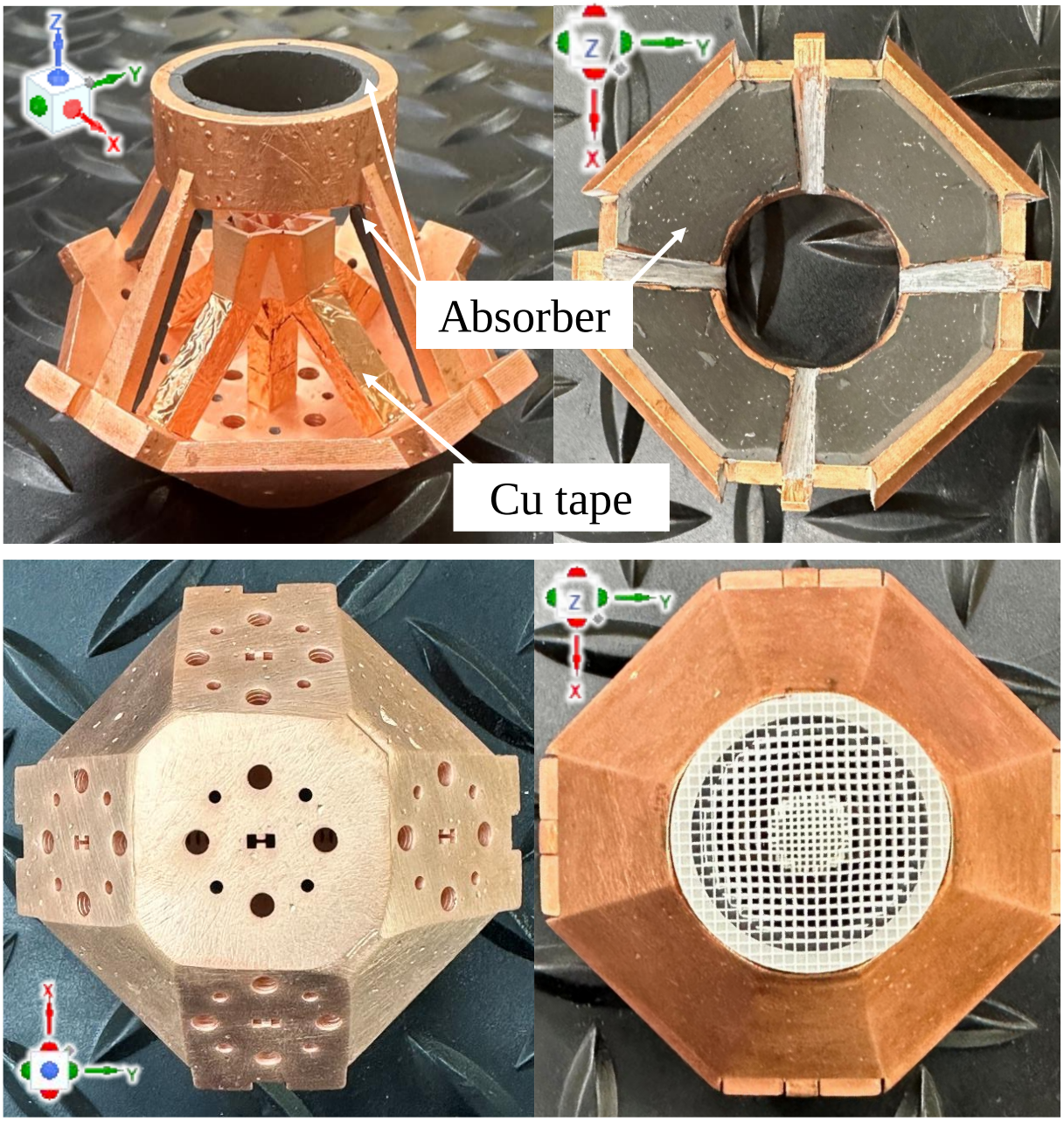

(c)

Fig. 4.20: Fabricated multi-beam array with shielding cover.

structure to minimize leakage through the holes. Post-plating destructive tests have demonstrated that tolerances are within < 0.025 mm and surface roughness is less than 15 µm.

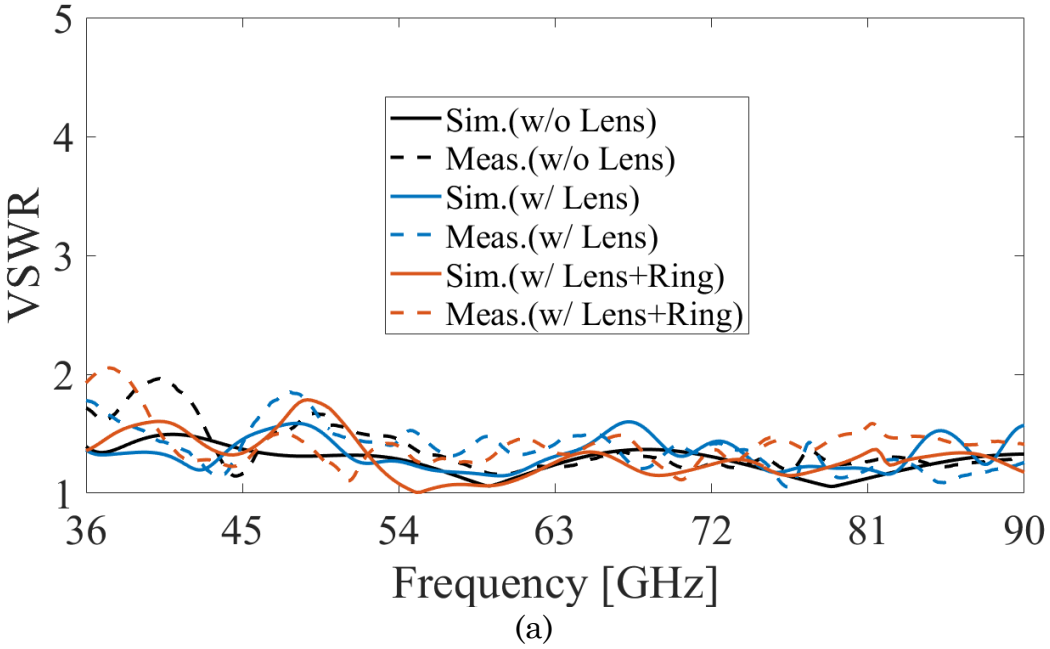

(a)

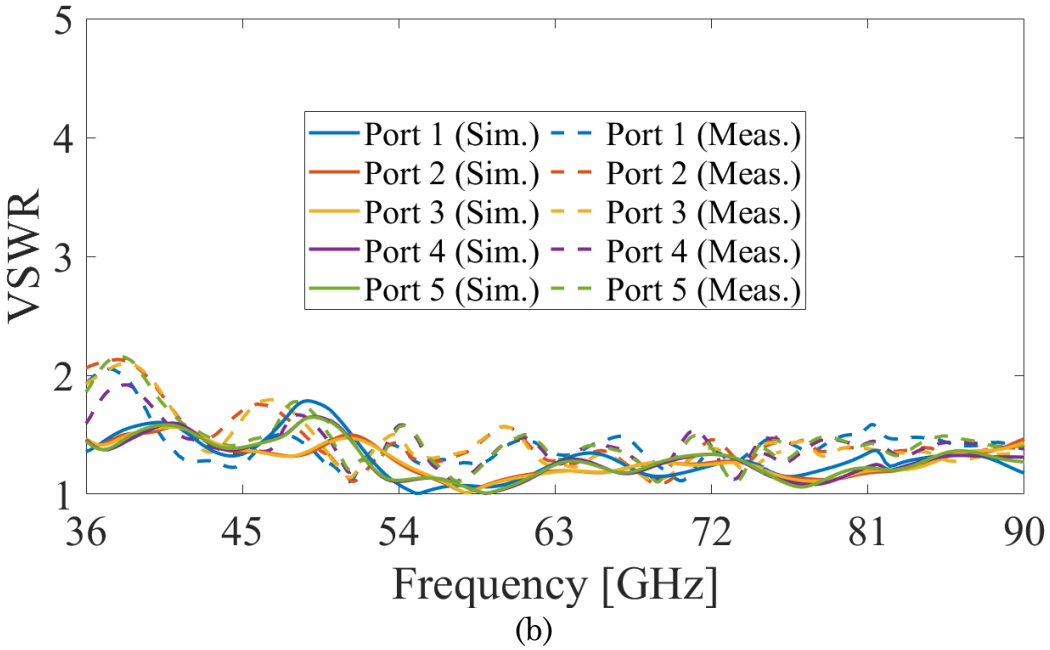

(b)

Fig. 4.21: Simulated and measured performance: (a) VSWRs of DRHs without/with lens and multi-beam array at boresight (b) VSWRs of multi-beam array

Figs. 4.19 and 4.20 show the fabricated components of the horn, lens, and array structures. These components are assembled without additional glue; the same resin used in their fabrication is applied and cured to secure them together. The

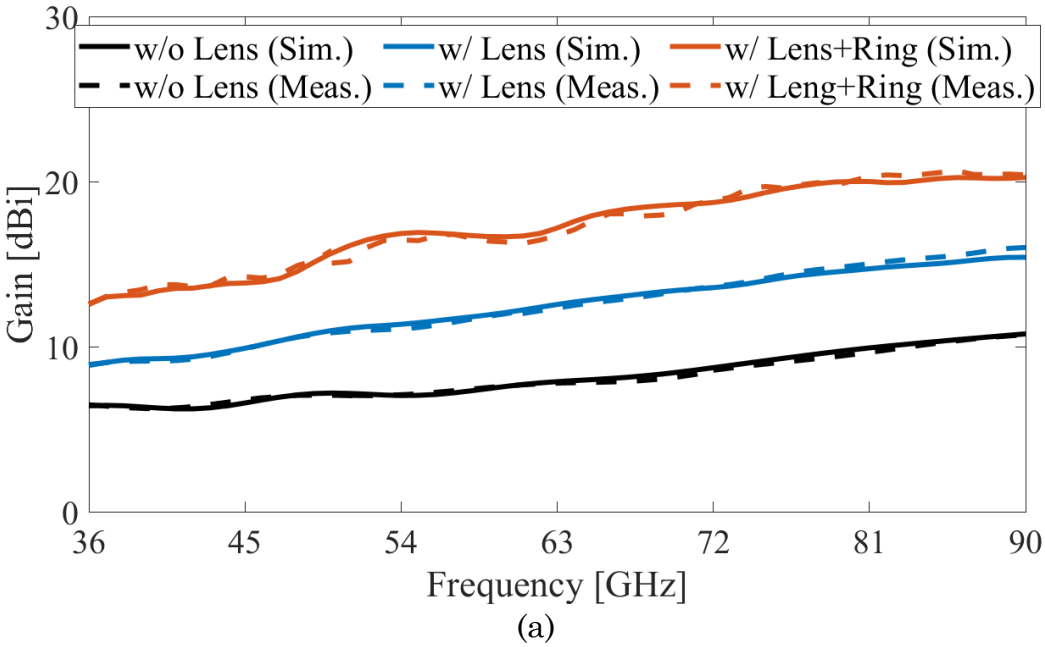

Fig. 4.22: Simulated and measured performance: (a) Gain of DRHs with/without lens and multi-beam array at boresight (b) Peak gains of multi-beam array

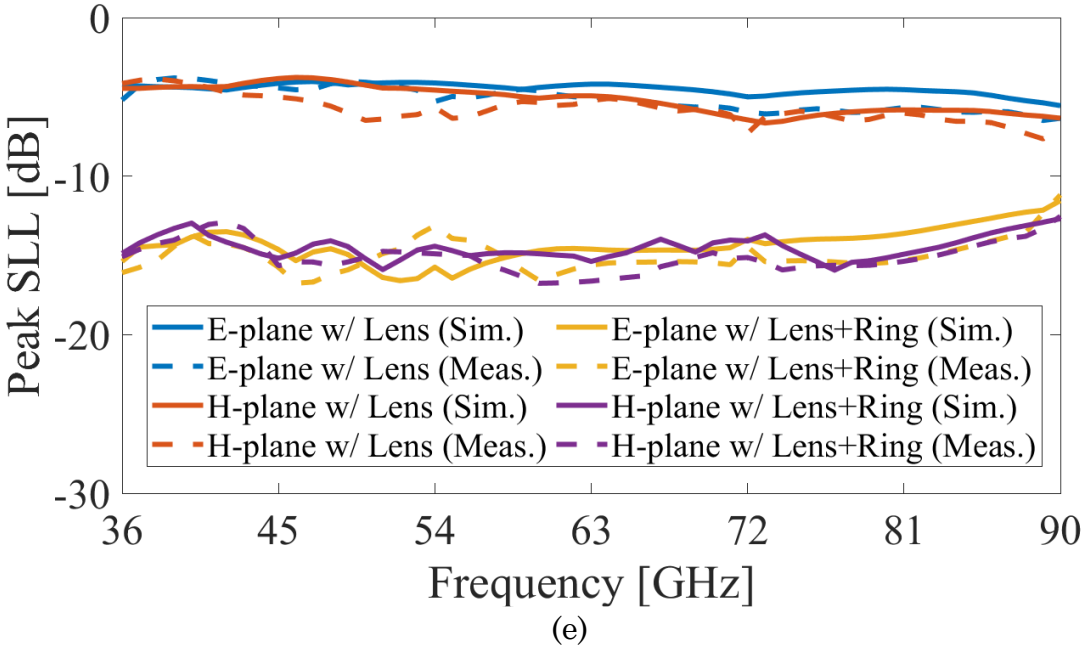

(e)

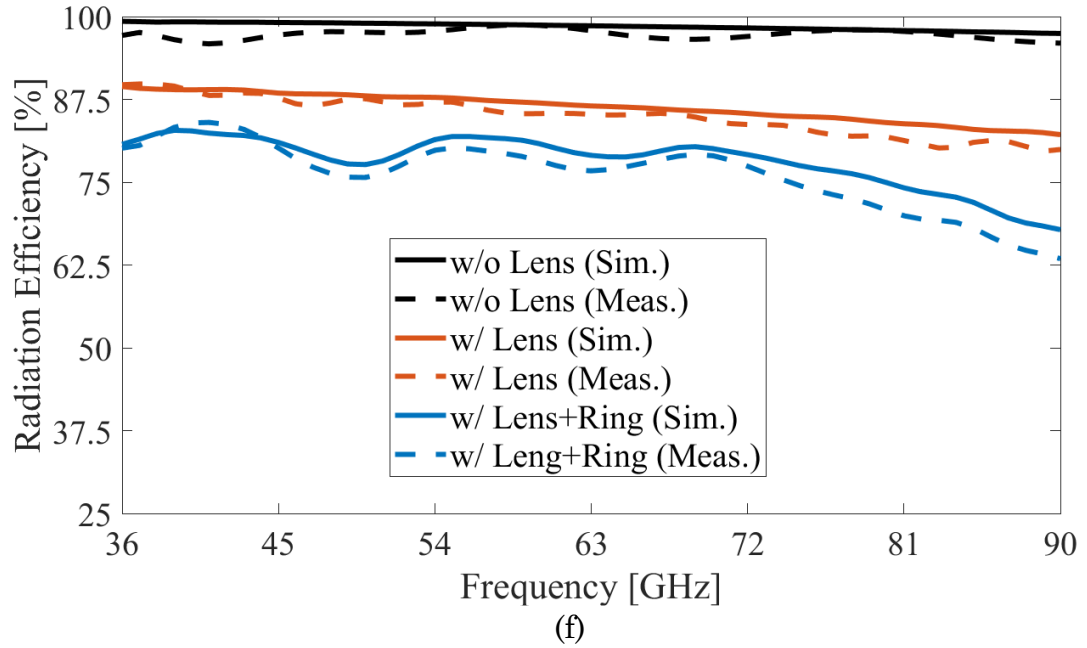

(f)

Fig. 4.23: Simulated and measured performance: (e) Peak SLL of DRH with lens and multi-beam array (f) Radiation efficiencies of DRHs without/with lens and multi-beam array

VSWR comparisons of all simulated and fabricated antennas, plotted at boresight and scanning conditions, are presented in Figs. 4.23(a)-(b), demonstrating a level below 2.1:1 at the lower end of the band.

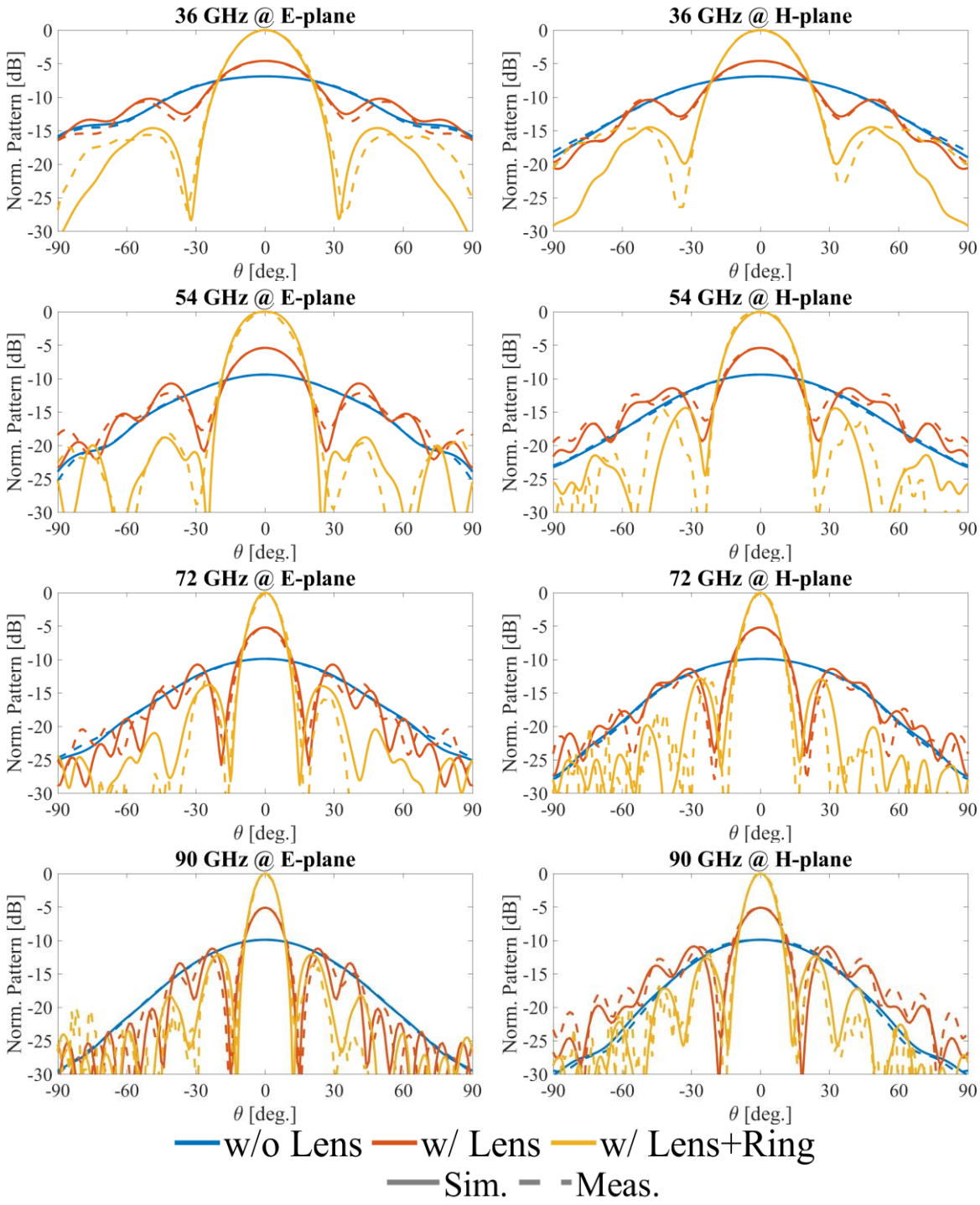

Fig. 4.24: Simulated and measured radiation patterns of DRHs without/with lens and multi-beam array at boresight in E- and H-planes

The far-field measurements, conducted in the anechoic chamber at the University of Colorado Boulder, reveal that the multi-beam array results show similarities between port 2 and port 4 (E-plane bending) and port 3 and port 5 (H-plane bending), as depicted in Figs. 4.23(b) and (d). The multi-beam array with a ring structure shows significant gain and SLL improvements compared to the baseline, lens-less case, as shown in Figs. 4.23(c) and (e). The measured gain exceeds 12 dBi, with the worst-case relative SLL in the E-plane at 90 GHz being less than -12 dB. Fig. 4.23(f) indicates that the radiation efficiency is greater than 62% across the entire frequency band. The radiation patterns in Figs. 4.24 and 4.25 are symmetric in both the E- and H-planes, maintaining high cross-polarization rejection (>30 dB) and increased directivity compared to the lens-less case. This suggests that fabrication imperfections with DLP do not significantly impact lens performance.

The excellent agreement between the measurements and full-wave simulations demonstrates the robustness of the proposed designs and the maturity of the 3-D printing technology required to produce such high-performing prototypes. To highlight this work's performance and innovation, Table 4.1 presents a comparison with other AM multi-beam arrays [131-138], showing that this work offers a viable wideband mmWave option with good performance across all key parameters.

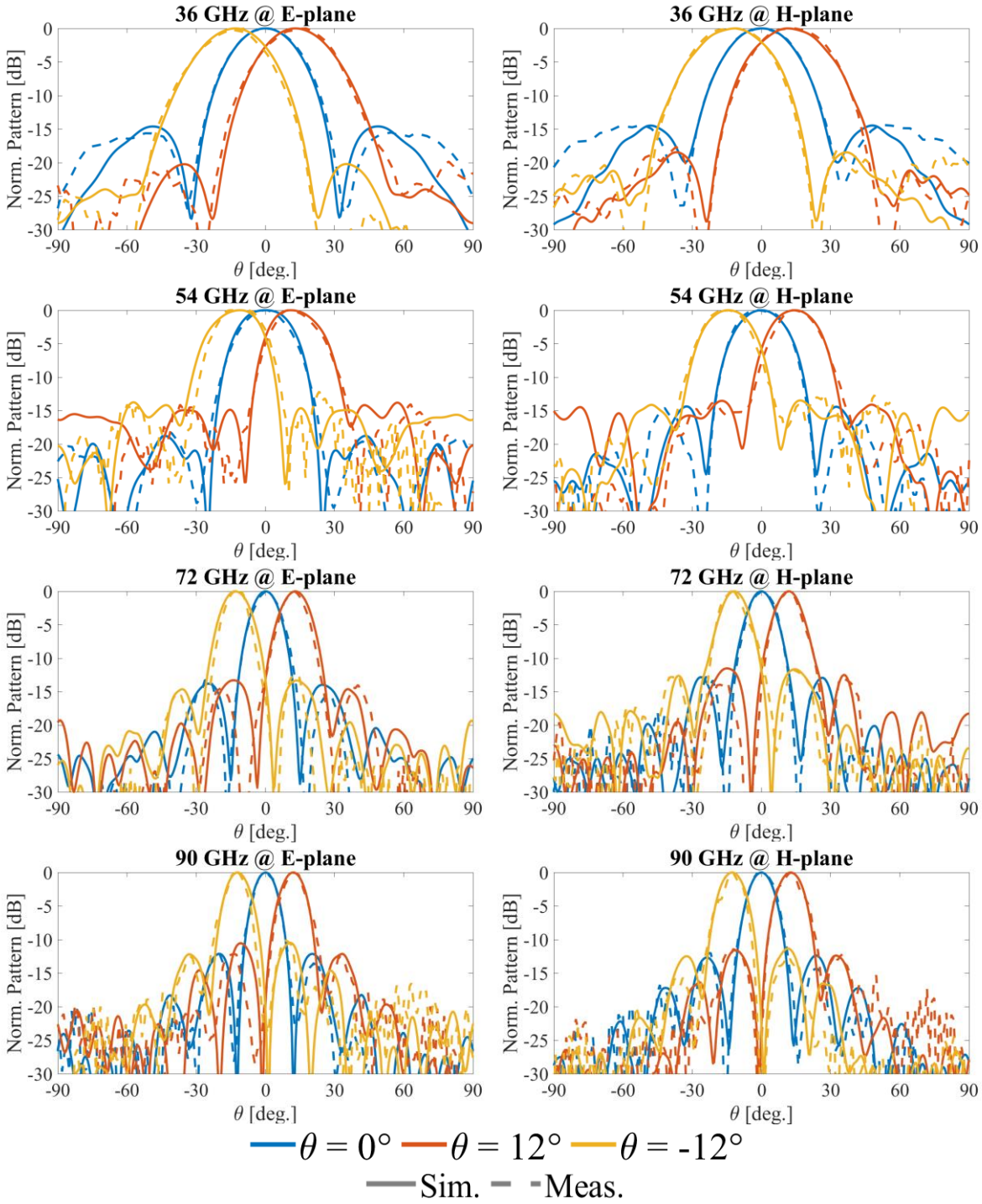

Fig. 4.25: Simulated and measured radiation patterns of multi-beam array at scanning conditions in E- and H-planes.

Table 4.1: Comparison with other 3-D printed multi-beam arrays

Ref.	Printing Technique	Frequency (GHz)	Peak Gain (dBi)	SLL (dB)	Crossover Level (dB)	Beam Scan
[131]	SLA	350-360 (1.03:1)	17.3	< -7	< -19	1D
[132]	PμSL	110-170 (1.55:1)	21.8	< -11.8	< -25	1D
[133]	-	7.7-8.2 (1.06:1)	15.3	< -9	-3 @ 7.9 GHz	2D
[134]	-	26-40 (1.5:1)	21.2	< -9	< -5.5	1D
[135]	SLA	18-25 (1.38:1)	26	< -5	< -13	2D
[136]	DMLS	26-40 (1.54:1)	23	< -11	-11 @ 33 GHz	1D
[137]	SLA	9.8-10.2 (1.04:1)	13.2	< -4	< -20 @ 10 GHz	1D
[138]	SLA	10 (-)	19.8	< -11.2	-2.5 @ 10 GHz	1D
This work	**DLP**	**36-90 (2.5:1)**	**20**	**< -12**	**< -3.4**	**2D**

4.5 Conclusion

An additively manufactured, ring-integrated, lens-corrected multibeam array operating from 36 to 90 GHz is presented. To enhance gain and reduce SLLs, a 3D-printed inhomogeneous lens and an absorber-lined ring are incorporated. The shielding cover structure proactively addresses potential issues related to EMI and EMC. The measured VSWRs across all channels are below 2.1:1 over the entire bandwidth, with a gain exceeding 12 dBi and SLLs less than -12 dB. This work demonstrates the capability of additive manufacturing to produce a low-cost multibeam array for wideband applications across the mmWave spectrum.

Chapter 5

Compact Unit-Cell for Wideband Circularly-Polarized Patch Array

5.1 Introduction

Widespread use of linearly polarized antennas and arrays in contemporary communication systems is mainly due to their simplicity, smaller size and cost, and typically lower loss. However, the utilization of these antennas causes some issues such as reduced resilience to multipath, higher polarization loss factors due sensitivity to orientation, just to name a few [139]. For these reasons, system designers often consider CP antennas for a range of applications from mobile and satellite communications to radar [140]-[142]. In this context, there has been a notable increase in interest in CP arrays that employ microstrip technology. This trend is attributed to ever increasing demands for devices that are not only smaller, but also more power-efficient while being cost-effective and amenable for mass production [143]. While microstrip patch arrays offer many of these advantages, they still face some challenges, chief being high-quality operation over wide instantaneous bandwidth. This is typically attributed to the resonant nature of individual patch elements [144, 145]. Moreover, mutual coupling between elements can degrade

performance by altering radiation patterns and efficiency [146], whereas surface waves if excited can cause scan blindness. This paper proposes a compact unit-cell with four patches that relies on coupling, mutual orientation, and excitation of its constituents to achieve wide CP bandwidth (see Fig. 5.1).

To increase bandwidth of microstrip patch antennas, several techniques are considered in literature. Multilayer stacking uses cumulative contributions of each layer to expand the overall bandwidth at expense of higher fabrication and tuning complexity [147-149]. Excitation of multiple modes can also increase impedance bandwidth; however, the common issues are increased height [150], small to moderate bandwidth limits [151], or pattern stability. Recent research in meta-surfaces have brought forward some interesting possibilities despite issues such as fabrication tolerances, increased size, and cost [152, 153]. Slot-coupled topologies also achieve wider bandwidth [154] at the expense of intricate impedance matching, high profile, and pattern contamination, particularly front to back ratio [155]. A sequential rotation technique requires a complex, typically analog, feed network to adjust electric field vectors to achieve CP across a wider bandwidth [156, 157]. Arrays that utilize tight coupling between elements have recently gained great popularity for various wideband RF applications. Decade of bandwidth with low active scanning coefficients and good patterns through wide scanning angles have been demonstrated. The challenges are associated with one or more among complex implementation, higher axial ratio (AR), lower gain, size, weight, power, and cost [158-161].

A compact unit-cell for CP patch antenna arrays is introduced in this paper. To expand the bandwidth, four small patches are chamfered, slotted, and sequentially rotated with appropriate excitation provided. The proximity of elements causes high coupling, which is explicitly included in the design of the unit-cell topology. Infinite and finite 8×8 array examples are discussed. Our previous work presents the

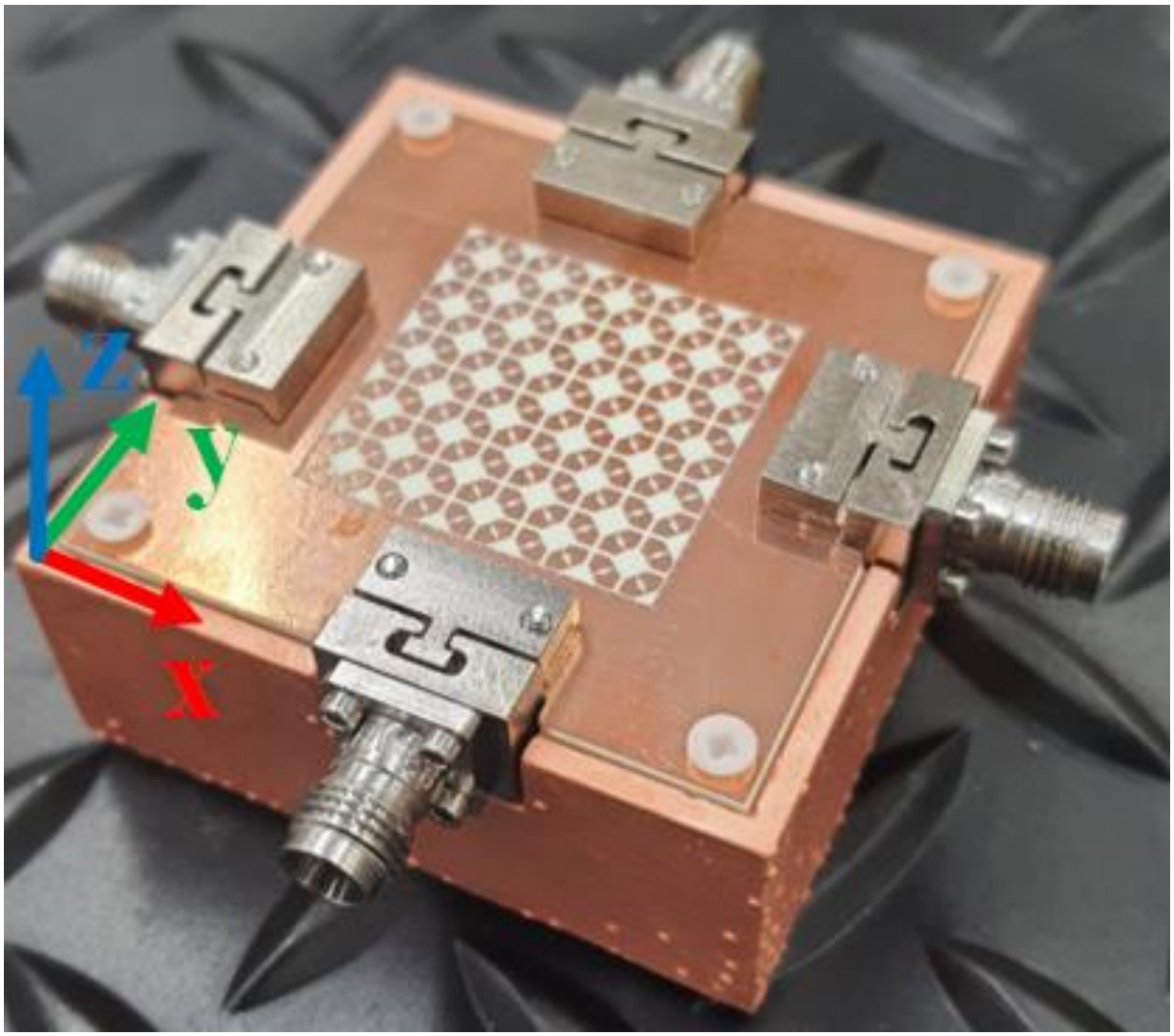

Fig. 5.1: Photographs of the fabricated 2×2 array with dummy elements.

simulations of a conventional CP patch array with cross-slots [162]. The herein proposed sequentially rotated configuration has significantly wider AR bandwidth while preserving compactness and broad impedance bandwidth over wider scanning angles. To assess the cost/complexity tradeoff and to validate the proposed concept, a 5×5 array, shown in Fig. 1, is fabricated. For experiments, four unit-cells (2×2 array) with integrated series power dividers at the center of the array are excited. The measured results show more than 56% wide impedance/AR bandwidth and their favorable agreement with simulations validates the proposed unit-cell. The arrays

with this kind of unit-cell can achieve higher radiated powers when directly driven by four-channel integrated circuit active beamformers.

The rest of the chapter is organized as follows: Section 5.2 discusses the design of the compact sequentially rotated unit cell and its implementation in infinite and finite 8×8 arrays. Section 5.3 presents the prototype with practical adjustments to validate previously discussed concepts and the design of a compact feed network. Section 5.4 discusses fabrication, measurements, and comparison with literature.

5.2 Unit-Cell Design and Demonstration

The proposed sequentially rotated microstrip patch array builds upon the work discussed in [162], where a tightly-coupled unit-cell was introduced. Past research showed that by optimizing loading cross-slot in rectangular chamfered patches, impedance bandwidths increased (from 19.2 to 36.5 GHz by 66%), and 3dB AR bandwidths improved (from 24.2 to 28 GHz by 15%). These changes also affected the currents inside the patch, leading to enhanced bandwidth and ensuring high aperture efficiency [162]. However, there was still a notable constraint in the 3dB AR bandwidth. This limitation paved the way for the use of the sequential rotation technique. Implementing sequential rotation in antenna arrays involves two main steps for each subarray element: physically adjusting its position relative to its neighbors and assigning an input phase value. Both steps are crucial for arrays with a specific number of elements predominantly radiating in their dominant mode. The determination of the physical rotation angle and the input phase value of m-th elements is mathematically described in equation (5.1) [163]:

$$\phi_p = \phi_e = \frac{p(m-1)\pi}{N} \tag{5.1}$$

where, ϕ_p represents the physical rotation angle, ϕ_e is the feeding phase shift of m-th element and N stands for the total number of radiating elements ($m \leq N$). Here, p is an integer such that $1 \leq p \leq N$-1, referencing its position relative to the first element. For this study, N is 4 and p is 2, resulting in $\phi_p = \phi_e = 90^o$. This configuration with 4 feeds has been observed to provide a better axial ratio than cases with N = 2 or 3, attributed to the cancellation of higher-order modes [164]. Results are presented for both the infinite array scenario and an 8×8 finite array case in the following sub-sections. is discussed in the context of an infinite array scenario and an 8×8 finite array case in the following sub-sections.

5.2.1. Infinite Array

The performance of the proposed unit cell is initially assessed in an infinite array environment using Ansys HFSS, as depicted in Fig. 5.2. The sequentially rotated unit cell measures 5×5 mm² ($0.44\lambda_{26\,GHz} \times 0.44\lambda_{26\,GHz}$). It is printed on a 0.762 mm-thick ($\lambda_{26\,GHz}$ / 15) Rogers 4350B substrate with a permittivity (εr) of 3.66 and a *tanδ* of 0.004. The patch, chamfer, cross-slot, and feed location dimensions are optimized to achieve a good impedance match and axial ratio over the 18.5-33 GHz frequency band. The array is designed for cost-effective fabrication on a single-layer substrate board. To counteract the pin's inductance, a 0.39 mm wide capacitive annular ring is integrated into the unit cell, allowing the inner radius to be adjustable while maintaining a constant outer radius of 0.85 mm. Active VSWR and far-field measurements of the proposed unit cell are illustrated in Fig. 5.3. The positive effects of the cross-slot and sequential rotation technique are evident from these data. The cross-slot integration enhances the impedance bandwidth through additional current perturbation while lowering the center frequency due to the increased effective

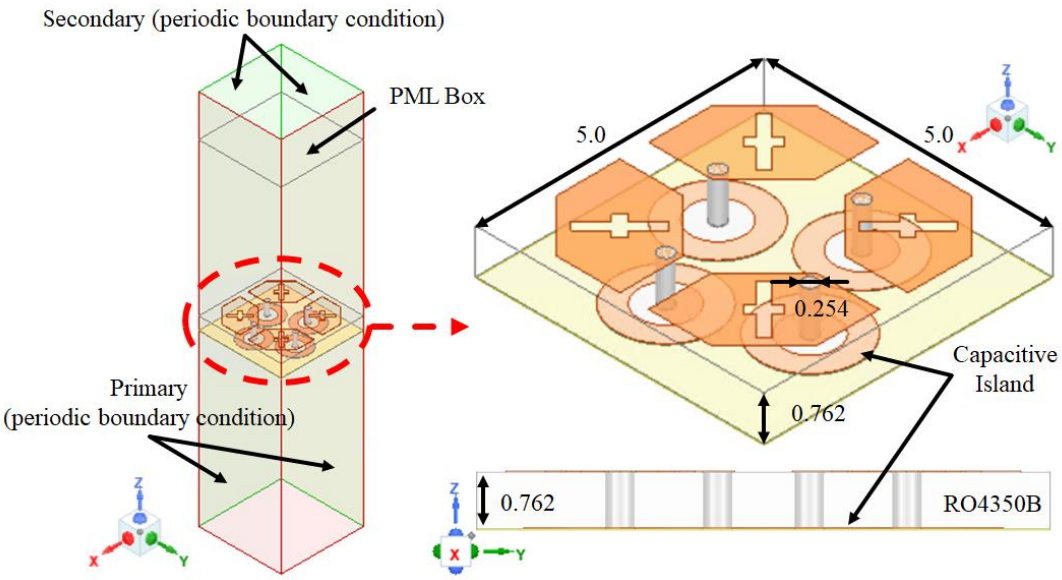

(a)

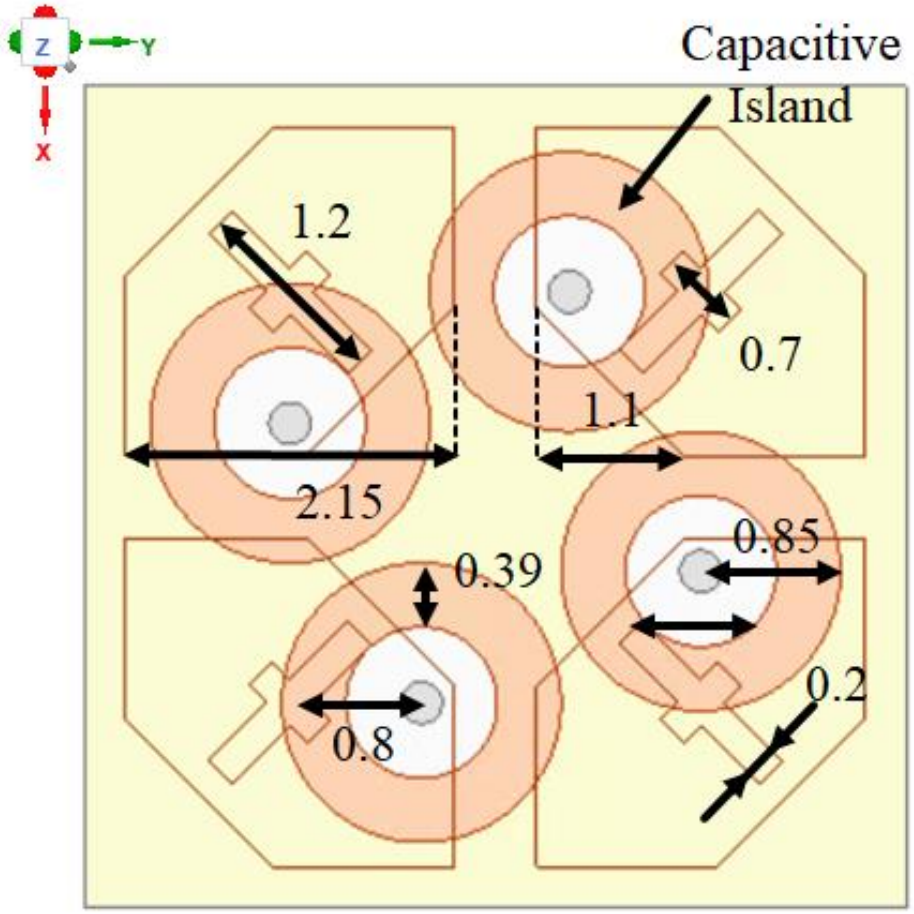

(b)

Fig. 5.2: (a) The proposed sequentially rotated patch antenna unit-cell in infinite array environment. (b) Top view. (Dimensions are in millimeters).

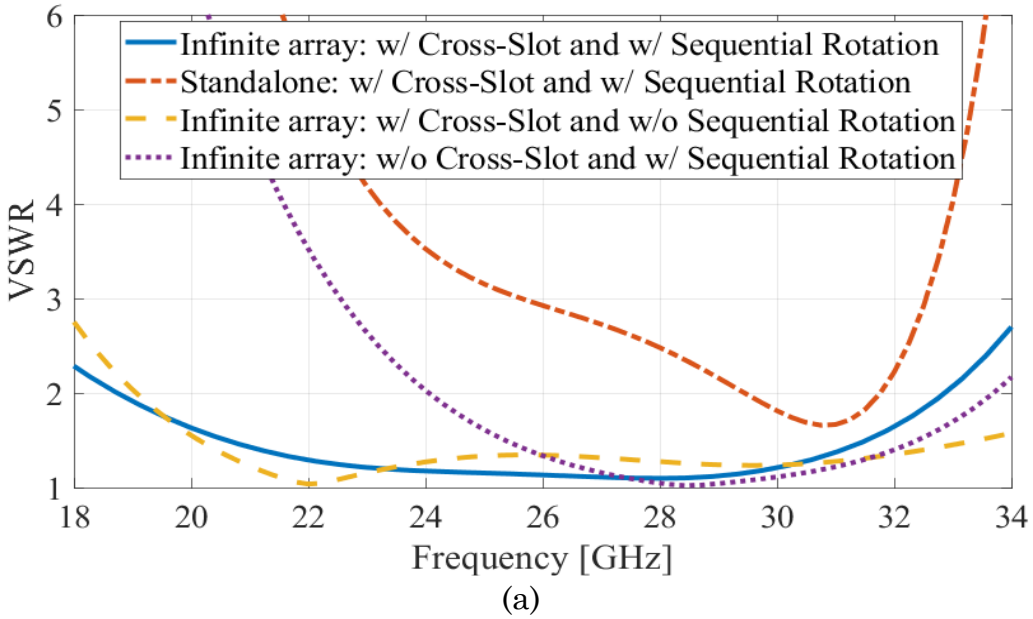

(a)

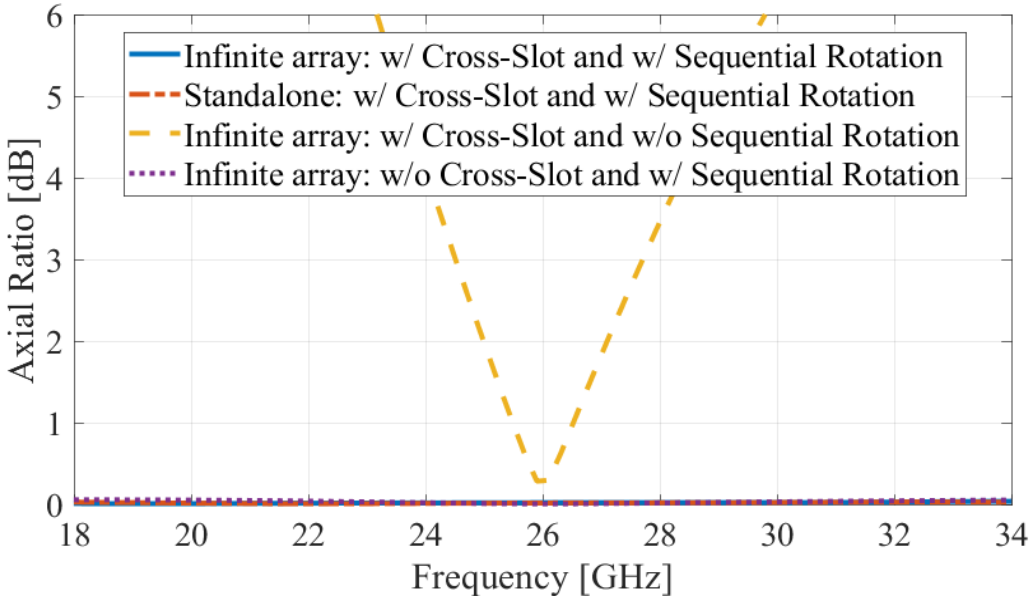

(b)

Fig. 5.3: Performance of the proposed unit-cell in infinite array environment (solid, dashed, and dotted lines) with (w/) and without (w/o) cross-slot and/or sequential rotation (a) VSWR. (b) Axial ratio at boresight.

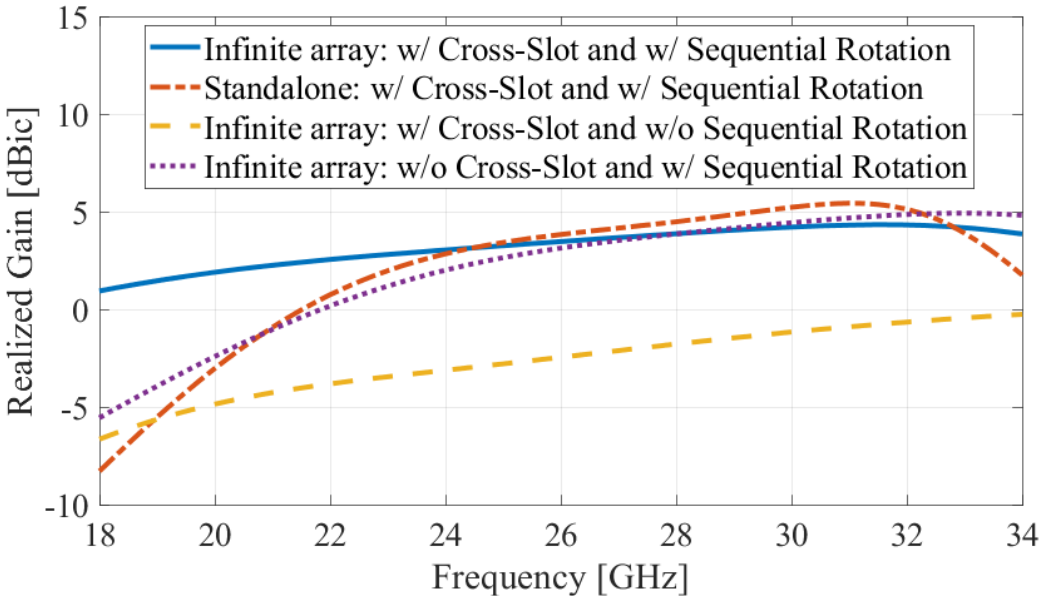

(c)

Fig. 5.3: Performance of the proposed unit-cell in infinite array environment (solid, dashed, and dotted lines) with (w/) and without (w/o) cross-slot and/or sequential rotation (c) Realized gain at boresight. The performance of standalone unit-cell (dash-dotted line) is also shown.

wavelength, contributing to the compactness of the unit cell structure. As shown in Fig. 5.3(a), a VSWR less than 2:1 is achieved from 18.5 to 33 GHz (~56%). Employing the sequential rotation technique results in a slight reduction in impedance bandwidth due to variations in mutual coupling. However, the axial ratio significantly improves with sequential rotation (see Fig. 5.3(b)), along with an enhanced realized gain (Fig. 5.3(c)). Additionally, the cross-slots contribute to a more uniform gain across a wide bandwidth.

For completeness, the performance of a standalone unit cell is also shown in Fig. 5.4. This individual element exhibits a noticeably smaller bandwidth, further highlighting the importance of strong mutual coupling to achieve the desired performance over a wide bandwidth. The proposed design achieves both unit-cell miniaturization (enabling more actives and higher effective isotropic radiated power (EIRP) per unit area) and improved gain and axial ratio bandwidth while

maintaining high radiation efficiency (>95%) and aperture efficiency (>97%). However, in the absence of direct element excitation and control with a chipset beamformer, this unit cell requires a compact feed network to achieve the necessary patch excitation, contributing to higher loss and complexity.

5.2.2. 8×8 Finite Array

The unit-cell shown in Fig. 5.2 is utilized to create a finite array configuration and assess the performance in a more realistic environment. The inset of Fig. 5.4(a) shows the top view of the designed 8×8 array of unit-cells from Fig. 5.2 having a total of 256 chamfered microstrip patches. The inter-element spacing is set to be 5 mm ($0.44\lambda_{26GHz}$), with the overall size being 40 × 40 mm².

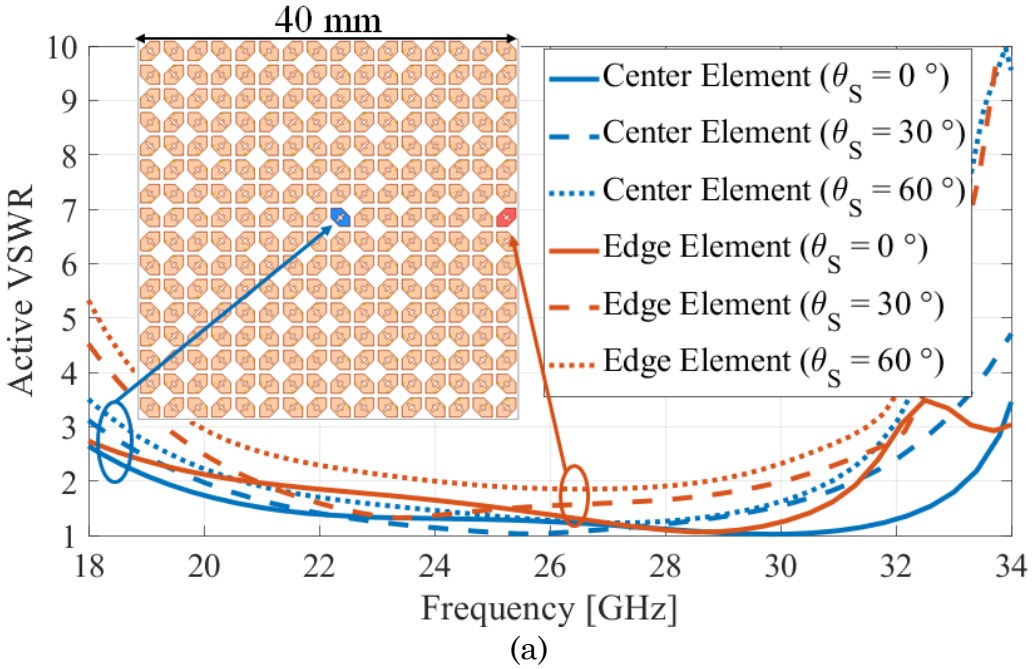

(a)

Fig. 5.4: Performance of the 8×8 array: (a) Active VSWRs of the center and edge elements while scanning to θ_S = 0, 30, and 60° (the configuration is shown in the inset).

Fig.5.4(a) shows the active VSWRs with scanning results (θS = 0º, 30º, and 60º) of the center [(row, column) : (8, 9)] and edge [(row, column) : (8, 16)] elements as

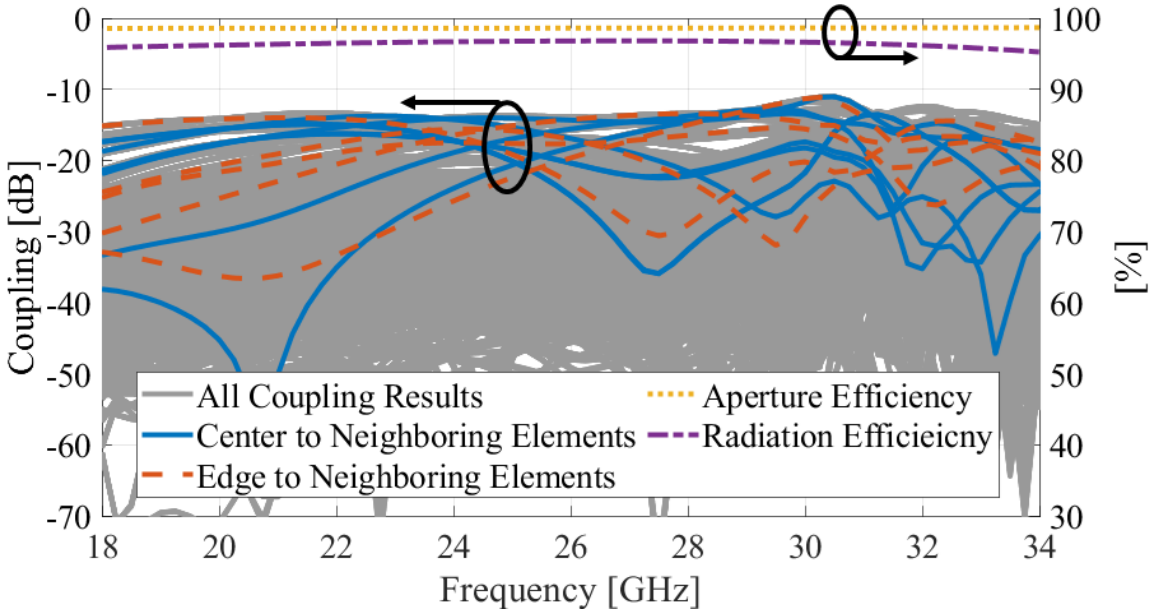

(b)

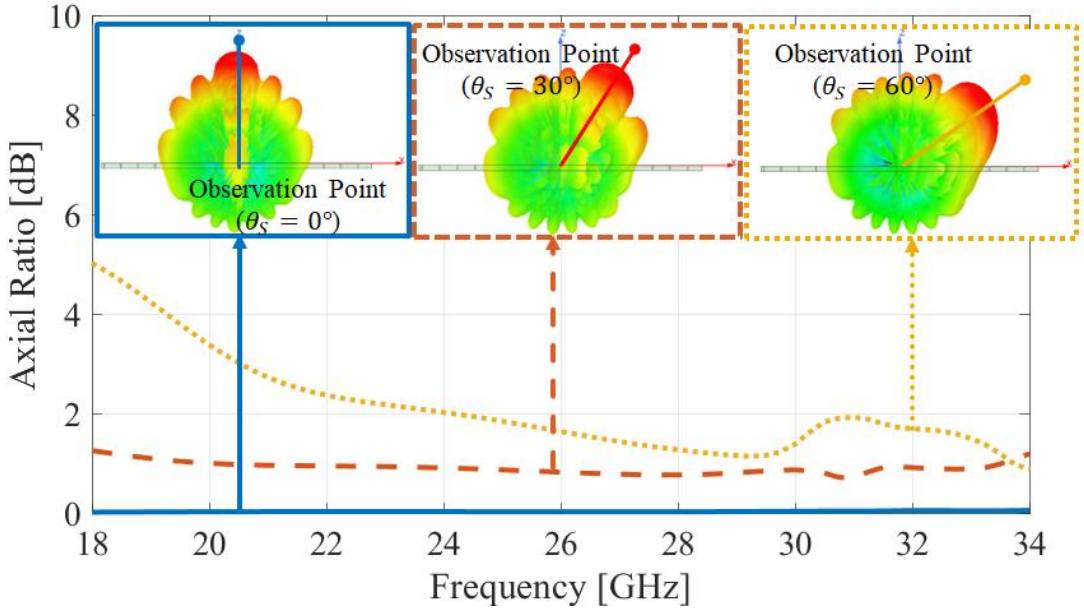

(c)

Fig. 5.4: Performance of the 8×8 array: (b) Coupling (grey: all results, blue: between center and its adjacent elements, red: between edge and its adjacent elements) and aperture/radiation efficiencies for the broadside beam. (c) Axial ratio at the beam peak while scanning.

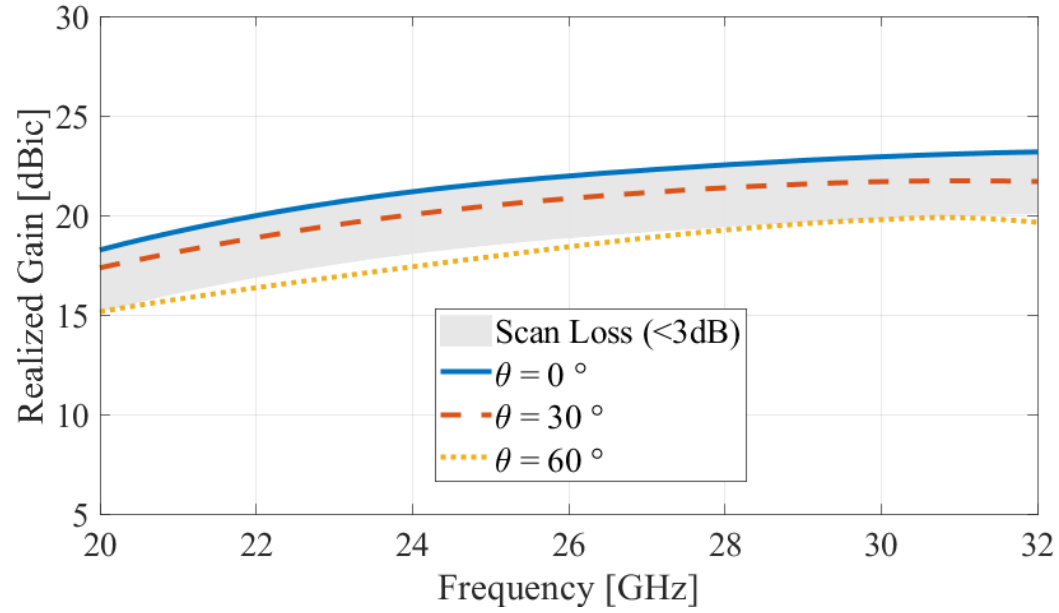

(a)

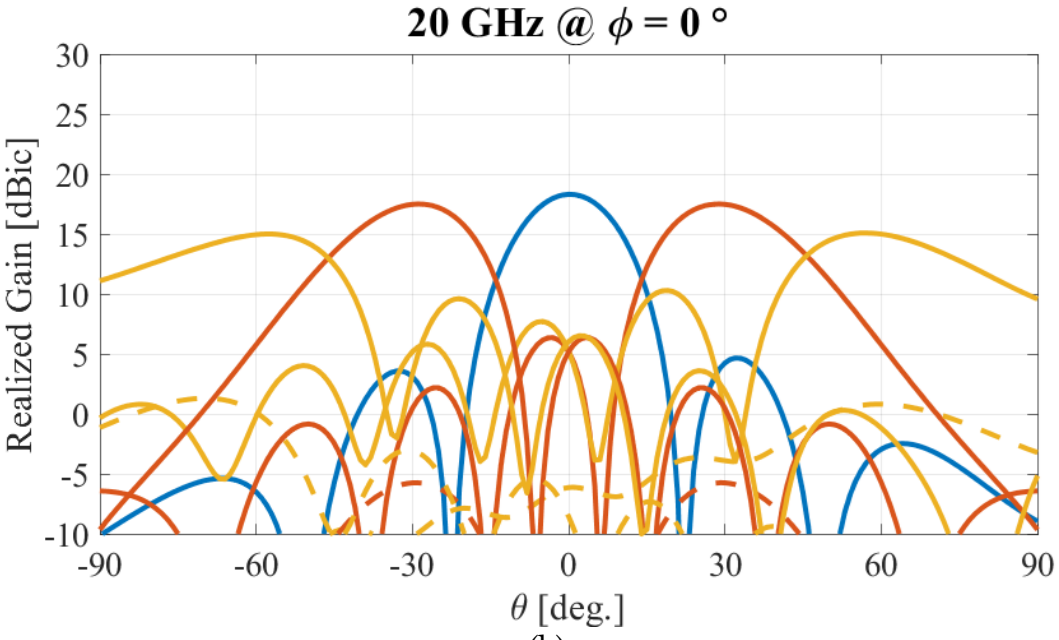

(b)

Fig. 5.5: (a) Realized gain over frequency, Radiation patterns (solid line: LHCP, dashed line: RHCP) for θ = 0º (blue), ±30º (red), and ±60º (yellow) beams in ϕ = 0° (b) At 20 GHz

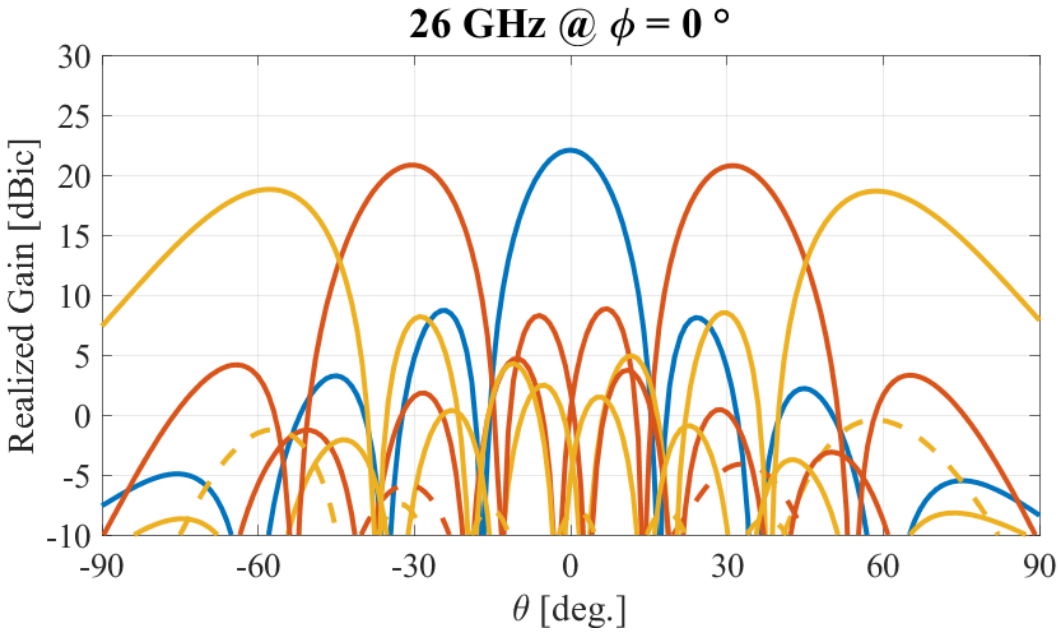

(c)

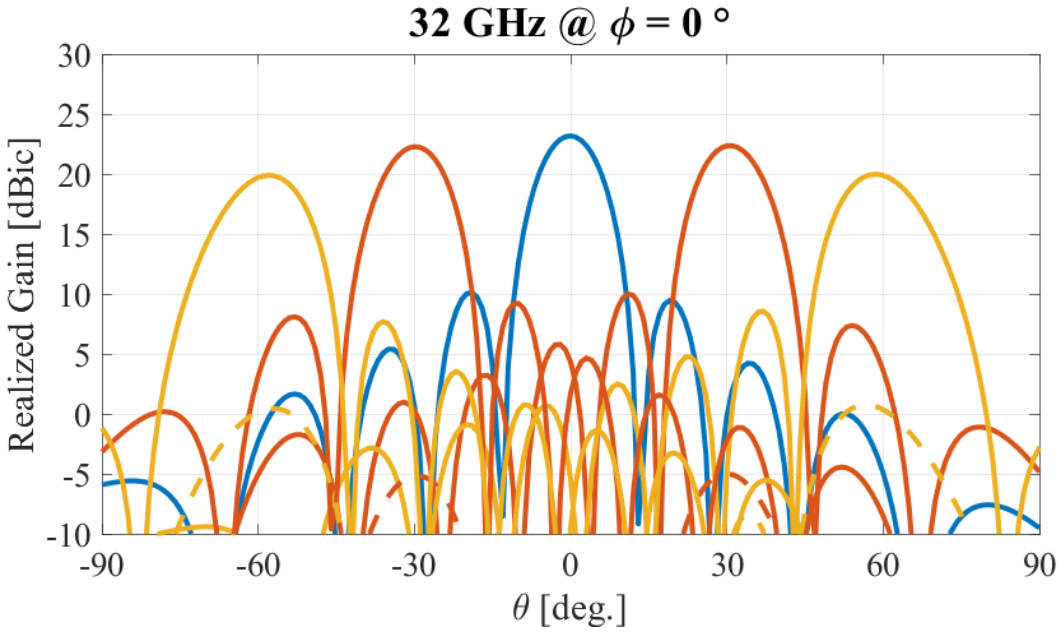

(d)

Fig. 5.5: Radiation patterns (solid line: LHCP, dashed line: RHCP) for θ = 0º (blue), ±30º (red), and ±60º (yellow) beams in ϕ = 0° (c) At 26 GHz, (d) At 32 GHz.

shown in the inset. As expected, the VSWR of the center element approaches that of the infinite array. Moreover, even with an elevation scan angle of 60º, the VSWRs remain below 3:1 over the operating frequencies (20 – 32 GHz). Regarding the scanning mechanism, each unit cell functions as a fundamental structural entity with a unique phase excitation differential with other unit cells to achieve the desired scan. Simultaneously, distinct electrical phase variations among the individual elements are preserved within each unit-cell. As shown in Fig. 5.4(b), the coupling between all elements (grey shade) is less than -10 dB. The central and edge element couplings with their neighbors are depicted by the blue- and red-colored lines, respectively. The axial ratio at the beam peak and the designated scanning angle remains below 3 dB over the operating frequency band (see Fig. 5.4(c)). The scanned realized gain over frequency and radiation patterns at 20, 26, and 32 GHz for $\theta = 0^{o}$, $\pm 30^{o}$ and $\pm 60^{o}$ in $\phi = 0^{o}$ are shown in Fig. 5.5. Due to the intrinsic symmetry of the unit-cell, similar patterns are obtained at differentϕ-planes with broadside realized gain > 18 dBic at 20 GHz. Symmetric patterns with AR < 3.5 dB, scan loss < 3.8 dB, and low SLL (< -12 dB) are maintained through the upper part of the band (32 GHz) and over the ±60° scan.

5.3. Prototype Design For Validation

A simplified, sequentially rotated array was prototyped to validate the proposed design. A 5×5 array, shown in Fig. 5.1 and detailed in Fig. 5.6, was fabricated. Instead of exciting all elements in the prototype, only four unit cells (16 patches) in the array's center were excited to demonstrate the impact of mutual coupling and sequential rotation on the performance of the circularly polarized (CP) array. This validation approach, based on [165], though unconventional since it only considers the excitation

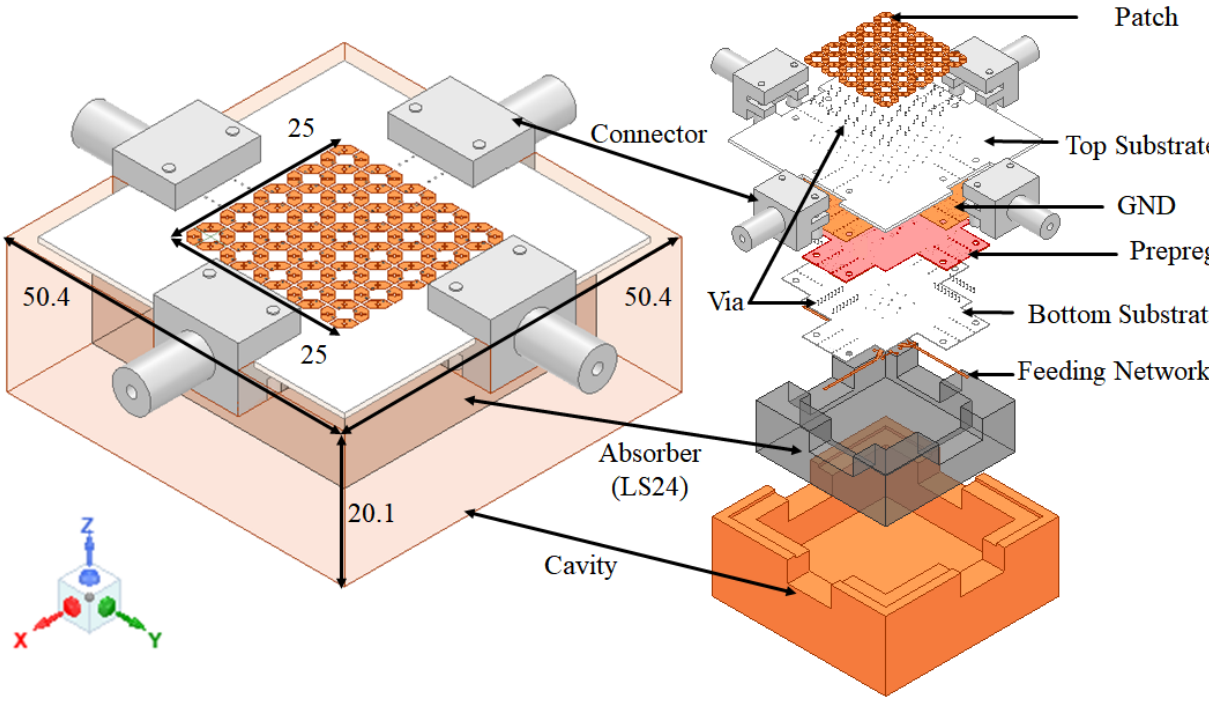

(a)

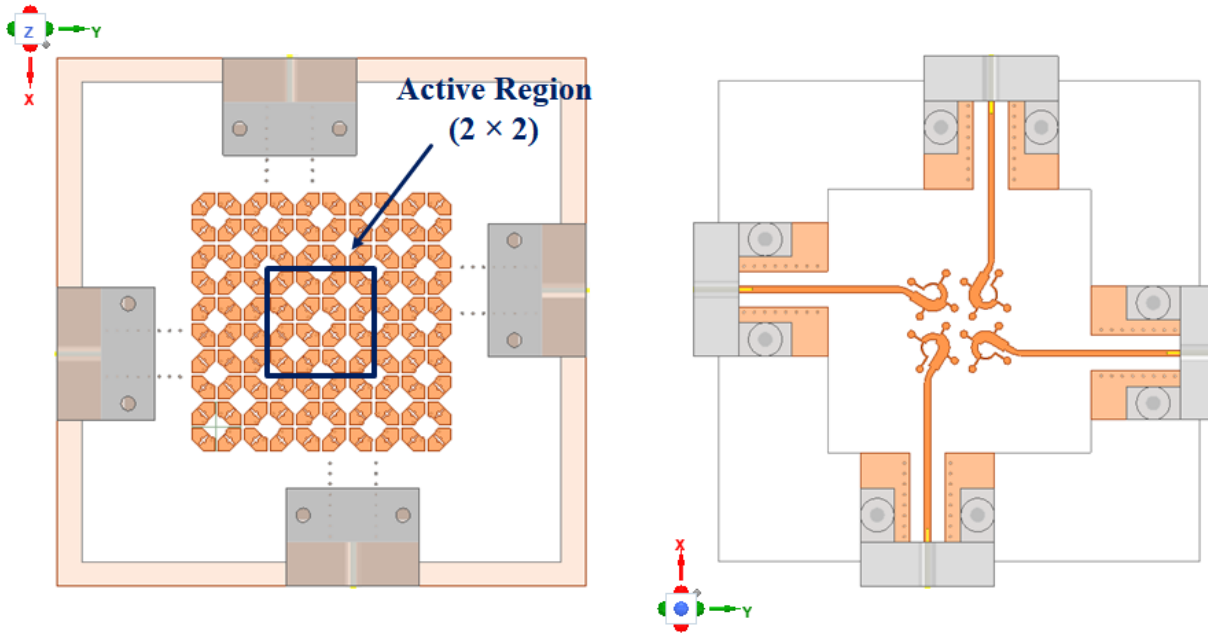

(b)

Fig. 5.6: (a) Illustration of the 2 × 2 prototype array modules with its integral parts (Dimensions are in millimeters). (b) Top and bottom views of the PCBs.

of a few elements in the array, is a simple, cost-effective, yet thorough method that fully validates the concept. In this design, the four sequentially rotated aspects of the central unit cells were excited with a 90° phase progression using a compact wideband microstrip power divider. Four power dividers were integrated with the array and connected using a microstrip transition, as shown in Fig. 5.7. The unexcited elements were grounded for simplicity. To eliminate backward radiation from the microstrip feed network, the array was backed by a cavity filled with a 6.25 mm-thick ECCOSORB LS-24 absorber [166].

5.3.1 1×4 Feeding Network

The series feed network of the prototype is discussed in this subsection. The design is based on a microstrip line series power divider which equivalent circuit model with an input and four output ports is shown in Fig. 5.7(a). Each output port is engineered for 90° phase progression and equal power distribution where each port receives a quarter of the normalized input power. These ports are characterized by a uniform load impedance, denoted as Z_L. To achieve this configuration, the four output ports are interconnected using quarter-wave impedance transformers. Following the divider's design approach from [167], the characteristic impedances of these transformers are obtained as in (5.2), (5.3), and (5.4):

$$\frac{1}{4}P_1 = P_2 = P_3 = P_4 = P_5 \tag{5.2}$$

$$Z_{IN,\,2} = Z_L\frac{P_2}{P_1},\;\; Z_{IN,3} = Z_L\frac{P_3}{P_1-P_2},\; Z_{IN,4} = Z_L\frac{P_4}{P_1-P_2-P_3} \tag{5.3}$$

$$Z_1 = \sqrt{Z_{IN,1}Z_{IN,2}},\quad Z_2 = \sqrt{\frac{Z_{IN,2}Z_{IN,3}Z_L}{Z_L-Z_{IN,2}}},$$

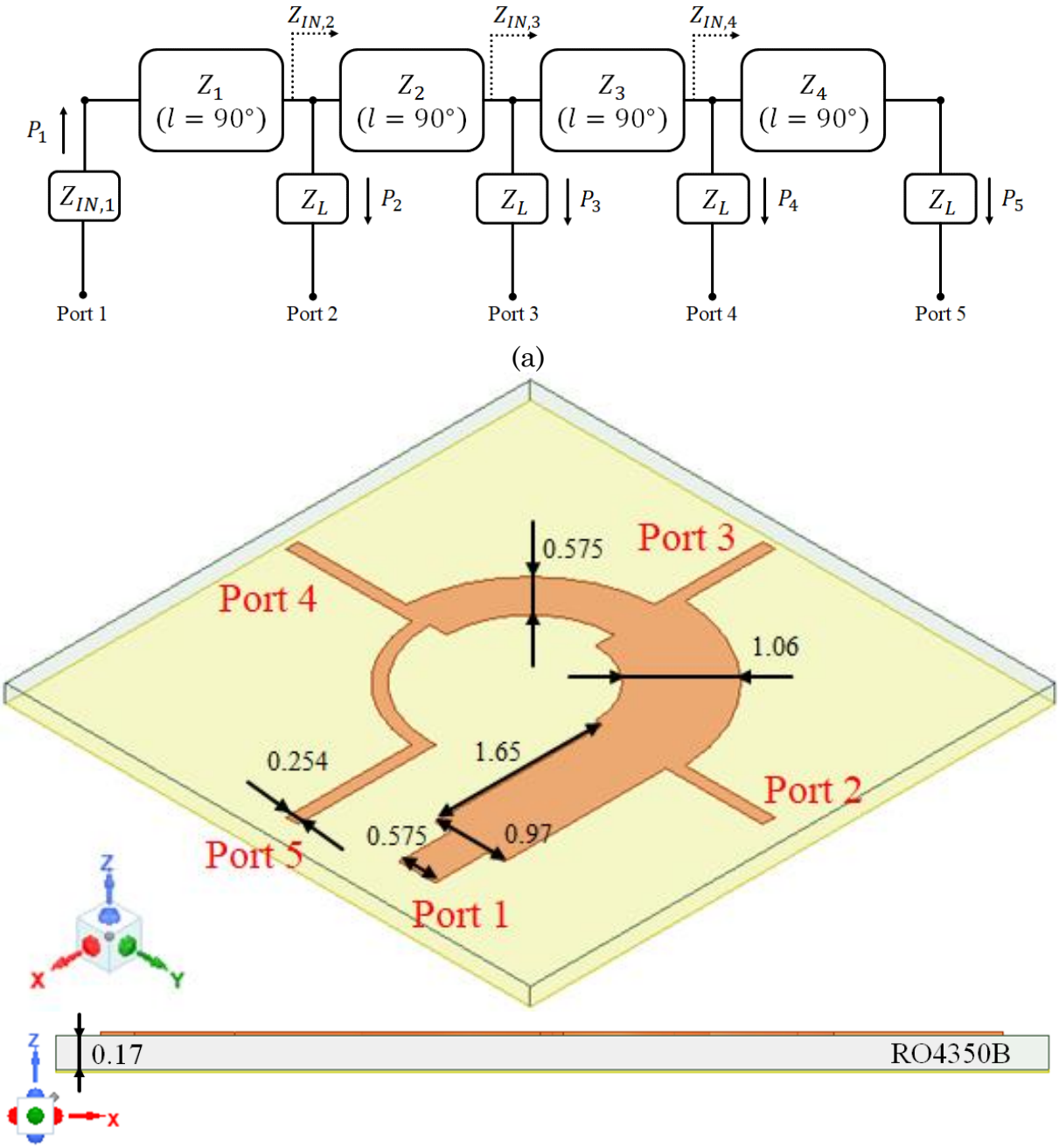

Fig. 5.7: Microstrip series power divider, specifically: (a) Equivalent circuit. (b) Layout of the proposed design. (Dimensions are in millimeters)

$$Z_3 = \sqrt{\frac{Z_{IN,3}Z_{IN,4}Z_L}{Z_L - Z_{IN,3}}}, \qquad Z_4 = \sqrt{\frac{Z_{IN,4}Z_L^2}{Z_L - Z_{IN,4}}} \tag{5.4}$$

Notice that a load impedance (Z_L) of 77 Ω is purposely selected after extensive numerical studies to facilitate the design of a well-matched and performing feeding

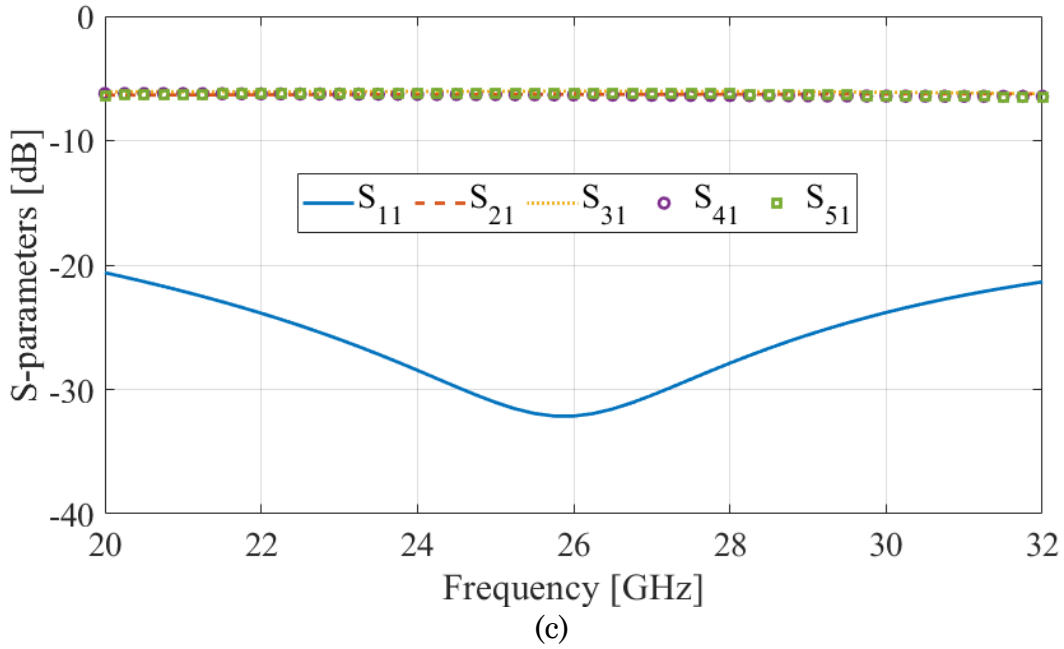

(c)

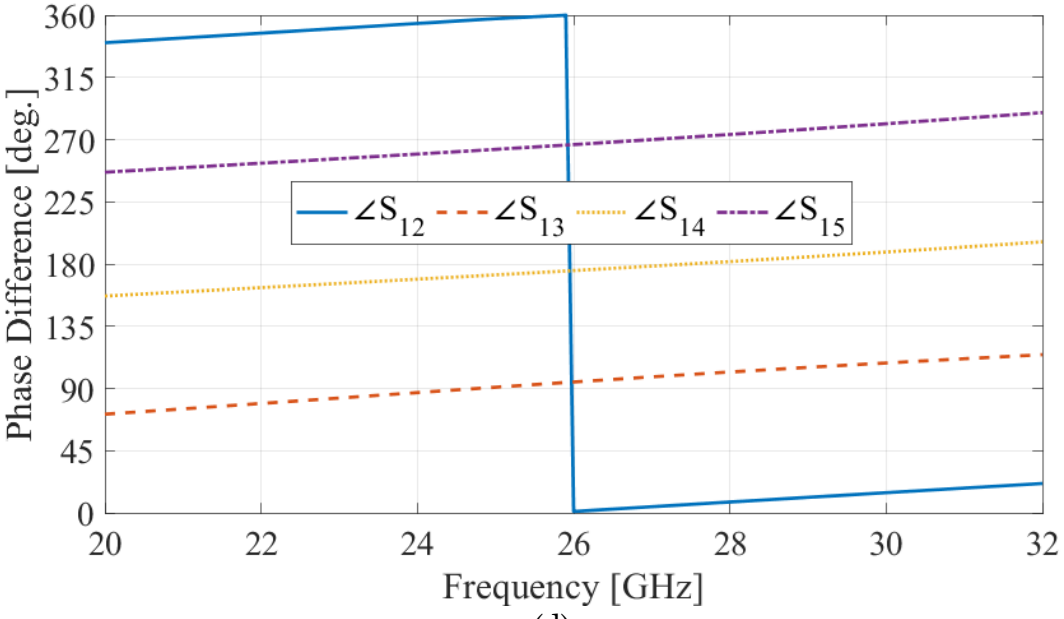

(d)

Fig. 5.7: Microstrip series power divider performance: (c) Magnitude of S-parameters. (d) Phase differences between port 1 and other ports 2, 3, 4, and 5.

network. The obtained line impedances Z_1 to Z_4 are 30.6, 25, 37.5 and 75 Ω, respectively. When a Z_L of 50 Ω load is utilized, it leads to impedance values of 25, 16, 25, and 50 Ω for Z_1 through Z_4, respectively. This requires the use of broader microstrip lines to achieve the required lower impedance values, consequently

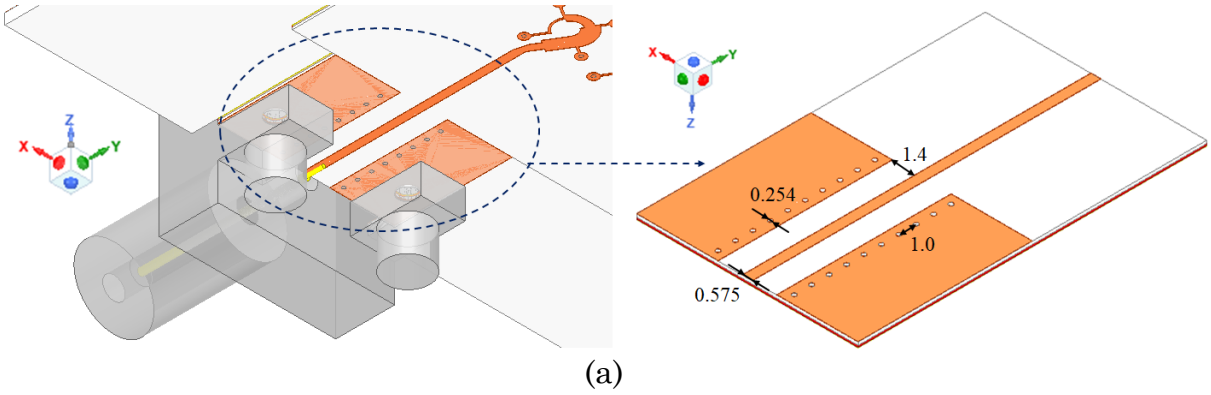

(a)

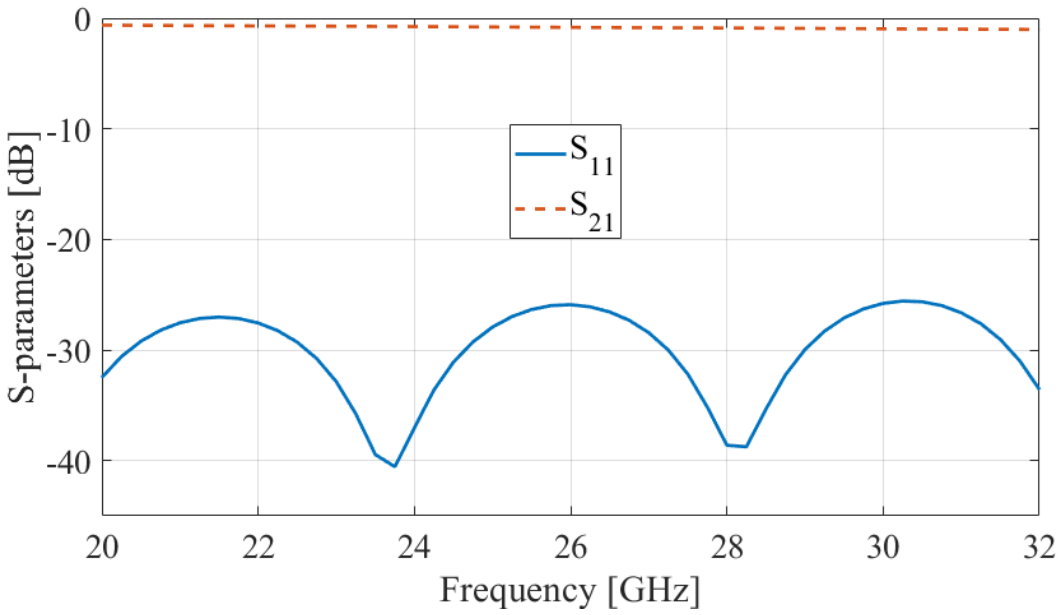

(b)

Fig. 5.8: (a) Illustration of the designed GCPW transition. (Dimensions are in millimeters) (b) Magnitude of computed S-parameters.

leading to a reduction in the inter-line spacing within the power divider. Such a configuration results in increased mutual coupling, which adversely affects the matching performance and increases the amplitude and phase imbalances. Fig. 5.7(b) shows the final configuration of the series power divider for a 0.17 mm thick Rogers 4350B substrate. As shown in Fig. 5.7(c), the designed power divider has an input reflection coefficient of less than -20 dB across the entire 20 to 32 GHz band. The phase differences at 26 GHz between port 1 and ports 2-5 are $\angle S_{12}$ = 1°, $\angle S_{13}$ = 94°, $\angle S_{14}$ = 177°, and $\angle S_{15}$ = 266°, respectively. The maximum phase and amplitude

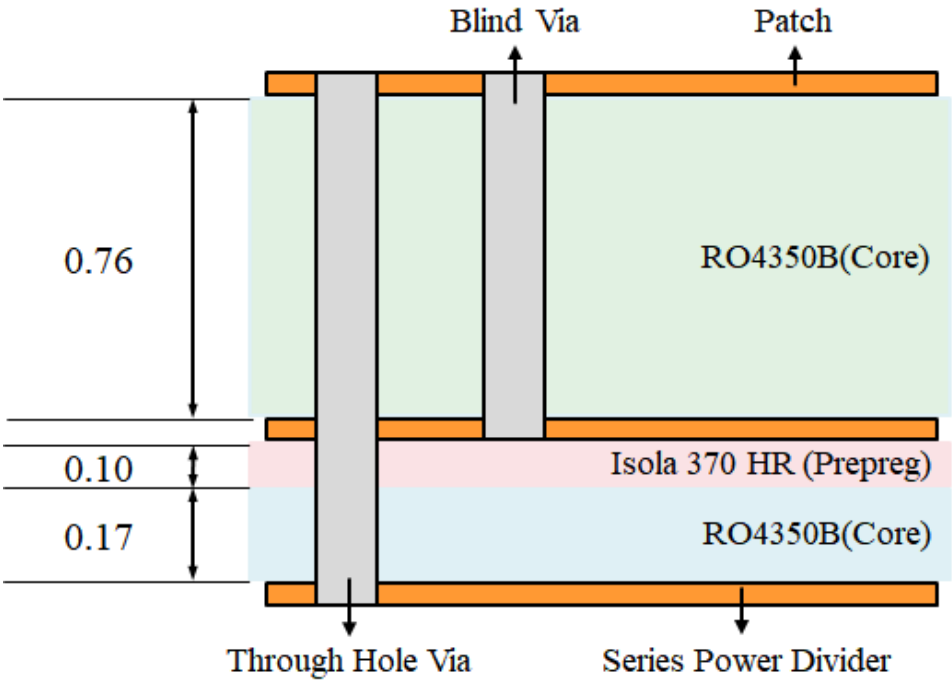

Fig. 5.9: Stack-up configuration. (Dimensions are in millimeters).

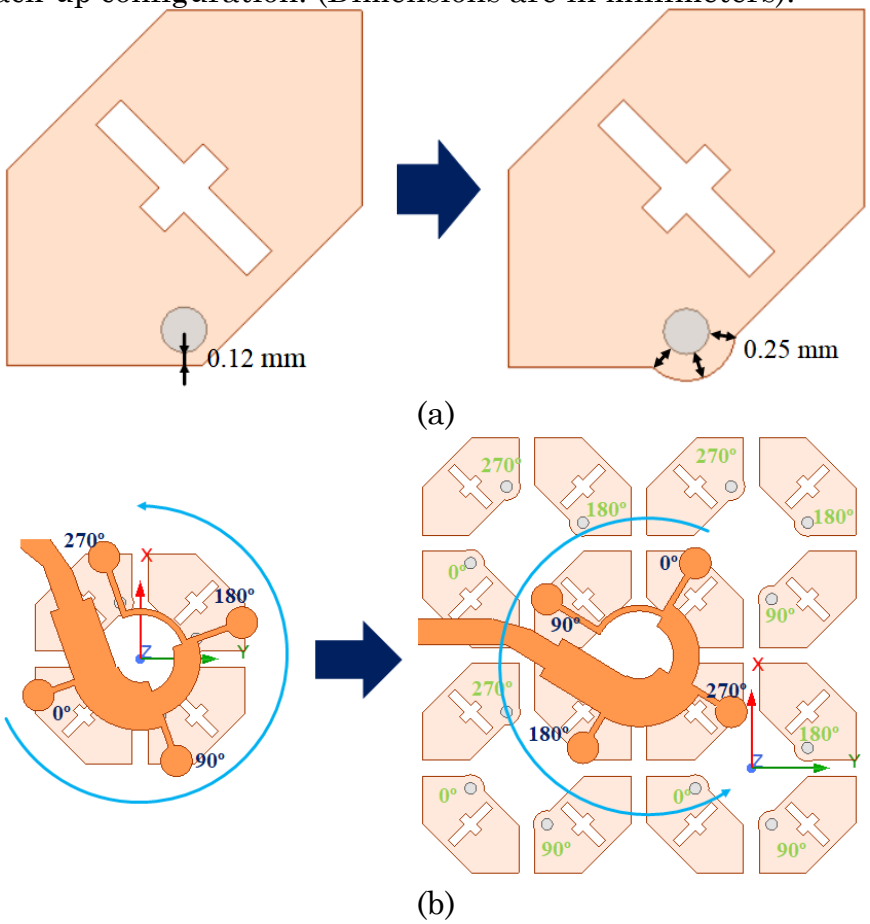

Fig. 5.10: (a) Illustration of patch modifications. (b) Series feed arrangement.

imbalances are 6º and 0.3 dB, respectively. A simple transition between the input microstrip line and grounded coplanar waveguide (GCPW) at the connector side is implemented as shown in Fig. 5.8. The power divider outputs are directly connected to the array elements through plated vias as can be seen from the PCB stack-up in Fig. 5.9. The patches are slightly modified to ensure a proper vias connection as suggested by the PCB manufacturer (see Fig. 5.10(a)). A 0.1mm-thick Isola 370 HR (ε_r = 4.04, $tan\delta$ = 0.021) layer is used as a prepreg to attach the power divider and patch array core substrates. Despite the reconfiguration of the integrated power divider to fit the compact unit-cell size as seen in Fig. 5.10(b), the LHCP operation is maintained. Finally, a Southwest Microwave end launch 2.92 mm connector [168] completes the assembly.

5.3.2 Metalization and Via-Walls

This subsection addresses challenges encountered during the prototype fabrication and introduces appropriate mitigation strategies. Fig. 5.11(a) displays the radiation patterns in the ϕ = 0° and 90° cuts at 26 GHz, both with and without substrate extension. The practical mounting's substrate extension induces distortion in the co-polarized LHCP radiation pattern and degrades cross-polarized performance. Upon analysis, this distortion is attributed to two primary factors. The first is related to the fringing fields, which can be mitigated by metalizing the top substrate extension, as shown in the orange-colored region of Fig. 5.11(b).

The second factor contributing to the aforementioned problem is the surface waves which cutoff frequency can be calculated using (5.5) [169]:

$$f_c = \frac{nc}{4h\sqrt{\mu_r\varepsilon_r - 1}} \quad \begin{cases} n = 0\,,\ 2,\ 4\ \ldots\ for\ TM\ mode \\ n = 1\,,\ 3,\ 5\ \ldots\ for\ TE\ mode \end{cases} \tag{5.5}$$

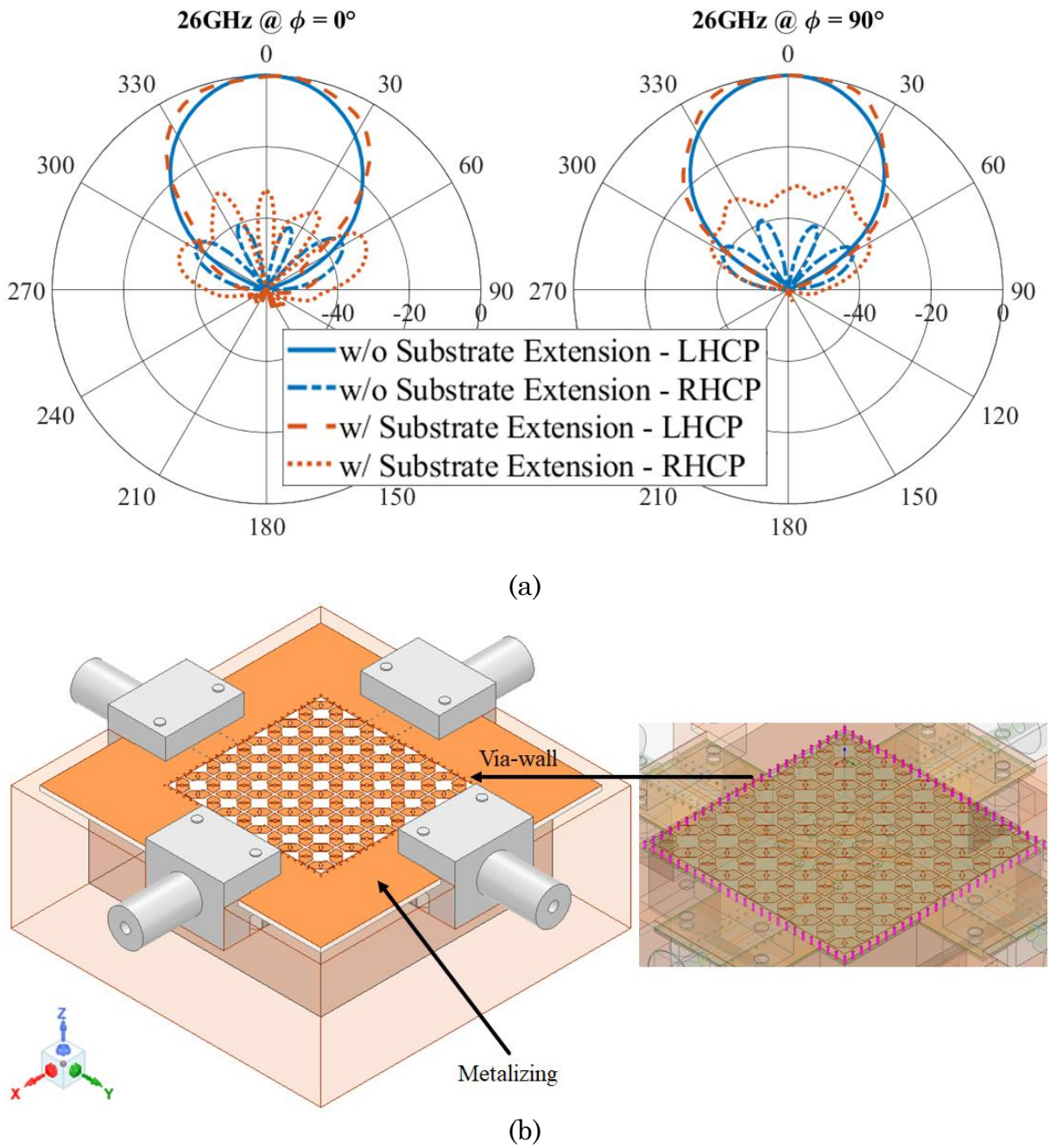

Fig. 5.11: (a) Normalized radiation patterns at 26 GHz in ϕ = 0 and 90° cuts without (w/o) substrate extension (blue solid- and dash-dotted lines) and with (w/) substrate extension (red- dashed and dotted lines). (b) Modified prototype with included mitigation (i.e., metallization and via-walls).

where c is the speed of light, h is substrate height, εr and μr are relative permittivity and permeability of substrate, respectively. As expected, the fundamental TM0 mode cutoff is at DC, while the TE1 mode starts at 60.3 GHz, which is beyond the operating

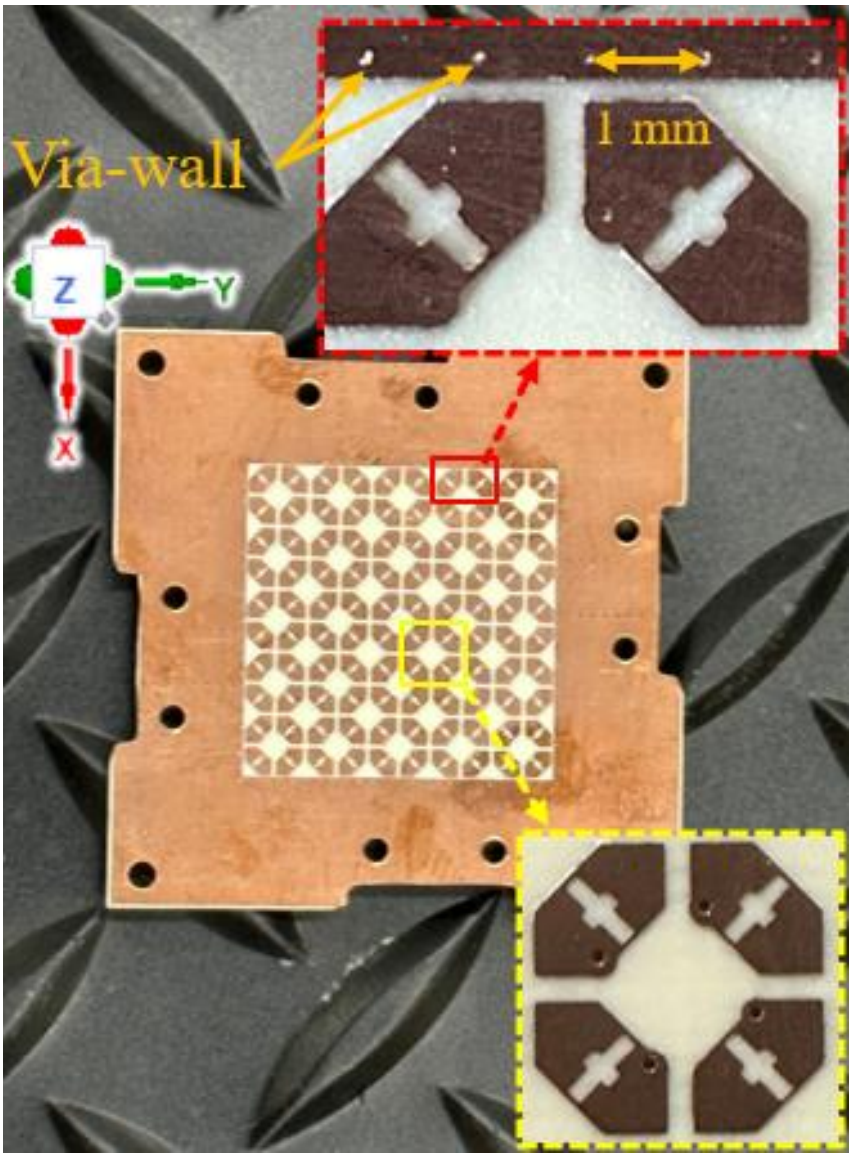

(a)

Fig. 5.12: Fabricated 2×2 prototype array module: (a) Top view with unit-cell and via-wall in the insets.

band. To mitigate the surface wave impact, a via-wall surrounding the patch is added (highlighted in magenta color in Fig. 5.11(b)). The via-walls function as a surrogate for a conductive fence and can significantly diminish the adverse effects of surface waves.

5.4. Fabrication and Measurement

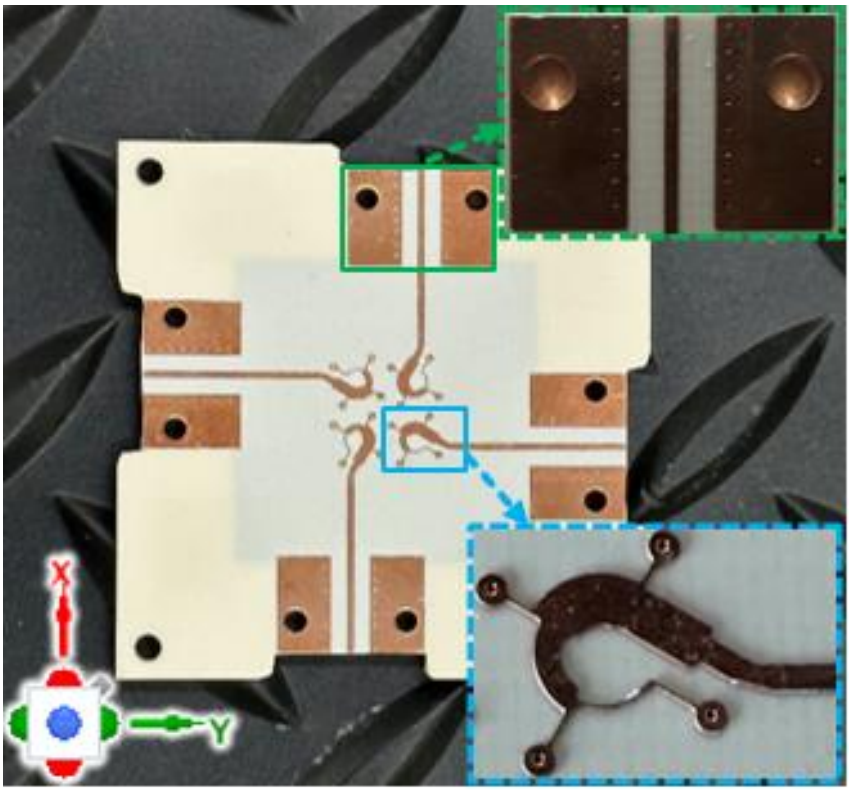

(b)

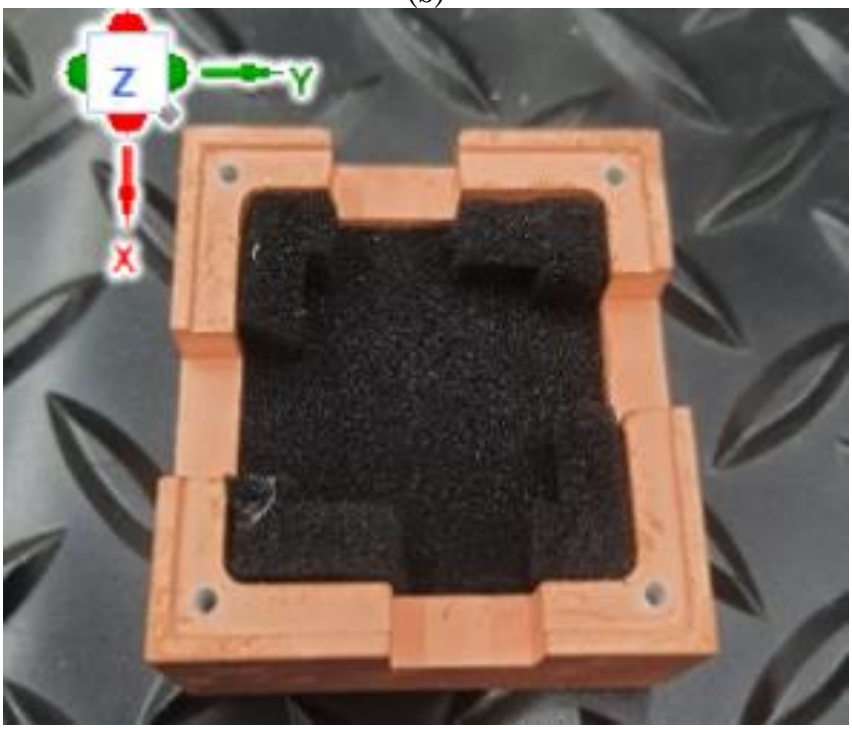

(c)

Fig. 5.12: Fabricated 2×2 prototype array module: (b) Bottom view with power divider and GCPW in the insets (c) Additively manufactured cavity with the absorber.

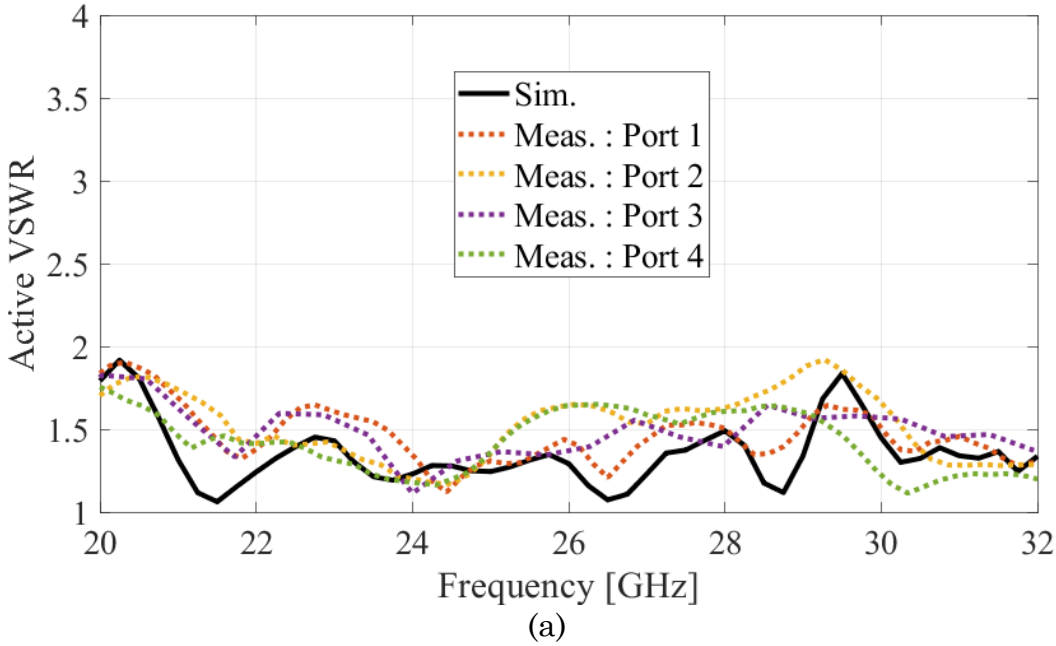

(a)

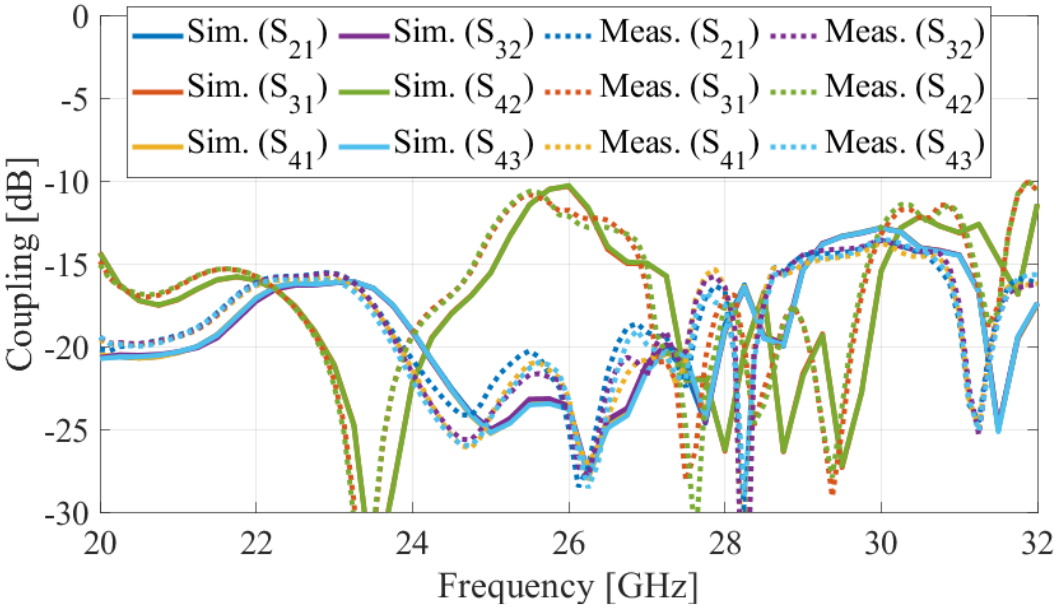

(b)

Fig. 5.13: Simulated and measured performance of the fabricated prototype, specifically: (a) Active VSWRs. (b) Coupling.

Figs. 5.12(a)-(b) show the top and bottom views of the fabricated sequentially rotated array. An additively manufactured and copper plated cavity with inserted absorber is depicted in Fig. 5.12(c). The cavity was fabricated using a 3D printer

(Formlabs Form3 [93]) employing stereolithography technology with Rigid 4000 resin.

Measured and simulated active VSWRs and coupling are plotted in Figs. 5.13(a)-(b). As seen, active VSWRs < 2:1 and coupling levels < -10dB are measured for all four ports across the entire bandwidth. The far-field is characterized in the anechoic chamber at the University of Colorado Boulder, with unmeasured ports terminated with 50 Ω loads, as shown in the inset of Fig. 12(c). The results are obtained by superimposing data from each port [165, 170]. As seen in Fig. 5.13(c), the axial ratio and gain are maintained < 1 dB and > 5.8 dBic, respectively, across the entire bandwidth (>56%) in both simulation and measurement. Moreover, as shown in Fig. 5.13(d), the AR pattern over the elevation remains fairly symmetric. Fixed beams with half-power beamwidth (HPBW) of 72, 45, and 64° are obtained at 20, 26, and 32 GHz, respectively. The AR remains < 4 dB within the HPBW. Measured radiation patterns at $\phi = 0^{o}$ from 20 to 32 GHz are shown in Fig. 5.14. As seen, the symmetry and clear cross-polarization discrimination with suppressed back radiation, are achieved. Furthermore, the effectiveness of the mitigation approach, involving metallization and the incorporation of via-walls, in addressing pattern distortion is confirmed. The comparison between the proposed configuration and the state-of-the-art sequentially rotated planar CP arrays, is given in Table 5.1. As seen, the proposed configuration has wider impedance and axial ratio bandwidths while maintaining compact unit-cell size and cost-effective fabrication. Specifically, the proposed unit-cell area ($\sim 0.2\lambda_0^2$) is significantly smaller than those reported in other studies. This compact size enables packing more elements within specific areas leading to a CP array with higher EIRP. Moreover, the absence of additional parasitic layers enables the integration of both, a patch, and a feeding network within the configuration comprising merely two substrate layers, thus reducing the cost, and improving the overall efficiency. Conclusively, the proposed array demonstrates a

wider impedance bandwidth (>56%), 1dB/3dB AR bandwidth (>56%), and a 3dB gain bandwidth of approximately 42%.

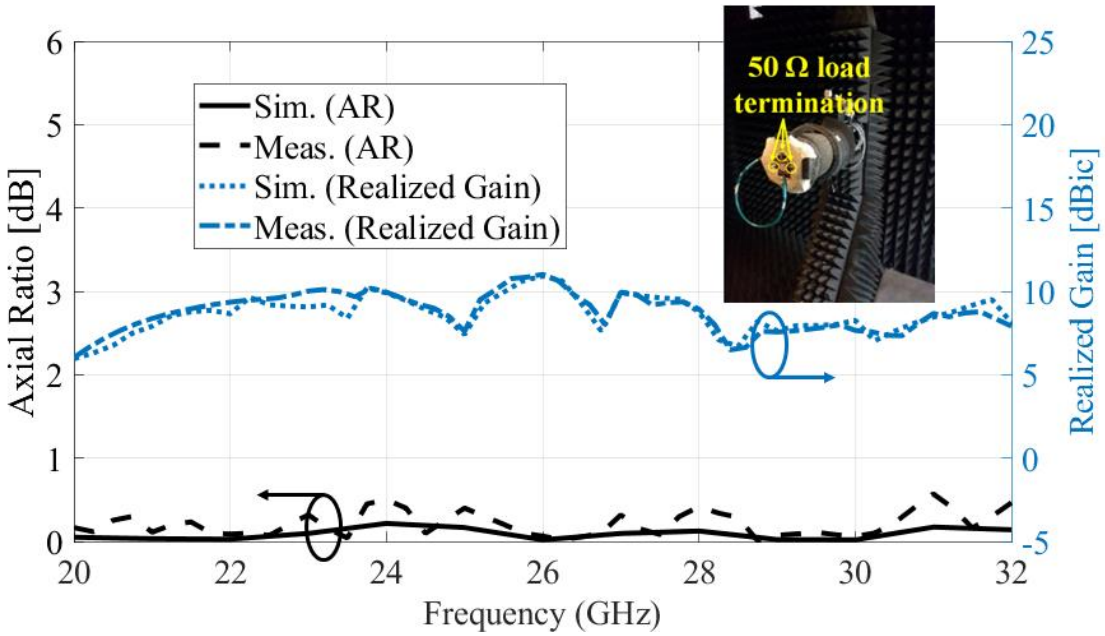

(c)

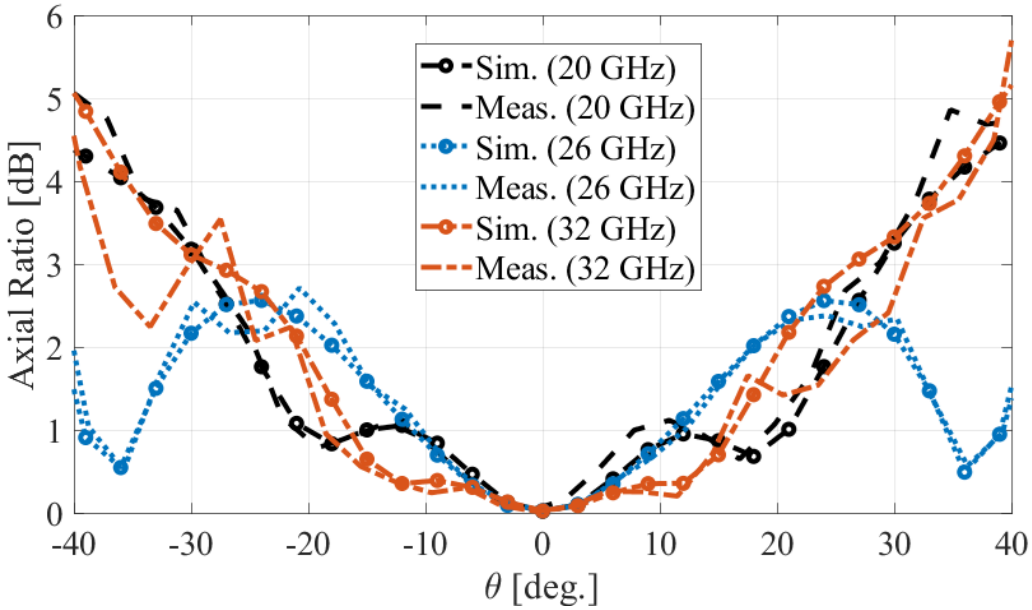

(d)

Fig. 5.13: Simulated and measured performance of the fabricated prototype, specifically: (c) Axial ratio and realized gain over frequency with measurement setup shown in the inset. (d) Axial ratio at 20, 26, and 32 GHz in the $\phi = 0°$ cut.

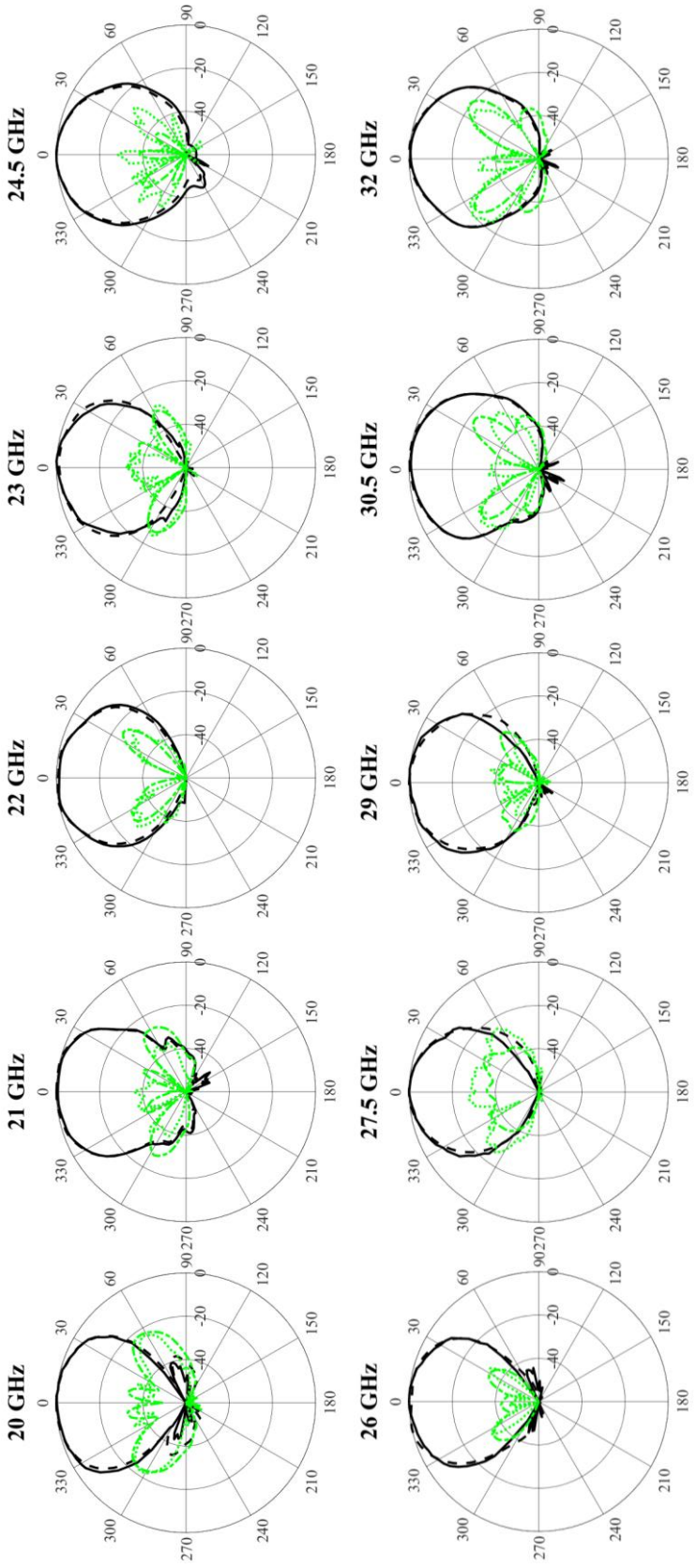

Fig. 5.14: Measured (solid and dotted lines) and simulated (dashed and dash-dotted lines) co- (black) and x-pol (green) normalized radiation patterns of the prototype at the $\phi = 0^{o}$ cut.

Table 5.1: Comparison with the published state-of-the-art-planar CP arrays

Ref.	Frequency band	Technique	Polarization	Unit-Cell Size (4 Elements)	Substrate Layers	Impedance BW (VSWR < 2:1)	3dB AR BW	1dB AR BW	3dB Gain BW
[156]	W-band	Sequential rotation	Single – CP	$1.64\lambda_0 \times 1.64\lambda_0$	3	23.8 %	24.6 %	13.0 %	27.7 %
[157]	K-band	Sequential rotation	Dual – CP	$1.04\lambda_0 \times 1.04\lambda_0$	2	45.0 %	17.0 %	4.0 %	21.7 %
[171]	K/Ka-band	Sequential rotation	Single – CP	$1.29\lambda_0 \times 1.29\lambda_0$	2	11.5 %	11.5 %	8.0 %	5.0 %
[172]	V-band	Slotted element, Sequential rotation	Single – CP	$1.21\lambda_0 \times 1.21\lambda_0$	3	> 16.5 %	11.5 %	3.0 %	10.1 %
[173]	X/Ku-band	Sequential rotation	Dual – CP	$1.24\lambda_0 \times 1.24\lambda_0$	6	21.4 %	32.0 %	4.0 %	-
[174]	K/Ka-band	Parasitic element, Matching stub, Sequential rotation	Single – CP	$1.00\lambda_0 \times 1.00\lambda_0$	2	26.8 %	> 36.0 %	> 36.0 %	>33.0 %
[175]	Ka-band	Sequential rotation	Dual – CP	$1.00\lambda_0 \times 1.00\lambda_0$	13	1.7 %	> 2.0 %	0 %	-
[176]	K/Ka-band	Parasitic element, Matching stub, Sequential rotation	Dual – CP	$1.00\lambda_0 \times 1.00\lambda_0$	6	64.2 %	> 40.0 %	-	48.7 %
[177]	K/Ka-band	Slotted element, Sequential rotation	Single – CP	$1.60\lambda_0 \times 1.60\lambda_0$	2	58.5 %	13.7 %	8.0 %	> 24.0 %
This work	K/Ka-band	Slotted element, Sequential rotation	Single – CP	$0.44\lambda_0 \times 0.44\lambda_0$	2	> 56.0 %	> 56.0 %	> 56.0 %	42.0 %

* λ_0 is the wavelength at center frequency

5.5. Conclusion

A compact, low-profile CP unit-cell is proposed and used to demonstrate a wideband array operating from 20 to 32 GHz. The design incorporates chamfered, cross-slot, and sequentially rotated four microstrip patch elements, leading to a small unit-cell size and low axial ratio over a wide bandwidth. Performances of infinite and 8×8 finite arrays with the proposed unit-unit cell show wide scanning while maintaining low-cost and scalability features across millimeter waves. A proof-of-concept prototype featuring a simple and integrated feed network is fabricated for experimental demonstration. Favorable agreement with simulations is achieved, therefore validating the proposed framework. Among other discussed benefits, the proposed compact unit-cell design can leverage active IC chip beamformers to realize phased arrays with enhanced effective radiated power per unit area.

Chapter 6

Conclusions and Future Work

6.1 Summary

This thesis delves into the theory, design, and practical implementation of wideband, highly directional antennas with fixed and steerable patterns, including unique lens antennas and a microstrip patch array. Chapter 2 discusses the high EIRP dielectric lens-corrected quad-ridge horn antenna for electronic warfare systems. Chapter 3 covers the additively manufactured modular lens-corrected horn with cavity, emphasizing its modularity and reconfigurability. Chapter 4 introduces the inhomogeneous spherical lens multi-beam array for the AODF system. A compact unit cell for a wideband circularly-polarized patch array employing sequential rotation techniques is developed in Chapter 5. The detailed explanations are as follows:

A lens-corrected QRH antenna operating from 6.5 to 20 GHz is introduced, featuring exponentially tapered ridges and a spline-based aspheric lens, which improve gain profiles over a wide bandwidth and required field of view (FOV). A

phase-matched OMT with a cone-loaded turnstile junction and custom single and double-ridge waveguides achieve dual-polarized operation and high-power handling. The fabricated antenna shows VSWR < 3, minimum gain > 21.5 dBi in the desired FOV, and high-quality radiation patterns with low side-lobe levels (SLL) and high cross-polarization discrimination (XPD) over the entire bandwidth. Compared to other designs, this antenna combines wide bandwidth, high directivity, effective isotropic radiated power, and robustness, making it suitable for commercial and defense applications.

An additively manufactured, dual-polarized, cavity-integrated, lens-corrected QRH, operating from 36 to 90 GHz, is demonstrated. The antenna integrates a phase-matched OMT with custom single- and double-ridge waveguides to achieve wide bandwidth and dual polarization. Gain and SLL improvements are achieved with 3D-printed homogeneous or perforated lenses and an absorber-lined cavity. The measured performance includes gain improvements of 8-10 dBi, radiation and beam efficiencies of >75% and 88%, respectively, and SLL < -25 dB. The VSWR across both channels is < 2:1 over 85% of the bandwidth (44-90 GHz), with port-to-port isolation > 34 dB, demonstrating the capability of additive manufacturing to produce high-quality modular and versatile antennas for wideband mmWave applications.

An additively manufactured, ring-integrated, lens-corrected multibeam array, operating from 36 to 90 GHz, is also demonstrated. To enhance gain and reduce SLLs, a 3D-printed inhomogeneous lens, and an absorber-lined ring are added. The shielding cover structure addresses EMI and EMC issues proactively. The array achieves VSWRs < 2.1:1 over the entire bandwidth, gain > 12 dBi, and SLL < -12 dB, illustrating the potential of additive manufacturing to produce cost-effective multibeam arrays for wideband mmWave applications. A framework using the

proposed antenna system with the correlation method AODF technique is also discussed for direction-finding applications.

A compact, low-profile CP unit cell is proposed and used to demonstrate a wideband array operating from 20 to 32 GHz. The design features chamfered, cross-slot, and sequentially rotated four microstrip patch elements, resulting in a small unit-cell size and low axial ratio over a wide bandwidth. Performance of both infinite and 8×8 finite arrays with the proposed unit cell shows broad scanning capabilities while maintaining cost-effectiveness and scalability across millimeter waves. A proof-of-concept prototype with a simple and integrated feed network is fabricated, showing favorable agreement with simulations and validating the proposed framework. The compact unit-cell design can leverage active IC chip beamformers to realize phased arrays with enhanced effective radiated power per unit area.

6.2 Contributions

The contributions of this dissertation are summarized as follows:

Chapter 2

- Introduces a lens-corrected QRHA and demonstrates dual-polarized operation from 7 to 20 GHz, featuring high minimum gain in the FOV, high power handling capability, symmetric radiation patterns, and acceptable SLL.

- A dielectric lens enhances performance by reducing quadratic phase error in the aperture, with lens permittivity and shape being critical factors.

- QRH and lens are constructed using EDM and CNC, respectively.

Chapter 3

- Designs dual-polarized directional antennas with lenses for 3D printing, operating over 36-90 GHz while maintaining high aperture efficiency (> 70%) and low SLL (< -15 dB).

- A single QRH performs well without the lens, exhibiting lower directivity, smaller SLLs, and wider HPBW.

- Performance with 3D-printed PP, LLDPE, and perforated lenses are similar, validating both design and realization approaches.

- Cavity and absorber can be employed to improve SLLs and beam efficiency.

Chapter 4

- Demonstrates an additively manufactured, ring-integrated, lens-corrected multibeam array with gain improvement, low SLLs, crossover levels, low fabrication cost, and immunity to EMI and EMC.

- Explores the feasibility of correlation-based amplitude-only direction finding (AODF) systems.

Chapter 5

- Proposes a strongly coupled circularly polarized K/Ka-band phased array configuration.

- Demonstrates wide bandwidth and scanning angle, good circular polarization, high radiation and aperture efficiencies, while maintaining

low-cost fabrication, compact size, and scalability across millimeter wave bands.

- The proposed array topology and concept are promising candidates for many applications.

6.3 Future Work

The work performed in this thesis could be expanded in many directions including:

- Investigating the elimination of adapter influence in Chapters 2 and 3 using the time gating technique, which presents a compelling avenue for future research.

- Exploring methods to reduce SLL without significantly increasing the volume of modular horn antenna structures..

- Developing a dual-polarized multi-beam array.

- Extending the field-of-view for direction-finding applications to achieve hemispherical (180°) coverage, thereby increasing the detection range of incoming signals.

- Designing an active phased array based on the compact unit-cell structure.

Bibliography

[1] S. B. Cohn, "Properties of ridged waveguide," Proceedings of the IRE, vol. 35, Aug. 1947.

[2] N. Marcuvitz, Ed., Waveguide Handbook, ser. MIT Radiation Laboratory. Lexington, MA: Boston Technical, 1964, vol. 10.

[3] S. Hopfer, "The design of ridged waveguides," IRE Trans. Microw. Theory Tech., vol. 3, Oct. 1955.

[4] J. P. Montgomery, "On the complete eigenvalue solution of ridged waveguide," IEEE Trans. Microw. Theory Tech., vol. MTT-19, Jun. 1971.

[5] M. H. Chen, G. N. Tsandoulas, and F. G. Willwerth, "Modal characteristics of quadruple-ridged circular and square waveguides (short papers)," IEEE Trans. Microw. Theory Tech., vol. 22, Aug. 1974.

[6] W. Sun and C. A. Balanis, "MFIE analysis and design of ridged waveguides," IEEE Trans. Microw. Theory Tech., vol. 41, pp. 1965–1971, Nov. 1993.

[7] W. Sun and C. A. Balanis, "Analysis and design of quadruple-ridged waveguides," IEEE Trans. Microw. Theory Tech., vol. 42, pp. 2201–2207, Dec. 1994.

[8] G. M. Coutts, "Octave bandwidth orthomode transducers for the expanded very large array," IEEE Trans. Antennas Propag., vol. 59, no. 6, pp. 1910–1917, Jun. 2011.

[9] C. Granet and G. L. James, "The quad-ridged omt: The effects of fin shape on performance," CSIRO, Australia, Tech. Rep. RPP 3879, Oct. 1996.

[10] R. J. Bauerle, R. Schrimpf, E. Gyorko, and J. Henderson, "The use of a dielectric lens to improve the efficiency of a dual-polarized quad-ridge horn from 5 to 15 GHz," IEEE Trans. Antennas Propag., vol. 57, no. 6, pp. 1822–1825, Jun. 2009.

[11] S. A. Soroka, "A physically compact quad ridge horn design," in 1986 Antennas and Propagation Society International Symposium, Jun. 1986.

[12] M. Gilbert, K. Higgins, and L. Romero, "Quad-ridge horn utilizing resistive films to reduce sidelobes," in 2007 IEEE Antennas and Propagation Society International Symposium, Jun. 2007.

[13] Advanced Optics, Pewaukee, WI, USA, 2015, [Online]. Available: https://www.advancedoptics.com/optical-lenses-tech.html

[14] K. Iizuka, Engineering Optics, 4th Edition. Cham, Switzerland, Springer, 2019.

[15] G. Peeler and H. Coleman, "Microwave stepped-index luneberg lenses," IRE Transactions on Antennas and Propagation, vol. 6, no. 2, pp. 202–207, 1958.

[16] B. Fuchs, L. Le Coq, O. Lafond, S. Rondineau, and M. Himdi, "Design optimization of multishell luneburg lenses," IEEE Trans. Antennas Propag., vol. 55, no. 2, pp. 283–289, 2007.

[17] K. F. Braun, "Electrical oscillations and wireless telegraphy," Nobel Price Lecture, Dec. 1909.

[18] C. A. Balanis, Antenna Theory: Analysis and Design, 4th Edition, New York, NY, USA: Wiley, 2016.

[19] Z. Mu, J. Ma, Y. Zhao, S. Liang, and C. Chen, "Wideband, low radar cross section circu larly polarized array antenna based on metasurface and sequential phase feed," International Journal of RF and Microwave Computer-Aided Engineering, pp. 1–9, apr 2021.

[20] B. A. Munk, Finite Antenna Arrays and FSS. Hoboken, NJ, USA: Wiley, 2003.

[21] M. Jones and J. Rawnick, "A New Approach to Broadband Array Design using Tightly Coupled Elements," MILCOM 2007-IEEE Military Communications Conference, Orlando, FL, USA, 2007, pp. 1-7.

[22] L. Zhang, S. Gao, Q. Luo, W. Li, Y. He, and Q. Li, "A wideband circularly polarized tightly coupled array," IEEE Trans. Antennas Propag., vol. 66, no. 11, pp. 6382–6387, Nov. 2018.

[23] I. Tzanidis, K. Sertel, and J. L. Volakis, "Interwoven spiral array (ISPA) with a 10:1 bandwidth on a ground plane," IEEE Antennas Wireless Propag. Lett., vol. 10, pp. 115–118, Mar. 2011.

[24] T. -L. Zhang, L. Chen, S. M. Moghaddam, A. U. Zaman and J. Yang, "Millimeter-Wave Ultrawideband Circularly Polarized Planar Array Antenna Using Bold-C Spiral Elements With Concept of Tightly Coupled Array," IEEE Trans. Antennas Propag., vol. 69, no. 4, pp. 2013-2022, April 2021.

[25] Ansys Inc., "Ansys HFSS," 2021 R2.

[26] Altair Engineering, "Feko," 2020.

[27] Dassault Syst`emes Simulia, "CST Studio Suite," 2021.

[28] MathWorks, "MATLAB," 2021b.

[29] Keysight Technologies, "Advanced Design System," 2020.

[30] C. Wang, E. Li, Y. Zhang and G. Guo, "Ridged horn antenna with adjustable metallic grid sidewalls and cross-shaped back cavity," IEEE Ant. Wireless Propag. Lett., vol. 15, pp. 1221-1225, 2016.

[31] R. E. Collin and F. J. Zucker, Antenna Theory. New York, NY, USA: McGraw-Hill, 1969.

[32] H. C. Moy-Li, D. Sánchez-Escuderos, E. Antonino-Daviu and M. Ferrando-Bataller, "Low-profile radially corrugated horn antenna," IEEE Ant. Wireless Propag. Lett., vol. 16, pp. 3180-3183, 2017.

[33] J.-C.-S. Chieh, B. Dick, S. Loui, and J. D. Rockway, "Development of a ku-band corrugated conical horn using 3-D print technology," IEEE Ant. Wireless Propag. Lett., vol. 13, pp. 201–204, Jan. 2014.

[34] F. Yang, D. Li, B. Du, Y. WU and Y. He, "Development of a 6-18GHz Quad-Ridged Flared Horn," 2018 IEEE Asia-Pacific Conference on Antennas and Propagation (APCAP), Auckland, New Zealand, Aug. 2018, pp. 108-109.

[35] T. S. Beukman, P. Meyer, M. V. Ivashina and R. Maaskant, "Modal-based design of a wideband quadruple-ridged flared horn antenna," IEEE Trans. Antennas Propag., vol. 64, no. 5, pp. 1615-1626, May 2016.

[36] E. Lier, D. H. Werner, C. P. Scarborough, Q. Wu, and J. A. Bossard, "An octave-bandwidth negligible-loss radiofrequency metamaterial," Nature Mater., vol. 10, pp. 216-222, 2011.

[37] K. Liu, Y. Ge and C. Lin, "A compact wideband high-gain metasurface-lens-corrected conical horn antenna," IEEE Ant. Wireless Propag. Lett., vol. 18, no. 3, pp. 457-461, Mar. 2019.

[38] F. Ahmed, M. U. Afzal, T. Hayat, K. P. Esselle and D. N. Thalakotuna, "Self-sustained rigid fully metallic metasurfaces to enhance gain of shortened horn antennas," IEEE Access, vol. 10, pp. 79644-79654, 2022.

[39] Y. He, N. Ding, L. Zhang, W. Zhang and B. Du, "Short-length and high-aperture-efficiency horn antenna using low-loss bulk anisotropic metamaterial," IEEE Ant. Wireless Propag. Lett., vol. 14, pp. 1642-1645, 2015.

[40] A. Paraskevopoulos, I. Gashi, M. Albani and S. Maci, "High aperture efficiency 3D-printed radial GRIN lens," 2022 16th European Conference on Antennas and Propagation (EuCAP), pp. 1-5, 2022.

[41] K. V. Hoel, M. Ignatenko, S. Kristoffersen, E. Lier and D. S. Filipovic, "3-D printed monolithic GRIN dielectric-loaded double-ridged horn antennas," IEEE Trans. Antennas Propag., vol. 68, no. 1, pp. 533-539, Jan. 2020.

[42] I. Goode and C. E. Saavedra, "3D printed linearly polarized X-band conical horn antenna and lens," IEEE Open Journal of Antennas Propag., vol.3, pp.549-556, 2022.

[43] W. -S. Yu, L. Peng, Y. -F. Liu, Q. -X. Zhao, X. Jiang and S. -M. Li, "An ultrawideband and high-aperture-efficiency all-dielectric lens antenna," IEEE Ant. Wireless Propag. Lett., vol. 20, no. 12, pp. 2442-2446, Dec. 2021.

[44] M. K. T. Al-Nuaimi, W. Hong and Y. Zhang, "Design of high-directivity compact-size conical horn lens antenna," IEEE Ant. Wireless Propag. Lett., vol. 13, pp. 467-470, 2014

[45] A. Rolland, A. V. Boriskin, C. Person, C. Quendo, L. Le Coq and R. Sauleau, "Lens-corrected axis-symmetrical shaped horn antenna in metallized foam with improved bandwidth," IEEE Ant. Wireless Propag. Lett., vol. 11, pp. 57-60, 2012.

[46] D.-C. Son, M. A. Elmansouri, L. Boskovic and D. S. Filipovic, "High EIRP dielectric lens loaded quad-ridge horn antenna," 2022 IEEE International Symposum on Antennas and Propagation and USNC-URSI Radio Science Meeting (AP-S/URSI), 2022.

[47] A. H. Akgiray, "New technologies driving decade-bandwidth radio astronomy: quad-ridged flared horn & compound-semiconductor LNAs," Ph.D. dissertation, Caltech, Pasadena, CA, USA, Apr. 2013.

[48] A. D. Olver, P.J.B. Clarricoats, A.A. Kishk, and L. Shafai, Microwave Horns and Feeds, New York, NY, USA: The Institution of Engineering and Technology, 1994.

[49] G. Godi, R. Sauleau, L. Le Coq, and D. Thouroude, "Design and optimization of three-dimensional integrated lens antennas with genetic algorithm," IEEE Trans. Antennas Propag., vol. 55, no. 3, pp. 770–775, Mar. 2007.

[50] J. A. Ruiz-Cruz, J. R. Montejo-Garai, C. A. Leal-Sevillano and J. M. Rebollar, "Orthomode transducers with folded double-symmetry junctions for broadband and compact antenna feeds," IEEE Trans. Antennas Propag., vol. 66, no. 3, pp. 1160-1168, March 2018.

[51] J. Shen and D. S. Ricketts, "Compact W-band "swan neck" turnstile junction orthomode transducer implemented by 3-D printing," IEEE Trans. Microw. Theory Techn., vol. 68, no. 8, pp. 3408-3417, Aug. 2020.

[52] Southwest Microwave Inc, Tempe, AZ, USA, [Online]. Available: https://mpd.southwestmicrowave.com/wp-content/uploads/2020/09/ Southwest-Microwave-Power-Rating.pdf

[53] Pasternack Enterprises Inc, Irvine, CA, USA, [Online]. Available: https://www.pasternack.com/wrd650-ug-square-flange-to-type-n-female-waveguide-coax-adapter-18ghz-pewca1111-p.aspx

[54] D. Henke and S. Claude, “Minimizing RF performance spikes in a cryogenic orthomode transducer,” IEEE Trans. Micro. Theory Techn., vol. 52, no. 4, pp. 840–850, Apr. 2014.

[55] N. Jastram, M. A. Altarifi, L. Boskovic and D. S. Filipovic, “On the split-block realization of millimeter-wave ridge waveguide components,” IEEE Microw. Wireless Compon. Lett., vol. 28, no. 4, pp. 296-298, Apr. 2018.

[56] Polymershapes, Boston, MA, USA, [Online]. Available: https://www.polymershapes.com/product/high-density-polyethylene-hdpe/.

[57] J. A. Ruiz-Cruz, J. R. Montejo-Garai, C. A. Leal-Sevillano and J. M. Rebollar, "Orthomode transducers with folded double-symmetry junctions for broadband and compact antenna feeds," IEEE Trans. Antennas Propag., vol. 66, no. 3, pp. 1160-1168, March 2018.

[58] General tolerances – Part 1: Tolerances for linear and angular dimensions without individual tolerance indications, ISO 2768-1, 1989. [Online]. Available: https://www.iso.org/obp/ui/#iso:std:iso:2768:-1:ed-1:v1:en.

[59] S. -f. Wang, Y. -z. Xie, M. -X. Gao, Y. -X. Qiu and Y. A. Andreev, “Optimizing high-power ultra-wideband combined antennas for maximum radiation within finite aperture area,” IEEE Trans. Antennas Propag., vol. 67, no. 2, pp. 834-842, Feb. 2019.

[60] L3Harris Technologies, Melbourne, FL, USA, [Online]. Available: https://www.l3harris.com/all-capabilities/ca-1177-3226a-urc-high-power-omnidirectional-dipole

[61] X. Zhang, Z. Wang, C. Pan, X. Ba and Y. Wang, “Dual-Polarized Inverted Quad-Ridged Flared Horn Antenna With One-Decade Bandwidth for OTA Testing,” IEEE Ant. Wireless Propag. Lett., vol. 21, no. 6, pp. 1233-1237, June 2022.

[62] A. R. Pitol, C. Müller, M. S. V. Arigony, C. M. Barth and L. Gerhardt, “Compact Dual-Polarization Quad-Ridge Horn,” IEEE Ant. Wireless Propag. Lett., vol. 22, no. 12, pp. 3142-3146, Dec. 2023.

[63] O. B. Jacobs, J. W. Odendaal, and J. Joubert, "Quad-ridge horn antenna with elliptically shaped sidewalls," IEEE Trans. Antennas Propag., vol. 61, no. 6, pp. 2948–2955, Jun. 2013.

[64] T. S. Beukman, P. Meyer, M. V. Ivashina, and R. Maaskant, "Modal based design of a wideband quadruple-ridged flared horn antenna," IEEE Trans. Antennas Propag., vol. 64, no. 5, pp. 1615–1626, May 2016.

[65] A. Akgiray, S. Weinreb, W. A. Imbriale, and C. Beaudoin, "Circular quadruple-ridged flared horn achieving near-constant beamwidth over multioctave bandwidth: Design and measurements," IEEE Trans. Antennas Propag., vol. 61, no. 3, pp. 1099–1108, Mar. 2013.

[66] E. Lier, and P. S. Kildal, "Soft and hard horn antennas," IEEE Trans. Antennas Propag., vol. 36, no. 8, pp, 1152-1157, Aug. 1988.

[67] J. Teniente, R. Gonzalo and C. del-Rio, "Innovative high-gain corrugated horn antenna combining horizontal and vertical corrugations," IEEE Ant. Wireless Propag. Lett., vol. 5, pp. 380-383, 2006.

[68] U. Beaskoetxea and M. Beruete, "High aperture efficiency wide corrugations Bull's-Eye antenna working at 60 GHz," IEEE Trans. Antennas Propag., vol. 65, no. 6, pp. 3226-3230, June 2017.

[69] J. W. Odendaal and C. W. I. Pistorius, "E-plane analysis of a modified horn antenna with suppressed far-out sidelobe level," IEEE Trans. Antennas Propag., vol. 40, no. 6, pp. 620-627, June 1992.

[70] W. Burnside, C. Chuang, "An aperture-matched horn design," IEEE Trans. Antennas Propag., vol. 30, no.4, pp. 790- 796, July 1982.

[71] K. K. Chan and S. Rao, "An accurate model for rectangular trifurcated horns," IEEE Trans. Antennas Propag., vol. 55, no. 12, pp. 1444-1445, 2008.

[72] T. Hongnara, K. Schraml, S. Chaimool, P. Akkaraekthalin and D. Heberling, "Side-lobe reduction of horn antenna using circular patch mushroom-like EBG structure," 2016 German Microwave Conference (GeMiC), 2016, pp. 413-416.

[73] D. Shamvedi, C. Danilenkoff, S. Karam, P. O'Leary and R. Raghavendra, "3D printed periodic structures in a horn antenna for side-lobe reduction using direct

metal laser sintering," Loughborough Antennas & Propagation Conference (LAPC 2017), 2017, pp. 1-4.

[74] H. Balegh, B. A. Arand, and L. Yousefi, "Side lobe level reduction in horn antennas using graphene," 24th Iranian Conf. Electr. Eng. (ICEE), May 2016, pp. 1937–1941.

[75] I. Gibson, D. Rosen, and B. Stucker, Additive Manufacturing Technologies: Rapid Prototyping to Direct Digital Manufacturing. Boston, MA, USA: Springer, 2010.

[76] D.-C. Son, L. Boskovic, M. A. Elmansouri and D. S. Filipovic, "Wideband dual-polarized 3D printed quad-ridge horn for mmWave applications," 2023 IEEE International Symposium on Antennas and Propagation and USNC-URSI Radio Science Meeting (USNC-URSI), Portland, OR, USA, 2023, pp. 1097-1098.

[77] Advanced Optics, Pewaukee, WI, USA, 2015, [Online]. Available: https://www.advancedoptics.com/optical-lenses-tech.html

[78] K. Iizuka, Engineering Optics, 4th Edition. Cham, Switzerland, Springer, 2019.

[79] TOPAS COC Polymers, Farmington Hills, MI, USA, 2019. [Online]. Available: https://topas.com/low-dielectric-constant-plastic-materials-low-permittivity-plastics-topas.

[80] M. Mrnka and Z. Raida, "An effective permittivity tensor of cylindrically perforated dielectrics," IEEE Ant. Wireless Propag. Lett., vol. 17, no. 1, pp. 66-69, Jan. 2018.

[81] Arkema Inc., Boulder, CO, USA, 2023, [Online]. Available:https://sartomer.arkema.com/en/webzine/post/sartomer/Expertise%20Articles/dielectric-resins/.

[82] Choy, Tuck C., Effective Medium Theory: Principles and Applications, 2nd Edition, Oxford, UK: Oxford University Press, 2015

[83] Z. Zhao, Z. Wang, J. R. Kelly and S. Gao, "Balanced Feed Low Cross-Polarization Quad-Ridged horn antenna with center cross fusiform loaded," IEEE Trans. Antennas Propag., vol. 69, no. 9, pp. 6004-6009, Sept. 2021.

[84] X. Zhang, Z. Wang, C. Pan, X. Ba and Y. Wang, “Dual-Polarized inverted quad-ridged flared horn antenna with one-decade bandwidth for OTA testing,” IEEE Ant. Wireless Propag. Lett., vol. 21, no. 6, pp. 1233-1237, June 2022.

[85] Yu-Lin-Shih and T. -W. Chiou, “Quad-ridged horn antenna with L shaped-slot fed by microstrip line,” 2014 International Symposium on Antennas and Propagation Conference Proceedings, Kaohsiung, Taiwan, 2014, pp. 243-244.

[86] A. R. Pitol, C. Müller, M. S. V. Arigony, C. M. Barth and L. Gerhardt, “Compact dual-polarization quad-ridge horn,” IEEE Ant. Wireless Propag. Lett., vol. 22, no. 12, pp. 3142-3146, Dec. 2023.

[87] P. V. Prasannakumar, M. A. Elmansouri and D. S. Filipovic, "Wideband decoupling techniques for dual-polarized bi-Static simultaneous transmit and receive antenna subsystem," IEEE Trans. Antennas Propag., vol. 65, no. 10, pp. 4991-5001, Oct. 2017.

[88] D. -C. Son, M. A. Elmansouri, L. Boskovic and D. S. Filipovic, “High EIRP dielectric lens loaded quad-ridge horn antenna,” 2022 IEEE International Symposium on Antennas and Propagation and USNC-URSI Radio Science Meeting (AP-S/URSI), Denver, CO, USA, 2022, pp. 589-590.

[89] D. Henke, N. Kelly, K. Marshall, I. Wevers and L. B. G. Knee, “A turnstile quad-ridge orthomode transducer (OMT) for octave-bandwidth receiver front-ends (24–51 GHz),” IEEE Trans. Microw. Theory Techn., vol. 71, no. 11, pp. 4906-4921, Nov. 2023.

[90] C. A. M. Hernández, L. B. Boskovic, M. A. Elmansouri, M. Ignatenko and D. S. Filipovic, “Fixed and steerable beam dual-polarized lens antenna with high Tx to Rx isolation,” IEEE Trans. Antennas Propag., vol. 69, no. 11, pp. 7213-7221, Nov. 2021.

[91] A. Navarrini and R. L. Plambeck, “A turnstile junction waveguide orthomode transducer,” IEEE Trans. Microw. Theory Techn., vol. 54, no. 1, pp. 272–277, Jan. 2006.

[92] A. R. Kerr. (Jul. 2001). Elements of E-Plane Split Block Waveguide Circuits, ALMA Memo 38, Jul. 2001. [Online]. Available: http://legacy.nrao.edu/alma/memos/html-memos/abstracts/abs381.html

[93] Formlabs, Somerville, MA, USA, 2019, [Online]. Available: https://formlabs.com/3d-printers/form-3/.

[94] B. S. Cross and D. S. Filipovic, "Millimeter-Wave Ridged Horn Performance in Lieu of Stereolithography Required Modifications," 2022 IEEE International Symposium on Antennas and Propagation and USNC-URSI Radio Science Meeting (AP-S/URSI), Denver, CO, USA, 2022, pp. 1598-1599.

[95] Raise 3D, Irvine, CA, USA, 2019, [Online]. Available: https://www.raise3d.com/products/pro2-3d-printer/.

[96] Phrozen Technology, Hsinchu City, Taiwan, 2019, [Online]. Available: https://phrozen3d.com/products/sonic-mini-8k.

[97] Laird Performance Materials, Wilmington, DE, USA, 2021, [Online]. Available: https://www.laird.com/sites/default/files/2021-02/MFS-DS-COOLZORB%20600%20101019.pdf.

[98] K. Lomakin, J. Schür and G. Gold, "Design optimization of pyramidal horn antennas for 3D printing in the mm-Wave range," 2022 16th European Conference on Antennas and Propagation (EuCAP), Madrid, Spain, 2022, pp. 1-4.

[99] I. Agnihotri and S. K. Sharma, "Design of a 3D metal printed axial corrugated horn antenna covering full Ka-band," IEEE Ant. Wireless Propag. Lett., vol. 19, no. 4, pp. 522-526, April 2020.

[100] N. Lee, C. Im, S. Park and H. Choo, "Design of a metal 3D printed double-ridged horn antenna with stable gain and symmetric radiation pattern Over a wide frequency range," IEEE Access, vol. 11, pp. 100565-100572, 2023.

[101] Y. Cheng and Y. Dong, "High-Gain all-metal 3-D printed lens–horn antenna for millimeter-wave applications," IEEE Ant. Wireless Propag. Lett., vol. 22, no. 2, pp. 308-312, Feb. 2023.

[102] I. Goode and C. E. Saavedra, "3-D Printed Dually Symmetric Orthomode Transducer and Horn Antenna at X-Band," IEEE Open Journal of Antennas and Propagation, vol. 4, pp. 383-391, 2023.

[103] I. Goode and C. E. Saavedra, "3D Printed Linearly Polarized X-Band Conical Horn Antenna and Lens," IEEE Open Journal of Antennas and Propagation, vol. 3, pp. 549-556, 2022.

[104] S. Zhang, D. Cadman and J. Y. C. Vardaxoglou, "Additively manufactured profiled conical horn antenna with dielectric loading," IEEE Ant. Wireless Propag. Lett., vol. 17, no. 11, pp. 2128-2132, Nov. 2018.

[105] F. Oktafiani, E. Y. Hamid and A. Munir, "Wideband dual-polarized 3D printed quad-ridged horn antenna," IEEE Access, vol. 10, pp. 8036-8048, 2022.

[106] K. V. Hoel, M. Ignatenko, S. Kristoffersen, E. Lier and D. S. Filipovic, "3-D printed monolithic GRIN dielectric-loaded double-ridged horn antennas," IEEE Trans. Antennas Propag., vol. 68, no. 1, pp. 533-539, Jan. 2020.

[107] R. L. Haupt and Y. Rahmat-Samii, "Antenna array developments: A perspective on the past, present and future," IEEE Antennas Propag. Mag., vol. 57, no. 1, pp. 86–96, Feb. 2015.

[108] Shun-Ping Chen, Heinz Schmiedel, RF Antenna Beam Forming: Focusing and Steering in Near and Far Field. Germany: Springer International Publishing, 2023.

[109] D. Parker and D. C. Zimmermann, "Phased arrays—Part I: Theory and architectures," IEEE Trans. Microw. Theory Techn., vol. 50, no. 3, pp. 688– 698, Mar. 2002

[110] W. Hong et al., "Multibeam antenna technologies for 5G wireless communications," IEEE Trans. Antennas Propag., vol. 65, no. 12, pp. 6231–6249, Dec. 2017.

[111] K. Trzebiatowski, M. Rzymowski, L. Kulas, and K. Nyka, "Simple 60 GHz switched beam antenna for 5G millimeter-wave applications," IEEE Ant. Wireless Propag. Lett., vol. 20, no. 1, pp. 38–42, Jan. 2021.

[112] M. Imbert, A. Papió, F. De Flaviis, L. Jofre, and J. Romeu, "Design and performance evaluation of a dielectric flat lens antenna for millimeter-wave applications," IEEE Ant. Wireless Propag. Lett., vol. 14, pp. 342–345, 2015.

[113] M. Imbert, J. Romeu, M. Baquero-Escudero, M. Martinez-Ingles, J. Molina-Garcia-Pardo, and L. Jofre, "Assessment of LTCC-based dielectric flat lens antennas and switched-beam arrays for future 5G millimeter-wave communication systems," IEEE Trans. Antennas Propag., vol. 65, no. 12, pp. 6453–6473, Dec. 2017.

[114] E. Garcia-Marin, D. S. Filipovic, J. L. Masa-Campos, and P. SanchezOlivares, "Ka-band multi-beam planar lens antenna for 5G applications," in Proc. 14th Eur. Conf. Antennas Propag., 2020, pp. 1–5.

[115] X. Wu, G. V. Eleftheriades, and T. E. van Deventer-Perkins, "Design and characterization of single- and multiple-beam mm-wave circularly polarized substrate lens antennas for wireless communications," IEEE Trans. Microw. Theory Techn., vol. 49, no. 3, pp. 431–441, Mar. 2001.

[116] J. Ala-Laurinaho et al., "2-D beam-steerable integrated lens antenna system for 5G E-band access and backhaul," IEEE Trans. Microw. Theory Techn., vol. 64, no. 7, pp. 2244–2255, Jul. 2016.

[117] B. Schoenlinner, X.Wu, J. P. Ebling, G. V. Eleftheriades, and G. M. Rebeiz, "Wide-scan spherical-lens antennas for automotive radars," IEEE Trans. Microw. Theory Techn., vol. 50, no. 9, pp. 2166–2175, Sep. 2002.

[118] P.-Y. Feng, S.-W. Qu, and S. Yang, "Defocused cylindrical Luneburg lens antennas with phased array antenna feed," IEEE Trans. Antennas Propag., vol. 67, no. 9, pp. 6008–6016, Sep. 2019.

[119] A. Artemenko, A. Maltsev, A. Mozharovskiy, A. Sevastyanov, V. Ssorin, and R. Maslennikov, "Millimeter-wave electronically steerable integrated lens antennas for WLAN/WPAN applications," IEEE Trans. Antennas Propag., vol. 61, no. 4, pp. 1665–1671, Apr. 2013.

[120] A. Artemenko, A. Mozharovskiy, A. Maltsev, R. Maslennikov, A. Sevastyanov, and V. Ssorin, "Experimental characterization of E-band twodimensional

electronically beam-steerable integrated lens antennas," IEEE Ant. Wireless Propag. Lett., vol. 12, pp. 1188–1191, 2013.

[121] C. Ballesteros, M. Maestre, M. C. Santos, J. Romeu, and L. Jofre, "A 3D printed lens antenna for 5G applications," in Proc. IEEE Int. Symp. Antennas Propag. USNC-URSI Radio Sci. Meeting, 2019, pp. 1985–1986.

[122] I. Gibson, D. Rosen, and B. Stucker, Additive Manufacturing Technologies: Rapid Prototyping to Direct Digital Manufacturing. Boston, MA, USA: Springer, 2010.

[123] S. Hopfer, "The Design of Ridged Waveguides," IRE Transactions on Microwave Theory and Techniques, vol. 3, no. 5, pp. 20-29, Oct. 1955.

[124] T. N. Anderson, "Double-Ridge Waveguide for commercial Airlines Weather Radar Installation," IRE Transactions on Microwave Theory and Techniques, vol. 3, no. 4, pp. 2-9, July 1955.

[125] Y. Y. Hu, "A method of determining phase centers and its application to electromagnetic horns," J. Franklin Inst., vol. 271, pp. 31–39, Jan. 1961.

[126] B. Fuchs, L. Le Coq, O. Lafond, S. Rondineau and M. Himdi, "Design Optimization of Multishell Luneburg Lenses," IEEE Trans. Antennas Propag., vol. 55, no. 2, pp. 283-289, Feb. 2007

[127] D.-C. Son, L. Boskovic, M. A. Elmansouri and D. S. Filipovic, "36-90 GHz Modular Lens-Corrected Dual-Polarized Horn with Cavity," IEEE Trans. Antennas Propag., 2024. (Early Access)

[128] Arkema Inc., Boulder, CO, USA, 2023, [Online]. Available:https://sartomer.arkema.com/en/webzine/post/sartomer/Expertise%20Articles/dielectric-resins/.

[129] K. V. Hoel, M. Ignatenko, S. Kristoffersen, E. Lier and D. S. Filipovic, "3-D printed monolithic GRIN dielectric-loaded double-ridged horn antennas," IEEE Trans. Antennas Propag., vol. 68, no. 1, pp. 533-539, Jan. 2020.

[130] B. S. Cross and D. S. Filipovic, "Millimeter-Wave Ridged Horn Performance in Lieu of Stereolithography Required Modifications," 2022 IEEE International

Symposium on Antennas and Propagation and USNC-URSI Radio Science Meeting (AP-S/URSI), Denver, CO, USA, 2022, pp. 1598-1599.

[131] B. Nie, H. Lu, T. Skaik, Y. Liu and Y. Wang, "A 3D-Printed Subterahertz Metallic Surface-Wave Luneburg Lens Multibeam Antenna," IEEE Trans. Terahertz Sci. Technol., vol. 13, no. 3, pp. 297-301, May 2023.

[132] W. Yu, X. Wang, H. Lu, H. Liu and C. Jin, "3D-Printed All-Metal Terahertz Multibeam Lens Antenna Based on Photonic Crystal," IEEE Access, vol. 11, pp. 41609-41617, 2023.

[133] K. Liu, C. Zhao, S. -W. Qu, Y. Chen, J. Hu and S. Yang, "A 3-D-Printed Multibeam Spherical Lens Antenna With Ultrawide-Angle Coverage," IEEE Ant. Wireless Propag. Lett., vol. 20, no. 3, pp. 411-415, March 2021.

[134] Y. Li, L. Ge, M. Chen, Z. Zhang, Z. Li, and J. Wang, "Multibeam 3-D-printed Luneburg lens fed by magnetoelectric dipole antennas for millimeter-wave MIMO applications," IEEE Trans. Antennas Propag., vol. 67, no. 5, pp. 2923–2933, May 2019.

[135] B. Zhang et al., "A Two-Dimensional Multibeam Lens Antenna for Hydrologic Radar Application," IEEE Ant. Wireless Propag. Lett., vol. 18, no. 12, pp. 2488-2492, Dec. 2019.

[136] Y. Bi, Y. Li and J. Wang, "3D-Printed Multi-Beam Planar Dual-reflector Antenna for 5G Millimeter-Wave Applications," 2019 IEEE Asia-Pacific Microwave Conference (APMC), Singapore, 2019, pp. 917-919.

[137] W. Shao and Q. Chen, "Performance analysis of an all-dielectric planar Mikaelian lens antenna for 1-D beam-steering application," Opt. Exp., vol. 29, no. 18, p. 29202, Aug. 2021.

[138] Y. Cao and S. Yan, "A low-profile high-gain multi-beam antenna based on 3D-printed cylindrical Luneburg lens," Microw. Opt. Technol. Lett., vol. 63, no. 7, pp. 1965–1971, Jul. 2021.

[139] S. Gao, Q. Luo, and F. Zhu, Circularly Polarized Antennas. Hoboken, NJ, USA: Wiley, 2013.

[140] B. J. Falkner, H. Zhou, A. Mehta, T. Arampatzis, D. Mirshekar-Syahkal and H. Nakano, "A circularly polarized low-cost flat panel antenna array with a high impedance surface meta-substrate for satellite on-the-move medical IoT applications," IEEE Trans. Antennas Propag., vol. 69, no. 9,pp. 6076-6081, Sept. 2021.

[141] J. Li, Y. Hu, L. Xiang, W. Kong and W. Hong, "Broadband circularly polarized magnetoelectric dipole antenna and array for K-band and Ka-band satellite communications," IEEE Trans. Antennas Propag., vol. 70, no. 7, pp. 5907-5912, July 2022.

[142] H. Kashihara, J. T. S. Sumantyo, Y. Izumi, K. Ito, S. Gao and K. Namba, "X-Band microstrip array antenna for UAV onboard full circularly polarized synthetic aperture radar," IEEE Trans. Antennas Propag., vol. 71, no. 2, pp. 1943-1948, Feb. 2023.

[143] R. Garg, P. Bhartia, I. Bahl, and A. Ittipiboon. Microstrip Antenna Design Handbook. Boston, MA: Artech House, 2000.

[144] C. A. Balanis, Antenna Theory: Analysis and Design, 4th Edition, New York, NY, USA: Wiley, 2016.

[145] H. Zhou, N. W. Kefauver and D. S. Filipovic, "A wideband patch antenna with dual-cylindrical probe feed," IEEE Ant. Wireless Propag. Lett., vol. 8, pp. 1321-1324, 2009.

[146] M. Li, S. Tian, M. -C. Tang and L. Zhu, "A compact low-profile hybrid-mode patch antenna with intrinsically combined self-decoupling and filtering properties," IEEE Trans. Antennas Propag., vol. 70, no. 2, pp. 1511-1516, Feb. 2022.

[147] H. Xu, J. Zhou, K. Zhou, Q. Wu, Z. Yu, and W. Hong, "Planar wideband circularly polarized cavity-backed stacked patch antenna array for millimeter-wave applications," IEEE Trans. Antennas Propag., vol. 66, no. 10, pp. 5170–5179, Oct. 2018.

[148] J. Zeng, Z. Zhang, F. H. Lin and F. Guan, "Penta-Mode ultrawideband circularly polarized stacked patch antennas using characteristic mode analysis," IEEE Trans. Antennas Propag., vol. 70, no. 10, pp. 9051-9060, Oct. 2022.

[149] Q. Wu, J. Hirokawa, J. Yin, C. Yu, H. Wang, and W. Hong, "Millimeterwave planar broadband circularly polarized antenna array using stacked curl elements," IEEE Trans. Antennas Propag., vol. 65, no. 12, pp. 7052–7062, Dec. 2017.

[150] J. Zeng, X. Liang, L. He, F. Guan, F. H. Lin, and J. Zi, "Singlefed triple-mode wideband circularly polarized microstrip antennas using characteristic mode analysis," IEEE Trans. Antennas Propag., vol. 70, no. 2, pp. 846–855, Feb. 2022.

[151] N.-W. Liu, L. Zhu, Z.-X. Liu, G. Fu, and Y. Liu, "Design approach of a single circularly polarized patch antenna with enhanced AR-bandwidth under triple-mode resonance," IEEE Trans. Antennas Propag., vol. 68, no. 8, pp. 5827–5834, Aug. 2020.

[152] M. Ameen and R. K. Chaudhary, "Metamaterial-based wideband circularly polarised antenna with rotated V-shaped metasurface for small satellite applications," Electron. Lett., vol. 55, no. 7, pp. 365–366, Apr. 2019.

[153] Y. Juan, W. Yang and W. Che, "Miniaturized low-profile circularly polarized metasurface antenna using capacitive loading," IEEE Trans. Antennas Propag., vol. 67, no. 5, pp. 3527-3532, May 2019.

[154] P. A. Ambresh, P. M. Hadalgi and P. V. Hunagund, "Effect of slots on microstrip patch antenna characteristics," 2011 International Conference on Computer, Communication and Electrical Technology (ICCCET), Tirunelveli, India, 2011, pp. 239-241.

[155] H. Wu and J. Shi, "A wideband dual-slot coupled multiple dense dielectric patch antenna," IEEE Ant. Wireless Propag. Lett., vol. 19, no. 6, pp. 944-948, June 2020.

[156] Z. Qi, Y. Zhu and X. Li, "Compact wideband circularly polarized patch antenna array using self-sequential rotation technology," IEEE Ant. Wireless Propag. Lett., vol. 21, no. 4, pp. 700-704, April 2022.

[157] R. F. Ma et al., "Theory, design, and verification of dual-circularly polarized dual-beam arrays with independent control of polarization: A Generalization of Sequential Rotation Arrays," IEEE Trans. Antennas Propag., vol. 69, no. 3, pp. 1369-1382, March 2021.

[158] M. Jones and J. Rawnick, "A new approach to broadband array design using tightly coupled elements," MILCOM 2007-IEEE Military Communications Conference, Orlando, FL, USA, 2007, pp. 1-7.

[159] L. Zhang, S. Gao, Q. Luo, W. Li, Y. He, and Q. Li, "A wideband circularly polarized tightly coupled array," IEEE Trans. Antennas Propag., vol. 66, no. 11, pp. 6382–6387, Nov. 2018.

[160] I. Tzanidis, K. Sertel, and J. L. Volakis, "Interwoven spiral array (ISPA) with a 10:1 bandwidth on a ground plane," IEEE Ant. Wireless Propag. Lett., vol. 10, pp. 115–118, Mar. 2011.

[161] T. -L. Zhang, L. Chen, S. M. Moghaddam, A. U. Zaman and J. Yang, "Millimeter-Wave ultrawideband circularly polarized planar array antenna using bold-C spiral elements with concept of tightly coupled array," IEEE Trans. Antennas Propag., vol. 69, no. 4, pp. 2013-2022, April 2021.

[162] D. -C. Son, A. Samaiyar, M. A. Elmansouri and D. S. Filipovic, "Design of a circularly-polarized tightly-coupled microstrip patch array," 2021 IEEE International Symposium on Antennas and Propagation and USNC-URSI Radio Science Meeting (APS/URSI), Singapore, 2021, pp. 513-514.

[163] T. Teshirogi, M. Tanaka, and W. Chujo, "Wideband circularly polarised array antenna with sequential rotations and phase shifts of elements." Int. Symp. on Ant. and Prop.(ISAP), Tokyo, Japan, 1985, pp. 117-120.

[164] P. S. Hall, J. S. Dahele, and J. R. James, "Design principles of sequentially fed, wide bandwidth, circularly polarised microstrip antennas," IEE Proc. H-Microw., Antennas Propag., vol. 136, no. 5, pp. 381–389, Oct. 1989.

[165] A. K. Awasthi and A. R. Harish, "Wideband tightly-coupled compact array of dipole antennas arranged in triangular lattice," Int. J. Microw. Wireless Technol., vol. 11, no. 4, pp. 382–389, Dec. 2018.

[166] Laird Technologies, Inc., Chesterfield, MO, USA, 2021, [Online]. Available: https://www.laird.com/sites/default/files/2021-01/RFP-DS-LS%2018062020.pdf.

[167] D. Inserra, G. Wen and W. Hu, "Sequentially rotated circular antenna array with curved PIFA and series feed network," IEEE Trans. Antennas Propag., vol. 66, no. 11, pp. 5849-5858, Nov. 2018.

[168] Southwest Microwave Inc., Tempe, AZ, USA, 2016. [Online]. Available: https://mpd.southwestmicrowave.com/wp-content/uploads/1092-0XA-6-91Y60926-RevB.pdf.

[169] A. S. Emhemmed and A. A. Aburwein, "Surface waves reduction in microstrip antennas," 2013 5th IEEE International Symposium on Microwave, Antenna, Propagation and EMC Technologies for Wireless Communications, pp. 438-442, 2013.

[170] D. M. Pozar, "The active element pattern," IEEE Trans. Antennas Propag., vol. 42, no. 8, pp. 1176-1178, Aug. 1994.

[171] H. Hijazi et al., "Circularly polarized in-band full-duplex antenna array for Ka-band inter-CubeSat links," 2022 20th IEEE Interregional NEWCAS Conference (NEWCAS), Quebec City, QC, Canada, 2022, pp. 80-83.

[172] H. Sun, Y. -X. Guo and Z. Wang, "60-GHz circularly polarized U-slot patch antenna array on LTCC," IEEE Trans. Antennas Propag., vol. 61, no. 1, pp. 430-435, Jan. 2013.

[173] J.-C. S. Chieh, E. Yeo, R. Farkouh, A. Castro, M. Kerber, R. B. Olsen, E. J. Merulla, and S. K. Sharma, "Development of flat panel active phased array antennas using 5G silicon RFICs at Ku- and Ka-bands," IEEE Access, vol. 8, pp. 192669–192681, Oct. 2020.

[174] S. Das, S. K. Sharma, and R. Banerjee, "A 4×4 K/Ka-band sequentially rotated wideband circularly polarized microstrip phased array antenna with stable gain performance," USNC-URSI Radio Sci. Meeting (Joint with IEEE AP-S Symp.), Singapore, Dec. 2021, pp. 25–26.

[175] X. Luo, J. Ouyang, Z.-H. Chen, Y. Yan, L. Han, Z. Wu, T. Yu, and K. Zheng, "A scalable Ka-band 1024-element transmit dual circularly polarized planar phased array for SATCOM application," IEEE Access, vol. 8, pp. 156084–156095, 2020.

[176] S. Das et al., "A flat-panel 8 × 8 wideband K-/Ka-band dual circularly polarized phased array antenna for CubeSat communications," IEEE Trans. Antennas Propag., vol. 71, no. 5, pp. 4153-4166, May 2023.

[177] J. Xu, W. Hong, Z. H. Jiang, H. Zhang and K. Wu, "Low-Profile Wideband Vertically Folded Slotted Circular Patch Array for Ka-Band Applications," IEEE Trans. Antennas Propag., vol. 68, no. 9, pp. 6844-6849, Sep. 2020.

[178] H. Krishnaswamy, G. Zussman, J. Zhou; J. Marašević, T. Dinc, N. Reiskarimian, T. Chen, "Full-duplex in a hand-held device—From fundamental physics to complex integrated circuits, systems and networks: An overview of the Columbia FlexICoN project," in Proc. 50th Asilomar Conf. Signals, Syst. Comput., Pacific Grove, CA, USA, Nov. 2016, pp. 1563–1567.

[179] E. A. Etellisi, M. A. Elmansouri, and D. S. Filipovic, "Wideband monostatic simultaneous transmit and receive (STAR) antenna," IEEE Trans. Antennas Propag., vol. 64, no. 1, pp. 6–15, Jan. 2016.

[180] P. Valaleprasannakumar, M. Elmansouri, and D.S. Filipovic, "Wideband Decoupling Techniques for Dual-Polarized Bi-static Simultaneous Transmit and Receive Antenna Subsystem", IEEE Trans. Antennas Propag., vol. 65, no. 10, pp. 4991-5001, Oct. 2017.

[181] P. Valale Prasannakumar, M. A. Elmansouri, L. B. Boskovic, M. Ignatenko and D. S. Filipovic, "Wideband Quasi-Monostatic Simultaneous Transmit and Receive Reflector Antenna," IEEE Trans. Antennas Propag., vol. 68, no. 4, pp. 2630-2637, April 2020.

Appendix A

Bi-Static Simultaneous Transmit and Receive (STAR) system

A.1 Introduction

With the increasing congestion of the electromagnetic spectrum (EMS), assigning channels to modern wireless services operating at different times (half-duplex) or on different frequencies (out-of-band full-duplex) has become both challenging and inefficient. To address this inefficiency, RF systems that can simultaneously transmit and receive (STAR) at the same frequency and time have been considered. STAR communication systems offer advantages such as reduced latency, higher data rates, increased throughput, the coexistence of data transmission and channel state information, and efficient reuse of the allocated EMS. In electronic warfare applications, a STAR-capable system can simultaneously jam, listen, and protect the entire platform from self-fratricide. Achieving this level of operation is challenging and requires multiple stages of isolation, especially when resources are scarce. STAR antenna systems can be monostatic, bistatic, or quasi-monostatic. Monostatic systems use the same antenna for both transmission and

reception, bistatic systems use separate apertures for transmission and reception, and quasi-monostatic systems use separated transmission and reception apertures that share the same volume determined by the larger antenna. Monostatic and bistatic systems typically maintain high cross-correlation between the transmission and reception beams, with bistatic systems achieving the highest isolation and best performance as antennas.

In this appendix, we first design a 10×10 narrowband array operating at K-band that maintains high-quality circular polarization over wide scanning angles in all cardinal and inter-cardinal planes. Next, we consider a topological reconfiguration where some elements are assigned as transmit (Tx) and others as receive (Rx). This scenario is appropriate when transmit/receive modules are directly attached to each antenna element in the array. For demonstration purposes and to ensure the highest quality radiation patterns from both arrays, we consider an equal aperture split. We then calculate the coupling from the Tx array to each Rx element and from the Tx to the Rx array for different scanning conditions. A simple approach to increase isolation is also evaluated, and relevant conclusions for different active scanning conditions are drawn.

A.2 Design and Performance

The designed array unit cell, shown in Fig. A1.1, features four metal layers on three Rogers 5880 substrates. Two prepreg sheets are used for bonding, and a radome is added for environmental protection. All relevant electrical parameters for this configuration are indicated in the figure. The corners of a 0.9 × 0.9 mm² single stripline-fed patch are chamfered to achieve the necessary current perturbations for elliptical polarization. A wide aperture-coupled parasitic patch is then integrated to

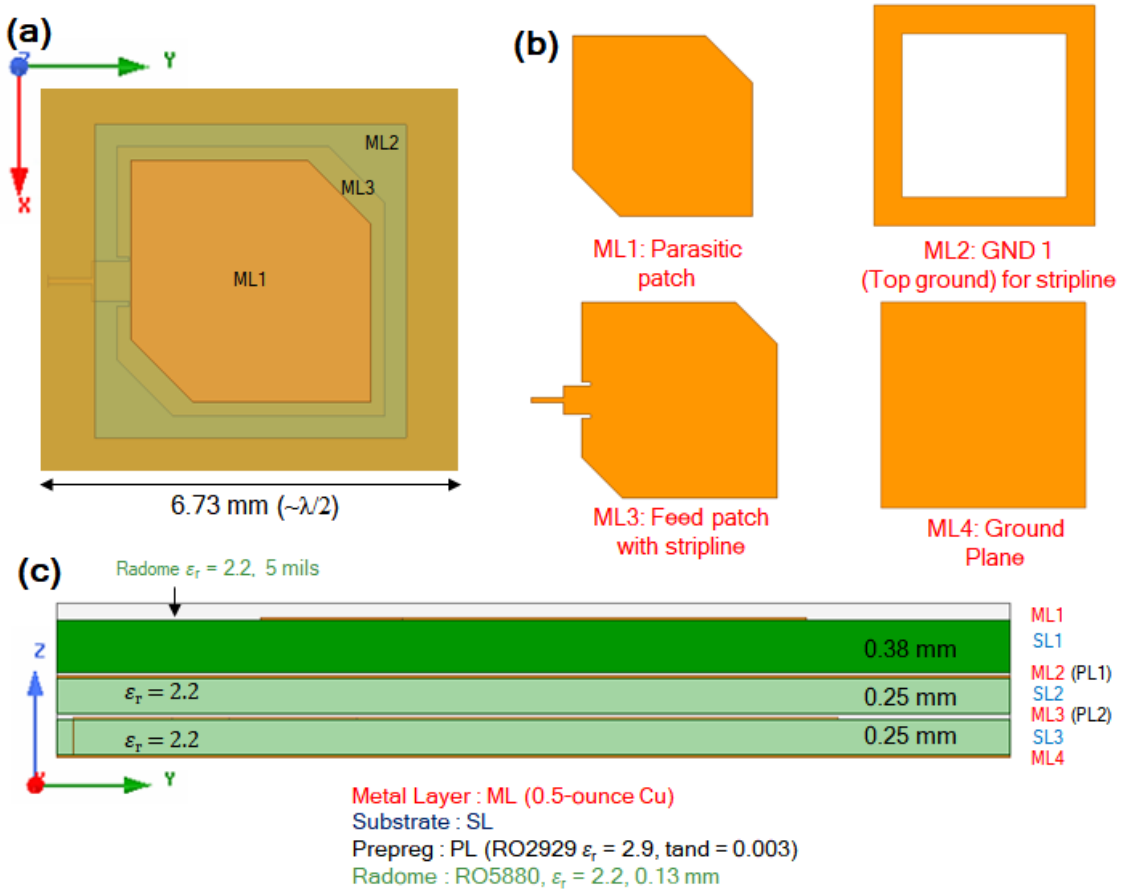

Fig. A1.1: Multi-layer patch antenna geometry: (a) patch parameters, (b) metal layer configurations, and (c) PCB stack up.

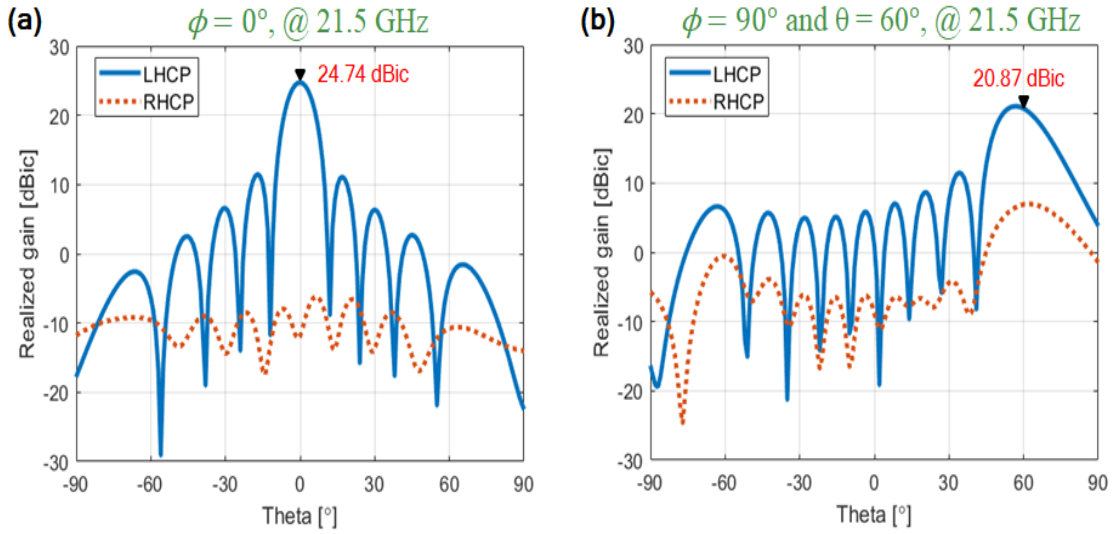

Fig. A1.2: Designed 10×10 phased array: (a) and (b) realized gains at (ϕ, θ) = (0, 0)°, and (0, 60)°, respectively.

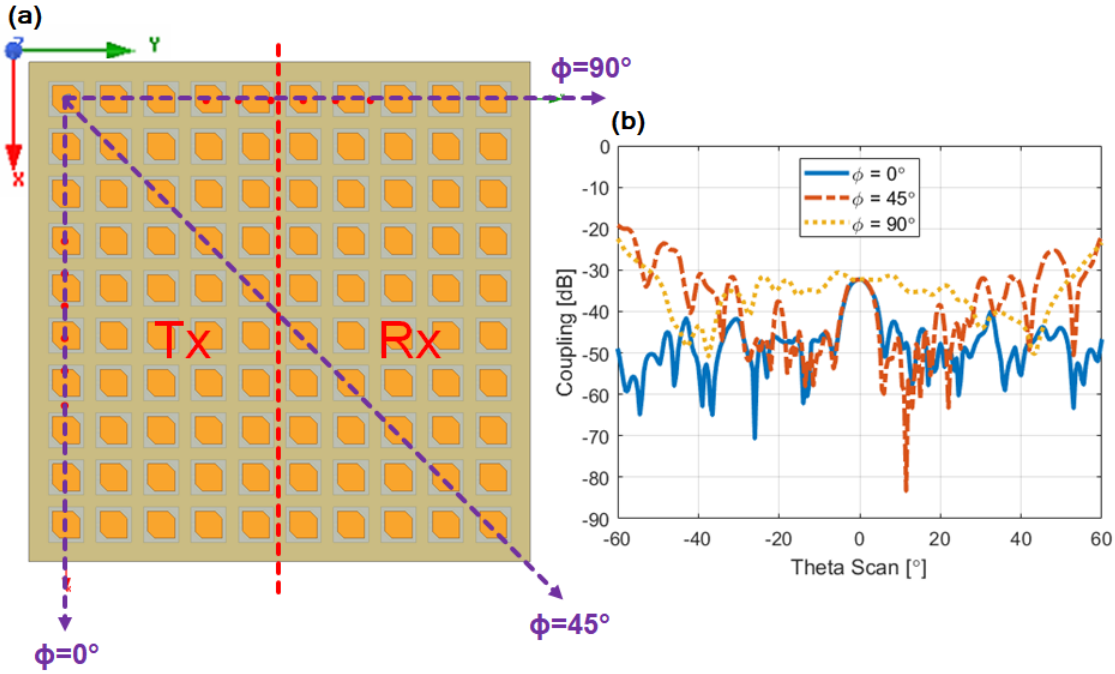

Fig. A1.3: (a) Bistatic array configuration with array split in two halves along ϕ = 0°, and (b) coupling in scan planes ϕ = 0°, 45°, and 90°.

achieve wider bandwidth and, more importantly, wide-angle scanning with a low axial ratio in all azimuthal planes. A 10×10 phased array antenna, incorporating the described unit cell as an embedded element, is designed, and the radiation patterns for two scanning conditions are shown in Fig. A1.2. The design achieves clear cross-polarization discrimination in both beams, maximum aperture efficiency, and expected side-lobe levels and positions.

The simplest reconfiguration with dislocated phase-centers of this phased array aperture for STAR is to assign ½ of the array for Tx and another half for Rx (see Fig. A1.3(a)). This way, we maintain high aperture efficiency for each subsystem while allowing space to factor in the system-level aperture isolation. Fig. A1.3(b) shows the Tx to Rx active couplings for scanning in three different azimuthal planes. As seen, at the design frequency of the array (note this is a narrowband system), the isolation between the Tx and Rx arrays remains more significant than 30dB over wide

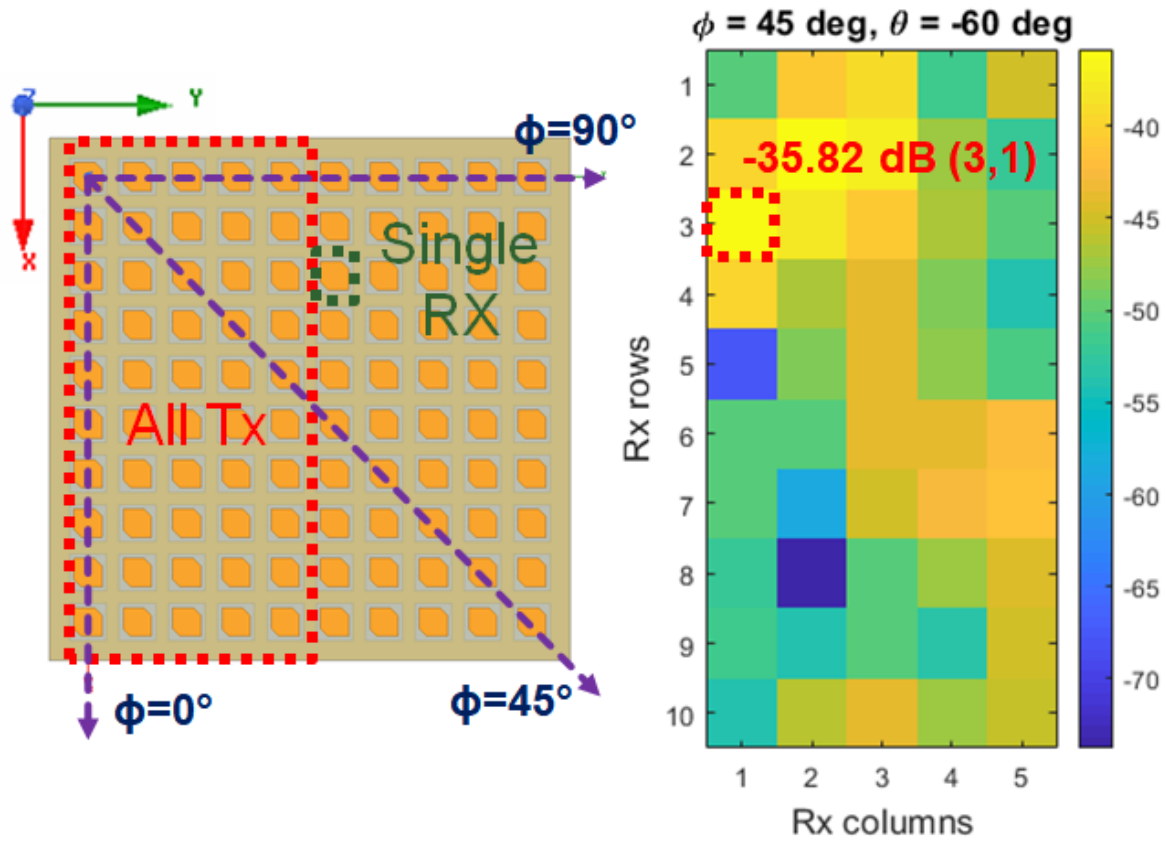

Fig. A1.4: Coupling (worst case : -35.82 dB) between all the Tx elements with a single Rx element (highlighted) at (ϕ, θ) = (45, -60)°.

Table A1.1: Worst case coupling levels for considered scans

ϕ scan / ***θ scan***	**ϕ = 0°**	**ϕ = 45°**	**ϕ = 90°**
θ = 0°	-52.7 dB	*-52.7 dB*	*-52.7 dB*
θ = +15 / -15°	-49.5 / -50.1 dB	*-51.6 / -48.0 dB*	*-53.6 / -53.8 dB*
θ = +30 / -30°	-52 / -50.4 dB	*-45.6 / -47.3 dB*	*-52.8 / -51.6 dB*
θ = +45 / -45°	-48.3 / -45.9 dB	*-38.7 / -35.9 dB*	*-48.4 / -50.8 dB*
θ = +60 / -60°	-44.3 / -46.2 dB	*-39.37 / -35.8 dB*	*-44.5 / -45.3 dB*

elevation scans. As expected, the worst case is when the Tx array scans in the plane along the bisecting axis for the system.

Coupling from the Tx array to each element in the receiving array under worst-case conditions is shown in Fig. A1.4. Results indicate this occurs when the Tx

array scans the intercardinal plane. Specific coupling values for all three cases are provided in Table A1.1. The worst-case isolation is approximately 35 dB, suggesting that robust low-noise amplifiers are necessary for the proper operation of this system. To reduce coupling, the elements on the boundary between the two arrays can be turned off (see Fig. A1.5(a)). For simplicity, a variable load (considered here as short, open, and 93 Ω) is attached to these elements, and active coupling for different scans is computed, with results shown in Figs. A1.5(b)-(d). For comparison, the coupling with all elements ON is also displayed. Significant improvement in isolation of more than 20 dB can be achieved over a narrower field of view for diagonal scans and over a wider field of view for scans in the two cardinal planes. The impact of the load

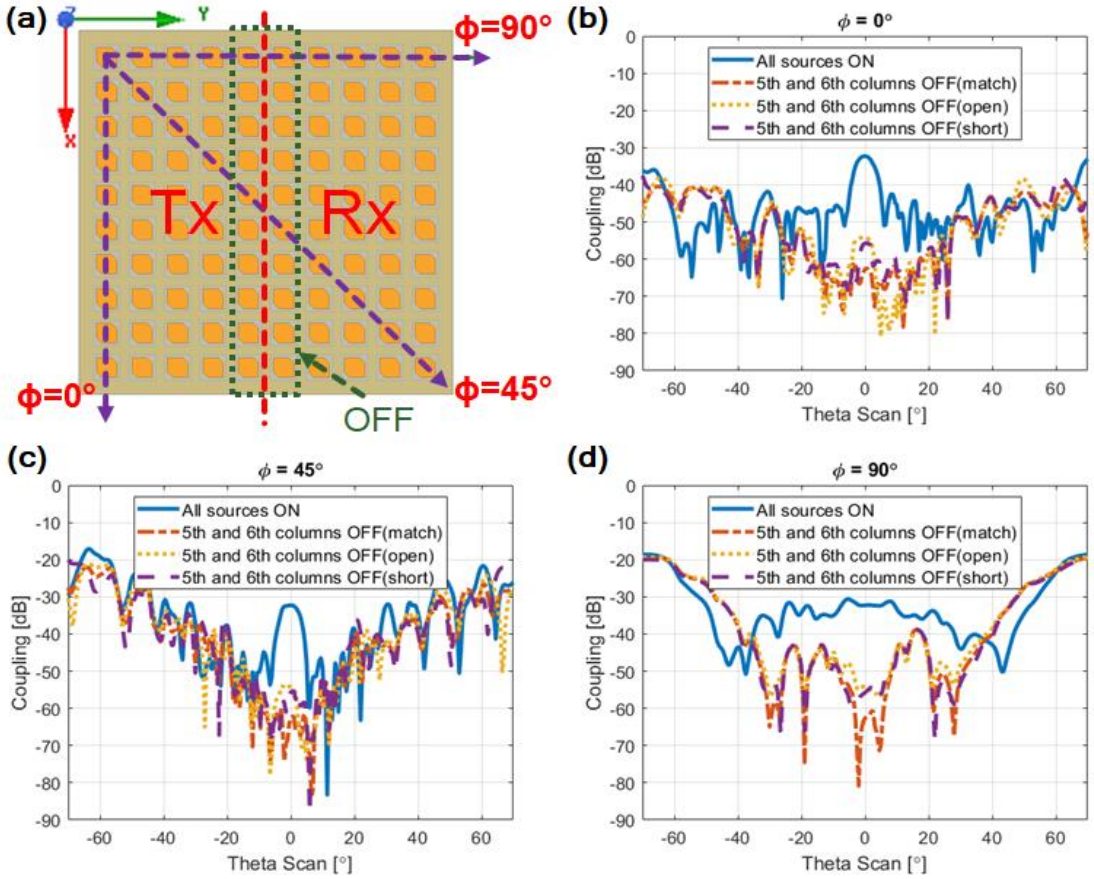

Fig. A1.5: Coupling between Tx and Rx when 5 and 6 columns elements are terminated in matched load, open, and short: (a) configuration, (b), (c), and (d) for scan planes ϕ = 0°, 45°, and 90°, respectively.

appears to be insignificant. It is important to note that the quality of radiation patterns during the scan is maintained; however, this approach results in lower aperture efficiencies, which must be considered. All results presented in this paper were obtained using Ansys HFSS, with proper modeling validations conducted at each design step.

A.3 Conclusion

A K-band circularly polarized planar phased array antenna achieving over 35 dB Tx to Rx isolation in a bistatic split-aperture STAR implementation is discussed. The array is designed for fabrication using a multi-layered PCB process and includes a radome. Element-to-element coupling coefficients determine the isolation from the Tx array to individual elements in the Rx array and the isolation to the fully beamformed Rx array. The approaches considered are simple and maintain good scan pattern integrity; terminating the boundary rows reduces the aperture efficiency.